Coastal Wave Hydrodynamics and Morphological Evolution

Marissa L. Yates

To cite this version:

Marissa L. Yates. Coastal Wave Hydrodynamics and Morphological Evolution. Environmental Sciences. Université Paris-Est, 2019. tel-03941084

HAL Id: tel-03941084
https://hal.science/tel-03941084v1

Submitted on 16 Jan 2023

École Doctorale SIE

Laboratoire d'Hydraulique Saint-Venant

Mémoire

Présentée pour l'obtention du
diplôme d'Habilitation à Diriger des Recherches
de L'UNIVERSITE PARIS-EST
par

Marissa Lauren YATES

L'hydrodynamique de vagues et l'évolution morphologique côtière

Spécialité : Sciences de l'ingénieur

Rapporteur	**Prof. G. Masselink**	(University of Plymouth)
Rapporteur	**Prof. S. Abadie**	(UPPA)
Rapporteur	**Prof. N. Senechal**	(Université de Bordeaux)
Examinateur	**Prof. P. Ferrant**	(Ecole Centrale Nantes)
Examinateur	**Dr. D. Idier**	(BRGM)
Directrice d'habilitation	**Dr. N. Goutal**	(LHSV, LNHE, EDF R&D)

Résumé

Ce manuscrit présente un résumé de mes travaux de recherche qui sont focalisés sur deux thèmes principaux : **l'évolution morphologique des plages** et **l'hydrodynamique de vagues en zone côtière**. Ces deux thèmes sont fortement liés, avec l'objectif commun d'améliorer, à la fois la connaissance des processus physiques qui contrôlent la dynamique en zone côtière, et aussi les modèles numériques capables de reproduire l'hydrodynamique et l'évolution morphologique dans cet environnement complexe.

Le premier chapitre présente succinctement ces deux thèmes, mes projets de recherche, les collaborations que j'ai développées et l'évolution de mes travaux de recherche pendant les 10 dernières années depuis la fin ma thèse. Pendant cette période, j'ai suivi une gamme d'approches différentes pour aborder ces thèmes, allant de l'analyse des observations in situ et des expériences en laboratoire, à la modélisation empirique et numérique des processus observés. Ces approches complémentaires m'ont d'abord permis d'étudier les processus physiques qui contrôlent la dynamique en zone côtière à plusieurs échelles d'espace et de temps pour développer une vision globale de cet environnement complexe. Ces travaux ont de plus contribué à mon deuxième objectif, à savoir le développement des modèles empiriques et numériques pour une variété d'applications, allant de l'évaluation des risques côtiers et l'estimation de la ressource des énergies marines renouvelables, au dimensionnement et à la gestion des structures marines et côtières.

Le deuxième chapitre est dédié au thème de la morphodynamique en zone côtière, avec deux grands axes de travail : (1) l'analyse de l'évolution morphologique des plages, basée sur des observations morphologiques de plusieurs sites d'étude et sur des mesures expérimentales effectuées en laboratoire, pour améliorer la compréhension des variations spatiales et temporelles observées, et (2) la modélisation empirique et numérique de l'évolution des profils de plage, validés avec les observations, pour améliorer les outils de prédiction. Ses travaux m'ont permis d'identifier des questions fondamentales qui continuent de structurer mes thèmes de recherche, en particulier une amélioration de la compréhension des processus d'érosion et d'accrétion, et notamment des variations en espace et en temps à une variété d'échelles. Ces connaissances me permettent de valider des modèles numériques basés sur des processus physiques et de les appliquer aux échelles spatiales locales et aux échelles temporelles des événements, mais aussi de proposer des modèles simplifiés, de type empirique, applicables aux échelles spatiales d'une plage ou d'un secteur du littoral et aux échelles temporelles des saisons, des années, des décennies. Mes travaux en cours explorent différents axes d'amélioration de ces types de modélisation, notamment pour améliorer la prise en compte des processus physiques dans un modèle empirique d'équilibre, incluant le transport longshore, les interactions entre les vagues et le niveau de l'eau et les impacts du changement climatique.

Le troisième chapitre est focalisé sur le thème de l'hydrodynamique de vagues en zone côtière, notamment avec le développement d'un modèle précis de propagation de vagues. Mes travaux de recherche sont concentrés sur deux axes de développement de ce modèle : (1) la prise en compte des processus physiques, et (2) la mise en œuvre numérique du modèle mathématique choisi. L'approche retenue est de développer un modèle complètement non-linéaire et dispersif, basé sur la théorie potentielle, en faisant un compromis entre la représentation des processus physiques et l'efficacité du modèle. Mes travaux en cours poursuivent le développement de ce modèle pour obtenir un modèle capable de simuler la propagation de vagues en zone côtière. Sur le premier axe, je me focalise sur la prise en compte des effets du déferlement de vagues et du run-up. Sur le deuxième axe, mes activités sont concentrées sur l'amélioration de la stabilité du modèle avec le traitement des frontières latérales dans la version 3D et aussi sur l'optimisation de l'efficacité du modèle. Enfin, ses travaux me conduisent à faire des études de comparaison avec d'autres codes existants pour identifier les avantages et les limites des approches retenues pour définir le périmètre des applications de ce modèle.

Enfin, le quatrième chapitre présente les conclusions avec un résumé des axes de travail futur et des collaborations à poursuivre. Les appendices présentent mes activités d'encadrement, d'enseignement et d'animation scientifique, mon curriculum vitae détaillé et une sélection de deux articles de mes deux thèmes de recherche.

Coastal Wave Hydrodynamics and Morphological Evolution

Contents

Chapter 1

Introduction

Throughout my scientific career, I have developed two primary research themes centered on **coastal morphological evolution** and **coastal wave hydrodynamics**. This document presents a summary of these research themes since I completed my PhD at the Scripps Institution of Oceanography (SIO), University of California, San Diego (UCSD) in 2009. I have pursued these subjects through my work as a post-doctoral scholar at UCSD, then as a research engineer at the BRGM (Bureau de Recherches Géologiques et Minières), and finally as a researcher for the CETMEF (Centre d'études techniques maritimes et fluviales), which is now the Technical Department of Water, Sea, and Rivers of the Cerema (Centre d'études et d'expertise sur les risques, l'environnement, la mobilité et l'aménagement), when I integrated in the Saint-Venant Hydraulics Laboratory (LHSV) in 2011.

My two research themes centered on coastal morphological evolution and wave hydrodynamics are closely related, with the common objective of improving the understanding of and capacity to model numerically coastal morphological evolution and wave propagation for a wide range of applications (Figure 1.1). In particular, my research is structured around using **observations** to improve knowledge of the dominant physical processes in the coastal zone and developing tools or **models** able to help marine and coastal engineers and managers evaluate coastal risks, estimate marine energy potential, aide coastal planners, and design and manage coastal structures.

The coastal zone is a highly complex and dynamic environment in which interactions between marine, terrestrial, and atmospheric processes all have an important role. Thus, it is critical to improve understanding of the dominant physical processes in coastal and maritime environments, and to do so, hydrodynamic and morphodynamic processes must be studied at a wide range of spatial and temporal scales. To achieve this, thoughout my work I have used different, complementary approaches, including in situ observations, laboratory experiments, theoretical analyses, and numerical models. Each of these approaches provides essential contributions to enhance the overall understanding of this complex environment.

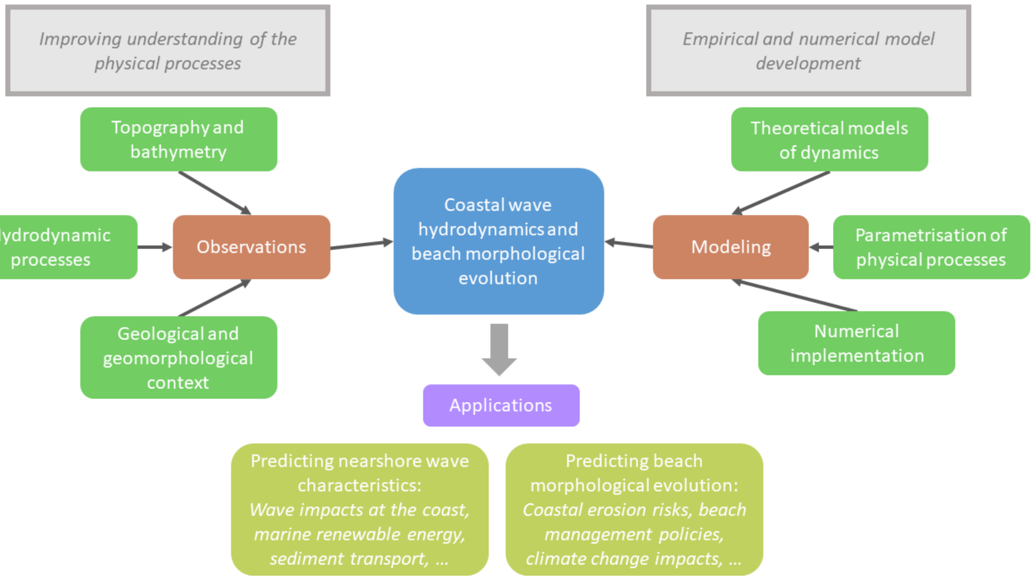

Figure 1.1: Summary of research themes, approaches applied, research objectives, and applications of this work.

Furthermore, research in these domains, focused on increasing knowledge of and predicting coastal hydrodynamics and beach morphological evolution has accelerated in recent decades. This acceleration is related to efforts to reduce the vulnerability of the coastal zone and society's energetic footprint, as well as to increased interest in using the ocean as a resource, all of which have become important public issues. Thus research in the fields of coastal hydrodynamics and beach morphological evolution have also increased to meet these demands. Much work remains to be done in these two broad fields, in particular in predicting large-scale, coastal morphological evolution on annual to decadal time scales, and in improving the ability to simulate accurately and efficiently nonlinear wave propagation in the nearshore zone. My work is focused on these two subjects, including identifying the fundamental research questions and using a variety of approaches to advance both understanding of the important physical processes and tools used to model them.

This document is organized in two chapters centered on these research themes, which are introduced briefly in the following two sections. In each chapter, the state of the art is presented before highlighting my main contributions, with selected articles included in the associated appendices at the end of the document.

Coastal morphological evolution

For coastal management and planning purposes, it is essential to further our understanding of the physical processes controlling coastal evolution at a wide range of spatial and temporal scales.

To address this need, I have combined a variety of approaches, including in situ observations of the complex environment, controlled laboratory experiments focusing on specific physical processes, and numerical studies reproducing the observations. I began to develop this research theme during my thesis and post-doctoral research at the Scripps Institution of Oceanography at UCSD. My work was focused on the observation and analysis of a unique, long time series of beach topographic surveys and wave conditions, which led to the development of an empirical equilibrium shoreline change model capable of reproducing the nearly decade-long observations of seasonal shoreline position variations. Following my post-doctoral work, I continued investigating shoreline evolution, this time focusing on longer time scales, while working in the Coastal Risks unit at the BRGM. I applied a variety of different statistical techniques to analyze historical shoreline position changes and to evaluate the predominant factors causing the observed morphological changes, with the objective of predicting future beach evolution. Since being recruited as a researcher with the CETMEF, now Cerema, I have expanded my research activities in this field to further understanding of equilibrium beach profiles and beach evolution, and to improve empirical and numerical modeling of observed morphological changes. I have used two main approaches, and my work during this time period has included notably:

Data-based shoreline evolution analyses

- investigating the principal forcing factors causing **local and large-scale spatial variability of shoreline evolution** using both qualitative and quantitative (e.g. machine learning) approaches;

- studying **short and medium-term beach morphological evolution** using laboratory experiments and in situ observations of beach profiles at several study sites;

Modeling beach evolution

- evaluating **process-based modeling of storm-induced beach profile evolution** with and without the presence of submerged structures; and

- extending the application of the **equilibrium beach change model** developed during my thesis to include the effects of the tide level and alongshore processes, through the development of a collaboration with researchers at the Institut Universitaire Européen de la Mer - Université de Bretagne Occidentale (IUEM-UBO) and in an international collaboration with the Port and Airport Research Institute (PARI), Kyoto University, and Toyohashi University of Technology in Japan within a Programme Hubert Curien (PHC) Sakura project.

Chapter 2 presents these research topics, describing previous work and outlining perspectives for future work and ongoing collaborations in this field.

Coastal wave hydrodynamics

In the field of coastal wave hydrodynamics, there exists a need for highly accurate and efficient nonlinear wave propagation models capable of simulating wave propagation and transformation at spatial and temporal scales relevant for applications in the nearshore zone. To achieve this goal, it is necessary to reproduce nonlinear interactions (including wave-wave and wave-bottom) and dispersive effects, including irregular, multidirectional sea states, and spatially and temporally varying bathymetries. A wide variety of mathematical and numerical modeling approaches have been developed over the last few decades to take into account some or all of these aspects, including:

- models based on the Reynolds-Averaged Navier-Stokes equations, calculating directly the nonlinearities, viscosity, and vorticity of a flow using Eulerian (e.g. OpenFOAM, Higuera et al., 2013a,b) or Lagrangian (e.g. SPH, Dalrymple and Rogers, 2006) approaches;
- potential flow theory models neglecting viscosity and turbulent effects, including fully nonlinear potential flow (FNPF) models (e.g. Grilli et al., 1989; Bingham and Zhang, 2007), or partially nonlinear and dispersive Boussinesq-type models (e.g. Nwogu, 1993; Madsen and Schäffer, 1998; Kennedy et al., 2001), and Serre-Green-Naghdi-type models (e.g. Bonneton et al., 2011);
- Nonlinear Shallow Water Equation models assuming that the wavelength is much larger than the water depth and thus that the flow is either homogeneous in the vertical (e.g. Open Telemac system, Galland et al., 1991) or can be divided into a series of vertical layers (e.g. SWASH, Stelling and Zijlema, 2003; Zijlema and Stelling, 2005);
- mild-slope equation models based on linear wave theory (e.g. REF-DIF, Kirby and Dalrymple, 1983).

However, this field of research remains largely open owing to the difficulties to reproduce accurately the nonlinear and dispersive wave effects, while maintaining reasonable calculation times for the desired spatial and temporal scales. Each of the families of models listed above are appropriate to be used for specific applications. For example, RANS models are an optimal choice for simulating wave breaking using local-scale, two-phase models, while simplified, Boussinesq or FNPF models may be sufficient for other applications, such as simulations of wave propagation in coastal and littoral zones. The final goal of this work is to develop and validate a nonlinear wave propagation model for marine and coastal research and engineering applications.

Since my arrival at the LHSV, I have co-developed a fully nonlinear and dispersive wave propagation model in collaboration with Michel Benoit, several interns, a thesis student, and two post-doctoral researchers whom we co-advised (within the ANR-France Energies Marines DiMe project and the LaBeX DEPHYMAN project). The model is based on fully nonlinear potential flow theory, assuming an inviscid fluid, incompressible and irrotational flow, and a continuous water column from the bottom to the free surface. These assumptions lead to a coupled set of nonlinear equations expressing the temporal evolution of the free surface position and potential, called the Zakharov equations (Zakharov, 1968). Significant contributions to the development of this model have included work both on the numerical implementation and efficiency of the 1DH and 2DH (one and two horizontal dimension) versions of this model, and on the representation of a range of physical processes, including:

- demonstrating the **accuracy and efficiency** of using a spectral approach to solve the "Dirichlet-to-Neumann" (or DtN) problem in the vertical to advance in time the Zakharov equations;
- taking into account **viscous effects** in the 1DH version of the model;
- **extending the model to 2DH** using a radial basis function - finite difference approach;
- including the **effects of wave breaking**.

These topics will be described in Chapter 3, and perspectives for future work and collaborations to develop in this field will be outlined.

Chapter 2

Coastal morphological evolution

2.1 Scientific context and challenges

In the highly dynamic coastal environment, a wide range of physical processes contribute to coastal morphological evolution, and they can be grouped into five broad families (Figure 2.1, Bird, 1996; Stive et al., 2002; Le Cozannet et al., 2014): hydrometeorological factors, human activities, biological processes, external geodynamic processes, and internal geodynamic processes. Climate change may be considered as an additional factor that impacts all of these families. Often, studies aimed at understanding coastal geomorphological changes focus primarily on the hydrometeorological factors, including waves, wind, and sea level (e.g. Aubrey, 1979; Morton et al., 1995; Fenster et al., 2001; Zhang et al., 2004; Coco et al., 2014; Harley et al., 2017), determining quantitative relationships between these factors and the resultant shoreline or beach profile changes. The remaining forcing factors or impacts are often more difficult to quantify and may be taken into account with more qualitative approaches (e.g. Gornitz et al., 1994; Shaw et al., 1998; McLaughlin and Cooper, 2010; Garcin et al., 2013). However, it is important to remember that these factors may be dominant at a given site. In particular, the challenges associated with identifying long-term morphological changes are often attributed to a lack of long-term observations, but it is essential to be able to quantify both the morphological trends and the forcing factors that cause these changes at the appropriate timescales (Burningham and French, 2017). An additional challenge is to be able to distinguish the impacts of different physical processes acting on different temporal scales (Hapke et al., 2016). Thus, it is important to develop an understanding of the local complexity of a given environment, including the general geomorphological and historical context, as well as the local hydrometeorological and other factors that may have a strong impact on morphological evolution.

Before discussing further coastal evolution, it is necessary to define the terminology used to describe a beach system, as shown for a representative beach profile in Figure 2.2. As waves propagate across the continental shelf and approach the shore, the offshore limit of the nearshore

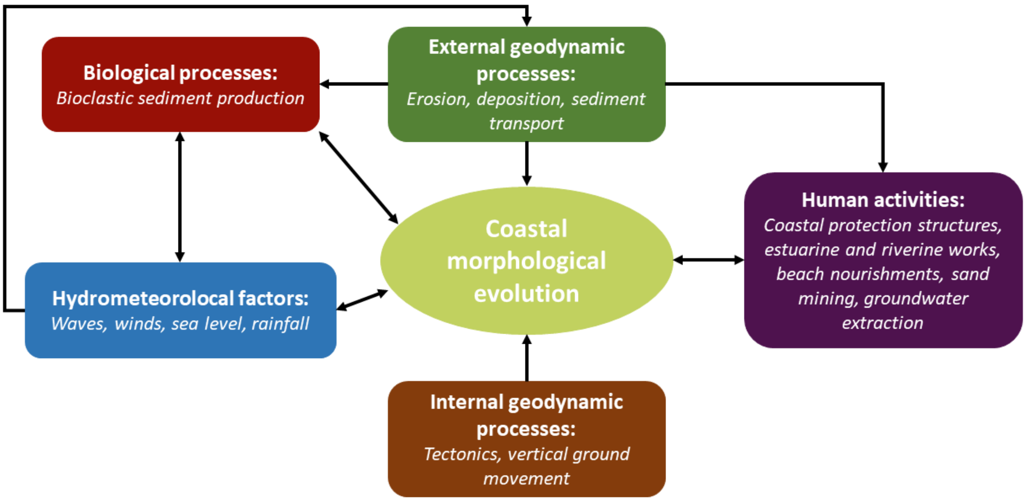

Figure 2.1: Families of forcing factors and important physical processes impacting coastal and shoreline changes, following Bird (1996), Stive (2004), Garcin et al. (2011), and Le Cozannet et al. (2014). One may consider climate change as an additional factor that impacts all of the families shown.

zone is typically defined by the depth of the wave base (water depth at which waves interact with the bottom, which depends on the wavelength), also referred to as the depth of closure, which depends on the wave height and wavelength (Hallermeier, 1980). Waves shoal in the nearshore zone as they interact with the bottom and then begin breaking in the surf zone. Depending on the wave exposure and tidal regime, a beach system may contain between 0 - 2 bars in the surf zone (and more than 2 bars along the full intertidal profile). The waterline limit varies temporally with wave action, and this part of the beach that is intermittently covered by water is referred to as the swash zone. The swash zone extends from the moving waterline up the exposed beach face to the base of dunes (if present) or higher, depending on the wave conditions. This zone, from the depth of closure to the upper limit of the swash zone is often referred to as the active beach profile, along which wave-induced cross-shore sediment transport causes erosion and accretion. Farther landward, aeolian processes and interactions with vegetation dominate dune evolution.

A beach system may also be classified by its tidal range, defined as the difference between low and high tide levels. Davies (1964) created a classification of tidal ranges that may also be used to describe the tide range on beaches (Masselink and Short, 1993): microtidal (<2m), mesotidal (2-4m), and macrotidal (>4m). In Figure 2.2 (bottom), the cross-shore beach profile is divided into three tidal zones: the subtidal zone, which is remains submerged, the intertidal zone, which is emerged or submerged as a function of the tide level, and the supratidal zone, which remains emerged. The tidal range of a beach may have a strong impact on the nearshore morphology and its evolution (Masselink and Short, 1993).

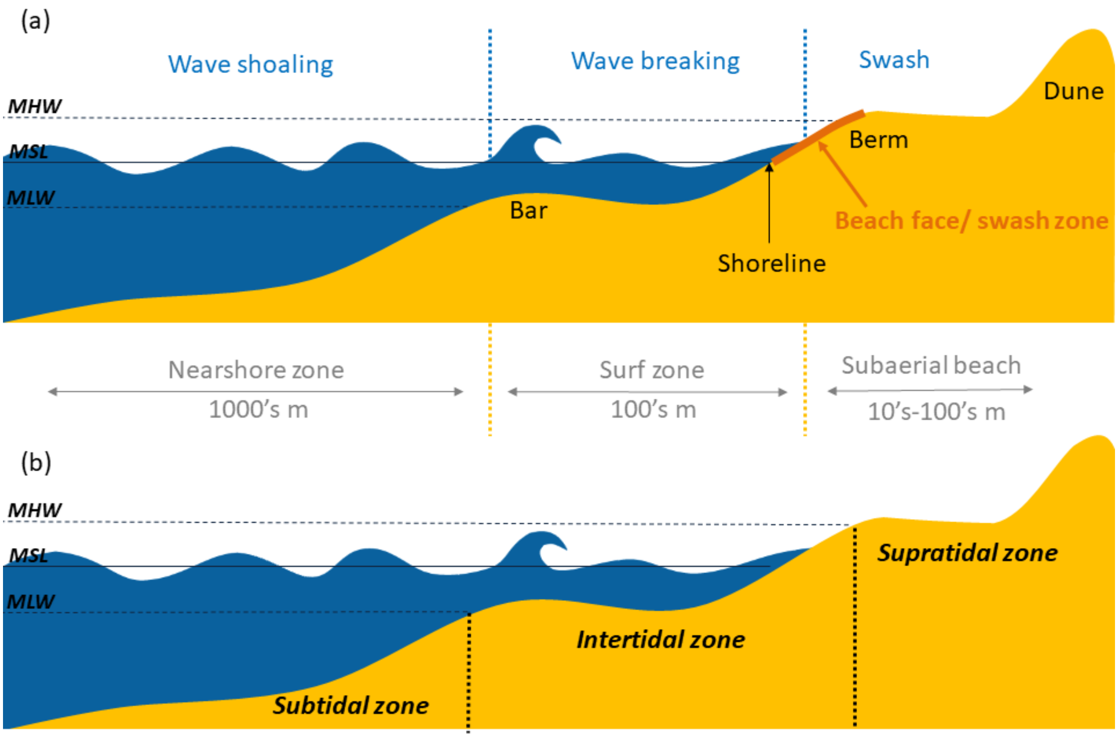

Figure 2.2: Diagram of a beach system identifying the main beach features, based on Figure 4.1 of Short and Woodroffe (2009). (a) For each zone, wave processes are described in blue and the morphology and spatial scales are described in gray. Three tidal datum are also indicated with horizontal lines: mean low water (MLW), mean sea level (MSL), and mean high water (MHW). (b) The vertical dotted lines indicate the horizontal extent of the three tidal zones, as defined by the vertical tidal datum.

Beach evolution occurs at a variety of spatial and temporal scales, related to the scales of the forcing conditions. The observed morphological evolution often is controlled primarily by the hydrodynamics (Figure 2.3, top), which causes the formation of different morphological features (Figure 2.3, bottom). For example, at the smallest temporal and spatial scales of the spectrum, turbulence acts at the scales of interactions between grains of sand. At longer timescales of seconds to minutes and hours, swash processes, waves, wave groups, surf zone currents, and storms become important, causing the formation of ripples and bars, and playing an important role in shoreline and dune evolution. At even longer temporal scales and larger spatial scales, storms, flooding events, tidal variability, shelf circulation, and sea level changes all interact to cause shoreline, dune, and coastline evolution.

Here, it is important to point out a difference in terminology between *shoreline* and *coastline* evolution. As defined by Woodroffe (2002), the shoreline is the margin between the land and the

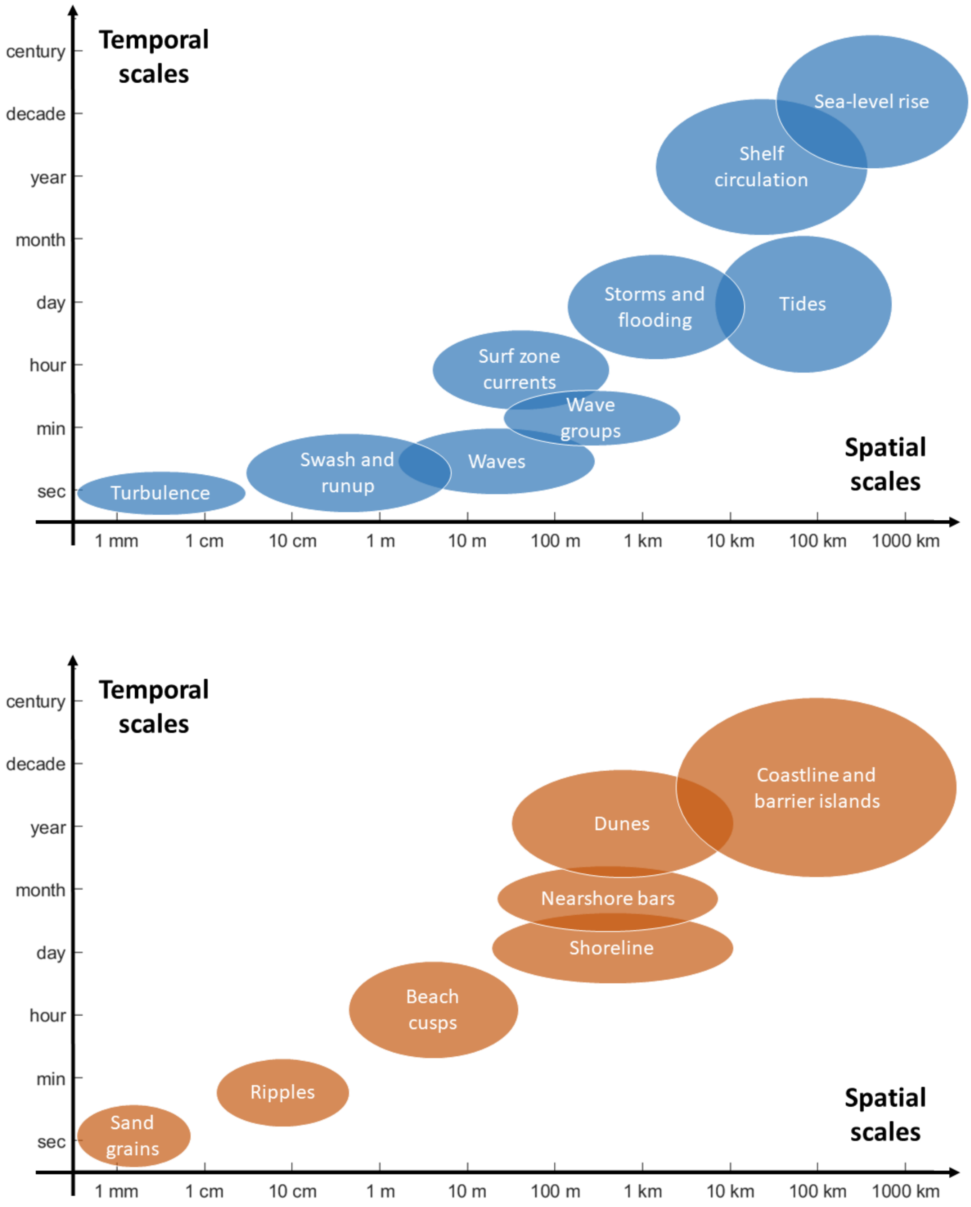

Figure 2.3: Temporal and spatial scales of important hydrodynamic processes (top, blue) and the resultant morphodynamic features (bottom, orange).

sea, whereas the coast is a much broader zone, including features above and below the waterline (e.g. cliffs, dunes, offshore bars). Thus the term shoreline evolution typically refers to the local-scale processes impacting the position of the limit between the land and the sea, and coastline evolution typically refers to larger spatial scale and the associated longer time scale changes (Figure 2.3, bottom).

In recent decades, the evaluation of coastal vulnerability has received increased attention owing to observations of coastal erosion and flooding, and their effects on coastal infrastructure and populations, and increased concerns about the impacts of sea-level rise and climate change in the coming decades (Nicholls et al., 2007; Le Cozannet et al., 2014; IPCC, 2014, etc.). The last concern is of particular importance for the development of local coastal management practices, which require methods to characterize the future response of beaches to climate change, including the impacts of changes in the wave climate and the mean sea level (e.g. Cooper and McLaughlin, 1998; Nicholls and de la Vega-Leinert, 2008; Hinkel and Klein, 2009; Nicholls et al., 2014; French et al., 2016; Dean and Houston, 2016). Shoreline change observations can be used as a proxy for estimating beach morphological changes (Smith and Bryan, 2007), as shown by the relationship between shoreline and beach volume variability (Farris and List, 2007; Harley et al., 2011).

Beach morphological change studies focused on understanding these different processes use a variety of different approaches that can be categorized broadly. Recently, Le Cozannet et al. (2014) reviewed existing approaches used to evaluate long-term shoreline changes in response to sea-level rise, distinguishing data-based and modeling approaches. While this review was focused on the long-term impacts of sea-level rise, the distinction between different types of coastal evolution studies is relevant more generally for classifying different types of shoreline evolution studies (Figure 2.4).

Within the category of data-based approaches, they further distinguished studies that focused on searching for common spatial or temporal trends between the forcing factors and the observed shoreline changes. Examples of some of the applied approaches include estimating direct correlations or using machine learning approaches to seek relationships between the observed forcing factors and resultant morphological changes. The distinction between modeling spatial versus temporal trends is discussed less often since numerical models often address both the spatial and temporal dynamics. Different types of modeling approaches are used to reproduce shoreline and coastline evolution, and they can be divided into two broad categories of models: *behavior-oriented models* and *process-based models*. Each of these categories can further be divided into subcategories, as will be discussed in Section 2.3. Research in recent decades has focused on using all of these methods to characterize historical decadal-scale coastal evolution and to predict short to long-term, future coastal evolution (Le Cozannet et al., 2014).

I began studying beach morphological evolution during my thesis work at the Scripps Institution of Oceanography at UCSD. Since the completion of my PhD in 2009, I have strived to improve understanding of the dominant physical processes causing shoreline evolution, and my work has covered a wide range of spatial and temporal scales, from the response of beach profiles to individual storms, to the analysis of observations of tens to hundreds of kilometers of decadal-scale coastal evolution. As outlined above, it is necessary to investigate the physical processes governing morphological evolution at a range of spatial and temporal scales to develop a complete understanding of the dominant physical processes at a given site. To accomplish this, I have applied a variety of approaches including analyzing in situ observations, conducting laboratory experiments, and developing and applying empirical and numerical models.

During the last 10 years, I have used both data-based and modeling approaches to characterize historical beach morphological changes and to predict future changes on medium to long temporal scales, and local to regional spatial scales. Here, section 2.2 outlines my work using data-based approaches to evaluate beach morphological evolution. The first half of section 2.2 describes my research at the BRGM using data-based approaches to analyze the large-scale spatial variability of decadal-scale shoreline changes, in collaboration with Gonéri Le Cozannet and Manuel Garcin. Then, the second half of section 2.2 presents my work evaluating the short (event-scale) and medium term (seasonal to interannual scale) temporal dynamics. These studies have been carried out since my arrival at the LHSV laboratory, while I co-advised the post-doctoral research of Mathieu Gervais focusing on laboratory measurements of storm-induced beach erosion, and while I have been working in collaboration with a group of researchers from the IUEM, in particular, Nicolas Le Dantec, France Floc'h, and Serge Suanez (co-advising five Masters interns and now one PhD thesis), studying the morphological evolution of two beaches in Brittany.

To extend my work beyond the analysis of these observations, I bridged the gap between data-based and modeling approaches. My research focused on modeling beach evolution is presented in section 2.3 through two studies concerning the validation and application of a process-based numerical model (during the Masters internship of Marine De Carlo), and the ongoing development of an empirical equilibrium shoreline change model in collaboration with Nicolas Le Dantec and France Floc'h. This second theme represents a significant part of my research focus in recent years. During five Masters internships and now the PhD studies of Teddy Chataigner, we have applied the empirical equilibrium shoreline change model developed during my thesis work at two study sites in Brittany. This work has allowed an evaluation of the advantages and limitations of the proposed approach and led to the extension of the model to take into account

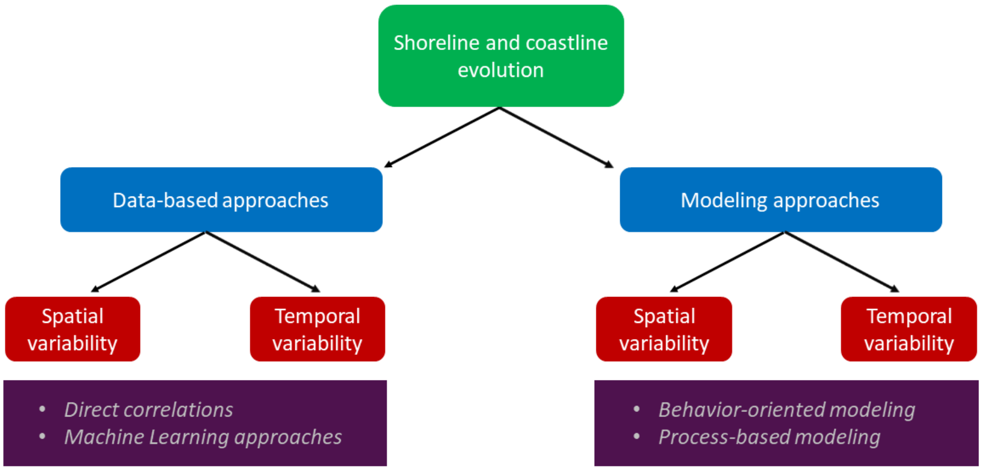

Figure 2.4: Classification of different types of shoreline and coastline evolution studies

additional physical processes not considered initially. In addition, since 2018, I am the French coordinator of a PHC (Programme Hubert Curien) Sakura project in collaboration with a team of Japanese researchers from the PARI (Port and Airport Research Institute), Kyoto University, and Toyohashi University of Technology. This project is focused on advancing the methods used for taking into account the impacts of climate change in equilibrium morphological change models.

Thus, throughout the last 10 years, I have used data-based and modeling approaches to evaluate coastal evolution on short-term to multi-decadal timescales and local to regional spatial scales, allowing me to outline the advantages and limitations of each method and to demonstrate how these different approaches are complementary. With this field of study, I have co-advised six Masters interns, one post-doctoral researcher, and one PhD student (2018-2021), and this work has been published in nine peer reviewed articles, two of which are presented in Appendix C.

2.2 Data-based shoreline evolution analysis

The objective of data-based shoreline evolution studies is to characterize shoreline change variability, to identify the dominant forcing factors, and to analyze how the shoreline variability is related to those forcing factors. Long-term shoreline evolution analyses rely on the existence of long-term observations of both shoreline position and the forcing factors (e.g. hydrometeorological factors, etc. Figure 2.1). The most commonly used approach to search for a relationship between forcing factors and the resultant morphological evolution is to investigate the direct spatial or temporal correlation between the desired quantities (e.g. Wright and Short, 1984; Morton et al., 1995; Garcin et al., 2013). For example, previous work has focused on comparing observations of morphological evolution with either: (1) the spatial variability beach characteristics, such as sand grain size or sediment fall velocity, or wave forcing conditions (e.g. Hapke et al., 2009; Yates et al., 2009b; Bradbury et al., 2013; Lazarus et al., 2011), or (2) the temporal variability of hydrometerological factors such as the wave height or wave energy flux (e.g. Morton et al., 1995; Lee et al., 1998; Anthony, 1998; Jiménez et al., 2008).

As previously mentioned, studies are often limited by a lack of long-term observations or by the uncertainties inherent in these qualitative or quantitative data (Le Cozannet et al., 2014; Garcin et al., 2016). However, in recent years there has been a rapid increase in the quantity and quality of high spatial and temporal resolution observations (Goldstein et al., 2018), including topographic and bathymetric data from GPS land and airborne (e.g. Lidar) based surveys, long-term wave buoy observations or hindcast model outputs, etc. These observations have renewed interest in efficient, empirical, data-driven approaches seeking to determine the dominant relationships between the forcing factors and the observed morphological response.

Previously, historical observations of coastal morphological changes often were used to estimate past trends, which were then simply extrapolated to predict future evolution (e.g. Shows, 1978; Council, 1990). This approach is still widely used by coastal planners and managers owing to its simplicity. However, it is limited by the assumption that the forcing factors causing historical changes do not evolve in time, and thus that historical shoreline change trends will be representative of future shoreline changes.

More recently, a range of approaches have been applied to search for more complex relationships between a range of qualitative and quantitative parameters using statistical, data-driven, or machine learning (ML) techniques to derive empirical relationships that may be used to forecast future morphological changes. Goldstein et al. (2018) present a detailed but non-exhaustive review of a wide variety of these techniques and their applications to estimate sediment transport, nearshore bar dynamics, shoreline evolution, and dune erosion, using Bayesian Networks (BN, e.g. Gutierrez et al., 2011; Yates and Le Cozannet, 2012; Plant et al., 2016), Artificial Neural Networks (ANN, e.g. Pape et al., 2007; Tsekouras et al., 2015; López et al., 2017), Genetic Algorithms or Programming (GA or GP, e.g. Grimes et al., 2015), Regression Trees (RT, e.g. Oehler et al., 2012), and Nonlinear Forecasting (NF, e.g. Jaffe and Rubin, 1996; Pape et al., 2007; Grimes et al., 2015). While nonlinear forecasting is not technically a ML technique, the authors present this approach with the other ML techniques since they are often used in conjunction. For more details concerning these different approaches, see Goldstein et al. (2018) and the primary references cited within.

Within this context of expanding data sets increasing interest in ML techniques, during my work at the BRGM, I used data-based approaches to relate historical observations of shoreline change to the primary forcing factors causing these changes. Two different methods were applied to address these questions by comparing the spatial variability of the potential forcing factors and morphological evolution trends with:

1. a quantitative approach using Bayesian networks to evaluate large-scale (but low resolution) variability using an existing European-scale database (section 2.2.1), and
2. a qualitative approach relating local-scale (high spatial resolution), long-term historical observations of shoreline changes on two Pacific atolls (section 2.2.2).

Then, extending beyond the analysis of the observed spatial variability, it is necessary to study the temporal variability of shoreline changes with high temporal resolution observations. In the LHSV, I have focused my recent work on studying two temporal scales, addressing:

1. short-term, storm-induced beach profile evolution in laboratory experiments, with and without the presence of submerged structures (section 2.2.3), and
2. medium-term, seasonal to interannual beach morphological evolution using monthly or more frequent observations of beach profiles at two study sites in Brittany (section 2.2.4).

These four studies, investigating the spatial and temporal variability of beach morphological evolution are described briefly in the next four sections.

2.2.1 Large-scale shoreline change variability analysis using Bayesian networks

In collaboration with Gonéri Le Cozannet (BRGM), I completed a large-scale analysis of decadal-scale shoreline changes using a ML technique using the European-scale Eurosion coastal dataset (http://www.eurosion.org). A Bayesian network was created to test statistically the relationship between quantitative estimations of the forcing factors, qualitative observations or characterization of the coastal zone, and the resultant coastal evolution, following the work of Gutierrez et al. (2011). Bayesian networks (BNs) previously have been used in a wide range of studies from artificial intelligence to ecological systems (Berger, 2000). Hapke and Plant (2010), Gutierrez et al. (2011), and Plant and Holland (2011) then applied this approach to study coastal (shoreline and cliff) morphological evolution and vulnerability. The objective of our study was to test the ability of BNs to “predict” large-scale shoreline evolution variability using conditional probabilities linking the existing observations.

The BN approach is based on the application of Bayes’ theorem (Bayes, 1763) relating the probability (p) of an event (F_i) to the occurrence of another event (O_j):

$$p(F_i|O_j) = p(O_j|F_i)p(F_i)/p(O_j). \tag{2.1}$$

The theorem relates the conditional dependencies of a set of quantitative or qualitative variables and is used frequently to estimate the likelihood that a particular cause contributes to a given event. In this work, a BN was constructed to evaluate the probability of the outcome of shoreline erosion or accretion (F_i) as a function of five variables (O_j, Figure 2.5), including mean significant wave height (H_s), mean tidal range, geomorphology, relative sea-level rise rate, and geology. The variables selected here were based on hypotheses about their potential contribution to shoreline changes, as well as the availability of data in the Eurosion database. They

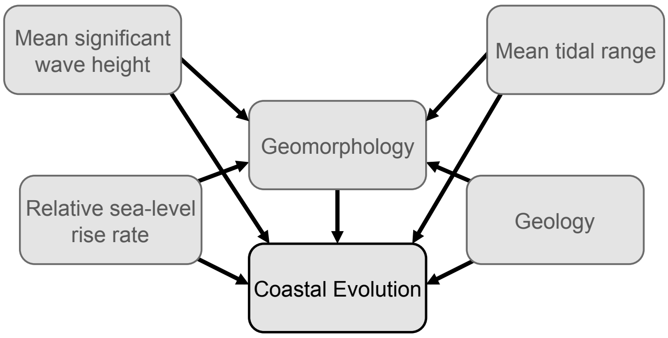

Figure 2.5: Bayesian network: the black arrows indicate the assumed causal relationships linking the forcing factors (gray boxes) and the response variable (coastal evolution, black box) (Yates and Le Cozannet, 2012).

Table 2.1: Bayesian Network qualitative characteristic categories

Geomorphology	**Geology**	**Shoreline evolution trend**
Rocky cliffs and platforms	Hard	Eroding
Erodible (sand, clay, etc.) cliffs	Soft	Stable
Beaches		Accreting
Wetlands		

correspond to the most commonly used indicators of coastal vulnerability (e.g. for the development of Coastal Vulnerability Indices (or CVI) in Daniels et al., 1992; Gornitz et al., 1994, 1997; Shaw et al., 1998; Doukakis, 2005) and are similar to those used in previous coastal vulnerability studies (e.g. Thieler and Hammar-Klose, 1999; Coelho et al., 2006; Gutierrez et al., 2011). It is important to point out here that one of the benefits of using the BN approach is the ability to draw probabilistic relationships between both quantitative and qualitative data, not limiting the analysis to estimates of correlations between quantitative variables.

In the BN, the variables are linked by causal relationships (black arrows, Figure 2.5), which were predetermined based on physical knowledge of coastal systems. The geology, mean significant wave height, relative sea-level rise rate, and mean tidal range impact the geomorphology through the erodibility of the sediments and underlying substrata, wave action causing sediment transport, and profile adjustments to the current mean sea level. Finally, it is also assumed that all five factors additionally impact directly the coastline evolution.

The geology, geomorphology, and shoreline evolution characteristics, and the offshore wave, tidal, and sea-level rise data were obtained from the EUROSION database (EUROSION, 2004). For more details concerning the data, see Yates and Le Cozannet (2012) and the references cited therein. The continuous, quantitative observations were discretized into four bins using quantiles, and the qualitative data were characterized as shown in Table 2.1. These observations were then used to calculate the conditional occurrence probabilities (Eq. 2.1) of a given shoreline evolution for each combination of variables using the Netica software package (Norsys Software Corp., v4.16).

2.2.1.1 BN model performance

The BN approach predicted the most likely coastal evolution outcome (erosion, stability, or accretion, Figure 2.6, right) by assigning to each combination of variables the coastal evolution outcome with the maximum probability (p), thus providing the level of uncertainty of the prediction (p ranges from 36 to 99%). No model prediction is made when no data is available or when all events have the same probability. This simple model correctly reproduces 65% of the observations (Figure 2.6, left).

A second measure of the model performance is the log-likelihood ratio (LR), which measures the improvement in the prediction probability when using the model (Gutierrez et al., 2011) when compared to the probability of the event occurring:

$$LR = log[p(F_i|O_j)] - log[p(F_i)]. \tag{2.2}$$

The LR is positive when the updated prediction is greater than the prior prediction, indicating that the updated distribution is either more accurate (the distribution corresponds to the observations) or more precise (the distribution is narrower). The LR ratio is positive for approximately 70% of all observations in this study and is most heavily influenced by the geomorphological characteristics (for more details see Yates and Le Cozannet, 2012).

2.2.1.2 BN predictions of shoreline evolution trends

The spatial distribution of the difference between the predicted and observed trends highlights areas in which the model is successful (Figure 2.6, left). The highest prediction probabilities are observed in areas with rocky cliffs or platforms (with mostly stable shorelines), and the lowest probabilities are in areas with wetlands (with eroding, stable, and accreting shorelines). For example, the stability of the rocky coastline along the northern coast of the United Kingdom is predicted accurately, whereas the shoreline change trends in regions with pocket beaches and erodible cliffs are less well predicted. In addition, accretion trends in areas experiencing relative

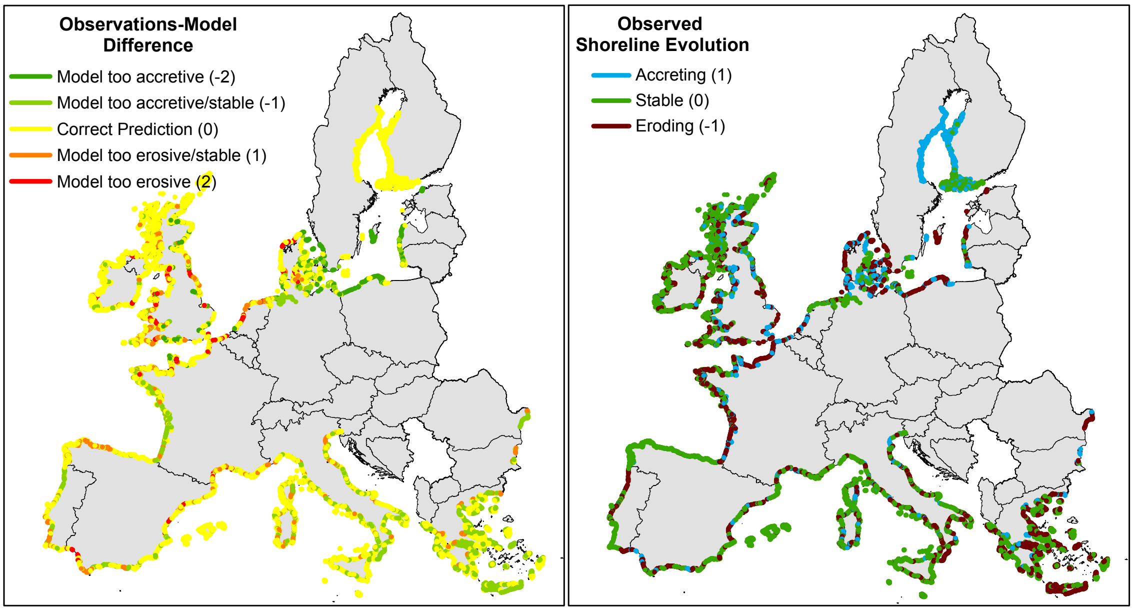

Figure 2.6: Spatial distribution of (left) the difference between the Bayesian Network model "prediction" and the observations of coastal shoreline evolution, and (right) the observed shoreline evolution (Yates and Le Cozannet, 2012).

sea-level fall caused by post-glacial rebound are also reproduced well (along the east and west coasts of Sweden and Finland, respectively). However, erosion is overpredicted along the coast of Holland and Belgium likely owing to the impacts of coastal management policies that maintain primarily stable or accreting shorelines (EUROSION, 2004). The BN model also was unable to predict the observed erosion trends along the French Atlantic coastline, potentially related to the importance of alongshore transport caused by obliquely incident waves (Castelle et al., 2007). The general trend of observed stability along the coastline of northern Spain and western Portugal is reproduced well, but local-scale pockets of erosion are not predicted. Finally, in the Mediterranean Sea, the observed shoreline change trends show significantly more spatial variability than the variables included in this model, and the BN is unable to explain this variability.

Overall, the model reproduces better the evolution of stable coasts (90% correct predictions) than of accreting (68%) or eroding (47%) coasts. The reduced predictive ability for eroding coasts suggests that the variables in this model are insufficient for determining erosive behavior, in particular the observed variability at local scales. Additional important factors, such as coastal structures, shoreline orientation, alongshore transport, sediment budgets, or other human impacts may have a dominant role in shoreline change trends at these scales and should be included in future BN models to try to improve predictions at sites experiencing erosion.

The objective of this study was to evaluate the ability of using BNs to predict large-scale shoreline evolution trends using existing databases of morphological characteristics and hydrodynamic conditions. The test presented here demonstrates the robustness of the approach in accurately reproducing more than 65% of decadal shoreline evolution trends, but also highlights the limitations of such a study. While this approach may be applied to make predictions of coastal evolution, the uncertainties in the results are highly dependent on the availability and quality of the data used to train the BN. This work emphasizes the importance of continuing and expanding long-term observations and databases of coastal evolution, including the characterization of the local environment and the dominant factors causing change. Future work should include additional variables characterizing the alongshore transport, sediment budgets, and the impacts of human activities (i.e. coastal structures, beach nourishments, etc.), which were not able to be analyzed in this study.

2.2.2 Local-scale shoreline change variability analysis using trend analyses

As indicated in the previous section, data availability significantly limits studies of long-term coastal evolution, in particular a lack of high spatial and temporal resolution morphological and hydrodynamic observations. In addition to these basic data requirements, observations of additional causes of coastal evolution, including biological processes, internal and external geodynamic processes, and human activities (Figure 2.1), may become dominant at longer temporal scales.

Table 2.2: Image data available for Manihi and Manuae shoreline evolution analysis

Atoll	Date	Data source	Image resolution	Scan resolution*
Manihi	1961	Aerial photographs	1m (1:20,000)	0.5m
	2001	Aerial photographs	0.5m (1:15,000)	-
Manuae	1955	Aerial photographs	2m (1:40,000)	1m
	2008	Quickbird satellite images	0.5-0.6m	-

*for paper photographs

In this work in collaboration Gonéri Le Cozannet and Manuel Garcin (BRGM) that pursued the Masters internship of Emilie Salaï, we studied the decadal-scale evolution of two Pacific atolls, Manihi and Manuae. This study was carried out within the ANR CECILE (Coastal Environment Changes Impact of sea LEvel) project, with the objective of evaluating the spatial variability of the observed morphological evolution and identifying the dominant forcing factors.

Historical aerial photographs and recent satellite images (available data shown in Table 2.2) first were used to estimate long-term shoreline change trends. The idealized definition of the shoreline position is the physical limit between land and water, and a common proxy for this limit is the use of a tidal datum (e.g. Mean Sea Level (MSL) or Mean Higher High Water (MHHW)). See Boak and Turner (2005) for a more in-depth discussion and a review of the definitions of shoreline position. For long-term analyses where georeferenced topographic records of shoreline position are unavailable, Thieler and Danforth (1994) suggest that the vegetation limit may be used. One limitation of this method is that the beach width (with respect to a predefined elevation contour) or beach volume may change without having an impact on the position of the vegetation limit. However, the vegetation limit may be used as a proxy for long-term shoreline evolution where more detailed topographic measurements are unavailable. Therefore, in this study, shoreline changes were evaluated by calculating the difference in the vegetation limit between two surveys (dates shown in Table 2.2), following Ford (2012) and Webb and Kench (2010). After digitizing the vegetation limit in the aerial photographs and satellite images, two metrics of change were calculated: (1) lagoon and ocean-side shoreline position change and (2) island (also called “motu”) surface area changes. In the shoreline evolution analyses, changes of less than 5 m were not considered significant owing to the image pixel resolution and differences in user interpretation of the vegetation limit (Yates et al., 2013).

2.2.2.1 Observed shoreline evolution and island surface area trends

The observed surface area changes on Manihi showed that 67% of the islands were increasing and 4% were decreasing, with strong spatial trends. In particular, the islands on the northern side of the atoll primarily increased in size (Figure 2.7). The ocean-side shoreline change rates also demonstrated this trend, with accretion on the northern side of the atoll, and small to no significant changes on the southern side. No significant shoreline evolution trends were observed

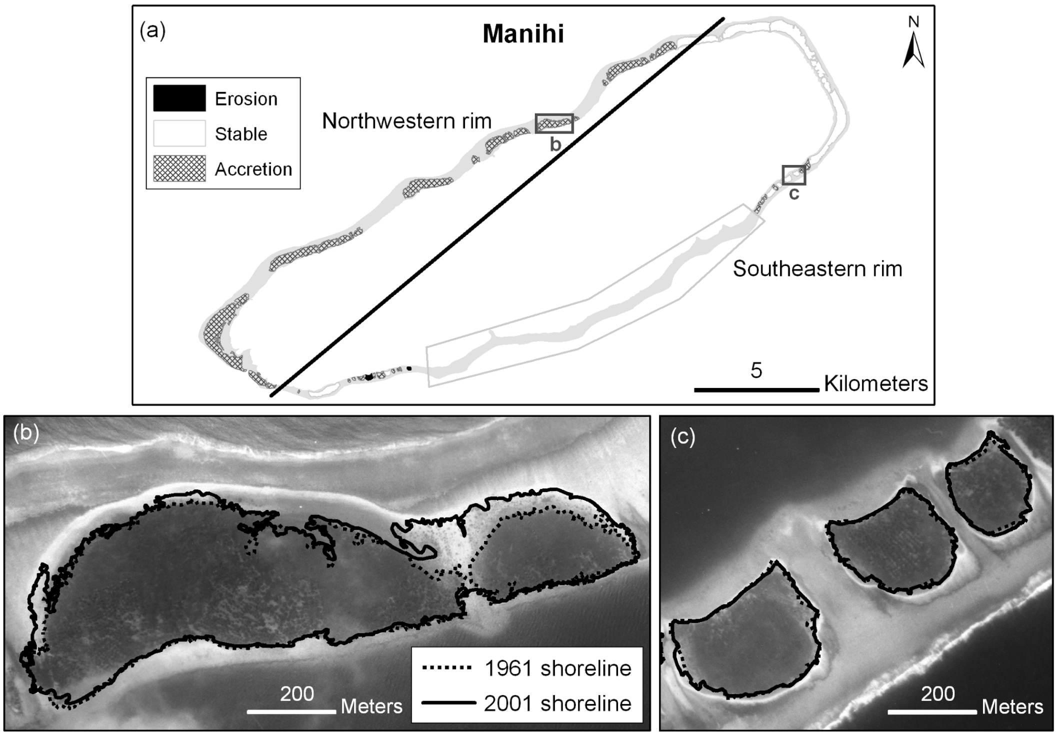

Figure 2.7: Observed changes on Manihi: (a) surface area changes for each island, and examples of 1961 (dotted line) and 2001 (solid line) shorelines, overlaid on the historical aerial photographs for islands on the (b) northern and (c) southern atoll rims. The lettered boxes in (a) indicate the location of insets (b) and (c). (Yates et al., 2013).

for the lagoon shoreline change rates (Figure 2.8a).

On Manuae, five out of the six islands decreased in surface area, while one island remained stable during the study period (Figure 2.9). Analysis of the shoreline evolution trends shows strong spatial dependence. The islands on the northeastern rim primarily demonstrated ocean shoreline accretion and lagoon shoreline erosion, while the opposite trend was observed for the two islands on the southeastern rim (Figure 2.8b).

2.2.2.2 Analysis of the dominant forcing factors

To relate the shoreline changes to the dominant forcing factors, first the spatial variability of sea level changes and wave conditions was evaluated. In atoll environments, sea-level rise is expected to cause ocean shoreline erosion or possible lagoonward “rollover” of islands (Dickinson, 1999). Increases in the water level relative to the atoll and the adjacent coral reefs exposes beaches to higher energy waves (Sheppard et al., 2005). The atolls of Manihi and Manuae are exposed to sea-level rise rates that are greater than the global average, with nearly linear trends of 2.5 mm/yr and 2.9 mm/yr, respectively (Becker et al., 2012). However, given the spatial variability of the observed

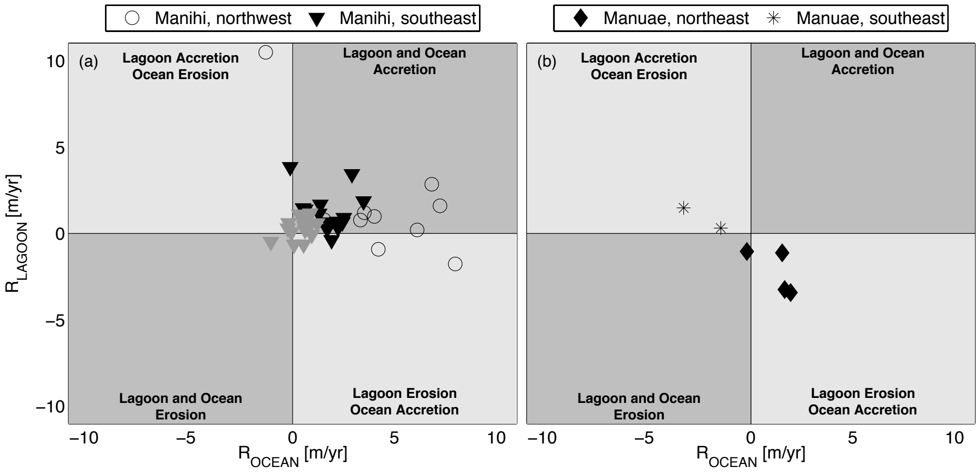

Figure 2.8: Observed ocean (R_{OCEAN}) and lagoon (R_{LAGOON}) shoreline change rates on (a) Manihi and (b) Manuae (black points indicate significant changes during the study period, > 5 m). The point shape (see legends) identifies the geographical location of each island on the two atolls, as defined by the black lines in Figures 2.7 and 2.9 (Yates et al., 2013).

evolution, sea-level rise impacts were not thought to be the primary forcing factor causing the observed island evolution. Sea level rise may, however, increase the impacts of waves and storms on exposed shorelines.

An analysis of the wave climate around the atolls shows strong spatial variation in wave exposure on both atolls. The wave data were obtained from WaveWatch III model hindcasts from 1997-2011, run by Ifremer, with 0.25° spatial resolution in a zone around French Polynesia (Ardhuin et al., 2010). While the annual wave energy fluxes affecting the northern and southern rims of Manihi are similar, the southern side is protected from more energetic events by an atoll “barrier” to the south in the Tuamotu islands. We analyzed the wave climate (for more details, see Yates et al. (2013)), showing that the northern rim typically has low energy waves with a mean wave height of 1 m or less, except when impacted by infrequent, high energy storms or cyclones (CREOCEAN, 1995). On Manihi, we hypothesized that the occurrence of cyclones may increase the sediment transport potential due to the potential to break up the reef and transport bioclastic sediments landward (as observed by Harmelin-Vivien and Laboute, 1986, on another atoll). In addition, these events impact the southern atoll rim via the process of lagoon flushing in which strong currents are generated and flow out of a single passage at Manihi or in the narrow channels between atoll islands, as observed on other atolls impacted by hurricanes (Stoddard and Fosberg, 1994; Callahan et al., 2006).

In contrast, the wave energy flux at Manuae is nearly four times greater than the wave energy flux at Manihi, and it is primarily dominated by waves originating in the south and east. This high wave energy flux may increase the sediment transport potential on the ocean side of the

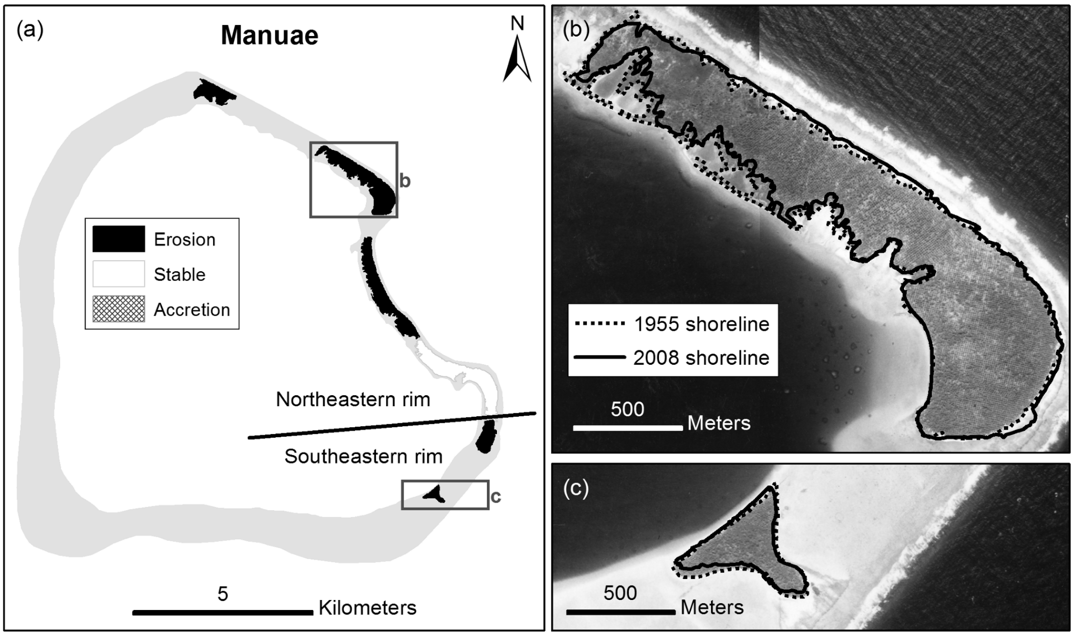

Figure 2.9: Observed changes on Manuae: (a) surface area changes for each island, and examples of 1955 (dotted line) and 2008 (solid line) shorelines, overlaid on the historical aerial photographs for islands on the (b) northeastern and (c) southeastern atoll rims. The lettered boxes in (a) indicate the location of insets (b) and (c). (Yates et al., 2013).

southern and eastern atoll rims. The extent of submerged reef on the western and southern rims of the atoll also suggests recurring erosion from southern swell (Andréfouët et al., 2001). With the absence of islands on the northern and western atoll rims, infrequent but large waves originating from the northwest may propagate across the western rim reef flat and lagoon, causing lagoon shoreline erosion trends on the islands located on the southern and eastern rims (Figure 2.8b).

Atoll island evolution also is impacted strongly by biological processes since offshore reefs are the primary source of carbonate sediments (Stoddard, 1969). However, sediment supply budgets were unable to be evaluated in this study due to a lack of data. Finally, human activities, including but not limited to sediment dredging, agriculture, pearl farming, tourism, and the construction of buildings and protective shoreline structures may also have important direct or indirect impacts on island sediment budgets and shoreline change (Aubanel et al., 1999; Ford, 2012). For example, two islands on Manihi were directly impacted by the construction of a port and the stabilization of the shoreline on the southwestern rim, and both of these islands show long-term accretion. Manuae, however, is an uninhabited island that presumably has not been affected significantly by anthropogenic activities. The indirect impacts of human activities were not able to be evaluated in our study.

This work showed the importance of wave forcing in controlling the spatial variability of the decadal-scale evolution of two atolls. While sea-level rise may indirectly have an impact on the magnitude of wave impacts at the shoreline, it was not identified as the primary cause of the observed shoreline evolution trends, even in this zone of the Pacific experiencing elevated sea-level rise rates. However, the hypothesis of the wave-forced response of the atoll islands needs to be validated with local hydrodynamic and morphological observations.

2.2.2.3 Uncertainties in data-based approaches

Finally, it is important to conclude this section about data-based approaches with a discussion of the different types of uncertainties inherent in these studies. One of the largest challenges to overcome in studying the spatial variability of shoreline changes is the existence of high quality observations of the forcing factors and morphological changes with adequate spatial and temporal resolution. The necessary observations (see Figure 2.1) and desired spatial and temporal resolution depend strongly on the local context of the study site. For example, at sites with a strong seasonal cycle in shoreline erosion and accretion, annual or bi-annual surveys may not be sufficient for analyzing long-term trends. Therefore, it is important to determine the appropriate spatial and temporal scales that can be evaluated with a given dataset, as well as to be aware of the limitations of the available data.

In addition, it is crucial to evaluate the uncertainties in the available measurements to asses the overall errors. This includes, but is not limited to the existence of metadata describing the data, the frequency and duration of the observations, and the measurement precision. There are uncertainties related to both the measurements and the analysis methods. In shoreline change studies, the definition of the shoreline position varies depending on the chosen proxy, which is often limited by data availability. For example, the shoreline position may be defined as the location of the vegetation limit, the wet-dry line at high tide, or the position of a selected elevation contour (e.g. MSL, MHHW, etc.). Once a shoreline proxy has been chosen, the interpretation of its position contributes to the uncertainties (i.e. in the visual interpretation of the wet-dry tide line or the digitalization of the vegetation limit in aerial images).

2.2.3 Short-term shoreline evolution

To study short-term, storm-induced shoreline evolution, we conducted a series of experiments in a controlled environment in a wave flume. The experimental work, financed by the Geocorail society, was completed in the LHSV by a post-doctoral researcher, Mathieu Gervais (2015-2016), whom I co-advised with Damien Pham Van Bang, and a laboratory technician, Vincent Vidal. The overall objective of this study was to investigate storm-induced beach erosion and the ability of submerged structures to reduce the observed erosion.

We used an innovative experimental protocol, following the work of Grasso et al. (2009), using lightweight plastic PMMA (polymethyl methacrylate) sand ($\rho = 1.19$ kg/m^3) in the 1/10-scale flume experiments (36-m long, 0.5m deep wave flume). At this scale, the nondimensional

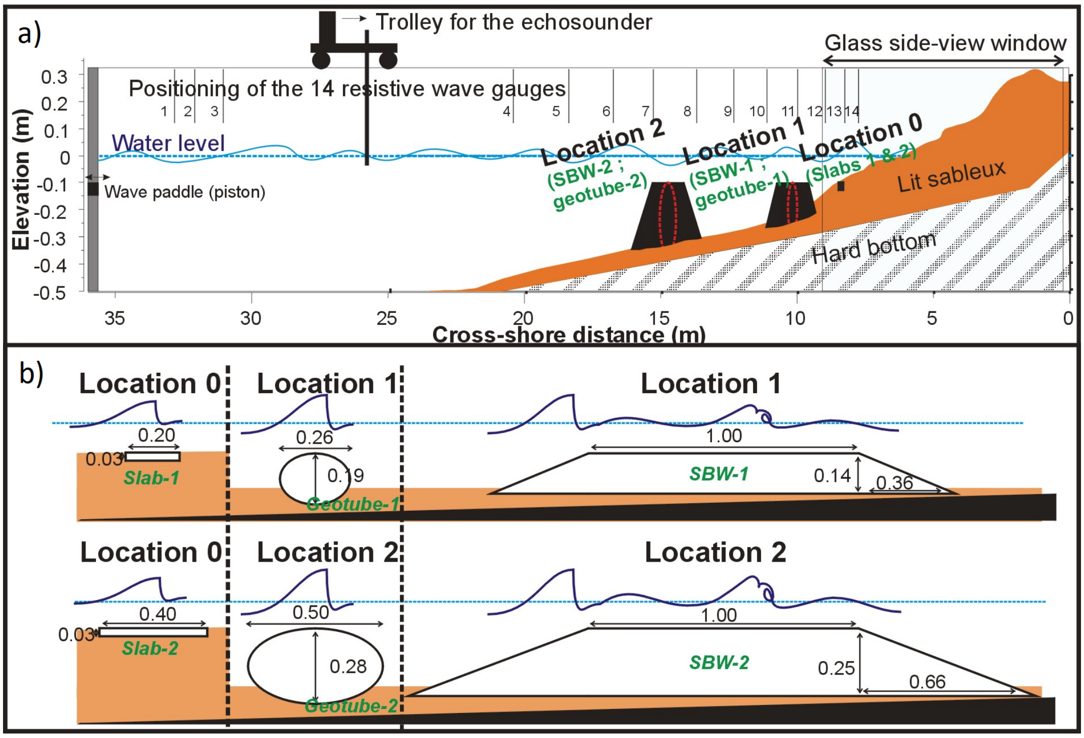

Figure 2.10: (a) Experimental setup in the wave flume showing the position of the wave gauges (numbered vertical lines) and the submerged structures, and (b) dimensions of the submerged structures (1/10 scale) for (left) the flat slabs, (center) the geotextile tubes, and (right) the submerged breakwaters (SBWs) (Gervais et al., 2016).

Froude number (Fr = 0.02-0.16), which is the ratio between inertial and gravitational forces, is respected to reproduce correctly the wave hydrodynamics. In addition, the nondimensional Shields (Sh =2-3) and Rouse (Ro =1.5-15) numbers are respected by using the low density PMMA sand. This allows reproducing well both the suspended sediment and bedload transport, respectively, in the swash and surf zones for natural environments with quartz sand of median grain size $d_{50} = 0.3$ mm and a significant wave height H_s of approximately 2 m (for more details, see Appendix A of Gervais et al. (2014)).

In these experiments, we tested the efficiency of three types of submerged structures placed in two different cross-shore positions: two submerged breakwaters (SBWs), two geotextile tubes, and two flat concrete slabs (Figure 2.10b). To evaluate the storm-induced erosion on a natural beach profile, the first series of experiments measured: (1) the initial beach profile formed under steady, calm wave conditions, and (2) the erosion experienced during a hypothetical storm. Then, to evaluate the ability of the submerged structures to reduce the erosion trends observed on the natural profile, the initial beach profile was reconstructed, and a series of experiments measured for each structure: (1) the new beach profile formed under the same, steady, calm wave conditions in the presence of the structure, and (2) the observed erosion during the same hypothetical storm.

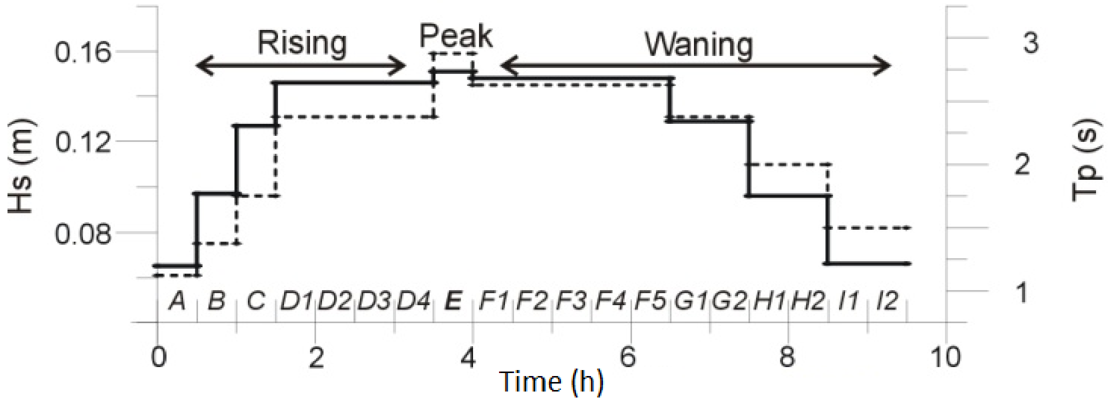

Figure 2.11: Selected storm wave conditions (H_s, T_p) for different phases (identified by letters) of the storm in the laboratory experiments (as a function of time at the laboratory scale) (Gervais et al., 2016).

Waves were generated in the wave flume using a flap-type wave generator by imposing a Jonswap spectrum. The selected calm (H_s= 0.15 m, T_p=1.6 s) and storm (Figure 2.11) wave conditions were based on wave conditions observed along the southern coast of France in the Mediterranean Sea (on microtidal beaches, where the tidal impacts are negligible). As mentioned above, the initial beach profile was formed by running steady wave conditions and measuring the beach profile evolution. As observed by Grasso et al. (2009), the beach profile adjusts to the incoming wave conditions, forming what is called an equilibrium beach profile, as observed previously on natural beaches (e.g. Bruun, 1954; Dean, 1977). In the laboratory experiments, the beach profile evolved to a nearly constant state, called the pre-storm equilibrium profile, after approximately 30 hours, when the vertical bed change rate was approximately 2 mm/hr (Figure 2.12, following Grasso et al., 2009). Therefore, to optimize the time required to reach equilibrium in subsequent experiments, the initial beach profile was first reconstructed using the previously observed pre-storm equilibrium profile and then allowed to adjust to the incoming wave conditions, reaching the equilibrium state in approximately two hours (Figure 2.12, tests A-C for wave conditions 'calm 1').

These controlled experiments confirm both the observations of:

- Bruun (1954); Dean (1977); Dean and Dalrymple (1991); Miller and Dean (2004); Yates et al. (2009a); Davidson et al. (2013), among others, of the existence of an equilibrium beach profile or equilibrium shoreline position in response to waves on natural beaches, and
- Kamali Nezhad (2004); Kamalinezhad et al. (2004); Wang and Kraus (2005); Michallet et al. (2007); Grasso et al. (2009), among others, of the existence of equilibrium beach profiles for constant wave conditions in laboratory experiments.

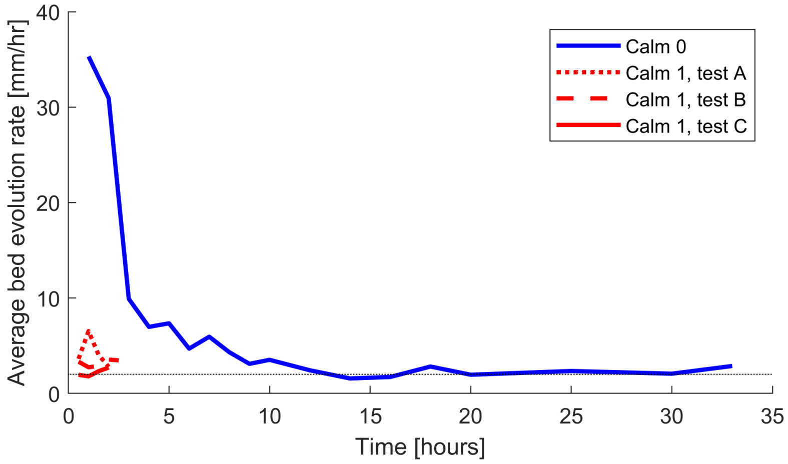

Figure 2.12: Average bed evolution rate along the beach profile for 2 obtained equilibrium profiles: calm 0 ($H_s = 0.15$ m, $T_p = 2$ s) and calm 1 ($H_s = 0.15$ m, $T_p = 1.6$ s), with the horizontal gray line indicating 2 mm/hr, the approximate average equilibrium bed evolution rate.

The early work of Bruun (1954) and Dean (1977) proposed that beaches form a concave equilibrium profile of the form $h(x) = Ax^{2/3}$, where h is the water depth, x is the distance offshore, and A depends on sediment grain size. However, most natural beaches typically have more complex shapes, and this simple profile is not largely applicable. Thus, other authors have suggested alternative shapes with finite slope or the inclusion of offshore sandbars (e.g. Larson and Kraus, 1989; Inman et al., 1993; Bernabeu et al., 2003; Özkan Haller and Brundidge, 2007). In this study, under steady wave forcing, pre-storm equilibrium profiles are obtained, but they do not respect the concave-up shape suggested by Dean (1977), especially with the presence of submerged structures. The demonstration of the existence of an equilibrium beach morphology for given wave conditions will be addressed further in section 2.2.4 in my work studying in situ observations of natural beach morphological evolution.

During the post-doctoral work of Mathieu Gervais at the LHSV, the results of the laboratory experiments focused on the observations of erosion near the shoreline, and in particular, the impacts of submerged structures in reducing the observed shoreline erosion. Attention was focused on erosion around the shoreline since this zone is most often the priority for coastal planning and management purposes (Stauble, 2003). Analysis of the laboratory experiments showed that during storm events, the upper beach profile typically eroded, with the eroded sediment being deposited along the lower portion of the beach profile. A transition zone between the sections of the profile experiencing erosion and accretion was typically located around cross-shore position x=10 m (defined from the top of the beach profile). Volume changes were thus calculated in these two pre-defined zones (shoreward and seaward of the transition at x=10 m) to quantify the observed morphological changes (Figure 2.13).

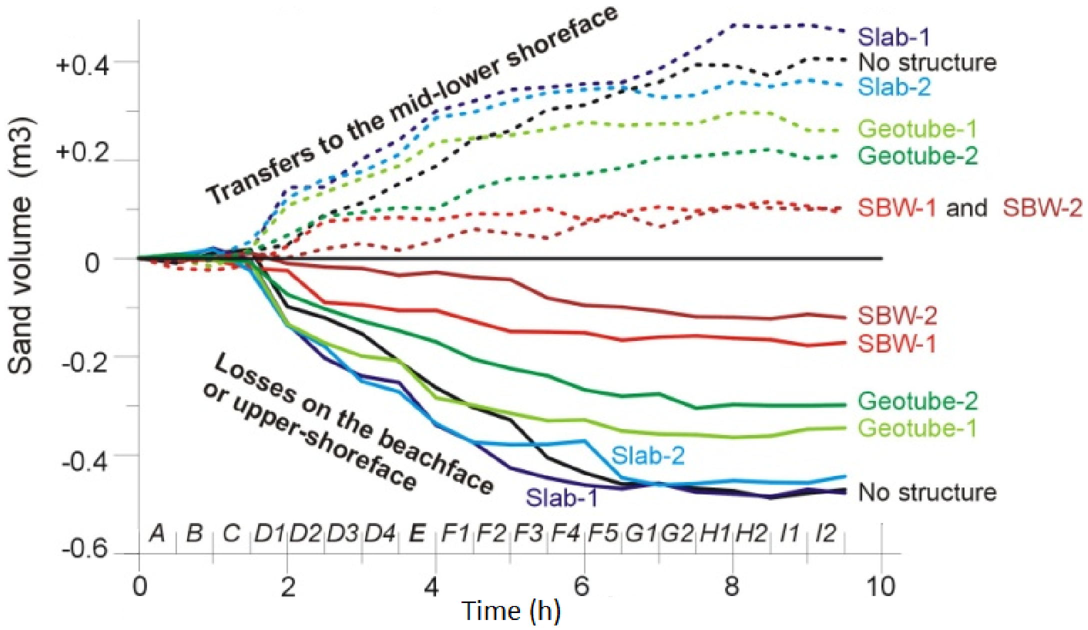

Figure 2.13: Sand volume evolution on the upper (solid lines) and lower (dashed lines) profile, defined as the zones shoreward and seaward of the transition zone approximated at x=10 m, for the 6 different submerged structures (colored lines) in comparison with the profile without structures (black lines) (Gervais et al., 2016).

The experiments demonstrated that the SBWs were the most efficient structures in reducing storm-induced shoreline erosion, followed by the geotextile tubes (red and green curves in Figure 2.13, respectively). The concrete slabs were the least efficient structures, as expected, since they were unable to prevent erosion and provided no reduction in shoreline erosion compared to the profile without any structure (blue/purple curves in comparison to the black curves, Figure 2.13). The SBWs and, to a lesser degree, geotextile tubes caused stronger wave breaking than that observed on the natural beach profile, thus reducing the nearshore wave energy (as shown at the end of the storm in Figure 2.14a). This reduction in wave energy likely caused the observed reduction in shoreline erosion (Figure 2.14b). However, in the experiments with the SBWs significant scouring occurred in front of the structures, suggesting the importance of further studies since scouring may have strong impacts on the long-term stability of such structures. This may, however, be due to the 2D nature of the experiments, whereas 3D effects are likely significant in real settings.

Additional experiments with a longer storm and a barred pre-storm equilibrium profile demonstrated that the preliminary conclusions were not highly dependent on the storm duration, but did depend strongly on the initial beach profile. The limited number of experiments completed in the laboratory emphasized several limitations of this study, including the need to test a wide variety of initial beach profiles (and geomorphological characteristics), storm wave characteristics, and submerged structure configurations (e.g. size and position). In addition, to extend these

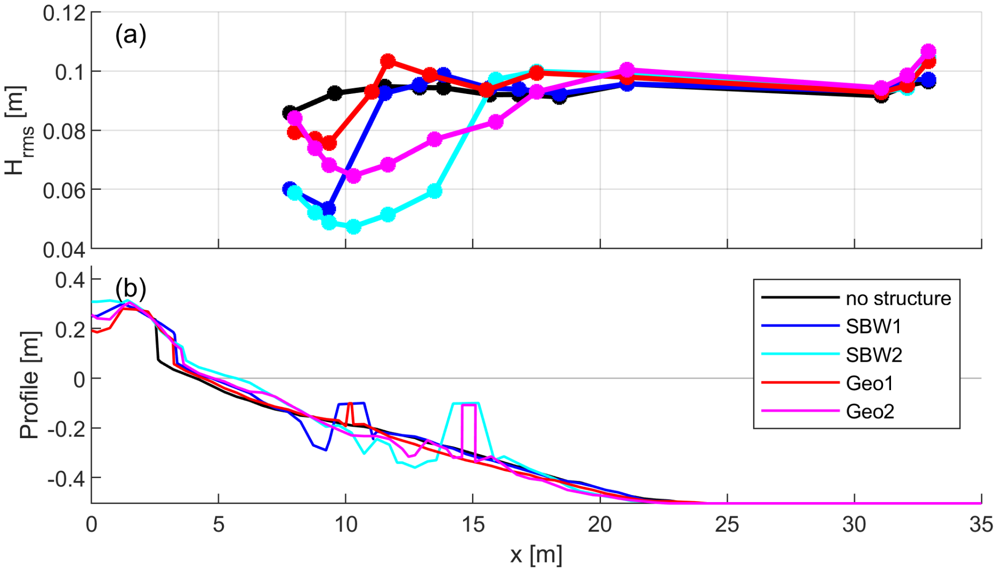

Figure 2.14: (a) Cross-shore evolution of the root-mean square wave height H_{rms} measured at the wave gauges at the end of each storm run for the tests without (black line) and with (colored lines, see legend) submerged structures. (b) Cross-shore bathymetric profiles at the end of each storm test.

results to be able to design structures for real applications, additional 3D tests are necessary. Given the resources required to conduct extended 2D and then 3D experiments, numerical studies were initiated to be able to test the ability to address some of these issues, and the results are presented in section 2.3.1.

2.2.4 Medium-term shoreline evolution

Evaluating medium-term, or seasonal to interannual scale beach morphological evolution requires adequate temporal resolution of the shoreline evolution and forcing factors. This research focus began during my thesis work, when access to high quality morphological observations and hydrodynamic model outputs of the wave characteristics enabled a study of the temporal dynamics of shoreline changes. After analyzing the large-scale spatial variability of shoreline changes along 10's to 100's of kilometers of coastline in Southern California (Yates et al., 2009c), I highlighted the seasonal variability of the wave field as the primary forcing mechanism causing seasonal shoreline changes at five surveyed study sites (Yates et al., 2009a).

This phenomenon of a strong seasonal cycle of shoreline evolution has been observed on beaches worldwide (e.g. Winant et al., 1975; Aubrey, 1979; Dubois, 1988; Masselink and Pattiaratchi, 2001), showing a strong relationship between the seasonal variations in wave characteristics and the advance and retreat of the shoreline position (e.g. Wright and Short, 1984; Stive et al., 2002; Davidson and Turner, 2009). Typical observations show moderate to severe erosion (shoreline retreat) in response to energetic winter storms, with sediments deposited along the beach profile in the nearshore zone (Winant et al., 1975; Dubois, 1988; Castelle et al., 2007; Splinter et al., 2014; Doria et al., 2016; Dodet et al., 2019). During time periods with moderate to low energy waves, this sediment is often transported back to the exposed beach face where accretion occurs, as observed with the seaward advance of the shoreline position (e.g. Winant et al., 1975; Stive et al., 2002; Brenner et al., 2018).

Studies often try to correlate temporal variations in the wave field to temporal variations in observed shoreline position or beach state with observations at weekly, monthly, biannual, or even annual timescales (Dalrymple, 1992; Masselink and Short, 1993; List and Farris, 1999; Larson et al., 2000; Miller and Dean, 2007; Quartel et al., 2008). However, many authors (e.g. Morton et al., 1995; Lee et al., 1998; Anthony, 1998; Jiménez et al., 2008) have suggested that low correlations between the instantaneous beach state (defined by the shoreline position, beach volume, or beach profile) and instantaneous wave conditions are often observed on beaches dominated by storms with seasonal or intermittent recovery periods. They attribute these low correlations to the different timescales of changes in the wave field and beach morphology. Searching for a direct correlation between these two time series may also be complicated further by two important observations:

1. detailed time series of the wave conditions are highly important, and comparing averaged wave conditions and morphological changes over the timescales of typical beach surveys (e.g. weekly, monthly, and longer) neglects the importance of the variable intensity and sequence of wave conditions (e.g. Morton et al., 1995; Lee et al., 1998); and

2. the impact of waves on a beach depends strongly on the current beach state, following the hypothesis of the existence of an equilibrium beach state (e.g. Bruun, 1954; Dean, 1977; Wright et al., 1985). Equilibrium beach theory assumes that a beach profile will reach an equilibrium profile in response to a constant wave forcing. Therefore, the observed profile or shoreline change depends both on the forcing conditions and the initial beach profile. For example, a moderate wave energy event may cause shoreline erosion if the beach was initially in an accreted state (shown schematically in Figure 2.15, top), while the same moderate wave energy event may cause shoreline accretion if the beach was initially in an eroded state (Figure 2.15, bottom).

These two concepts have been discussed previously in the literature, in particular in relation to the development of morphological shoreline evolution models (Wright et al., 1985; Miller and Dean, 2004; Yates et al., 2009a; Davidson and Turner, 2009).

During my thesis work, using a five-year time series of shoreline change observations and incident wave conditions at Torrey Pines beach, these concepts were demonstrated clearly with observations (Yates et al., 2009a). First, the dependence of the magnitude and sign of shoreline changes on the initial beach state and wave conditions was demonstrated using high spatial

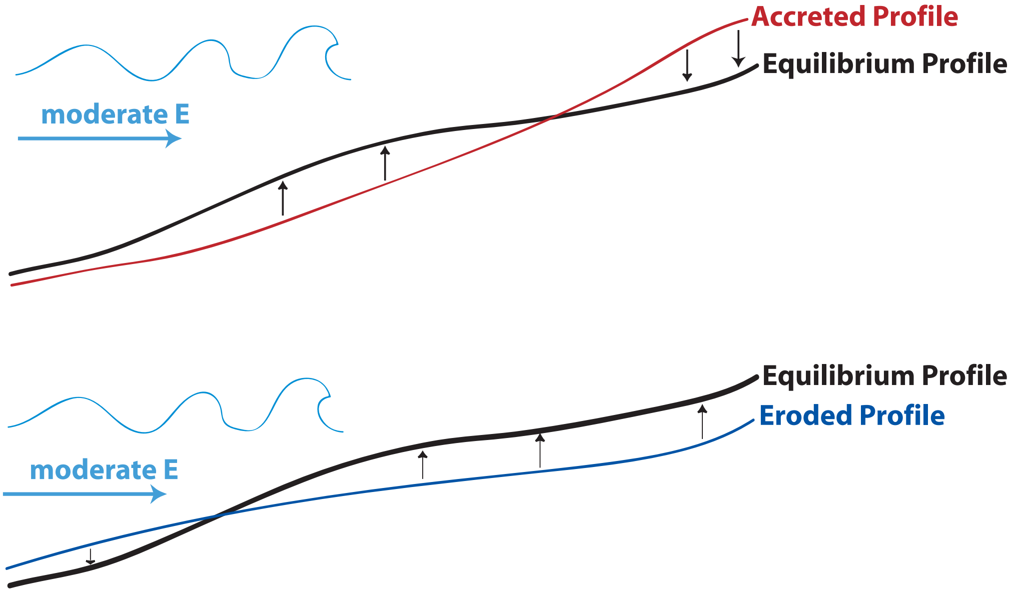

Figure 2.15: Schematic demonstrating the equilibrium beach profile hypothesis. When exposed to constant wave forcing, a beach will evolve to form an equilibrium profile (black line), and thus the observed profile changes (black arrows) will depend on the initial beach state.

and temporal resolution shoreline change observations and modeled wave characteristics (Figure 2.16) by relating the current beach state S, described using the cross-shore position of the MSL contour (m), the average normalized wave energy $\overline{E}$ (m^2) between survey dates, and the average shoreline change rate $\overline{dS/dt}$ (m/day). The color of each point indicates observed erosion (red) or accretion (blue), while the intensity of the color indicates the magnitude of the observed changes. Even though averaged (over weekly, bi-weekly, or monthly periods) wave conditions and beach changes were analyzed, which likely contributes to the observed scatter, the data demonstrated that the equilibrium wave energy is dependent on the initial state of the beach. For example, in Figure 2.16, when the beach is wide (e.g. 15 m MSL position), an average wave energy of 0.75 m^2 typically causes shoreline erosion (red points). However, when the beach is narrow (e.g. -15 m MSL position), the same average wave energy typically causes shoreline accretion (blue points). For each beach state S, the equilibrium wave energy $E_{eq}(S)$ is thus the wave energy causing no further changes in the beach state (transition between red and blue points in Figure 2.16). In addition, the observations demonstrate that the shoreline change rate depends on the wave energy disequilibrium, defined as the difference between the measured wave energy and the equilibrium wave energy for the given beach state, or $\Delta E = E - E_{eq}(S)$.

Since 2014, I have pursued this work of observing beach profile evolution and investigating the existence of equilibrium beach response in collaboration with France Floc'h, Nicolas Le Dantec,

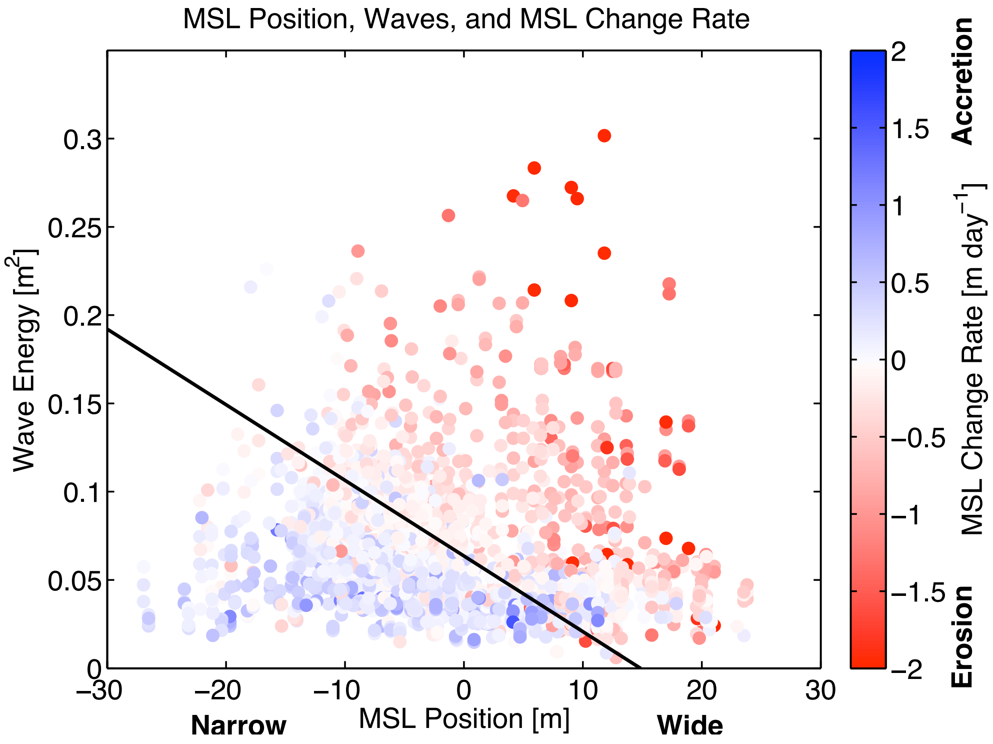

Figure 2.16: Shoreline change rate (dS/dt, color and intensity of points) as a function of the beach state (S, or shoreline position, defined by the MSL position here) and average wave energy between topographic measurements ($\overline{E}$) at Torrey Pines Beach (Yates et al., 2009a).

and Serge Suanez from the IUEM/UBO. Using long-term, high resolution beach profile observations, I am collaborating with this group to study the morphological evolution of two macrotidal beaches in Brittany: Porsmilin and Vougot. This work builds on a preliminary study completed during the Masters internship of Klervi Hamon (Hamon, 2014), followed by the Masters internships of Clara Lemos and Gabin Bouvard (co-advised with France Floc'h and Nicolas Le Dantec), studying the morphological evolution of Porsmilin and Vougot, respectively (Lemos, 2016; Bouvard, 2017), and the PhD project of Teddy Chataigner (2018-2021), which I am currently co-advising with Nicolas Le Dantec and Nicole Goutal. Over 10 years of approximately monthly topographic measurements were studied along one and six cross-shore profiles at Porsmilin (alongshore uniform, embayed beach) and Vougot (high bathymetric alongshore variability) beaches, respectively.

The macrotidal nature of these two sites provides an interesting environment to study further the existence and evolution of equilibrium beach profiles. While it is well known (e.g. Bagnold, 1940; Bascom, 1951) that beach morphodynamic behavior depends strongly on the beach sediment characteristics, wave conditions, and tidal effects, Bernabeu et al. (2003) point out that most morphological evolution models depend solely on the beach characteristics and wave forcing.

Wright and Short (1984) defined a beach classification system based on the nondimensional fall velocity, or Dean parameter $\Omega = \frac{H_b}{w_s T}$, where H_b is the breaking wave height, w_s is the sediment fall velocity, and T is the wave period. They identified six beach states ranging from dissipative to reflective-type beaches. However, this classification does not take into account the tide range, which plays an important role in the morphological evolution of macrotidal beaches owing to the temporal variations in the position of the swash, surf, and shoaling zones and therefore wave energy dissipation and wave-driven sediment transport processes. Davis and Hayes (1984) suggested the importance of the relative tide range, $RTR = TR/H$, or ratio between the tide range TR and wave height H. Masselink and Short (1993) then used this nondimensional number (RTR) and the Dean number (Ω) to develop a conceptual beach evolution model including the impacts of the tidal range.

Using the classification proposed by Masselink and Short (1993), Porsmilin and Vougot beaches are Low Tide Terrace (LTT) beaches, with a compound intertidal profile composed of a reflective upper zone and a dissipative lower zone. The hydrodynamic and morphodynamic behavior of these two zones differs, as shown by the temporal evolution of beach contours located in these two sections of the intertidal beach profile (e.g. for Porsmilin beach, Figure 2.17). For example, we observed that the seasonal variations in beach contour position and beach volume in the upper intertidal zone of Porsmilin beach (e.g. MHWS = Mean High Water Spring, Figure 2.17, left) show trends similar to observed shoreline trends on microtidal beaches. In particular, there is significant erosion and contour retreat during storms (typically during the winter months), and accretion and beach recovery with the offshore contour advancement during calm wave conditions (typically during summer months). The opposite behavior is observed in the lower intertidal zone at Porsmilin (e.g. MW = Mean Water level, Figure 2.17, right), with sediment

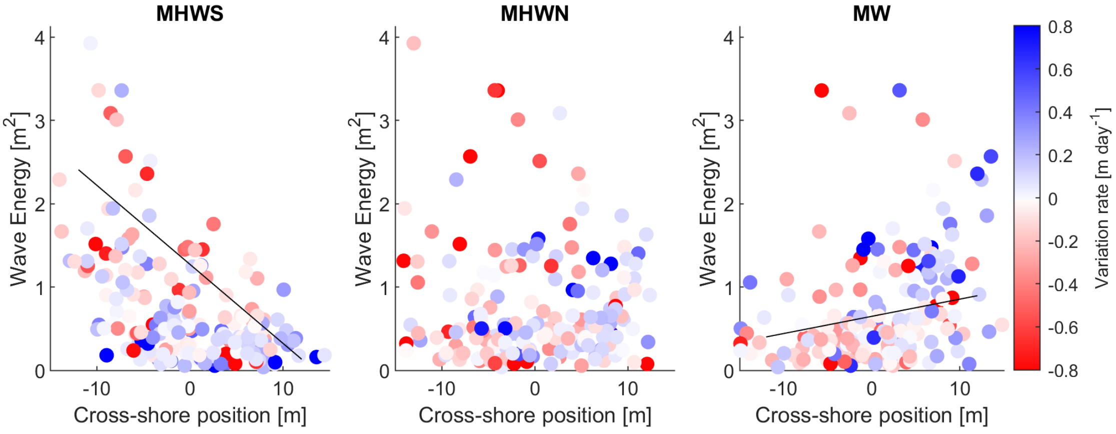

Figure 2.17: Observations of equilibrium beach states at three altitudes along the intertidal beach profile at Porsmilin beach (MHWS = Mean High Water Spring (reflective zone), MHWN = Mean High Water Neap (transition zone), MW = Mean Water (dissipative zone), same format as Figure 2.16.

eroded from the upper intertidal profile distributed in this zone during energetic wave events, and the subsequent loss of this sediment during calmer wave conditions as it returns to the upper intertidal zone. In the transition zone between the reflective and dissipative regions, the observed morphological changes do not demonstrate clear trends. We hypothesize that this is caused by the fact that the contour altitudes in this zone are alternatively located in reflective and dissipative zones of the intertidal profile (e.g. MHWN = Mean High Water Neap, Figure 2.17, center).

Similar trends are observed along the two westernmost profiles (5 and 6) at Vougot Beach (results from profile 6 are shown in Figure 2.18). These two profiles appear to be more strongly controlled by cross-shore processes than the profiles located on the northeastern side of the beach (1 to 4), where the offshore and nearshore bathymetry varies significantly alongshore (see Bouvard (2017) for more details). In Figure 2.18, as observed at Porsmilin beach, the upper tidal zone (reflective, represented by MHWS) typically experiences erosion during energetic storms, and this sediment is deposited in the lower intertidal zone (dissipative, represented by MW). Again, no clear trends are observed in the transition zone (represented by MHWN). In Figure 2.18, the equilibrium curves estimated with the averaged observations are drawn with dotted lines to indicate the lack of confidence in these estimated curves given the relatively small number of observations.

The observations at these two sites demonstrates that the morphodynamic evolution of macrotidal beaches is therefore highly dependent not only on the wave and sediment characteristics, but also on the relative water depth, which varies temporally as a function of the tide level.

Finally, it is interesting to note that the relationship between the beach state, wave conditions, and shoreline change is present in the observations averaged over intervals between the topo-

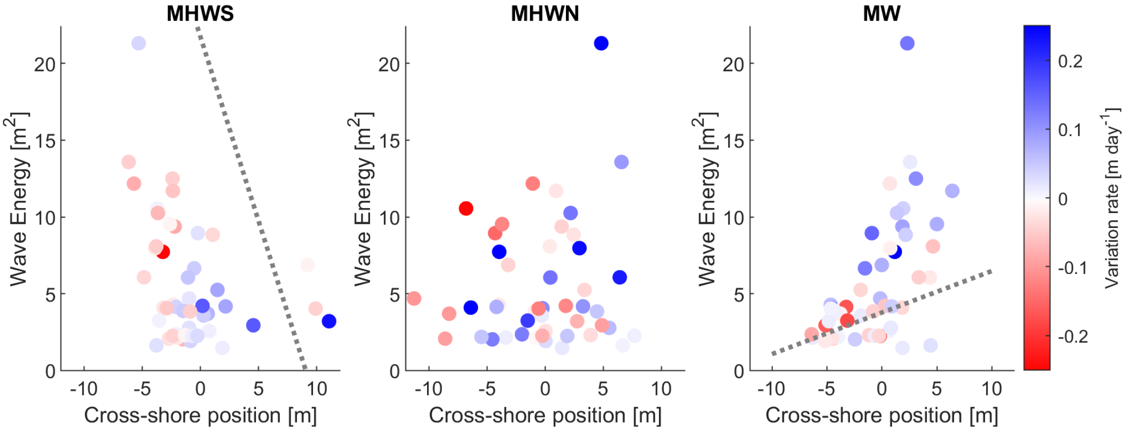

Figure 2.18: Observations of equilibrium beach states at three altitudes along the intertidal beach for profile 6 at Vougot beach (MHWS = Mean High Water Spring (reflective zone), MHWN = Mean High Water Neap (transition zone), MW = Mean Water (dissipative zone), same format as Figure 2.16.

graphic surveys (weekly to monthly) shown at Torrey Pines (Figures 2.16), but less so for Pormilin and Vougot beaches (Figures 2.17 and 2.18, respectively). During my thesis work, I demonstrated the need to investigate the temporal dynamics at shorter timescales by showing an example of the observed morphological evolution during two time periods with the same average wave conditions $\bar{E}$ and approximately the same initial beach state S but different time series of waves $E(t)$ (Yates et al., 2009a). In the presented example from Torrey Pines Beach (Figure 2.19), for a two-week period with an average wave energy of $\bar{E} = 0.05$ m^2, the first set of wave conditions caused a net change of 2.3 m of erosion, while the second set of wave conditions caused a net change of 2.1 m of accretion. These differences are likely caused by the intensity and sequence of wave conditions, with larger waves arriving at the end of the two-week period in the first case, where the larger waves arrived at the beginning of the two-week period in the second case, allowing time for recovery. Therefore, it can be hypothesized that part of the scatter observed in Figure 2.16, and even more so in Figures 2.17 and 2.18 can be attributed (at least partially) to averaging the observations over the time periods between measurements. All other longshore or cross-shore processes that are not wave-forced, may also contribute to this scatter. The importance of timescales will be addressed further in the discussion of equilibrium beach modeling in section 2.3.2.

Finally, although both Porsmilin and Vougot beaches are macrotidal beaches located along the western coast of France, there are several important differences between the two sites that make them interesting and unique sites for studying different physical processes. First of all, Porsmilin is an embayed beach, where cross-shore processes are dominant, whereas Vougot is a longer beach along the open coast, showing significant bathymetric variability alongshore, as explained above. Porsmilin beach is located in the Iroise Sea, whereas Vougot beach is located along the Atlantic coastline, and the wave energy fluctuations are approximately five times as large at Vougot beach (e.g. Figure 2.17 compared to Figure 2.18). In addition, it is also important to highlight the presence of dunes loacted along the backbeach at Vougot. The cross-shore dynamics at Vougot beach thus include interactions with the dune system, including the loss of sediment from the exposed beach to the dunes via aeolian transport, as well as the gain of sediments from the dunes during storm events. Finally, for wave events of the same magnitude, the observed contour position changes at Vougot beach are typically smaller than those observed at Porsmilin beach, likely related to the larger sediment grain size at Vougot (d50 = 438 μm) in comparison to Porsmilin (d50 = 320 μm). The availability of high quality, long-term topographic and hydrodynamic observations at these two sites provides an opportunity to study their morphological response in two unique environments.

In this work comparing the temporal dynamics of the wave forcing and the observed morphological changes, I highlighted the importance of the instantaneous beach state and the magnitude and timing of individual wave events in controlling beach morphological evolution. These concepts, while not new, were demonstrated clearly in my thesis work Yates et al. (2009a) and then again with the observations of the macrotidal beach of Porsmilin with unique sets of long-term

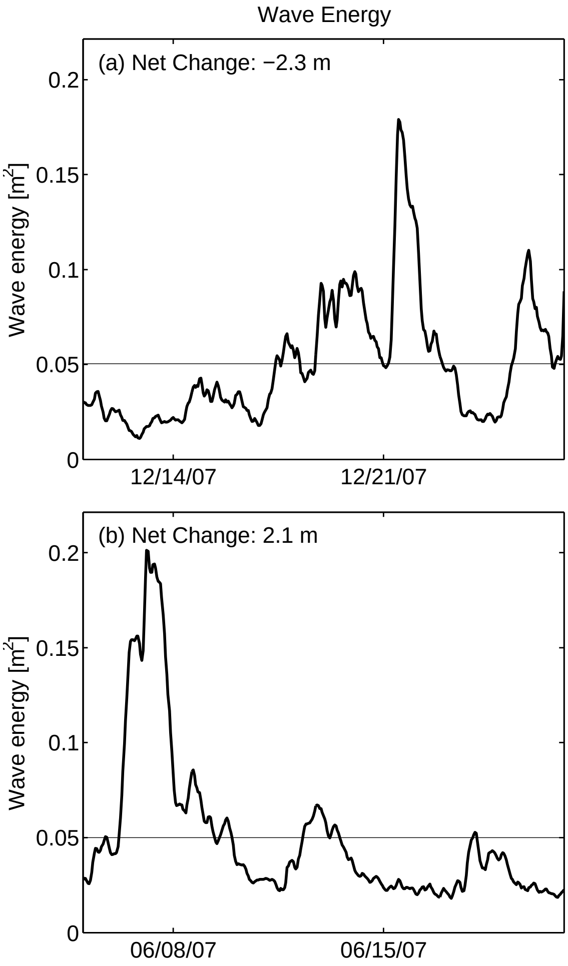

Figure 2.19: Two weeks of modeled hourly wave energy time series at Torrey Pines Beach for two time periods with the same average wave energy ($\bar{E}$, horizontal line) but different morphological evolution: (a) December 2007 with 2.3m of observed net shoreline erosion and (b) June 2007 with 2.1m of observed net shoreline accretion (from Yates et al., 2009a).

observations of the shoreline position and incident wave conditions. This work led naturally to the development of an empirical equilibrium shoreline change model, which will be described briefly in section 2.3.2.

2.3 Modeling beach evolution

Coastal scientists and engineers seek reliable, accurate methods for forecasting shoreline erosion and accretion to contribute to coastal management practices. However, predicting coastal evolution at seasonal, to annual, to decadal or longer timescales remains a significant challenge (Safak et al., 2017; Davidson et al., 2017), and a variety of approaches are currently used, ranging from empirical, to one- or n-line, to 3D process-based models.

A wide variety of process-based modeling approaches exist, which can be divided broadly into three categories (de Vriend et al., 1993; Southgate and Brampton, 2001; Hanson et al., 2003; Roelvink et al., 2012): coastal profile models, coastline models, and coastal area models. Different temporal and spatial scales, ranging from micro- to macro- and mega-scales, and thus different physical processes, can be simulated with these different modeling approaches (Figure 2.20, based on Cowell et al. (2003); Brommer and van der Burgh (2009); Winter (2012)). Cowell et al. (2003) defined this hierarchal (or 'cascade tract') approach to describing morphological evolution, stating that the natural system can be divided into naturally occurring levels that interact with each other in systemic ways. For example, at a given position in the hierarchy, the lower levels (e.g. macro and mega-scales) place extrinsic constraints (or boundary conditions, gray arrows in Figure 2.20), whereas the higher levels (e.g. micro or meso-scales) describe the subgrid processes, which must then be parameterized (blue arrows in Figure 2.20). However, Hanson et al. (2003) emphasized that upscaling of first principle physical or process-based modeling approaches to much longer timescales is restricted owing to a range of theoretical and practical limits. Brommer and van der Burgh (2009) and Winter (2012) extended the hierarchal approach to describe which types of morphological evolution models may be used at different spatial and temporal scales, ranging from 3D non-hydrostatic process-based models at micro-scales, to 2DH (two horizontal dimension) and 2D morphodynamic coastal area models at meso-scales, and finally to 1D coastal profile and coastline models at macro- and mega-scales.

The spatial scales of these three categories of models are thus inherent, with some variability between different models in the same category. In general, they are applicable at the scales of a beach profile (hundreds of meters in the cross-shore direction), of a coastline (several, tens, or hundreds of kilometers alongshore), or of a beach or littoral zone (several kilometers in the alongshore and cross-shore directions) as shown by the x-axis in Figure 2.20. With respect to temporal scales, morphological evolution models are often divided into short- (seconds, hours, days), medium- (days, seasons, years), and long- (years, decades, centuries) term models (HR Wallingford, 2000). Depending on the spatial and temporal scales of interest, process-based models, or simplified versions, called behavior-based models, using semi-empirical or averaged formula to represent the hydrodynamic and/or morphodynamic processes (de Vriend et al., 1993; Niedoroda et al., 1995), may be used. Within the three broad categories defined above, individual models treat different temporal scales, as shown by the y-axis for each of the boxes in Figure 2.20. These three different types of models are described further below.

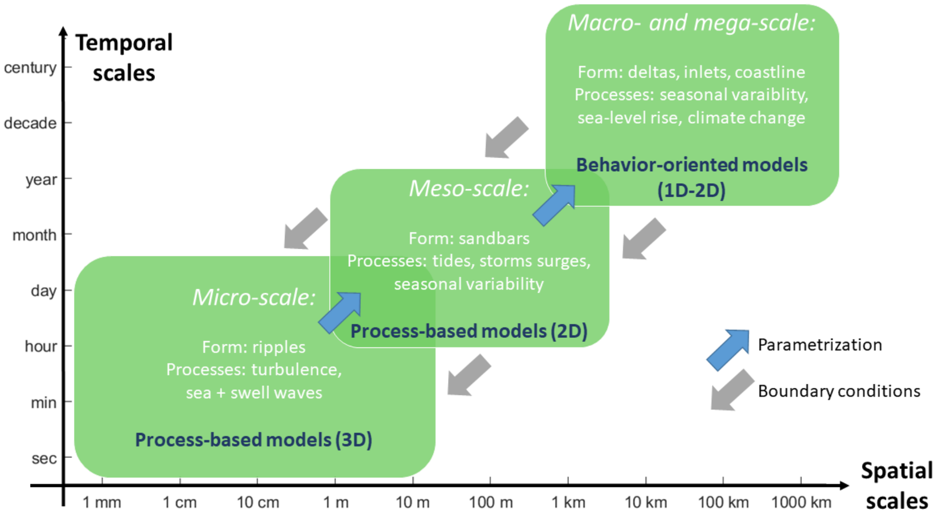

Figure 2.20: Spatial and temporal scales of the relevant physical processes and the applicable morphological models, based on Cowell et al. (2003); Brommer and van der Burgh (2009); Winter (2012).

Coastal profile models are based on the assumption that the littoral zone is uniform in the alongshore direction and that the morphological evolution can be represented along a cross-shore profile. By removing one spatial dimension, these types of models are able to provide a more detailed representation of cross-shore processes while maintaining short computational times (e.g. Larson and Kraus, 1989; van Rijn et al., 2003; Roelvink et al., 2009). Depending on the complexity of the model, typical temporal scales may range from hours to days, and more recent work is focused on extending these approaches to longer timescales (e.g. Pender and Karunarathna, 2013; Zimmermann et al., 2015). To model changes along gently varying coastlines, multiple cross-shore profile models have been combined to evaluate alongshore variability. In this approach of multiple profile modeling, the cross-shore profiles are often independent of each other with respect to the offshore wave and current forcing, but may be related by the alongshore sediment transport processes.

Coastline models, on the other hand, are based on the assumption that cross-shore processes are assumed to counterbalance in time and that the net cross-shore changes at the timescales of interest (years) are small, such that alongshore processes dominate the coastline evolution. In this family of models, a representative coastline contour (often defined by an isobath) evolves in time based on behavior-oriented rules, analytical expressions, or numerical approaches (e.g. Pelnard-Considére, 1956; Larson et al., 1997; Jiménez and Sánchez-Arcilla, 2004; Ashton et al., 2001; Ashton and Murray, 2006; Hanson et al., 2003; Bouchette et al., 2014; Hurst et al., 2015; Limber et al., 2017). Coastline models are typically used to evaluate large spatial scale, medium to long-term temporal scale morphological evolution.

Coastal area models simulate both cross-shore and alongshore sediment transport processes at the relevant timescales in 2DH (two horizontal dimension) or 3D models. A variety of models exist that are designed for specific studies in idealized settings, such as estuaries (e.g. Hibma et al., 2003; Winter, 2006), inlets (e.g. Wang et al., 1995; Ranasinghe and Pattiaratchi, 1999), and beaches and the littoral zone (e.g. Lesser et al., 2004; Tonnon et al., 2007). These process-based models are typically designed to be applicable at engineering temporal and spatial scales, for a wide range of applications, taking into account coastlines of arbitrary geometry as well as the presence of coastal structures. The main disadvantage is the computational time required, thus limiting the temporal and spatial scales of their application.

Even with the development of a wide range of process-based models able to hindcast short-term beach and shoreline evolution, these models remain limited in their ability to hindcast, and even more so, forecast erosion and recovery at seasonal and longer timescales (Davidson et al., 2017). Process-based models are mostly concentrated on the timescales of the hydrodynamical processes (de Vriend et al., 1993), which are much shorter than the temporal scales of interest here. Owing to the nonlinear nature and complexity of coastal systems, there still exists a strong need for models able to predict current and future beach changes (Davidson et al., 2017).

A universal model for predicting coastal evolution spanning short to long timescales, or small to large spatial scales, does not exist (Hanson et al., 2003). In addition, while significant progress has been made in modeling beach erosion, the ability to use process-based models to simulate beach recovery processes remains a significant challenge (de Vriend et al., 1993; Roelvink and Brøker, 1993; Davidson et al., 2017). This may thus lead to significant errors when simulating long recovery periods.

To be able to make regional-scale predictions of shoreline change and to analyze erosion risks on medium to long timescales, empirical modeling approaches based on equilibrium concepts may be an optimal choice. Equilibrium beach profile concepts, discussed previously in section 2.2.4, can be extended to develop equilibrium beach change models that use empirical functions to relate incident wave conditions, beach characteristics, and beach morphological evolution (e.g. Dean and Dalrymple, 1991; Miller and Dean, 2004; Davidson and Turner, 2009; Yates et al., 2009a; Davidson et al., 2010; Kuriyama et al., 2012; Long and Plant, 2012; Splinter et al., 2014). Empirical equilibrium beach models quantify the hypotheses that: (1) for a constant wave forcing, an equilibrium beach response exists (e.g. Figure 2.15 in section 2.2.4), and (2) a beach in disequilibrium with the wave field will evolve toward an equilibrium state at a rate proportional to the disequilibrium (e.g. Miller and Dean, 2004; Yates et al., 2009a; Davidson and Turner, 2009; Splinter et al., 2014). During my thesis work, I developed an empirical equilibrium shoreline change model based on these two concepts (Yates et al., 2009a, 2011). Equilibrium theory has also been used to model the evolution of beach profiles (Larson and Kraus, 1989), including the response to beach nourishment projects (Dean and Dalrymple, 1991), as well as interannual variations in sandbar crest (Plant et al., 1999), alongshore variability in sandbar crest position (Splinter et al., 2011) and shoreline response to sea-level rise (Dubois, 1990), storm surges (Kriebel and Dean, 1993), storms (Miller and Dean, 2004), and daily to interannual variations in wave conditions (Davidson and Turner, 2009; Davidson et al., 2010; Splinter et al., 2014).

The following two sections present two projects in which I have used different modeling techniques to study short-term (hours to days) and medium-term (seasonal to interannual to decadal scale) morphological evolution. First, in section 2.3.1, the work of the Masters internship of Marine De Carlo (2017, co-advised with Damien Pham Van Bang) is presented, detailing the process-based modeling of storm-induced beach erosion using the XBeach model. Then, in section 2.3.2, the ongoing development of the empirical equilibrium morphological change model developed during my thesis work is described. This work is part of the ongoing collaboration with Nicolas Le Dantec and France Floc'h (IUEM), including the Masters work of Clara Lemos (2016), Matthew Leary (2018), and the ongoing PhD project of Teddy Chataigner (2018-2021). The objective of this work is to reproduce and ultimately predict short to medium-term to long-term beach morphological evolution.

2.3.1 Process-based modeling of storm-induced beach erosion

At short temporal and small spatial scales, such as the storm-induced response of a beach profile, process-based models are an optimal choice for representing the dominant physical processes controlling morphological evolution. However, observations are still needed to validate and calibrate these approaches, in particular in complex environments.

Approximately a decade ago, the open source, process-based model XBeach was developed with the goal of reproducing well extreme beach and dune erosion during storm events (Roelvink et al., 2009). The model simulates both short and long (infragravity) wave transformation processes, as well as wave-induced setup and unsteady currents in 1D or 2D settings. XBeach can be run in either hydrostatic or non-hydrostatic mode. In the hydrostatic mode, the short wave amplitude is solved using the wave action and roller equations, separately from the long wave, current, and morphological evolution, which are solved at the scales of wave groups. In the non-hydrostatic mode, the model additionally solves the phase-resolved, short wave motions, with the nonlinear shallow-water equations and a corrective pressure term, but with significantly increased computational time. For more details about the model equations, see (Roelvink et al., 2009) and the XBeach Open Source Community website (https://oss.deltares.nl/web/xbeach/).

Originally designed to model dune erosion and overtopping processes (Roelvink et al., 2009; McCall et al., 2010), the hydrostatic mode of the XBeach model has been tested and validated for modeling beach and dune erosion on a wide variety of beaches, in both 1D and 2D (e.g. Bolle et al., 2011; Harley et al., 2011; Vousdoukas et al., 2012; Splinter and Palmsten, 2012). Additional work also has tested and improved the simulation of beach recovery and nearshore accretion after storms (van Rooijen et al., 2012; Pender and Karunarathna, 2013; Daly et al., 2017), but work remains to be done to validate the ability of XBeach to reproduce accurately beach accretion

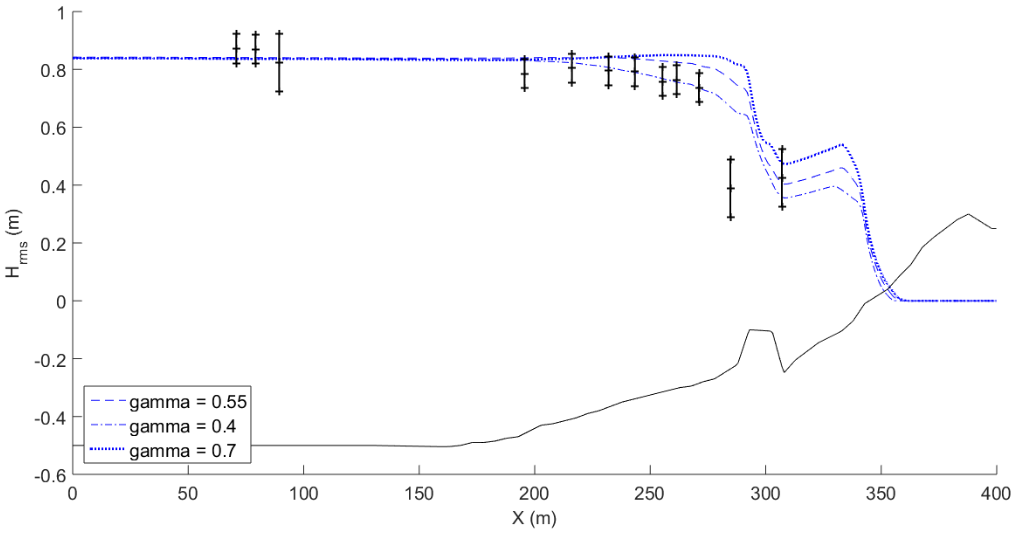

Figure 2.21: Observed (black crosses, with error bars) and simulated (blue) root-mean square wave height (H_{rms}) evolution along the cross-shore profile for storm 1 for the small submerged breakwater (SBW1) using the 'Roelvink2' wave breaking model with three values of γ (see legend).

processes. Daly et al. (2017) suggest using the non-hydrostatic mode of XBeach to reproduce well accretion processes, but Roelvink et al. (2018) caution that further validation of sandy beach morphological evolution using the non-hydrostatic model is still necessary. Finally, other recent extensions also allow modeling gravel beach response to waves and tides (Williams et al., 2012; McCall et al., 2014), and the impacts of coral fringing reefs (Dongeren et al., 2013) and vegetation (van Rooijen et al., 2016) on nearshore hydrodynamics.

During the Masters internship of Marine De Carlo (2017), we selected the XBeach morphological change model to study storm-induced cross-shore beach profile evolution with and without the presence of submerged structures, reproducing the laboratory experiments described in section 2.2.3. Since the XBeach model has been used extensively to model erosion on natural beaches, the objective of our work was to evaluate the ability of the model to reproduce the observed morphological changes on beach profiles with submerged structures. In particular, the ultimate goal of the study was to evaluate the feasibility of using XBeach to conduct future studies optimizing the configuration of structures to develop design criteria for real applications.

In this study, we calibrated the model free parameters in two phases using first the hydrodynamic and then the morphological measurements (described in section 2.2.3). The hydrodynamic calibration phase was completed during time periods when the bathymetry was in an equilibrium state, thus remaining nearly constant, suggesting that the morphological evolution could be considered negligible. During these simulations, the sediment transport module therefore was deactivated in XBeach to allow comparing the simulated and measured hydrodynamics, without

Table 2.3: XBeach hydrodynamic tests

Test	**Wave breaking model**	γ	γ_2	**Normalized $\mathbf{H_{rms}}$ errors** SBW1	SBW2	Geo1	Geo2
1	Roelvink2 (default)	0.55	-	0.12	0.05	0.15	0.14
2	Roelvink2 (default)	0.4	-	0.09	0.05	0.16	0.15
3	Roelvink_Daly (default)	0.55	0	0.09	0.05	0.15	0.14
4	Roelvink_Daly (default)	0.4	0.1	0.08	0.05	0.17	0.15
5	Roelvink_Daly (default)	0.4	0.2	0.08	0.05	0.17	0.15
6	Roelvink_Daly (default)	0.4	0.3	0.09	0.05	0.17	0.15

simulating the impacts of the morphological evolution. Finally, owing to limitations in simulating the reduced-scale particle density, which is below the threshold recommended for use in XBeach, the simulations were conducted at full scale.

In this numerical study, we completed simulations for the 4 submerged structures that were able to reduce shoreline erosion (SBW1, SBW2, Geo1, and Geo2). In addition to the normalized root-mean square error (RMSE), the Brier Skill Score (BSS, van Rijn et al., 2003; Sutherland et al., 2004) was used to evaluate the model skill since it has been shown to be a good measure of morphological evolution model performance (Roelvink et al., 2009; Davidson et al., 2010; Pender and Karunarathna, 2013; Berard et al., 2017).

Among the seven different hydrodynamic model parameters evaluated (for more details, see De Carlo (2017)), the hydrodynamic calibration phase showed the sensitivity of the results to the choice of wave breaking model and to the free parameter γ (breaking wave height to water depth ratio, Figure 2.21). This parameter is the criterion used to initiate wave breaking in the model and therefore has a strong impact on the cross-shore location of wave breaking. However, with a limited number of wave gauges in and shoreward of the wave breaking zone (x=280-350 m in Figure 2.21), a series of different tests with γ values ranging from 0.4 to 0.55 produced similar normalized errors in H_{rms} (Table 2.3). It was therefore not possible to evaluate quantitatively the best γ value using only the hydrodynamic observations.

The morphodynamic calibration phase presented a stronger challenge, and a systematic series of tests were completed to evaluate the sensitivity of the simulation results to 32 different model parameters (for more details, see De Carlo, 2017). The tests demonstrated that once calibrated (using the SBW1 observations), XBeach was able to reproduce well the observed changes on the upper beach profile for all four submerged structure experiments (SBW1 and Geo1 shown in Figure 2.22). This was achieved primarily by adapting γ and the asymmetry parameter $facAs$, which is known to have an important role in defining the direction and magnitude of sediment transport. However, XBeach was unable to reproduce the morphological changes near the structures (e.g. for SBW1 and Geo1 in Figure 2.22). In particular, the observed scouring at the base of

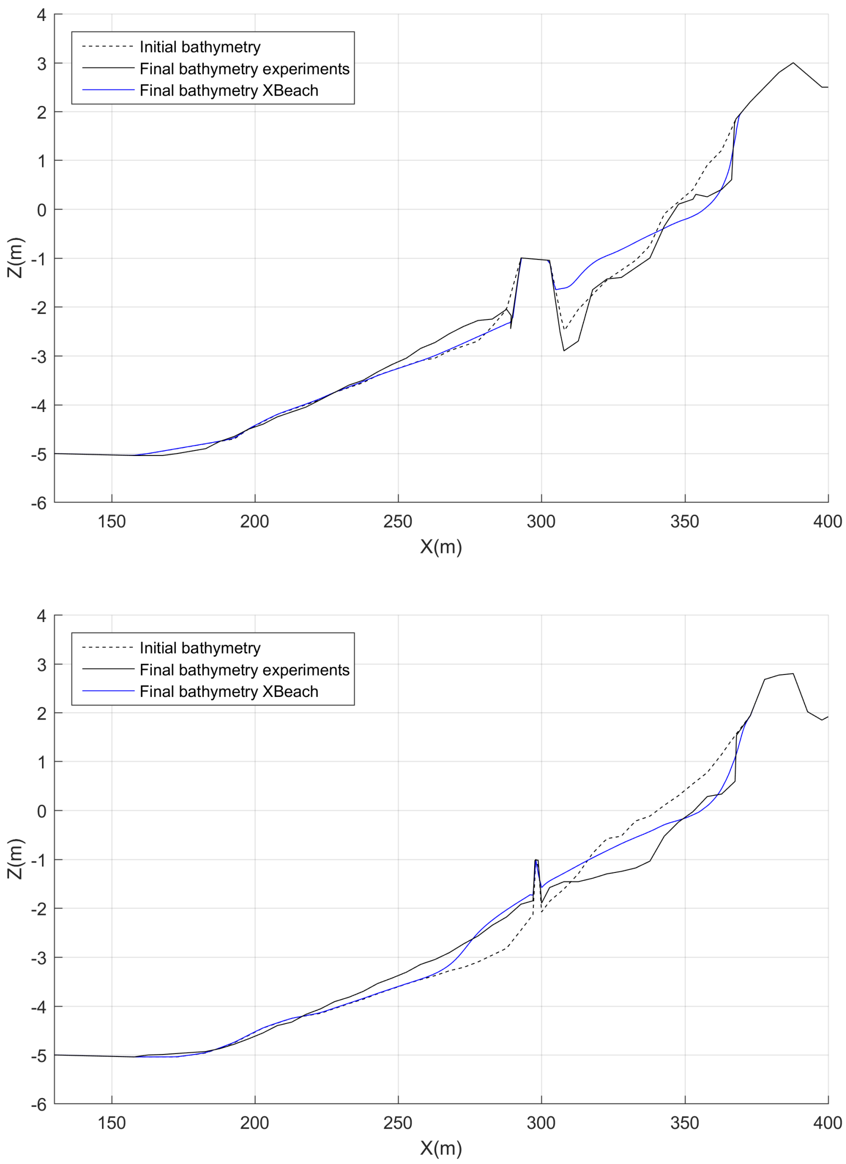

Figure 2.22: Observed (black) and simulated (blue) profile evolution for storm 1 (Figure 2.11) for: (top) the nearshore submerged breakwater (SBW1), and (bottom) the nearshore geotextile tube (Geo1). In both cases, the initial cross-shore profile is shown with the dashed black line.

the structure (most significant for SBW1) and the bar-like morphology between the structures and the shoreline was not reproduced well. Overall, XBeach produces much smoother predictions of beach profile changes than those observed in the experiments.

The retained optimal model parameters were: the Roelvink_Daly wave breaking model, with $\gamma = 0.7$, $\gamma 2 = 0.2$, and $fac_{ua} = 0.3$ (which takes into account both the asymmetry and skewness). Using these settings, which were chosen to minimize the shoreline position error and maximize the BSS, it was possible to obtain horizontal shoreline position errors less than 0.1 m, and upper beach and total profile BSS values greater than 0.55 and 0.75, respectively (in the good to excellent range, (van Rijn et al., 2003)), for the four studied structures (e.g. for SBW1 and Geo1, shown in Figure 2.22). If the objective is to analyze only the storm-induced shoreline erosion in the presence of submerged structures, the XBeach model may be used for preliminary studies. However, Berard et al. (2017) forewarned that erosion near the shoreline can be over-predicted, causing greater deposition along the lower beach face, as shown by Van Dongeren et al. (2009). Therefore, one must be cautious in using this calibration, since we, in this study, and previous authors (e.g. Splinter and Palmsten, 2012) have shown XBeach to be sensitive to the input parameters, in particular in the swash zone (van Rooijen et al., 2012).

Quantification of the repeatability of the experiments, as well as additional measurements of the wave height in the breaking zone could allow improving the XBeach model calibration. However, a more detailed model of the sediment transport around the structure, including 2DH experiments and simulations, would be necessary before validating the use of the XBeach model to define design criteria and to validate the efficiency of submerged structures in real settings.

2.3.2 Development of an equilibrium beach contour change model

During my thesis work advised by Bob Guza, we developed a simple empirical equilibrium beach change model (Yates et al., 2009a) based on high resolution morphological and hydrodynamic observations (Figure 2.16). The model assumes that the shoreline change rate ($\frac{dS}{dt}$) can be estimated as a function of the instantaneous wave energy (E) and wave energy disequilibrium (ΔE):

$$\frac{dS}{dt} = C^{+/-} E^{1/2} \Delta E, \quad \text{with} \quad \Delta E = E - E_{eq}(S), \tag{2.3}$$

where $C^{+/-}$ are accretion (C^{+}, $\Delta E < 0$) and erosion (C^{-}, $\Delta E > 0$) rate change coefficients, and E_{eq} is the equilibrium wave energy, or wave energy causing no further changes for a given shoreline position S. E_{eq} is defined as a linear function of S: $E_{eq}(S) = aS + b$, where a and b are free parameters that depend on the beach characteristics. The model free parameters are determined using an optimization algorithm, which requires medium to long-term time series of beach morphology and wave conditions. During my thesis work, we and then Splinter et al. (2013) studied the necessary requirements for morphological data (frequency, duration) to calibrate accurately empirical equilibrium models, demonstrating the need for at least monthly, multi-year time series of beach morphology for making short to medium-term predictions. However, Doria et al. (2016) demonstrated the limitations of applying a model calibrated with typical wave conditions to predict erosion during less frequent events with wave characteristics not observed during the calibration period. The skill of the model in predicting beach shoreline changes was demonstrated at five microtidal beaches in California (for more details, see Yates et al., 2009a, 2011), with the model skill varying from 70% to 80%.

More recently, Castelle et al. (2014) showed that the Yates et al. (2009a) shoreline change model also could be used to predict beach elevation contour movement at different altitudes along the intertidal beach profile on a mesotidal beach. The only adaptation introduced in the model (relative to Yates et al. (2009a)) was the addition of a fifth free parameter d, indicating the uncertainty in the initial shoreline position. Castelle et al. (2014) demonstrated the skill of this model, as well as the Davidson et al. (2013) model in reproducing the evolution of a range of altitudes on a mesotidal beach (Truc Vert, France).

2.3.2.1 Equilibrium model formulations

As discussed previously, a variety of empirical equilibrium models have been developed based on equilibrium beach concepts. Two more recent contributions are the model that I developed during my thesis work (Yates et al., 2009a), described in the previous section and used throughout this work, and the ShoreFor model developed by Davidson et al. (2013) and Splinter et al. (2014). While based on similar theoretical concepts, these two models differ in their definitions of the equilibrium beach state and in their explicit formulations. The ShoreFor model is thus described here and the similarities and differences with the Yates et al. (2009a) are highlighted.

To begin with, the concept of an equilibrium beach state is treated differently in the two models. In the Yates et al. (2009a) model, a single equilibrium wave energy E_{eq} exists for each beach state S. In the ShoreFor model, the concept of equilibrium is defined based on the antecedent morphological beach states (and therefore wave conditions), thus allowing the equilibrium condition to vary temporally. The shoreline change rate (dS/dt) is defined as a function of the dimensionless fall velocity Ω, which can be related the morphological state of the beach (Wright and Short, 1984):

$$\frac{dS}{dt} = C^{+/-} P^{1/2} \frac{\Delta\Omega}{\sigma_{\Delta\Omega}} + b, \quad \text{with} \quad \Delta\Omega(t) = \Omega_{eq}(t) - \Omega_b(t), \tag{2.4}$$

where $C^{+/-}$ are accretion ($C^+ = c, \Delta\Omega > 0$) and erosion ($C^- = rc, \Delta\Omega < 0$) rate coefficients, similar to Yates et al. (2009a), P is the wave energy flux at breaking, and b is a linear trend added to the model to take into account all other long-term processes not simulated explicitly. In addition, $\sigma_{\Delta\Omega}$ is the standard deviation of $\Delta\Omega$ (used to normalize $\Delta\Omega$), c is a rate parameter, and r is the erosion ratio, defined empirically as a function of the wave forcing (see Splinter et al. (2014) for more details). The equilibrium condition $\Omega_{eq}(t)$ is assumed to be dependent on the memory of the antecedent beach states, following Wright et al. (1985) such that:

$$\Omega_{eq}(t) = \frac{\sum_{i=1}^{2\phi} \Omega_i 10^{-i/\phi}}{\sum_{i=1}^{2\phi} 10^{-i/\phi}}. \tag{2.5}$$

This weighted sum of antecedent beach morphological conditions has one important free parameter ϕ, the response factor. It is defined to represent the number of days in the past such that the weighting factor reaches 10%, 1%, and 0.1% at ϕ, 2ϕ, and 3ϕ days before the current time t. To reduce the number of model free parameters, the weighted sum in Eq. 2.5 was truncated at 2ϕ, as suggested by Davidson et al. (2013). The only remaining free parameter in Eq. 2.5 is thus ϕ, the response factor that determines the time period over which the weighted sum is taken, which indicates the importance given to antecedent beach conditions over a shorter or longer span of time. This parameter can range from days to hundreds of days and is site specific.

In terms of the range of application of these models, both formulations are based on the temporal variability of the wave conditions, and thus the models are designed for beaches where waves are the primary forcing factor causing shoreline changes. Short temporal and/or small spatial scale processes affecting beach cusps, bar dynamics (e.g. ridge-runnel systems, bar welding), or local geomorphological features (e.g. rip embayments, exposed peat or bedrock) are not taken into account. In addition, alongshore sediment transport, as well as changes in the water level (e.g. storm surge, interannual sea level changes related to climate cycles like El Niño-Southern Oscillation (ENSO), and long-term changes in the mean sea level) are not explicitly modeled. The ShoreFor model does, however, include a linear term b that may implicitly take into account any contributions of these processes that are linear in time. Both models are thus expected to have higher skill at sites that are dominated primarily by wave-forced cross-shore sediment transport processes on micro- to meso-tidal beaches, at seasonal to annual, to decadal timescales.

To summarize the comparison between the two models, the main differences in representing physical processes are:

1. the definition of a stationary equilibrium (E_{eq} in Eq. 2.3) in the current model in comparison to a temporally varying equilibrium ($\Omega_{eq}(t)$ in Eq. 2.4) in the ShoreFor model; and
2. the presence of a linear trend b added to the ShoreFor model (Eq. 2.4) to implicitly take into account all other linear processes not explicitly modeled in the wave-forced term.

With respect to model free parameters, the Yates et al. (2009a) model has four free parameters: $C^{+/-}$ defining the accretion and erosion rate change coefficients, and a and b defining the relationship between the beach state and the equilibrium wave energy. In the ShoreFor model, there are three free parameters: c defining the rate parameter, ϕ defining the time period used to calculate $\Omega_{eq}(t)$, and b the linear trend. In both models, the free parameters are determined using optimization algorithms comparing the simulated and observed shoreline changes. Therefore, both models require observations for the calibration phase. While site-specific calibration of these parameters is recommended for both models, Splinter et al. (2014) applied the ShoreFor model at 12 different sites to evaluate the obtained optimal model free parameters, and they proposed a generalized form of the model in which the wave-driven free parameters c and ϕ can be estimated using empirical relationships depending on $\overline{\Omega}$ (the temporal mean of Ω).

Finally, the wave conditions used to force both models also differ. In the Yates et al. (2009a) model, the offshore wave conditions are used, whereas in the ShoreFor model, the wave power and dimensionless fall velocity are calculated using the wave conditions at the depth-limited breaking point (assuming a breaking parameter $\gamma = 0.78$), as described by Splinter et al. (2014).

2.3.2.2 Equilibrium modeling of macrotidal beaches

As described above, the model is designed ideally to simulate shoreline changes on micro- to mesotidal beaches where the impacts of the tide level are not significant. When extending the model to meso- and macrotidal beaches, it is important to consider the percentage of time that a given elevation contour is impacted by the incoming wave energy. During the Masters internship of Clara Lemos (2016), we therefore proposed an extension to the equilibrium model to take into account the impacts of the varying water level. A vertical threshold of the relative water level L was defined to determine the time periods when sediment transport is significant and thus contour evolution is simulated (Lemos et al., 2018). The assumption is that the vertical limits of sediment transport along a beach profile are defined by the maximum runup level and the water depth at the offshore limit of the surf zone. We then tested two approaches in the equilibrium model: (1) L symmetric about the water level (instantaneous tide level) for simplicity, with L varying in the range of 0.5 m to 6 m, or (2) L proportional to the incoming wave height. In the second approach, L is assumed to be a function of the wave height to approximate more realistic thresholds corresponding to zone of the beach impacted by the maximum level of wave runup ($L \sim H_s$, following Caulet et al. (2017)) and by the limit of the wave breaking zone ($L \sim 2H_s$, following Dehouck et al. (2009)).

Once the L threshold has been defined, it is used to determine the time periods when a given contour elevation Z_0 will be modified by the incoming wave energy (Figure 2.23b). When Z_0 is

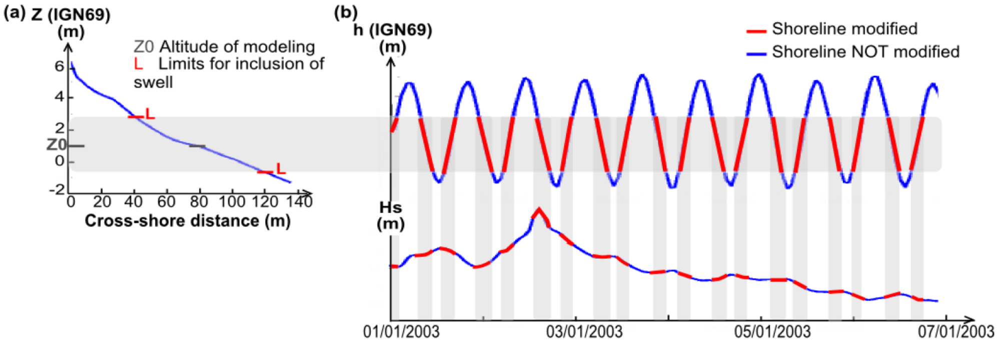

Figure 2.23: Extended equilibrium model taking into account the tide level: (a) beach profile with the selected elevation contour Z_0 and modeling threshold L, and (b) tide level determining the time periods (red) when the model takes into account the wave forcing to simulate change in the contour elevation cross-shore position (Figure 7 in Lemos et al., 2018).

within the range defined by L around the instantaneous still water level (from hourly observations of the SHOM), the simulated contour elevation position is modified (red zones, Figure 2.23b). Outside of this threshold range, no elevation contour changes are simulated (blue zones, Figure 2.23b). This extended model is a simple, first attempt to take into account the effects of the tide level in an equilibrium beach change model.

Before implementing the extended version of the empirical equilibrium model, the original model formulation was applied to reproduce the observed changes at a range of contour altitudes, extending from approximately -2.0m to +6.0m (IGN NGF) at the two study sites, Porsmilin and Vougot. Lemos et al. (2018) demonstrated the skill of the model in reproducing the interannual variations in contour position at Porsmilin beach, with a good predictive ability in the upper intertidal zone (60%), which is reduced in the lower intertidal zone (40%). Following Yates et al. (2009a) and Ludka et al. (2015), alternative model formulations were tested by forcing the model with the wave power instead of the wave energy, thus taking into account the impacts of the wave period. The model skill increased to nearly 70% in both the upper (small increase in skill) and lower intertidal (nearly 30% increase in skill) zones. We suggest the importance of the wave period in reproducing well the sediment transport dynamics, related to the importance of infragravity waves at this site, in particular in the dissipative lower intertidal zone, which merits further study (Lemos et al., 2018).

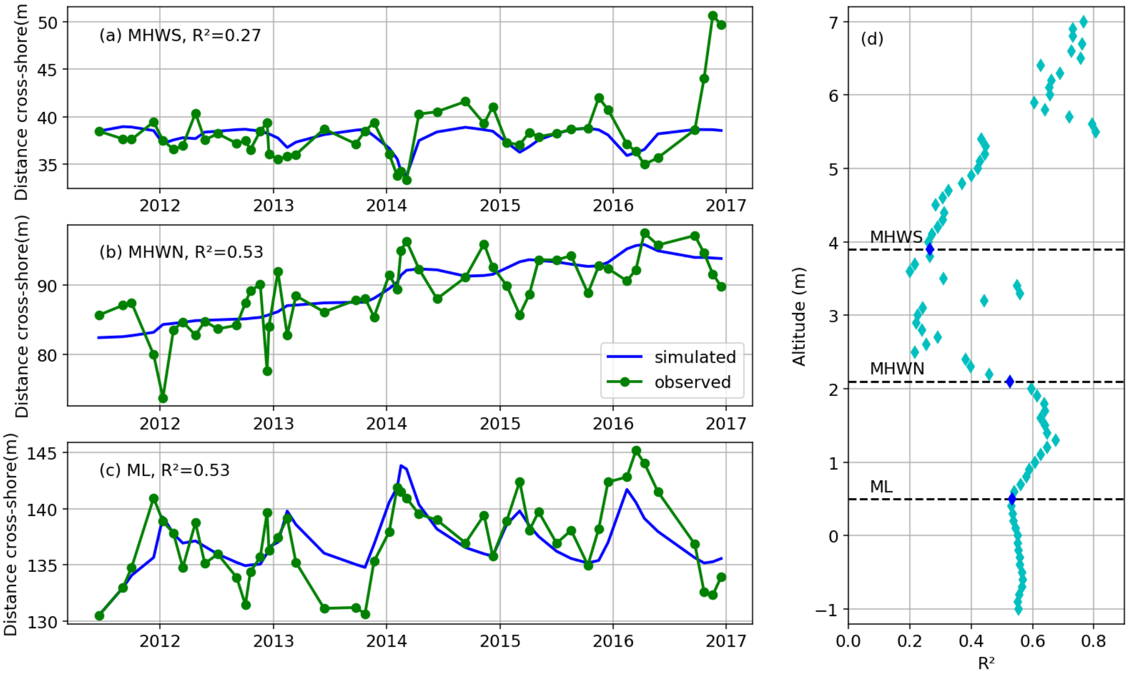

Figure 2.24: Equilibrium model application at profile 6 at Vougot beach: simulated (blue) and observed (green) contour evolution for: (a) MHWS, (b) MHWN, and (c) MW levels. (d) R^2 correlation coefficient as a function of altitude, where the horizontal dashed lines indicate the contours shown in plots (a)-(c).

During the Masters internship of Gabin Bouvard (2017) and the ongoing thesis work of Teddy Chataigner, we then applied the model at the second study site, Vougot, demonstrating relatively high skill ($> 60\%$) in reproducing contour evolution in the upper and lower intertidal zones along two cross-shore profiles (profiles 5 and 6, Figure 2.24), located at the southwestern end of the beach. However, the model demonstrated reduced skill in reproducing contour evolution along Profiles 1-4, which are located near a section of the beach with high alongshore bathymetric variability, suggesting the importance of alongshore sediment transport for these profiles.

Then the extended version of the model taking into account the impacts of the tide (or more generally water) level was applied, showing equally high model skill as the previous version of the model, with essentially the same cross-shore evolution, independent of the threshold L. While the simulated contour evolution does not change significantly, the rate change coefficients C^+ and C^- do vary as a function of L. The rate change coefficients depend strongly on the duration of events, which, for a given contour elevation Z_0, changes as a function of the applied threshold L. For example, Figure 2.25 shows the percentage of time that the model simulates beach changes as a function of the contour elevation.

When using the more realistic model of L as a function of the incoming wave height, optimal rate change coefficients correspond to the case when $L = 0.5$ m for C^+ and to $L = 3.0$ m for C^- at Porsmilin. For the accretion rate coefficient C^+, this value of L corresponds to the mean wave height at Porsmilin beach. For the erosion rate coefficient C^-, which typically is applied during events with large H_s, this implies that the majority of the beach is impacted during storm events. Based on the results of this work, we have retained the approach using a variable L that is proportional to the significant wave height for future modeling applications.

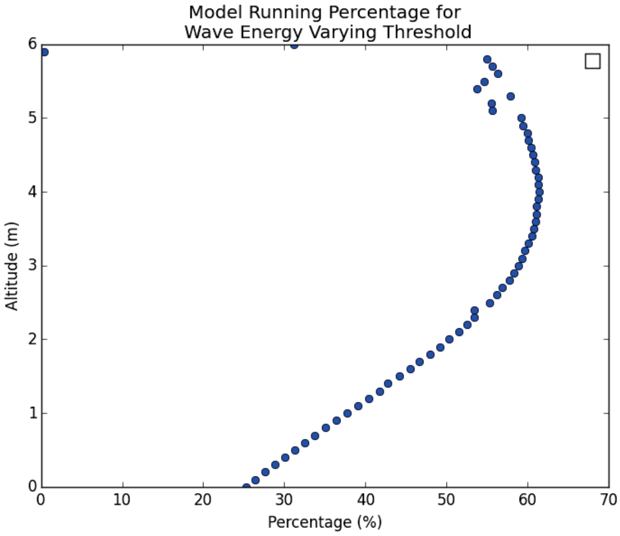

Figure 2.25: Percentage of time the model simulates contour elevation changes at profile 5 at Vougot beach using the variable threshold L that is proportional to the wave height.

Finally, at Porsmilin beach,the added value of the extended version of the model is that it not only represents a more physically-based model (evolution of beach contours only when the altitude may be impacted by the water level), but also that the rate change coefficients $C^{+/-}$ attain values of the same order of magnitude as those obtained for microtidal beaches (Lemos et al., 2018). This remains to be validated at Vougot beach, as well as other meso- and macrotidal beaches.

2.4 Ongoing work and perspectives

This chapter provides a summary of my research activities in the field of coastal morphological evolution, covering a range of spatial and temporal scales and using a variety of different techniques, ranging from the analysis of observations, to laboratory experiments, and empirical and numerical modeling. As my career has evolved at the LHSV, I have participated in experimental studies to take advantage of the available resources, and I have focused more particularly on numerical and empirical modeling. This work has allowed me to identify a number of challenges and open research questions, and my ongoing work and future perspectives aim to address several important concepts in these fields. My future work will be focused primarily on the two themes of numerical and empirical modeling, including:

- **Investigation and application of process-based modeling approaches** to test, improve understanding of, and propose simplified models of the dominant physical processes causing morphological evolution (section 2.4.1), and
- **Ongoing development and analysis of empirical equilibrium-based modeling approaches** to extend their application to take into account alongshore processes, to predict beach evolution in response to climate change, to understand and define better the advantages, limits, and uncertainties of such models (section 2.4.2).

Ongoing work and perspectives in these two themes are presented in the following two sections.

2.4.1 Process-based modeling approaches

My previous work using process-based models began with the evaluation of the capacity of the XBeach model to reproduce a series of laboratory flume experiments. The objective of the experiments was to test the efficiency of three types of submerged structures in reducing storm-induced shoreline erosion. These experiments presented a number of limitations, including their two dimensional nature and the limited number of different structure configurations, wave conditions, and beach characteristics that could be tested. To begin to address the limitations of the experimental work, we conducted a numerical study to test the skill of XBeach in reproducing the measured shoreline erosion. The preliminary study allowed calibrating the hydrostatic version of the XBeach model with the experimental data to then be able to expand the range of tests for a specific site.

However, this preliminary work highlighted the challenges in using the XBeach model to simulate the complex sediment transport patterns around submerged structures. The calibrated model was able to reproduce the upper beach and shoreline erosion during the storm events, but the beach profile evolution near the structure was not simulated well. To further the study of the use of process-based models to aide in engineering studies, with and and without the presence of submerged structures, in the next five years I plan to pursue this research theme by:

- **Improving understanding of the cross-shore variability of sediment transport processes** in the surf zone through the continued analysis of the experimental wave conditions. In particular, the objective here is to evaluate the observed and simulated wave skewness and asymmetry in relation to the observed and simulated morphological changes, following on the work of Grasso et al. (2009). They evaluated the wave hydrodynamics in a series of laboratory experiments reproducing equilibrium beach profiles, identifying the cross-shore variability of these wave characteristics. The goal here is to pursue this study by relating the wave hydrodynamics to the observed morphodynamics, both in the observations and in the simulations.

  The cross-shore variability of wave hydrodynamic processes and the induced morphological changes (erosion and accretion patterns) is particularly important for understanding the formation of equilibrium beach profiles. This theme is of significant interest both for validating the dynamics of the XBeach model, and for using this information to refine equilibrium beach profile change models, as will be discussed next.

- **Evaluating the capacity of the XBeach model to reproduce well the observed profile evolution** in the laboratory experiments (in its non-hydrostatic mode) and on natural beaches (in both the non-hydrostatic and hydrostatic modes). In particular, the focus of this work is aimed at reproducing both storm erosion events and the subsequent beach recovery, which remains an open challenge in process-based morphological evolution models (Davidson et al., 2017). These studies are focused on reproducing the short-term (daily to weekly) morphological fluctuations, and to do so, this research theme will continue to benefit from an ongoing collaboration with researchers at the IUEM (with short-term, daily to weekly observations of beach profile evolution at the study sites in Brittany) and abroad (within the PHC Sakura project and the initiation of new collaborations).

- **Applying the XBeach model to evaluate the sensitivity** of the simulated shoreline changes to a wide range of wave and beach characteristics, both with and without the presence of submerged structures. First, this work may address the ability to use the XBeach model to predict beach profile response in the presence of submerged structures, depending on the results of the calibration tests proposed above. Second, it is of interest to run a wide range of tests of beach profile evolution (with varying initial profiles, and beach and wave characteristics) to investigate the development of equilibrium beach profiles in process-based numerical models. This work may address a number of research questions relating process-based and empirical equilibrium modeling, such as:

- can process-based models accurately reproduce observed equilibrium profiles?
- are the simulated erosion and accretion change rates and the time to attain an equilibrium profile representative of observations?
- can process-based models be used as a tool to identify the main physical processes governing morphological change rates?

The goal of my work in this domain is to test the ability to use process-based models to advance understanding of both the complexities of the physical processes governing beach morphological changes, and the potential simplifications of these dynamics that can then be integrated in empirical modeling approaches.

2.4.2 Empirical equilibrium-based modeling approaches

Equilibrium beach change models are currently the focus of much work at the international level because of their simplicity, ability to be applied to any site with adequate observations, and usefulness for coastal managers and planners (e.g. Banno and Kuriyama, 2014; Vitousek et al., 2017; Davidson et al., 2017; Lemos et al., 2018). However, these types of models have a number of limitations, which have been described in the previous sections. To overcome these limitations, my work during the next five years will be focused on:

- Integrating an **alongshore transport model** in the cross-shore only model, which was the subject of the preliminary work of the Masters internship of Matthew Leary, and is now an integral part of the PhD work of Teddy Chataigner (2018-2021). Several different types of alongshore sediment transport models are currently being considered, following the recent work of Vitousek et al. (2017), Bouchette et al. (2014), and Robinet et al. (2018). These approaches calculate the alongshore sediment transport based the incident wave energy flux, using widely known formula for estimating the alongshore sediment transport rate Q (Komar and Inman, 1970; Kamphuis, 1991; USACE, 1984; Bayram et al., 2007), but they differ in the calculation of the contribution of alongshore transport to the shoreline movement and the methods used to discretize the shoreline. These approaches will be explored to select the optimal approach to couple with the existing cross-shore equilibrium beach change model. A second important point to address, which has not been treated in current coupled cross-shore equilibrium-based approaches and one-line longshore sediment transport models is the importance of the cross-shore distribution of sediment, which is most often assumed constant along the active beach profile (Vitousek et al., 2017; Robinet et al., 2018). The cross-shore distribution of longshore sediment transport has been studied on sandy beaches (e.g. Kamphuis, 1991; Bayram et al., 2001), and this is an important element that will be investigated in our implementation of an alongshore transport model.

- Investigating an extended approach to take into account the **impacts of the water level**, going beyond the preliminary approach proposed during the Masters internship of Clara Lemos (Lemos et al., 2018). As described in section 2.3.2, this simple approach limited the simulated evolution of beach contours to time periods when the relative water level is in a predefined range $[+H_s, -2H_s]$ around the contour elevation. This binary approach does not take into account the effects of the relative water level on the sediment transport rates, and current work is focused on evaluating a new approach. This new approach also has the potential to unify the application of the proposed modeling strategy along the beach profile instead of applying the model independently at each elevation contour, as tested previously (Yates et al., 2011; Castelle et al., 2014; Lemos et al., 2018).

- Applying the newly developed model at additional study sites (via national and international collaborations) to validate the proposed methods (Lemos et al. (2018) and the current work in progress) and to explore the **generalization of the model free parameters**, in particular the erosion and accretion rate coefficients $C^{+/-}$. It has been suggested that the free parameters in equilibrium beach change models depend strongly on the local beach characteristics (Miller and Dean, 2004; Davidson and Turner, 2009; Yates et al., 2009a, 2011). By applying the developed model on a range of different beaches, the variability of the optimal model free parameters can be studied to evaluate their dependence on the local beach characteristics, such as the beach slope or sediment grain size. This work may include the use of machine learning approaches to determine the optimal model free parameters as a function of beach characteristics.

- Extending the existing model to take into account the **impacts of climate change**, including the impacts of sea level rise and changes in the future wave climate. Current practice for integrating the impacts of sea level rise in morphological models predicting beach profile and shoreline evolution consists in applying the Bruun Rule (e.g. Bruun, 1962; Davidson-Arnott, 2005; Banno and Kuriyama, 2014; Anderson et al., 2015; Vitousek et al., 2017). In recent years, a second approach called the Probabilistic Coastline Recession (PCR) model (Ranasinghe et al., 2012), has gained in interest due to the integration of the impacts of dune toe erosion on beach profile and shoreline evolution. These two simple approaches are based on different assumptions of the processes controlling the long-term shoreline evolution, and given the assumptions and limitations in validating these methods, one must apply them with caution (Le Cozannet et al., 2019). It is therefore necessary to continue to explore additional methods that enable taking into account changes in the mean water level. The objective here is to extend the approach discussed above, which was developed for profiles exposed to tidally-varying water levels based on equilibrium beach change concepts, to predict the impacts of long-term changes in the mean water level. The results of the proposed approach will be compared with the above-mentioned existing approaches to evaluate the variability in long-term predictions of beach evolution using different approaches. Finally, making deterministic predictions of beach morphological evolution is highly unrealistic, and statistical approaches will be used to take into account the uncertainties in the predictions. This work is currently being completed (during the Masters internship of Nicolas Cailler and the thesis work of Teddy Chataigner) in collaboration with a group of Japanese researchers via the PHC Sakura project (2018-2020).

- **Comparing empirical equilibrium and process-based models**, in particular by analyzing quantitatively not only the modeled beach changes, but also the accretion and erosion statistics of natural beaches. This study will allow evaluating the relevance and limitations of each modeling approach, as discussed in the section concerning process-based modeling. In particular, this proposed work will focus on investigating both the appropriate timescales of application of empirical equilibrium models and the accuracy as a function of the optimal observations required to calibrate the model free parameters. Several open questions in using empirical equilibrium morphological change models are related to the appropriate timescales of application:
    - are equilibrium-based models valid on timescales as short as hours to days?
    - or is the bulk parameterization of the physical processes of erosion and accretion more appropriate for weekly to monthly, seasonal, and interannual timescales?
    - additionally, is it possible to extend these approaches for longer timescales or is there an inherent assumption of stationarity in the beach characteristics that prevents the application of these simple models to decadal and longer timescales?

  When asking these types of questions, it becomes rapidly apparent that it is necessary to investigate the variability of the model free parameters and the possibility to develop generalized approaches to determine their dependence on the local beach characteristics and/or wave conditions, as described above. Finally, these questions are strongly linked to the proposed work with process-based modeling approaches, which may be an optimal choice at short timescales.

The goal of my work in this domain is to pursue the development of empirical equilibrium beach evolution models first to be able to reproduce accurately past sandy beach morphological evolution. Ultimately, these tools may then be extended to make future predictions, keeping in mind the uncertainties in these methods. As proposed here, a number of fundamental questions concerning the theory and application of empirical equilibrium morphological change models will be explored to achieve this goal.

Chapter 3

Coastal wave hydrodynamics

3.1 Scientific context and challenges

In recent decades, the need for accurate and efficient models of wave propagation in the nearshore zone has increased owing to the wide variety of applications such as evaluating and managing coastal risks, and designing and maintaining coastal and offshore structures, as well as marine renewable energy devices. In the past, linear wave propagation models were used in wave engineering studies (Maguire, 2011) because of the computational costs associated with studying wave propagation in large spatial domains with nonlinear propagation models. Today, there is rapidly growing interest in providing more detailed representations of waves in the nearshore zone (e.g. D'Alessandro and Tomasicchio, 2008; Kurnia and van Groesen, 2014). Therefore, linear models are being replaced by nonlinear wave propagation models that represent more accurately wave propagation at these spatial and temporal scales (e.g. Zijlema and Stelling, 2008; Engsig-Karup et al., 2009; Roeber et al., 2010; Ducrozet et al., 2012; Zhao et al., 2014; Belibassakis and Athanassoulis, 2011; Filippini et al., 2018; Raoult et al., 2019).

More generally, a wide range of phase-resolving modeling approaches are used to simulate coastal wave propagation depending on the desired spatial and temporal scales and the dominant physical processes at those scales. The focus here is on phase-resolved modeling as opposed to phase-averaged modeling because of the spatial and temporal scales of interest in the coastal zone. These modeling approaches can be classified into different families (Figure 3.1) ranging from simple, linear models based on the mild slope equations and their extensions (Berkhoff, 1972; Chamberlain and Porter, 1995; Lee and Suh, 1998) that are frequently used in coastal and port engineering applications, to computationally intensive CFD (Computational Fluid Dynamics) models that resolve the Reynolds Averaged Navier-Stokes (RANS) equations (Liu et al., 1999; Shao, 2006; Lara et al., 2006; Dalrymple and Rogers, 2006; Higuera et al., 2013a) to simulate local-scale processes (with spatial scales on the order of one to several wavelengths and temporal scales ranging from minutes to hours).

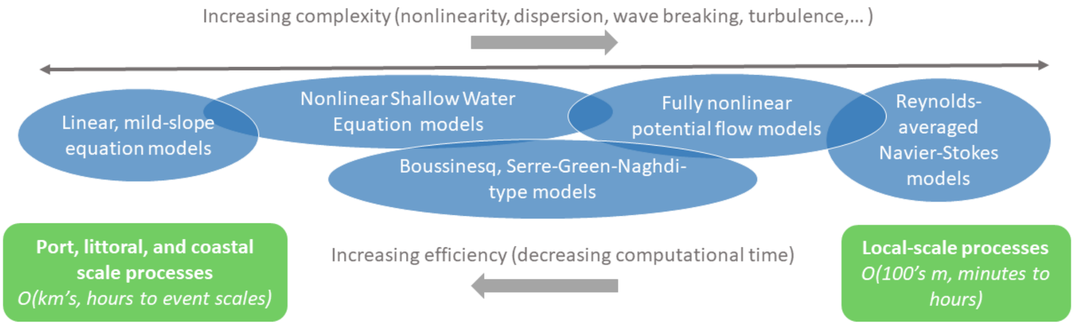

Figure 3.1: Spectrum of families (blue) of phase-resolving wave propagation models and their domains of application (green), ranging from linear models resolving the mild-slope equations (left) to CFD models resolving the Reynolds-averaged Navier-Stokes equations (right).

At the complex end of the spectrum (Figure 3.1) there are wave models solving the RANS equations with a turbulence closure scheme, and the dynamics of nonlinear wave propagation, interactions with the bottom and structures, and wave breaking processes can be simulated. However, the computational costs limit the domain size of applications of these models, and the numerical methods used to resolve the free surface position are often unable to propagate accurately waves over large spatial or long temporal scales owing to numerical diffusion. At the simplified end of the spectrum (Figure 3.1) there are linear wave propagation models that are computationally efficient, but unable to simulate nonlinear wave transformation processes (e.g. wave shoaling, nonlinear wave interactions, etc.).

In the nearshore zone, it is essential to simulate accurately the nonlinear and dispersive characteristics of waves. These effects can be characterized by the wave steepness $\epsilon = kH/2$, relative wave height H/h, and relative water depth $\mu = kh$ (where H, k, and h are the characteristic local wave height, wave number, and water depth, respectively). In particular in the nearshore zone, the wave steepness ϵ and relative wave height H/h increase in shallow water as waves shoal, and the relative water depth μ increases in intermediate and deep water where waves are dispersive. Thus when simulating the propagation of waves from deep water conditions to the coast, it is necessary to simulate accurately both of these effects, and wave propagation models can be classified in this way. Between the two extremes of wave propagation models based on linear wave propagation or the RANS equations, there exist several families of models that make different hypotheses about the nonlinear and dispersive properties of the waves and the fluid flow to simplify this complex problem.

By assuming an incompressible fluid and a vertically homogeneous flow (i.e. that vertical variations are small in comparison to horizontal variations, also known as long wave or shallow water approximation), it is possible to integrate vertically the Navier Stokes equations to derive the Nonlinear Shallow Water Equations (NLSWE, center, Figure 3.1). However, models based on these equations are valid only for shallow water conditions by ignoring dispersive effects, and short waves are not simulated correctly. These kinds of models may be used for simulations extending from the mid- to inner surf zone shoreward, where wave nonlinearity dominates (Brocchini and Dodd, 2008). One advantage of the NLSWE is that they provide a natural framework for simulating wave bores. However, these models are limited by their inability to take into account the effects of wave dispersion. To improve this, one approach is to add a non-hydrostatic pressure term at the free surface and to divide the water column in multiple layers (Zijlema and Stelling, 2008; Zijlema et al., 2011). The model accuracy can be improved further by optimizing the position of these layers (Zhu et al., 2014).

However, these approaches are still limited in representing the dispersive effects of waves in intermediate to deep water conditions, and thus more complex models have been derived assuming that the vertical variability can be described using a polynomial expansion, and estimating the velocity at a fixed vertical level z_α with Boussinesq-type or Serre-Green-Naghdi (SGN) methods (Figure 3.1, center, e.g. Nwogu, 1993; Agnon et al., 1999; Madsen et al., 2002; Fuhrman et al., 2005; Chazel et al., 2009). A variety of models have been derived that are valid to different orders of nonlinearity (ϵ) and dispersion (μ), and they are widely used in coastal engineering applications for their efficiency and relative accuracy (e.g. Madsen and Sørensen, 1992; Schäffer et al., 1993; Wei et al., 1995; Kennedy et al., 2000; Chen et al., 1998; Roeber et al., 2010).

Going one step further along the spectrum, a fully nonlinear and dispersive model can be derived by returning to the Navier Stokes equations and assuming an inviscid fluid to obtain the Euler equations. Then by assuming irrotational flow, thereby restricting the application of the model to non-breaking waves, these equations can be reduced to a fully nonlinear potential flow problem requiring the resolution of the Laplace problem in the fluid domain (Figure 3.1, center). Several different approaches may be used, including projecting the resolution of the Laplace equation in the interior of the fluid onto the boundary surface using Boundary Integral Equation Methods (BIEM, e.g. Romate and Zandbergen, 1989; Grilli et al., 2001, 1989; Newman and Lee, 2002; Fochesato et al., 2007; Nimmala et al., 2013), or onto a fixed level in the fluid using pseudo-spectral or high-order spectral methods to treat the nonlinear free surface boundary conditions (e.g. West et al., 1987; Dommermuth and Yue, 1987; Chern et al., 1999; Ducrozet et al., 2007, 2012).

More recent work has concentrated on the direct numerical resolution of the 3D Laplace equation in the fluid domain by discretizing the entire domain but taking local derivatives only using finite element (Wu et al., 1998; Ma et al., 2001) or finite difference (Li and Fleming, 1997; Bingham and Zhang, 2007; Engsig-Karup et al., 2009; Yates and Benoit, 2015) approaches, or by searching for fast numerical methods for solving the Laplace problem, such as integral equations (Clamond and Grue, 2001; Fructus et al., 2005) or coupled modes (Belibassakis and Athanassoulis, 2011; Belibassakis et al., 2014). Each method presents its own advantages and limitations, in particular concerning the mathematical complexity, numerical efficiency, and domain flexibility.

Since my arrival at the LHSV in 2011, I have been working in collaboration with Michel Benoit on developing a fully nonlinear potential flow theory model. With the objective of fulfilling the need for highly accurate, nonlinear wave propagation models capable of simulating coastal wave propagation and transformation, we chose to solve the Zakharov equations (Zakharov, 1968; Craig and Sulem, 1993) by directly solving the 3D Laplace equation. My work in this field will be outlined in the remainder of this chapter. First, section 3.2 describes the mathematical and numerical model, before section 3.3 evaluates the accuracy and efficiency of the spectral approach chosen to resolve the model in the vertical. The 1DH (one horizontal dimension, (x, z)) version of the model is then validated with a series of test cases in section 3.4, before the 2DH (two horizontal dimension, (x, y, z)) version of the model is developed and validated in section 3.5. Finally, recent work to take into account the effects of wave breaking is described in section 3.6, before future work is outlined in section 3.7.

This collaborative project with Michel Benoit continued after his departure from the LHSV in 2015 when he took a position at the IRPHE/ECM (Institut de Recherche des Phenomenes Hors Equilibre / Ecole Centrale Marseille). During the 8-year time period that we have worked on co-developing the model, we have co-advised 2 Engineering and Masters interns, one PhD student, and two post-docs. This work has been published in four peer-reviewed articles, two of which are presented in Appendix D, and three additional articles are currently under review.

3.2 Mathematical and numerical model

Modeling highly nonlinear and dispersive waves remains an open research topic due to the difficulties in representing well a wide range of physical processes impacting wave propagation in the nearshore zone at different temporal and spatial scales. As mentioned in the introduction, a variety of different models exist, and here the choice was made to develop a fully nonlinear potential flow theory model, based on the Zakharov-Craig-Sulem system of equations (Zakharov, 1968; Craig and Sulem, 1993).

To derive this model, a fluid domain Ω of density ρ is described by the fluid velocity $\underline{u}(x, y, z, t) = (u, v, w)^T$, with the temporally-varying free surface at $z = \eta(x, y, t)$ and bottom boundary at $z = -h(x, y, t)$ (Figure 3.2). The fluid is assumed to be incompressible (constant and homogeneous density), and the flow is assumed to be inviscid, allowing the simplification of the Navier-Stokes equations to the Euler equations. By additionally assuming the flow is irrotational, it can be represented following potential flow theory with the velocity potential Φ such that $\underline{u} = \nabla\Phi$. Then, the kinematic (KFSBC) and dynamic free surface boundary conditions (DFSBC) are expressed as the impermeability of the free surface and the continuity of the free surface normal stress, respectively. In the DFSBC, the atmospheric pressure p_{atm} is arbitrarily set to 0 without loss of generality.

The system of nonlinear potential flow equations, also known as the “water wave problem”, thus consists of four equations:

1. the conservation of mass in the fluid domain (or Laplace equation, where Δ is the Laplace operator)

$$\Delta\Phi = 0 \quad \text{in } \Omega, \tag{3.1}$$

2. the KFSBC

$$\frac{\partial\eta}{\partial t} + \nabla_{\mathrm{H}}\Phi.\nabla_{\mathrm{H}}\eta - \frac{\partial\Phi}{\partial z} = 0, \quad \text{at } z = \eta(x,y,t), \tag{3.2}$$

3. the DFSBC rewritten using the Bernoulli equation at the free surface (derived from the Euler equations)

$$\frac{\partial\Phi}{\partial t} + \frac{1}{2}(\nabla_{\mathrm{H}}\Phi)^2 + g\eta = 0, \quad \text{at } z = \eta(x,y,t), \text{ and} \tag{3.3}$$

4. the bottom boundary condition

$$\frac{\partial h}{\partial t} + \nabla_{\mathrm{H}}\Phi.\nabla_{\mathrm{H}}h + \frac{\partial\Phi}{\partial z} = 0, \quad \text{at } z = -h(x,y,t), \tag{3.4}$$

   where $\nabla \equiv (\frac{\partial}{\partial x}, \frac{\partial}{\partial y}, \frac{\partial}{\partial z})^T$ is the gradient operator, and ∇_{H} denotes the horizontal gradient operator.

This model is derived for a uniform and constant pressure at the free surface, neglecting the effects of surface tension. The assumption that surface tension effects are negligible is valid for real applications with wavelengths on the order of meters to hundreds of meters. Surface tension effects become important for short waves with wavelengths on the order of millimeters (capillary waves) to centimeters. During the thesis work of Cécile Raoult, (Raoult, 2017), the

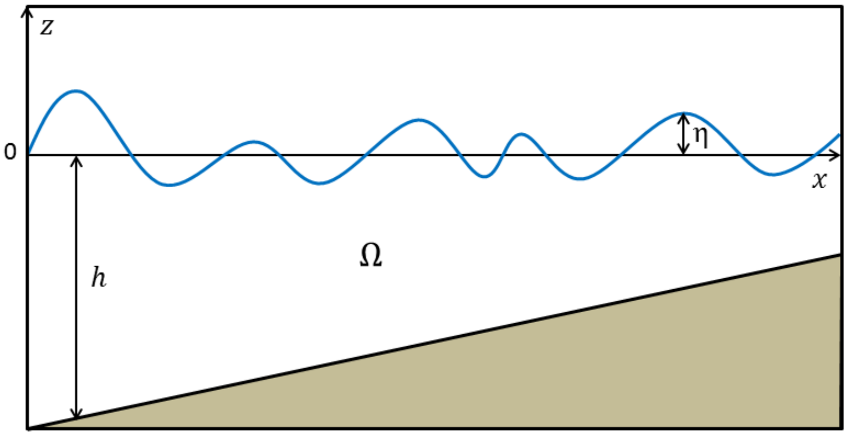

Figure 3.2: Notation used to describe the fluid domain Ω and the free surface η and bottom h boundaries in the 1DH version of the model.

effects of surface tension were included in the model in the DFSBC (following Dingemans, 1997) to simulate small-scale laboratory experiments (Monsalve et al., 2015) where the effects of surface tension were no longer negligible (see section 3.4.2). The remainder of the work shown here will neglect the effects of surface tension under the assumption that they are negligible for full-scale modeling of waves propagating in the nearshore environment.

An additional assumption is made requiring that the water column is continuous from the bottom to the free surface (i.e. single-valued free surface position η, and no overturning waves). The KFSBC and DFSBC then can be rewritten as the temporal evolution of the free surface elevation η and the free surface velocity potential as $\tilde{\Phi}(x,y,t) \equiv \Phi(x,y,\eta(x,y,t),t)$ following Zakharov (1968) and Craig and Sulem (1993):

$$\eta_t = -\nabla_{\mathrm{H}}\eta . \nabla_{\mathrm{H}}\tilde{\Phi} + \tilde{w}\left(1 + (\nabla_{\mathrm{H}}\eta)^2\right) , \tag{3.5}$$

$$\tilde{\Phi}_t = -g\eta - \frac{1}{2}(\nabla_{\mathrm{H}}\tilde{\Phi})^2 + \frac{1}{2}\tilde{w}^2\left(1 + (\nabla_{\mathrm{H}}\eta)^2\right) , \tag{3.6}$$

which are functions of only η, $\tilde{\Phi}$, and $\tilde{w}$, the vertical velocity at the free surface, defined as:

$$\tilde{w}(x,y,t) \equiv \frac{\partial\Phi}{\partial z}(x,y,\eta(x,y,t),t). \tag{3.7}$$

This set of equations (Eqs. 3.5-3.6), known as the Zakharov-Craig-Sulem equations, must be supplemented by lateral and bottom boundary conditions to solve the Laplace boundary value problem (BVP) in the domain. Thus far, we have implemented fully reflective, periodic, or wave generating lateral boundary conditions and an impermeable bottom boundary condition. The primary difficulty in solving this coupled set of equations is to evaluate the vertical velocity at the free surface $\tilde{w}$ as a function of η and $\tilde{\Phi}$ (often called the "Dirichlet-to-Neumann" or DtN problem).

A wide variety of different methods are used to solve the DtN problem. One approach is to solve directly the Laplace equation using finite element (Wu et al., 1998; Ma et al., 2001) or finite difference (Li and Fleming, 1997; Engsig-Karup et al., 2009) methods. If the problem is simplified to a rectangular domain with a flat bottom, a high-order spectral (HOS) approach may be optimal (Dommermuth and Yue, 1987; West et al., 1987; Chern et al., 1999; Ducrozet et al., 2012), and recent work has extended HOS models to simulate variable and moving bottoms (Smith, 1998; Guyenne and Nicholls, 2007; Gouin et al., 2015). Another efficient approach is to use a spectral method only in the vertical (thereby regaining flexibility in the horizontal domain structure) using a local mode series expansion (Belibassakis and Athanassoulis, 2011; Athanassoulis and Papoutsellis, 2015; Papoutsellis et al., 2018) or a projection on a polynomial basis (Kennedy and Fenton, 1997; Tian and Sato, 2008). Additional approaches have been proposed such as a fast, iterative algorithms for calculating the DtN operator (Clamond and Grue, 2001; Fructus et al., 2005), but these methods introduce additional mathematical complexity.

Since my arrival in the LHSV, I have worked on co-developing the numerical model Misthyc solving the mathematical model presented here, known as the nonlinear water wave problem. The numerical model requires three main components:

1. a method to compute the Laplacian and horizontal gradient operators,
2. a technique for solving the Laplace BVP for Φ at each time step, and
3. a temporal integration scheme to advance η and $\tilde{\Phi}$ in time.

Figure 3.3 presents a schematic of the resolution of the Misthyc model at a given time t, identifying the main steps (boxes, outlined below) and principle variables are passed between each step (black arrows).

First, to calculate the gradient and Laplacian operators in the horizontal domain (Figure 3.3, orange box), two different approaches are used are in the 1DH and 2DH versions of the model:

- **1D high-order finite difference schemes** are used on structured grid in the 1D horizontal domain (Figure 3.4a), and
- **2D radial basis function - finite difference schemes (RBF-FD)** are used on an unstructured grid in the 2D horizontal domain (Figure 3.4b).

These approaches were chosen to achieve high-order accuracy while maintaining the flexibility of the approach for variable bathymetries and irregularly-shaped domains. In the 1DH model, flexible, high-order finite difference schemes were implemented following Fornberg (1988) and Bingham and Zhang (2007). In the applications shown here, fourth-order schemes (Figure 3.4a) are used as an optimal choice to obtain high-order accuracy, while minimizing both the appearance of instabilities and the computational time (Bingham and Zhang, 2007; Yates and Benoit,

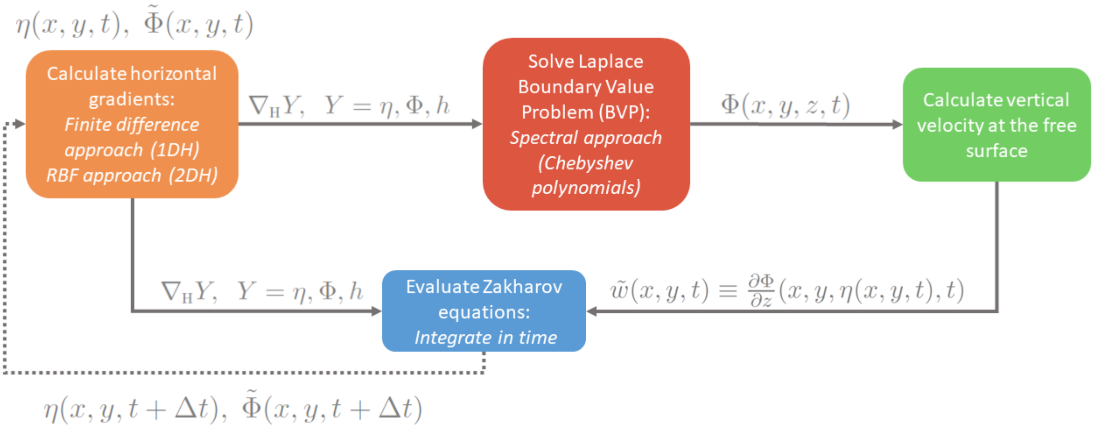

Figure 3.3: Schematic of the resolution of the Misthyc model. The dotted black line indicates the temporal integration step.

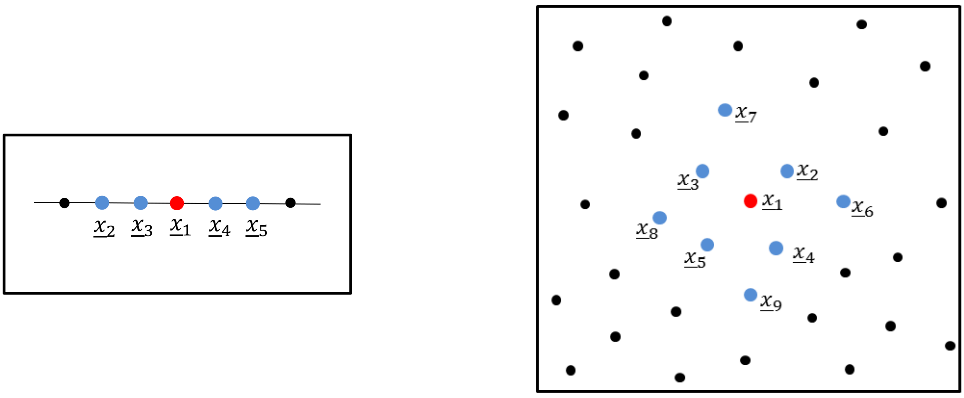

(a) 1DH

(b) 2DH

Figure 3.4: Examples of the horizontal discretization for 1DH (finite difference) and 2DH (radial basis function - finite difference) stencils.

2015). The radial basis function-finite difference approach used in the 2DH version of the model will be described in more detail in section 3.5.

Second, both the 1DH and 2DH versions of the model use a spectral approach in the vertical (Yates and Benoit, 2015) to solve the Laplace boundary value problem (Figure 3.3, red box). The choice of method and details of the vertical resolution are discussed further in section 3.3. For a horizontal domain with N_{XY} points and a vertical approximation with basis functions of maximum order N_T, the Laplace BVP (consisting of Eqs. 3.1-4) and the lateral boundary conditions (periodic or fully reflective vertical walls with $\frac{\partial \Phi}{\partial n} = 0$) is solved at each time step by solving a linear system of $N_{XY} \times (N_T + 1)$ equations. The linear system of equations forms a sparse matrix, which is solved in the Misthyc model using the direct solver MUMPS (MUltifrontal Massively Parallel Solver, v4.10.0, Amestoy et al., 2001, 2006). This solver was chosen as an efficient choice of a parallel sparse direct solver that can be interfaced easily with Fortran.

Finally, the vertical velocity at the free surface $\tilde{w}$ is calculated (Eq. 3.7, Figure 3.3, green box) from Φ, and then the Zakharov equations are integrated in time using the classical, explicit fourth-order Runge-Kutta (RK) scheme with a constant time step (Figure 3.3, blue box). This approach was chosen as a reliable, accurate, and stable method. Both higher and lower-order temporal integration schemes, as well as a variable time step, could be tested to optimize the simulation calculation time and accuracy.

As described in the introduction, work on this model was initiated upon my arrival in the LHSV. The next four sections outline my contributions to the model development and validation (sections 3.3-3.6), including the work of the students and post-doctoral researchers co-advised with Michel Benoit, before the last section presents future work I propose to do in this field (section 3.7).

3.3 Accuracy and efficiency of the spectral approach

We first studied the accuracy and efficiency of different approaches for resolving the vertical domain in 1DH. The 1DH version of Misthyc initially was developed using high-order finite difference schemes in both the horizontal and vertical domains to solve the Laplace equation and the DtN problem. In the following, Model A refers to this version of Misthyc, with a vertical discretization using N_Z layers (or $N_Z + 1$ points). Following Bingham and Zhang (2007), Engsig-Karup et al. (2009), and Ducrozet et al. (2012), the vertical coordinate first is transformed into σ-coordinates to simplify the resolution of the system of equations by creating a fixed rectangular domain:

$$\sigma(x, z, t) = \frac{z + h(x)}{\eta(x, t) + h(x)} = \frac{z + h(x)}{d(x, t)}. \tag{3.8}$$

I then studied the optimal vertical discretization of points following the analysis presented by Engsig-Karup et al. (2009), comparing a uniform linear distribution, the roots of the Chebyshev-Gauss-Lobatto (CGL) polynomials, and the roots of the Legendre-Gauss-Lobatto (LGL) polynomials. The convergence of the Misthyc model is improved with inhomogeneous point spacing, with a higher density of points near the free surface (Yates and Benoit, 2015). This improves the estimates of Φ near the free surface and therefore of $\tilde{w}$. For example, for the same number of points N_Z, smaller errors are obtained when calculating the vertical velocity at the free surface $\tilde{w}$ for a linear wave with $kh \sim 4$ using the roots of CGL polynomials (Figure 3.5, center) than using a linear distribution of points (Figure 3.5, left).

This optimal discretization was then compared to the use of a spectral Chebyshev-tau approach to solve for Φ in the vertical, following Tian and Sato (2008). In this case, the vertical domain also is transformed into a fixed rectangular domain, but with a vertical coordinate s varying from -1 at the bottom to 1 at the free surface:

$$s(x, z, t) = \frac{2z + h^-(x, t)}{h^+(x, t)}, \tag{3.9}$$

with $h^+(x, t) = h(x) + \eta(x, t)$ and $h^-(x, t) = h(x) - \eta(x, t)$. Then, the velocity potential $\varphi(x, s)$ is expressed using a spectral approach as a sum of Chebyshev polynomials of the first kind $T_n(x)$, where n indicates the order of the polynomial:

$$\varphi(x, s) \simeq \varphi_{N_T}(x, s) = \sum_{n=0}^{N_T} a_n(x) T_n(s), \tag{3.10}$$

where N_T is the highest order Chebyshev polynomial and $a_n(x)$ are the $N_T + 1$ coefficients calculated at each point in x. For $N_T = 6$, the first seven Chebyshev polynomials are shown in Figure 3.5(top row, right). To solve for the $a_n(x)$ coefficients, the Laplace BVP and boundary conditions (lateral and vertical) are expressed by applying the Chebyshev-tau method (e.g. Boyd,

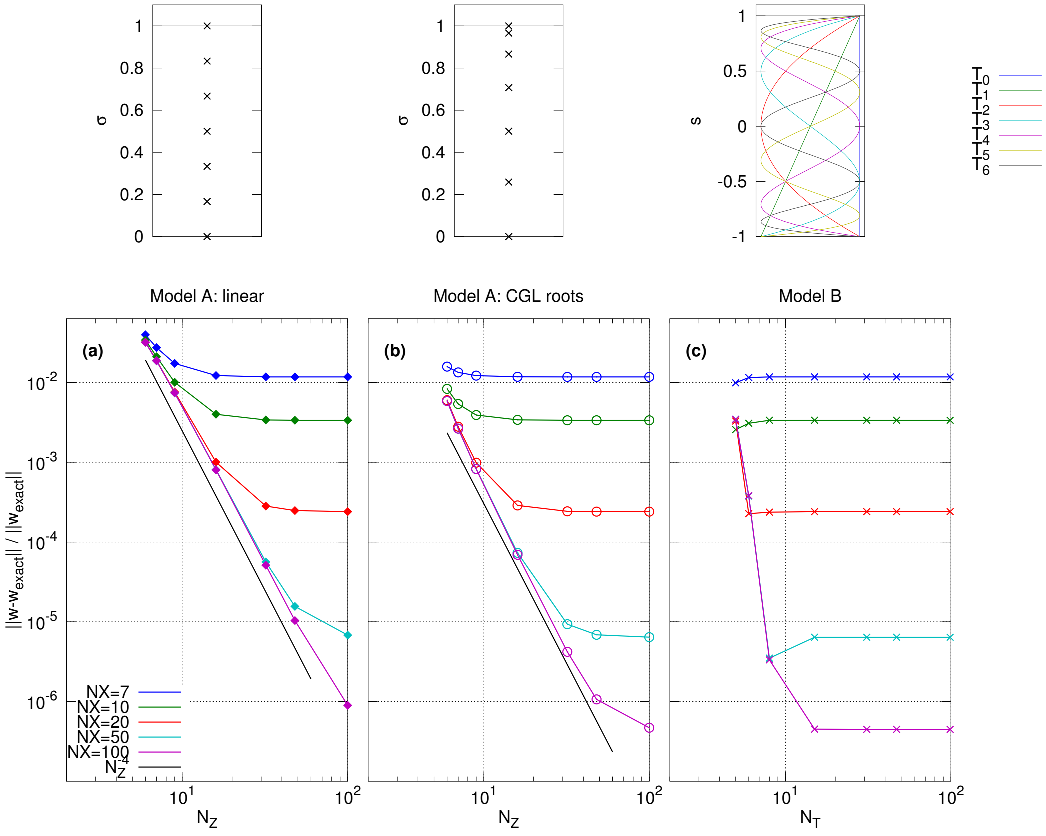

Figure 3.5: Convergence of the vertical velocity at the free surface $\tilde{w}$ for a linear wave with $kh \sim 4$, evaluated as a function of N_X, N_Z, and the vertical resolution: (a) Model A: linear distribution, (b) Model A: roots of Chebyshev-Gauss-Lobatto (CGL) polynomials, and (c) Model B: spectral method. In the top row, examples of the vertical point distributions are shown for Model A (with $N_Z = 7$) and of the Chebyshev polynomials for Model B (with $N_T = 6$) (Yates and Benoit, 2015).

2001) to the Laplace equation (3.1) and the boundary conditions to obtain a system of equations as a function of s, $T_n(s)$, $T'_n(s) \equiv \frac{dT_n}{ds}$ and $T''_n(s) \equiv \frac{d^2T_n}{ds^2}$. For more details about this method, see Yates and Benoit (2015), shown in Appendix D.1.

Finally, a system of $N_X(N_T + 1)$ linear equations must be solved for the coefficients $a_n(x)$, and then the vertical velocity at the free surface $\tilde{w}$ is calculated:

$$\tilde{w}(x_i) = \Phi_s s_z\big|_{s=1} = \frac{2}{h^+(x_i)} \sum_{n=0}^{N_T} a_n(x_i) n^2, \tag{3.11}$$

and the Zakharov equations (Eqs. 3.5 and 3.6) can be stepped forward in time. In the following, Model B refers to this version of Misthyc, with the vertical variability resolved using a spectral approach with Chebyshev polynomials of maximum order N_T. Figure 3.5 shows that when estimating $\tilde{w}$ for a linear wave with $kh \sim 4$, convergence is achieved for Model B with smaller values of N_T than for either discretization in Model A.

To further demonstrate the accuracy and efficiency of these methods in calculating the free surface vertical velocity, I evaluated the convergence properties for a regular nonlinear wave of permanent form, in a constant depth (h), periodic domain (L). The errors depend on both the horizontal (N_X) and vertical (N) resolution. The vertical resolution N is determined by the number of layers $N = N_L$ for the finite difference method (Model A with CGL polynomial roots) and by the maximum order Chebyshev polynomial $N = N_T$ (e.g. number of polynomials) for the spectral method (Model B). The Laplace BVP is solved, and the vertical velocity at the free surface is calculated and compared to a reference solution calculated using a Fourier series approximation of the stream function method (to 20th order), following Chaplin (1980) and Rienecker and Fenton (1981). As expected, both methods (Models A and B) demonstrated similar accuracy, but the spectral method shows faster convergence (exponential) than the finite difference method (algebraic, for the CGL polynomial discretization) as a function of N (Figure 3.6).

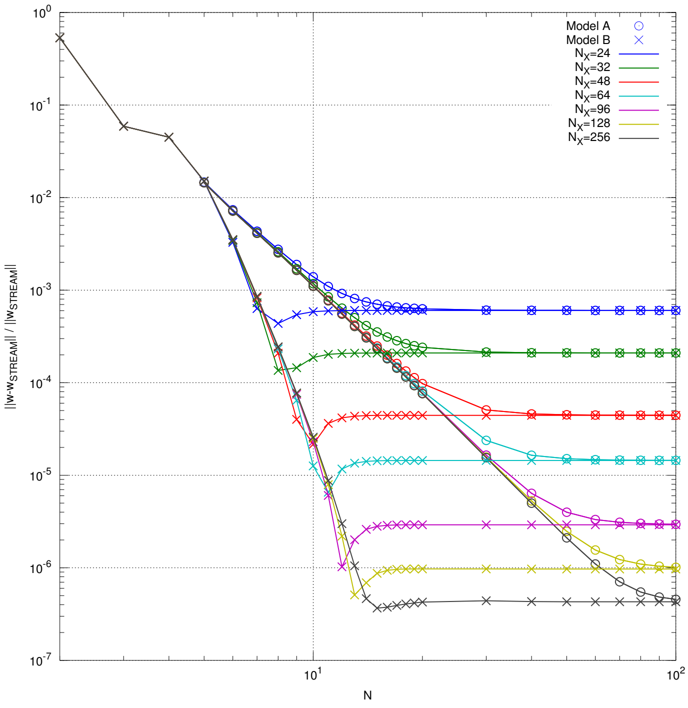

Figure 3.6: Convergence of the free surface vertical velocity $\tilde{w}$ for a regular nonlinear wave with wave steepness $H/L = 0.1$ ($ka = \pi/10$) and relative water depth $h/L = 1$ ($kh = 2\pi$). Convergence of Model A with CGL polynomial roots (circles, vertical discretization) and Model B (crosses, spectral approach) is plotted as a function of the vertical resolution N for a range of horizontal resolutions N_X (colored lines).

After testing the convergence of these methods for solving the Laplace BVP, I then evaluated accuracy and efficiency of the Misthyc model using the optimal vertical discretization with CGL polynomials and the spectral method for three cases including: (1) the long-time propagation of stable, regular nonlinear waves in a periodic domain, (2) the temporal evolution of a nonlinear standing wave in a domain with fully reflective boundaries, and (3) the propagation and shoaling of a train of waves on a slope (see Yates and Benoit (2015) for the detailed comparisons).

With these three test cases, we demonstrated the accuracy and efficiency of the spectral method in comparison to fourth-order finite difference schemes through analysis of the model propagation errors and CPU time. The spectral approach was thus retained in the Misthyc model without loss of flexibility in the model applications. We also concluded that the optimal vertical resolution for practical applications, which is a compromise between accuracy and efficiency, is approximately in the range $7 \leq N_T \leq 15$. Therefore, in the following model developments, the spectral approach is used with a maximum order Chebyshev polynomial of $N_T = 7$, unless otherwise specified.

3.4 Validating the 1DH model

3.4.1 Simulating nonlinear wave propagation

During the thesis work of Cécile Raoult, the accuracy of the Misthyc model in reproducing highly nonlinear and dispersive waves was demonstrated further with a series of test cases in 1DH (Raoult et al., 2016a). First, several analytical or accurate numerical solutions for highly nonlinear waves were simulated to evaluate the accuracy and convergence of the model. Then a series of laboratory experiments were simulated to demonstrate these properties when the model is applied to practical test cases.

The analytical and numerical test cases included simulating linear wave propagation and reflection over a steep, smooth change in depth (Roseau, 1976; Athanassoulis and Belibassakis, 1999) and solitary wave propagation over a flat bottom (Clamond and Dutykh, 2013). The latter test case will be presented here to evaluate the convergence properties of the model for nonlinear wave propagation (section 3.4.1.1).

Then, comparisons of simulation results with observations from a series of laboratory experiments cases demonstrated the ability of the model to simulate accurately regular or irregular wave propagation (without wave breaking) over a flat bottom (Chapalain et al., 1992), a sloping beach (Ting and Kirby, 1994), a submerged bar (Dingemans, 1994), and a barred beach profile (Becq-Girard et al., 1999). Additional test cases included the generation and propagation of waves from an impulsive bottom movement, simulating tsunami-like waves (Hammack, 1973; Fuhrman and Madsen, 2009). The simulation of these experiments demonstrated the ability of the model to reproduce accurately dispersive waves and nonlinear wave-wave and wave-bottom interactions, including the transfer of energy between the peak frequency and higher-order harmonics (up to the fifth harmonic in some cases). The results of the Becq-Girard et al. (1999) comparisons are presented here (section 3.4.1.2).

3.4.1.1 Model convergence properties

To evaluate the convergence properties of the model as a function of the temporal, horizontal, and vertical resolution, we completed a series of simulations propagating a solitary wave generated using the highly accurate numerical solution of Clamond and Dutykh (2013). Solitary waves are characterized by the nonlinearity parameter $\delta = H/h$, also called the nondimensional wave height, calculated as the ratio of the wave height to the water depth, with $\delta = 0.3$, 0.5, and 0.7 for the three cases tested here. Each simulation was initialized with a solitary wave at $x = 0$, which was then propagated for $\tilde{T} \equiv T\sqrt{g/h} = 500$ in a domain with water depth $h = 1$ m, and horizontal extent $x/h = [-25, 675]$. The domain was sufficiently long to avoid the effects of wave reflection.

First, the model convergence was verified as a function of Δx and Δt by analyzing the wave phase, wave amplitude, and conservation of energy and volume, which should all remain constant (Raoult et al., 2016a). Global volume and energy errors were calculated as the arithmetic mean of the relative volume and energy evolution:

$$Err_Y = \left| \frac{\langle Y(t) \rangle_t - Y_0}{Y_0} \right|, \tag{3.12}$$

where $\langle Y(t) \rangle_t = \frac{1}{NDT} \sum_{i=1}^{NDT} Y(t_i)$, NDT is the number of time steps, Y_0 is the value at $t = 0$, and $Y = V$ or E, for volume or energy, respectively. The wave amplitude and phase errors were calculated relative to the initial amplitude and to the theoretical position of the wave at the end of the simulation (at $t = \tilde{T}$) :

$$Err_{ampl} = \left| \frac{\eta_{max}(\tilde{T}) - H}{H} \right|, \qquad Err_{phase} = \left| \frac{x_{max}(\tilde{T}) - C\tilde{T}}{C\tilde{T}} \right|. \tag{3.13}$$

For the vertical convergence tests, the maximum order N_T of the Chebyshev polynomial was varied from $N_T = 3$ to 15, and the relative errors were calculated using the results of the simulation with the highest order as the reference value (here $N_T = 15$). In this case, the relative volume and energy errors, and relative amplitude and phase errors are calculated using Eqs. 3.12 and 3.13 by replacing Y_0 and the theoretical values (H, C) with the values obtained when $N_T = 15$.

For each set of test cases, two parameters were held constant (e.g. vertical resolution and time step) and the last parameter varied (e.g. horizontal resolution). The energy conservation convergence trends are presented in the following. The volume conservation, amplitude, and phase convergence trends (not shown here, see Raoult (2017) for more details) showed similar trends.

For the case examining the convergence as a function of the horizontal resolution Δx (e.g. energy conservation, Figure 3.7a), the vertical resolution and CFL number were held constant, with $N_T = 7$ and CFL $\equiv C_0\Delta t/\Delta x = 1.25$. Fourth-order algebraic convergence in space was verified for the most nonlinear solitary wave ($\delta = 0.7$), as expected for fourth-order finite difference schemes. Slightly higher-order (faster) convergence (4-5) was demonstrated for the two smaller values of δ. Convergence was then evaluated as a function of the time step Δt (e.g. energy conservation, Figure 3.7b) by holding constant the spatial and vertical resolution, $\Delta x = 0.1$ m and $N_T = 7$. As a function of the time step, slightly slower than fourth-order convergence (3.3-4.1) was observed for the most nonlinear test case, while the convergence was again faster than fourth-order for the two smaller values of δ (4-5).

The model convergence was also evaluated as a function of the vertical resolution N_T (maximum order Chebyshev polynomial) to provide guidelines for the values to be used in future simulations. At $\tilde{T} = 500$, the amplitude and phase of the solitary wave depends on the vertical resolution N_T and the wave nonlinearity δ (Figure 3.8). Similar to the convergence tests as a function of the horizontal and temporal resolution, the model converges faster for smaller values of the nonlinearity parameter δ (e.g. Figure 3.8a-b). In addition the model converges rapidly even with relatively small values of N_T (also as observed previously by Yates and Benoit (2015)). For example, the relative amplitude error (compared to the solution with the highest order Chebyshev polynomial) is less than 10^{-6} for $N_T = 6$, 7, and 11, for $\delta = 0.3$, 0.5 and 0.7, respectively. Here, it must be noted that the model converges to a solution with a phase difference from the analytical solution due to the underestimation of the amplitude and phase speed (Figure 3.8c).

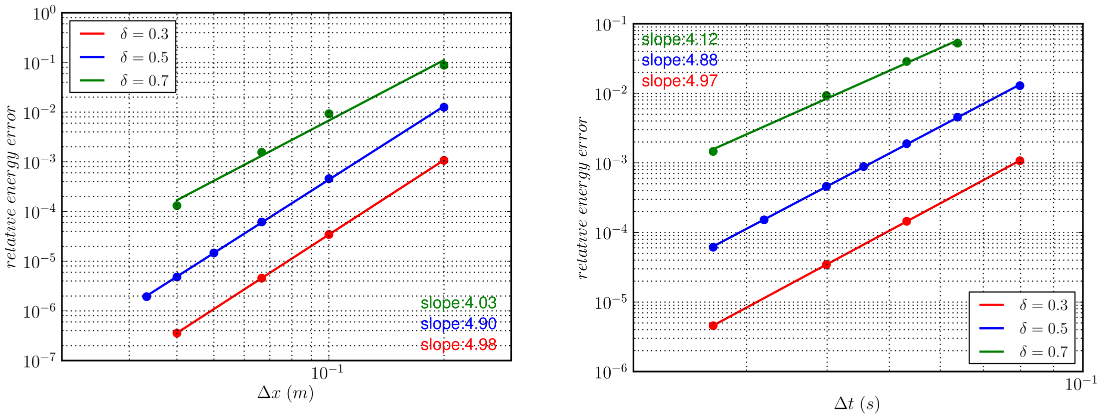

(a) Δx

(b) Δt

Figure 3.7: Convergence of the relative energy as function of the (a) horizontal resolution Δx (with $CFL = 1.25$ and $N_T = 7$) and (b) time step Δt (with $\Delta x = 0.1$ m and $N_T = 7$) for the three solitary waves with δ = 0.3, 0.5, and 0.7.

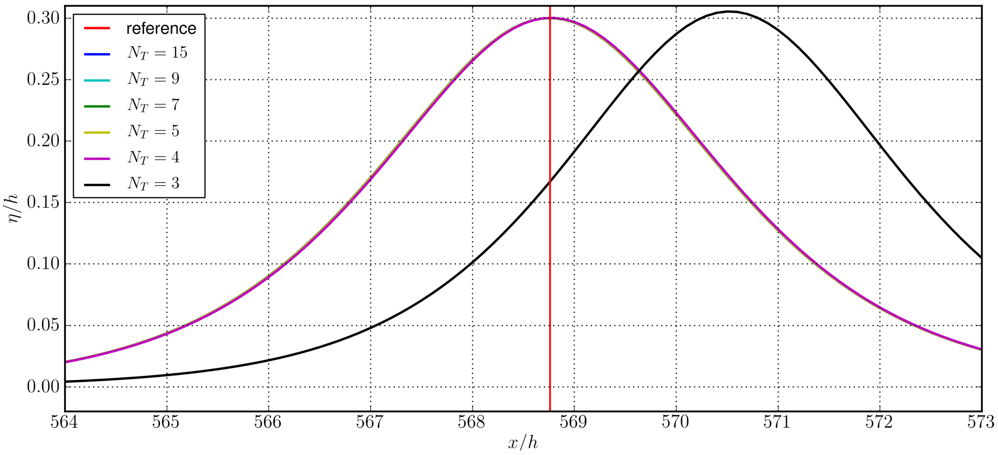

(a) $\delta = 0.3$

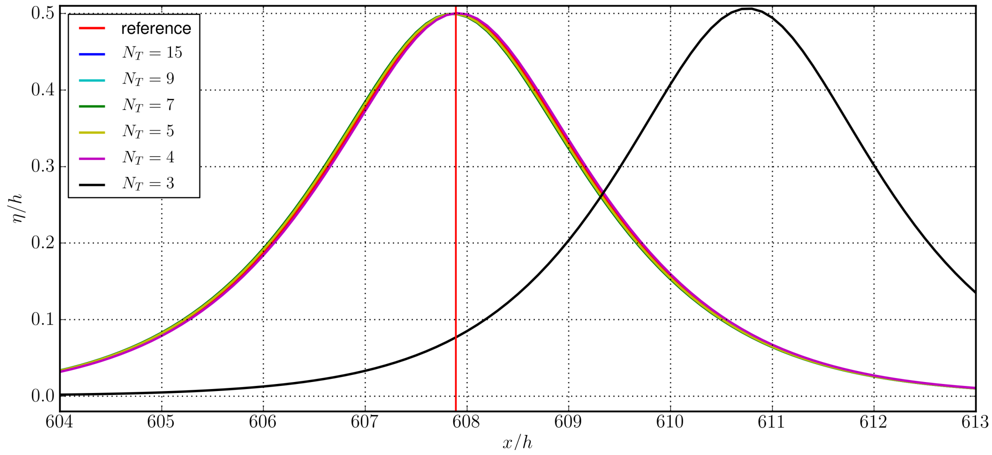

(b) $\delta = 0.5$

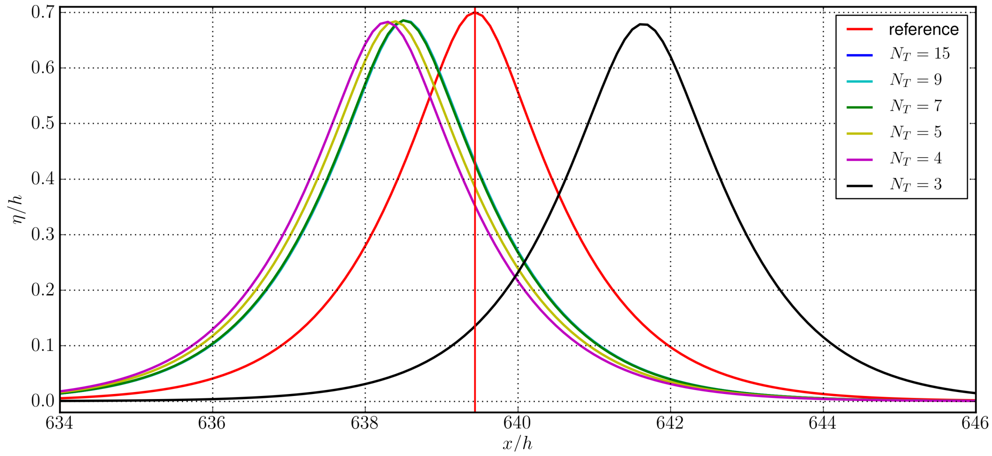

(c) $\delta = 0.7$

Figure 3.8: Free surface profiles at $\tilde{T} = 500$ for several values of N_T (see legend) for (a) $\delta = 0.3$, (b) $\delta = 0.5$ and (c) $\delta = 0.7$.

Finally, the CPU time was also calculated for each of these test cases, and the following relationship was obtained:

$$T_{CPU} \approx \frac{N_T^{1.5}}{\Delta t \Delta x^2}.$$

This relationship indicates the relative importance of minimizing the horizontal (Δx), vertical (N_T), and temporal (Δt) resolution, in that order.

3.4.1.2 Reproducing highly nonlinear laboratory experiments

We then validated the accurate simulation of wave-wave and wave-bottom interactions with a series of laboratory experiments. In the Becq-Girard et al. (1999) experiments described here, the model reproduced well nonlinear wave interactions and the transfer of wave energy between higher- and lower-order harmonics.

In the experiments, irregular waves were generated using a piston-type wave generator and then propagated over a barred bathymetric profile (Figure 3.9) to evaluate the generation of higher harmonics and the transfer of energy between these frequencies. The irregular wave field was generated using a JONSWAP spectrum with an enhancement factor $\gamma = 3.3$, a significant wave height of $H_s = 3.4$ m, and a peak frequency $f_p = 2.39$ s. Sixteen resistive-type wave probes measured the free surface position (Figure 3.9) during 40 minutes with a sampling rate of $\Delta t = 0.07$ s.

In the model, waves were generated in a 5-m long relaxation zone imposing the velocity potential and free surface position ending at the foot of the bar ($x = 0$ m) and absorbed in a 10-m long relaxation zone starting at $x = 15$ m. The waves were generated by reproducing the observed wave spectrum at wave probe 2. The simulation parameters were defined as: horizontal resolution $\Delta x = 0.05$ m, vertical resolution N_T=7, and time step $\Delta t = 0.07$ s.

In agreement with the laboratory observations, the simulation results demonstrate in the wave spectra (Figure 3.10) the transfer of wave energy from the peak frequency at the foot of the barred beach profile (probe 2, Figure 3.9a) to the second to fifth harmonics over the bar (probes 7-11, Figure 3.9b-d). In the trough after the bar, wave energy is transferred from the higher-order (third

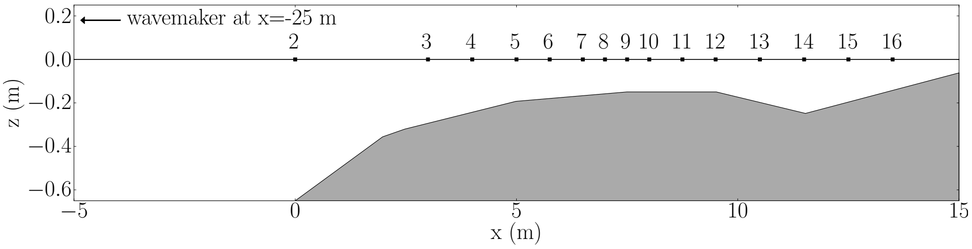

Figure 3.9: Bathymetric profile of the experiments of Becq-Girard et al. (1999), indicating the position of the probes along the wave flume.

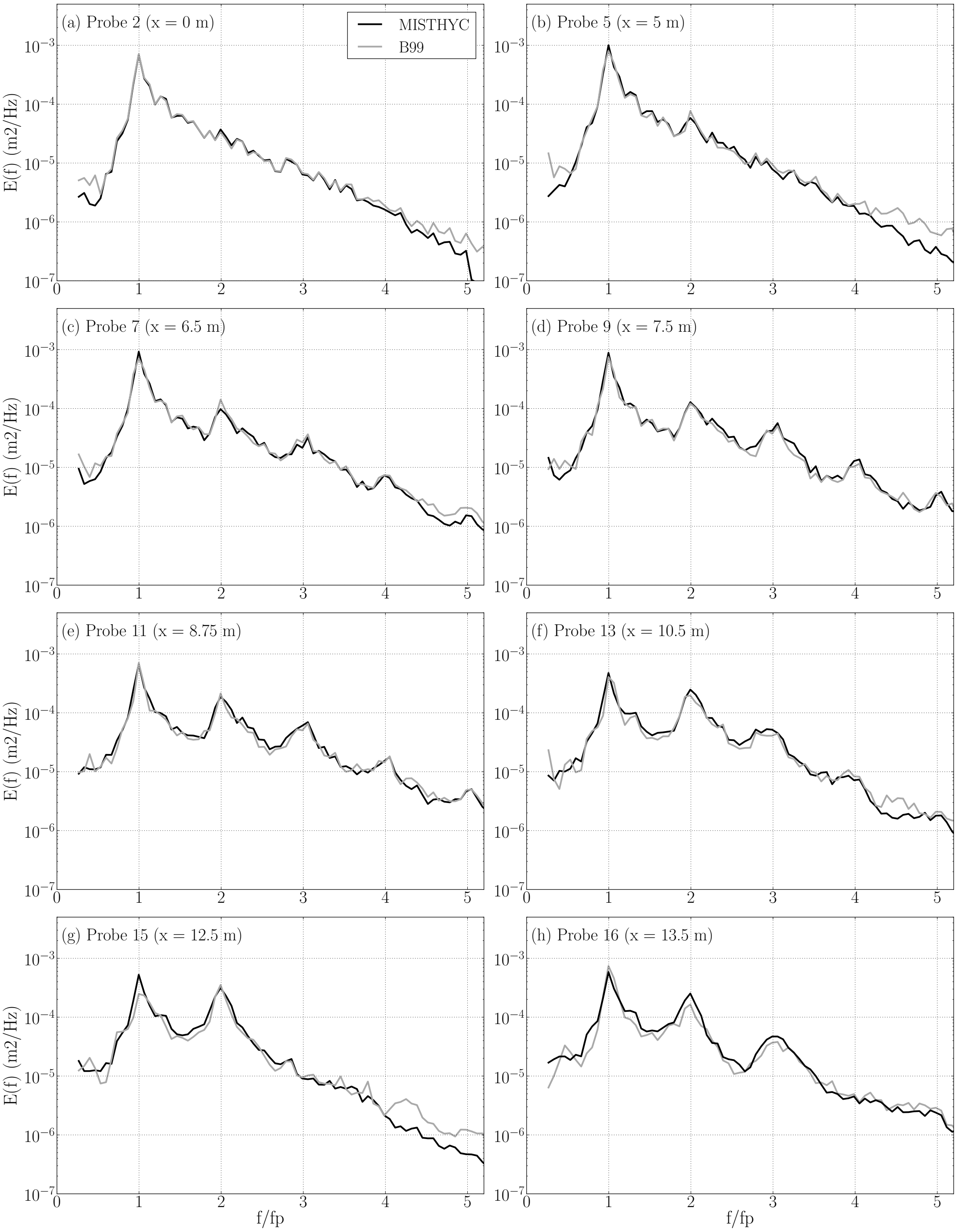

Figure 3.10: Comparison of measured and simulated wave spectra (as a function of the wave frequency normalized by the peak frequency) at eight probes (a-h) placed along the wave flume for the experiments of Becq-Girard et al. (1999). Vertical lines indicate the frequency of the primary wave and the second to fifth harmonics.

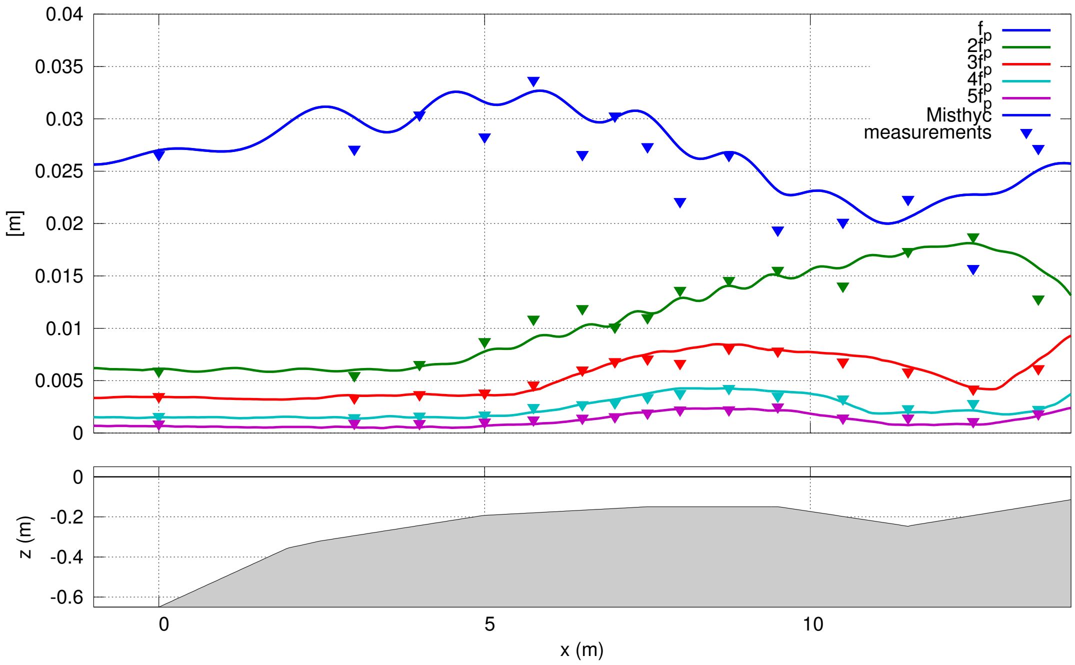

Figure 3.11: Comparison of the evolution of the first five harmonics from the measurements (triangles) and simulations (lines), with the bottom bathymetry shown in the bottom panel for reference for the experiments of Becq-Girard et al. (1999).

to fifth) harmonics back to the peak frequency and second harmonic (probes 13-15, Figure 3.9f-g). Finally, as the water depth increases again near the end of the tank, the third harmonic increases in energy again (probe 16, Figure 3.9h).

The simulation reproduces correctly the spatial evolution of the first five harmonics over the submerged bar (Figure 3.11), representing well the different phases described above. The oscillations observed in the observed and simulated harmonic amplitudes are caused by wave reflections. In the model, wave reflections are caused by an imperfect wave absorption zone (10 m-long relaxation zone) and the impermeable boundary at the right side of the domain. This test demonstrated the ability of the model to reproduce well nonlinear interactions between waves, including transfers between the primary wave and higher-order harmonics, and waves and the bottom bathymetry during the shoaling process.

3.4.2 Simulating viscous effets

In particular cases with shallow water or long propagation times, dissipative processes may become important, and viscous effects, including bottom friction, cannot be neglected. To take into account viscous effects in Misthyc, we first integrated the effects of bulk viscosity into the potential flow theory model following the theoretical work of Liu and Orfila (2004), Dutykh and Dias (2007), and Dias et al. (2008). They derived new sets of visco-potential equations by introducing dissipative terms in the dynamic and kinematic free surface boundary conditions (Eqs. 3.5-3.6) such that they become:

$$\frac{\partial \eta}{\partial t} = -\nabla_H \tilde{\Phi}.\nabla_H \eta + \tilde{w}(1 + (\nabla_H \eta)^2) + 2\nu \Delta_H \eta, \tag{3.14}$$

$$\frac{\partial \tilde{\Phi}}{\partial t} = -g\eta - \frac{1}{2}(\nabla_H \tilde{\Phi})^2 + \frac{1}{2}\tilde{w}^2(1 + (\nabla_H \eta)^2) - 2\,\nu \frac{\partial^2 \Phi}{\partial z^2}. \tag{3.15}$$

The additional terms added to these equations were derived following linear theory and then added to the nonlinear Zakharov equations, following the suggestion of Dias et al. (2008). The authors assume that the terms derived from linear theory are applicable at least to first order in the nonlinear evolution equations. Then, in addition to taking into account the effects of bulk viscosity, a nonlocal term was added to the bottom boundary condition, following Liu et al. (2006), to take into account the effects of bottom friction:

$$B(t, x) = \int_0^t \frac{\frac{\partial^2 \Phi}{\partial z^2}(\tau, x)}{\sqrt{t - \tau}} d\tau. \tag{3.16}$$

For the detailed derivation and description of the numerical implementation of these terms, see Raoult (2017).

We first validated this approach in the linear regime by evaluating the dissipation of a regular wave propagating in a periodic domain of constant water depth. These simulations (not shown here) showed that the two terms added to the free surface boundary conditions (Eqs. 3.14 and 3.15) contribute equally to the dissipation of the wave, observed by the decrease in the wave amplitude. Here, two test cases are presented evaluating simulations of (1) the decay of a linear standing wave in comparison to theoretical expressions and (2) small-scale laboratory experiments of wave propagation over an abrupt change in bathymetry.

3.4.2.1 Standing wave decay

The mathematical and numerical implementation of the effects of viscosity were evaluated in the model by investigating the decay of a standing wave oscillating in a periodic domain. A series of test cases were completed to analyze the wave decay in both infinite and finite depth cases (Raoult, 2017; Raoult et al., 2016b) and to compare the simulation results to theoretical results (e.g. Figure 3.12).

Lamb (1932) originally derived an expression for the decay rate of a homogeneous (in space) gravity wave of amplitude a and wave number k propagating in finite depth by doing a dissipation calculation and then by using the linearized Navier-Stokes equations:

$$\frac{da}{dt} = -2\nu k^2 a. \tag{3.17}$$

He thus estimated that the wave amplitude decay is exponential in time $a(t) = a(t=0)\, e^{-2\nu k^2 t}$ and that shorter waves (large k) dissipate faster than longer waves (small k). This would suggest that longer waves (swell) are expected to propagate farther with less amplitude decay in the deep ocean, as observed by Snodgrass et al. (1966). In this derivation, Lamb (1932) assumed small viscosity values and infinite depth.

More recently, Antuono and Colagrossi (2013) extended the work of Lamb (1932) by deriving a new expression from the linearized Navier-Stokes equations that relaxes the assumption of small viscosity and removes the infinite depth assumption. In deep water conditions, their expression simplifies to that of Lamb (1932) at first order for small values of the viscosity (as shown in Figure 3.12c). For larger values of the viscosity, the decay rate predicted by Antuono and Colagrossi (2013) is slower than that of Lamb (1932) because of a second-order correction term (as shown in Figure 3.12b). In shallow water (finite depth), the two solutions show even larger differences since the expression of Antuono and Colagrossi (2013) takes into account bottom friction, which is not included in the expression of Lamb (1932) (Eq. 3.17).

To compare to the expressions derived by Lamb (1932) and Antuono and Colagrossi (2013), we simulated the decay of a viscous standing wave for five different combinations of $(kh,\ Re)$ with relative depths $kh = \pi/12 - \pi$ (shallow to deep water conditions) and Reynolds numbers $Re = 50 - 2500$. Here, the Reynolds number is defined as a function of the viscosity $Re = h\sqrt{gh}/\nu$, for viscosities ranging from $\nu = 0.001253 - 0.06264\ m^2/s$ (medium to large viscosity values to emphasize viscous effects). The simulated waves have an amplitude of $a = 0.05$ m in a water depth $h = 1$ m, in a periodic domain that is one wavelength (L) long. To compare to the analytical expressions, these tests also were carried out in the linear regime (the nonlinear terms in the Misthyc model were de-activated).

In the small viscosity, deep water limit (Figure 3.12c, $kh = \pi$), the simulations (both pure slip and no slip) agree well with the expressions of Lamb (1932) and Antuono and Colagrossi (2013) since the effects of bottom friction are negligible. As the viscosity increases, the difference between the solutions of Lamb (1932) and Antuono and Colagrossi (2013) increases because of the second-order correction term. In these cases (Figures 3.12a and 3.12b), the model simulations agree with the decay rate of Lamb (1932) since the dissipative terms added to the KFSBC and DFSBC are based on the assumption of small viscosity.

As mentioned above, in intermediate and shallow water conditions, the differences between the expressions of Lamb (1932) and Antuono and Colagrossi (2013) increase because the effects of bottom friction increase. For example, for $kh = \pi/3$ (Figure 3.13), the decay rate of Antuono and Colagrossi (2013) is much faster than that of Lamb (1932). Simulations using pure slip boundary conditions at the bottom boundary agree well with the expression of Lamb (1932), whereas the simulation results using a no slip bottom boundary condition (taking into account the effects of bottom friction) agree well with the results of Antuono and Colagrossi (2013) (Figure 3.13). It must be noted, however, that the nonlocal term in (3.16) caused the development of high fre-

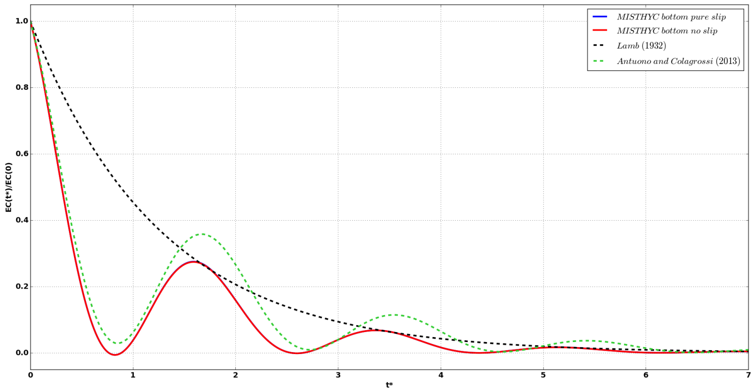

(a) $Re = 50$ ($\nu = 0.06264\ m^2/s$)

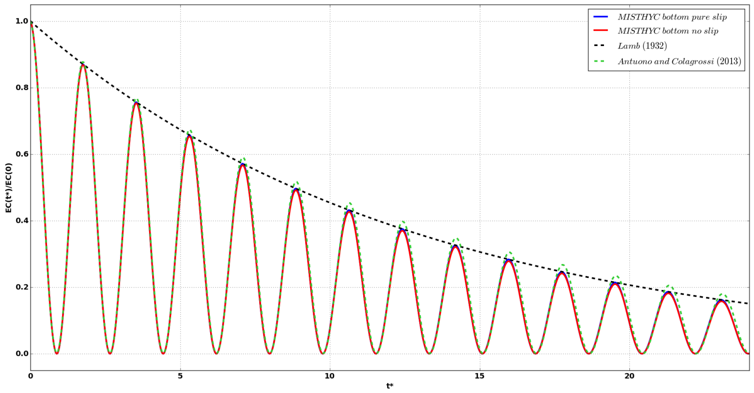

(b) $Re = 500$ ($\nu = 0.006264\ m^2/s$)

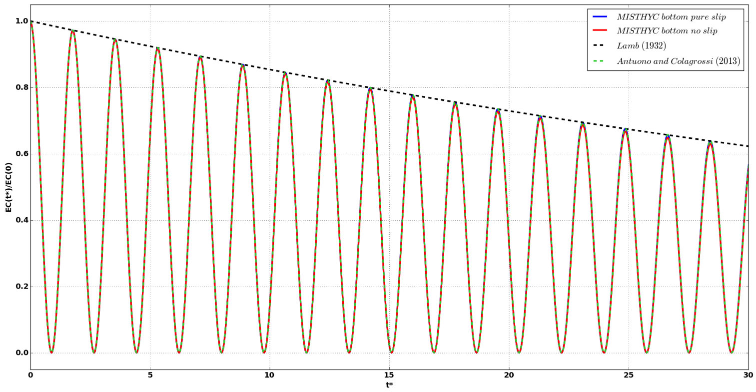

(c) $Re = 2500$ ($\nu = 0.0011253\ m^2/s$)

Figure 3.12: Evolution of the normalized kinetic energy of the system as a function of nondimensional time for $kh = \pi$ (deep water) (Raoult, 2017).

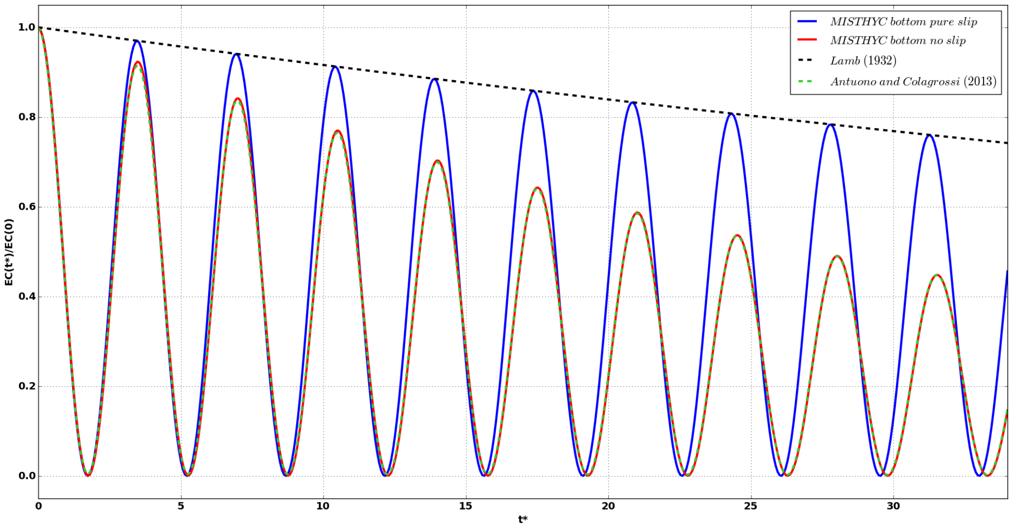

Figure 3.13: Evolution of the normalized kinetic energy of the system as a function of nondimensional time for $kh = \pi/3$ and $Re = 500$ ($\nu = 0.06264\ m^2/s$) (Raoult, 2017).

quency instabilities in the model for some simulations with large viscosity values (e.g. in the intermediate water depth case $kh = \pi/3$, with a relatively high viscosity $\nu = 0.006264\ m^2/s$). Decreasing the time step, or increasing the horizontal or vertical resolution did not stabilize the simulations, so a low pass filter was applied to the $\frac{\partial^2 \Phi}{\partial z^2}$ term in (3.16) at every time step, keeping only the first ten modes. These instabilities may be attributed to the large value of the viscosity, which no longer satisfied the small viscosity assumption used in the derivation of this term. These test cases demonstrate the agreement of the simulation results with the theoretical work of Lamb (1932) and Antuono and Colagrossi (2013) in the linear regime in deep and intermediate to shallow water depths, respectively.

3.4.2.2 Small-scale laboratory experiments

Then the model was tested to evaluate its ability to simulate a series of small-scale experiments in which the effects of viscosity were important. In collaboration with P. Petitjean and E. Monsalve from the PMMH laboratory (Physique et Mécanique des Milieux Hétérogènes, UMR CNRS, ESPCI), A. Maurel from the Institut Langevin (ESPCI), and V. Pagneux from the LAUM (Laboratoire d'Acoustique de l'Université du Mans) laboratory, Misthyc was applied to simulate small-scale experiments of wave propagation over abrupt changes in bottom bathymetry (Monsalve et al., 2015). The objective of their work was to evaluate experimentally and theoretically the interactions between the bottom bathymetry and waves as they propagated over a step, including the generation and propagation of forced and free harmonics. Within the thesis work of Cécile

Raoult, our objective was to test the ability of Misthyc to simulate viscous effects, while maintaining high accuracy in reproducing the nonlinear interactions.

The experiments were conducted as part of the thesis work of E. Monsalve in the PMMH laboratory in a 1 m-long tank with a step transition between a deep water region with $h^{(I)} = 6.5$ cm and a shallow water region with $h^{(II)} = 2.0$ cm. A flap-type wavemaker generated waves at the left end of the tank, and an absorbing beach with an 8% slope was added at the right end of the tank to dissipate the waves and to reduce wave reflections. High temporal resolution, two-dimensional measurements of the free surface position were obtained using a non-intrusive method, called Fourier Transformed Profilometry (Cobelli et al., 2009; Monsalve et al., 2015). By adding TiO_2 particles to the free surface, the projection of a sinusoidal pattern is measured, and the phase difference of the deformed pattern is used to reconstruct the free surface position (Cobelli et al., 2009).

At these scales (centimeters), both capillary effects and bottom friction play an important role in wave transformation processes, and it was necessary to take into account these two physical processes in the Misthyc model (Figure 3.14a). Thus, surface tension effects were added to the KFSBC following Dingemans (1997) by adding a correction term to the free surface pressure:

$$p(x, y, \eta(x, y, t), t) = p_{atm}(x, y, t) - \sigma \nabla_{\mathrm{H}} . \left(\frac{\nabla_{\mathrm{H}} \eta}{\sqrt{1 + |\nabla_{\mathrm{H}} \eta|^2}} \right), \tag{3.18}$$

where σ is the surface tension coefficient, or $\sigma = 0.074$ N/m (for an air-water interface at 20 ℃). Surface tension effects are important at the spatial scale of these experiments, especially for reproducing well the evolution of the higher-order harmonics because surface tension modifies the linear dispersion relation causing an increase in the wavelength for a given wave frequency (Dingemans, 1997).

To evaluate the contributions of surface tension and viscosity effects, these terms were added to the model first independently and then together. By including the effects of surface tension in the model, the estimation of the second harmonic beat length improved significantly (Figure 3.14c). By including the effects of viscosity in the model, the agreement between the observed and simulated amplitude decay improved significantly (Figure 3.14b). The best simulation results were obtained when both terms were taken into account, showing good agreement with the observations (Figure 3.14d).

These test cases, as well as the test case simulating the attenuation of a solitary wave propagating in a wave flume across a flat bottom and then up a slope (experiments of Liu et al. (2006), not shown here) demonstrated good agreement with the developed theories and experimental data for small bottom slopes and viscosity values $\nu < 10^{-3}$. The limitations of the viscosity approach implemented here include the assumption of small viscosity, the extension of the expressions derived for a linear model being applied in a nonlinear model, and the stability of the bottom friction term in its numerical implementation.

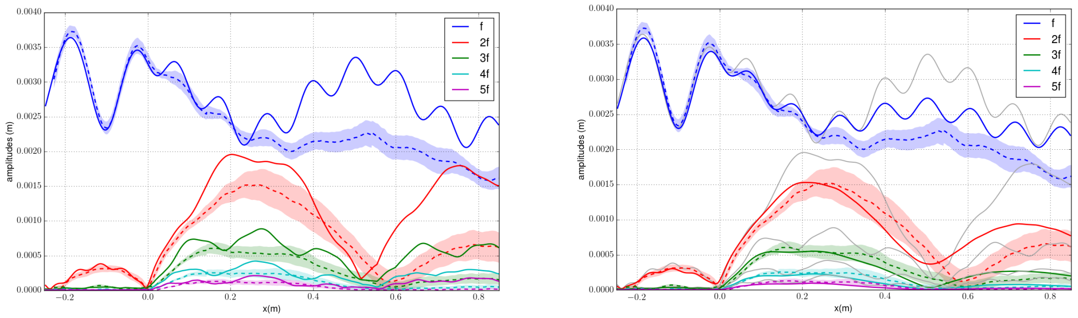

(a) no surface tension or viscous effects
($\sigma = 0N/m, \nu = 0\ m^2/s$)

(b) viscous effects only
($\sigma = 0\ N/m, \nu = 4.10^{-5}\ m^2/s$)

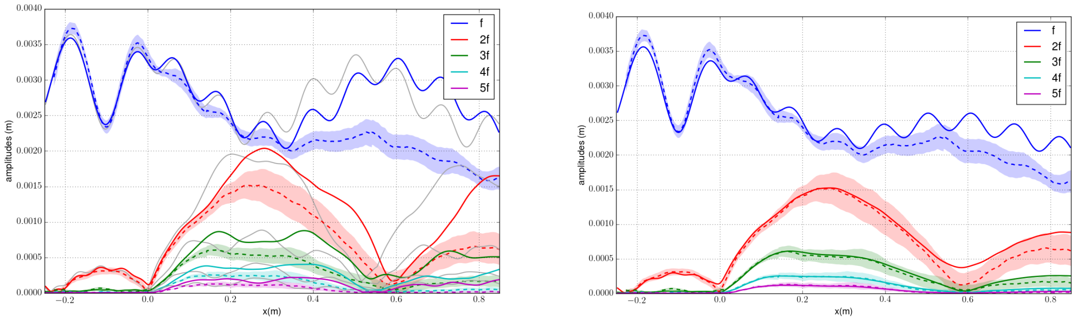

(c) surface tension effects only
($\sigma = 0.071\ N/m, \nu = 0\ m^2/s$)

(d) surface tension and viscous effects
($\sigma = 0.071\ N/m, \nu = 4.10^{-5}\ m^2/s$)

Figure 3.14: Spatial evolution of the simulated (solid line) and measured (dashed line) first five harmonic amplitudes for $f = 1.9837$ Hz. The dashed lines and shaded areas are the transversal mean and standard deviation, respectively, of the two dimensional free surface measurements. (Raoult, 2017)

Ongoing work includes a collaboration with Michel Benoit, Cécile Raoult, and two researchers in the LHSV laboratory, Sébastien Boyaval and Jeffrey Harris, comparing the simulation results for the test case of Antuono and Colagrossi (2013) to simulations with a numerical model resolving the linearized version of the Navier-Stokes equations and a numerical model resolving the Navier-Stokes equations (*Code_Saturne*, EDF R&D).

3.5 2DH extension of the model using RBFs

Continued work in the final year of Cécile Raoult's thesis led to the extension of the 1DH model to 2DH using a meshless radial basis function - finite difference (RBF-FD) approach to estimate the horizontal derivatives (in the x, y plane) for a set of scattered nodes. The objective of this work was to demonstrate the ability to apply this numerical approach to simulate accurately wave propagation. The goal of using a meshless approach is to enable domain flexibility, including irregularly shaped domains, as well as local refinement in areas of interest.

Much of the early literature on RBFs focused on the use of these functions as a meshless method for interpolation (e.g. Hardy, 1971; Franke, 1982), which was then extended to estimate partial derivatives or to solve PDEs (e.g. Stead, 1984; Kansa, 1990). The RBF-FD approach is based on estimating the value of $Lf(\underline{x}_1)$, where L the desired linear differential operator (i.e. $\frac{\partial}{\partial x}, \frac{\partial^2}{\partial x^2}$...) for any point $\underline{x}_1 = (x_1, y_1)$ in the domain. The linear operator is expressed as:

$$Lf(\underline{x}_1) \approx \sum_{i=1}^{N_{sten}} w_i \, f_i, \tag{3.19}$$

where f_i are the function values at points in the stencil of size N_{sten}, and w_i are weights to be found using a RBF interpolant. The RBF interpolant here is supplemented with a polynomial of degree l (general case) such that:

$$s(\underline{x}) = \sum_{k=1}^{N_{sten}} \lambda_k \, \phi(||\underline{x} - \underline{x}_k||) + \sum_{j=1}^{M} \beta_j p_j(\underline{x}) \tag{3.20}$$

with ϕ the chosen radial basis function, $p_j(\underline{x})_{j=1}^{\binom{l+2}{2}}$ a basis of polynomials up to degree l, $\{\lambda_k\}_{k=1}^{N_{sten}}$, $\{\beta_j\}_{j=1}^{M}$ the interpolation coefficients, and $M = \binom{l+2}{2}$. Evaluating the derivative of the interpolant at $\underline{x}_1$:

$$Ls(\underline{x}_1) = \sum_{k=1}^{N_{sten}} \lambda_k \, L\phi(||\underline{x}_1 - \underline{x}_k||) + \sum_{j=1}^{M} \beta_j L p_j(\underline{x}_1), \tag{3.21}$$

which can be expressed in matrix representation and then solved to obtain the unknown weights (see Bayona et al. (2011) and Raoult (2017) for more details). The added polynomial is necessary in some cases (discussed in more detail later) to maintain the inversability of the coefficient matrix.

Application of the local RBF-FD method requires the choice of a radial basis function, including the type or regularity of the function (piecewise (PS) or infinitely (IS) smooth), a shape parameter C for IS functions, the size of the stencil N_{sten}, the node spacing, and the degree of the added polynomial. Raoult et al. (2019) tested six commonly used RBF functions (Table 3.1), including 4 IS functions requiring a shape parameter C and 2 PS functions. Contrary to intuition, some of the proposed RBF functions $\phi(r)$ increase with increasing distance r from the center of the stencil (e.g. MQ, PHS, and TPS in Table 3.1). For these functions, the corresponding calculated interpolation coefficients λ_k decrease with increasing distance r such that points farther from the center of the stencil still have a smaller impact on the estimated derivatives.

RBF (Acronym)	$\phi(r)$	Condition	Regularity
Multiquadric (MQ)	$\sqrt{r^2+C^2}$	$C \in \mathbb{R}$	IS
Inverse Multiquadric (IMQ)	$\frac{1}{\sqrt{r^2+C^2}}$	$C \in \mathbb{R}$	IS
Inverse Quadratic (IQ)	$\frac{1}{r^2+C^2}$	$C \in \mathbb{R}$	IS
Gaussian (GA)	e^{-r^2/C^2}	$C \in \mathbb{R}$	IS
Polyharmonic Spline (PHS)	r^m	m odd integer	PS
Thin Plate Spline (TPS)	$r^m \log r$	m even integer	PS

Table 3.1: RBF functions ϕ, describing the free parameter constraints and regularity.

3.5.1 Estimation of derivatives with RBF-FD

We conducted a thorough study of the parameters listed above for a representative sinusoidal wave function of the form:

$$f(x,y) = A\cos\left(\frac{2\pi}{L}(x\cos\theta + y\sin\theta)\right), \tag{3.22}$$

and concluded that the choice of a PS RBF was optimal to avoid the difficulties in making the appropriate choice for the shape parameter C. The shape parameter controls the flatness of the RBF functions and has a significant impact on the accuracy of the RBF approximation. For example, for the four IS RBFs shown in Table 3.1, the normalized root-mean-square error in calculating the horizontal derivatives f_x for a sinusoidal wave shows variability over several orders of magnitude depending on the value of C (Figure 3.15a). The four IS functions show the same general trends, with large errors for small values C, a significant decrease to a minimum error for a narrow range of C values, and then a subsequent increase in error associated with the coefficient matrix becoming ill-conditioned. The optimal value of C depends on many factors, including the function f, the estimated derivative (e.g. f_x, f_y, f_{xx}, f_{yy}), the RBF function, the stencil size N_{sten}, and the node spacing (Δx, Δy).

In Misthyc, the RBF-FD approach is used to estimate all horizontal derivatives, including the free surface position η, the free surface potential Φ, and the bottom topography or water depth h. These surfaces have different forms, and therefore the optimal function and shape parameter C may not be the same for each variable or even for each test case (e.g. waves propagating over a flat bottom or highly variable bathymetry). Tests using PS PHS or TPS functions demonstrate their robustness in comparison to the IS functions (e.g. Figure 3.15b). Thus, to avoid the difficulties associated with finding the optimal C parameter for each study, we recommend using PHS, in agreement with the work of Barnett (2015).

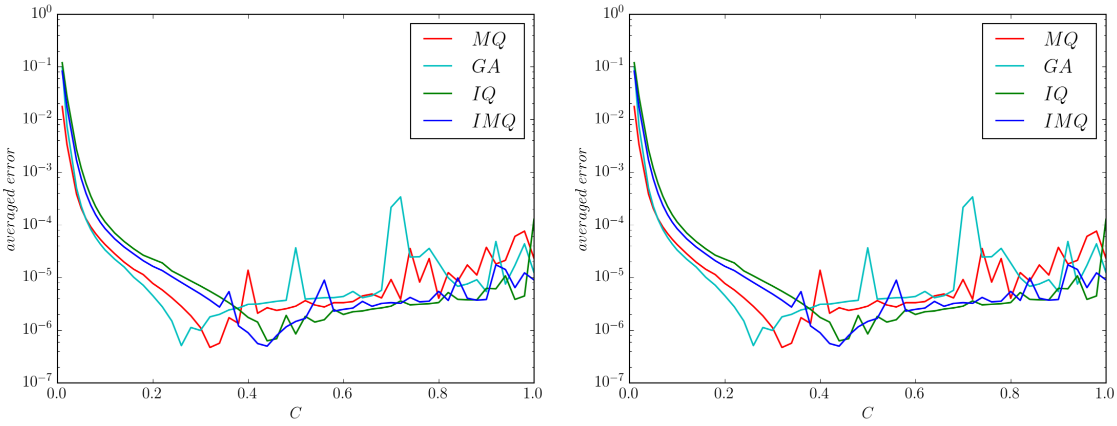

(a) IS RBFs

(b) PS RBFs

Figure 3.15: Normalized error in estimating f_x for different IS and PS RBFs as a function of the shape parameter C (with $N_{sten} = 21$, $\Delta x = \Delta y = L/100$, and added polynomial of degree 0). (Raoult, 2017)

Finally, after an analysis of the optimal stencil size and order of the added polynomial, the thesis work of Cécile Raoult showed that using PHS functions of the form $r^k + pl$, where k is the highest order of the polynomial function, and l is the highest order of the added polynomial, is optimal (Raoult, 2017; Raoult et al., 2019). For example, it is recommended to use a $PHS\ r^7 + p3$ for a targeted stencil size between 20 and 30 nodes, or $PHS\ r^5 + p4$ or $r^7 + p4$ for a targeted stencil size between 30 and 40, making a compromise between accuracy and increased computation time.

3.5.2 Simulating laboratory experiments

Two sets of wave basin experiments were accurately reproduced using the RBF-FD approach with $PHS\ r^7 + p3$ ($N_{sten} = 21$): regular waves propagating over a semi-circular step (Whalin, 1971), and regular and irregular waves propagating over an elliptical shoal (Vincent and Briggs, 1989). These two test cases demonstrated the advantages and disadvantages of this modeling approach, and the case of (Whalin, 1971) will be described further here.

The experiments of Whalin (1971) investigated the convergence of regular waves propagating over a semi-circular, strongly convergent step. To reproduce one set of the laboratory experiments, regular waves with a wave height $H = 0.015$ m and wave period $T = 2$ s ($L = 3.91$ m in the deeper end of the domain) were generated in a one wavelength-long relaxation zone at the left end of the domain and absorbed in a three wavelength-long relaxation zone at the right end of the domain. The bathymetric profile defined by Shao and Faltinsen (2014) was used here (Figure 3.16) to represent the convergent shoal, with the domain discretized by 137,712 regularly-spaced nodes ($\Delta x \approx \Delta y \approx 0.04$ m, or approximately $L = 98$). Waves were propagated with a constant time step of $\Delta t = 0.0178$ s ($\approx T = 112$) for 18 s to reach the steady state.

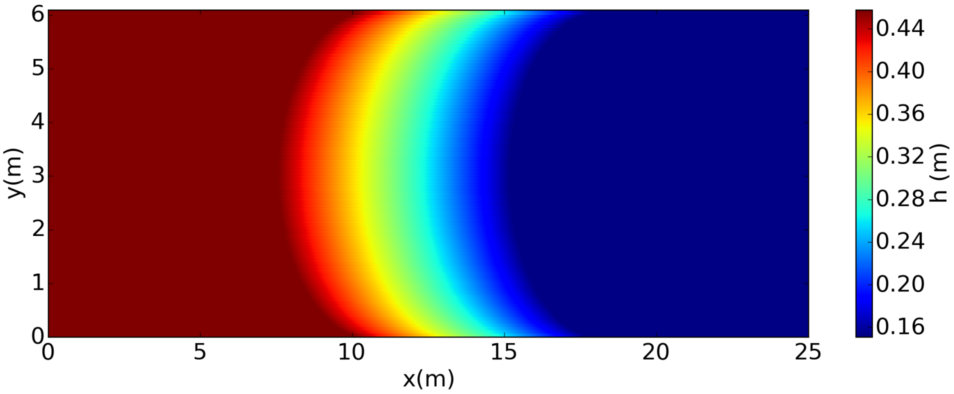

Figure 3.16: Bathymetry of the wave basin test of Whalin (1971).

The free surface position at the end of the simulation shows the 2D free surface wave patterns and the wave convergence over the shoal (Figure 3.17a). The simulation wave envelope (maximum and minimum free surface position during the simulation) and the free surface position along the centerline of the tank show an increase in wave height over the step caused by both wave shoaling and the convergence of wave energy (Figure 3.17b). The generation of higher-order harmonics is also observed by the presence of side lobes around the maximum wave near $x = 20$ m.

Energy transfers to higher-order harmonics were reproduced well in the simulations (Figure 3.18). Wave energy was transferred from the incident regular wave to the second and third harmonics as the waves propagated over the step. The first harmonic amplitude does not, however, decrease in amplitude because of the wave convergence over the semi-circular shoal (for this particular test case with $H = 0.015$ m and $T = 2$ s). The sensitivity of the simulation results to the chosen parameters for the RBF-FD approach was tested (Table 3.2), and using stencil sizes ranging from 18 to 21, regularly or irregularly-spaced nodes, and different horizontal discretizations, and different time steps did not influence significantly the simulation results for the ranges of values tested (Figure 3.19).

Simulations	node set	$\Delta x(m)$	RBF type	N_{sten}	Δt (s)
reg PHS 1	regular	0.040	$r^7 + p3$	21	0.0178
reg PHS 2	regular	0.060	$r^7 + p3$	21	0.0267
reg PHS 3	regular	0.075	$r^7 + p3$	21	0.0333
irreg PHS 1	irregular	≈ 0.060	$r^7 + p3$	21	0.0267
irreg PHS 2	irregular	≈ 0.060	$r^5 + p2$	18	0.0267

Table 3.2: Numerical parameters for the simulation test cases with with $T = 2$ s, $H = 0.015$ m of Whalin (1971). The original simulation results presented in Figures 3.17 and 3.18 correspond to case ‘reg PHS 2’.

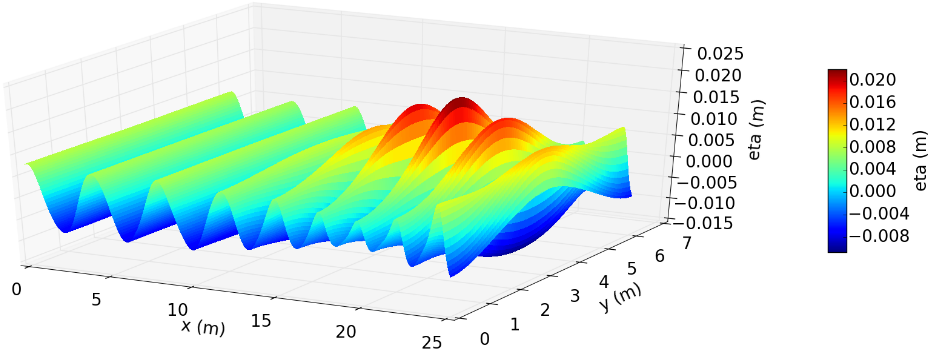

(a) 2D free surface position

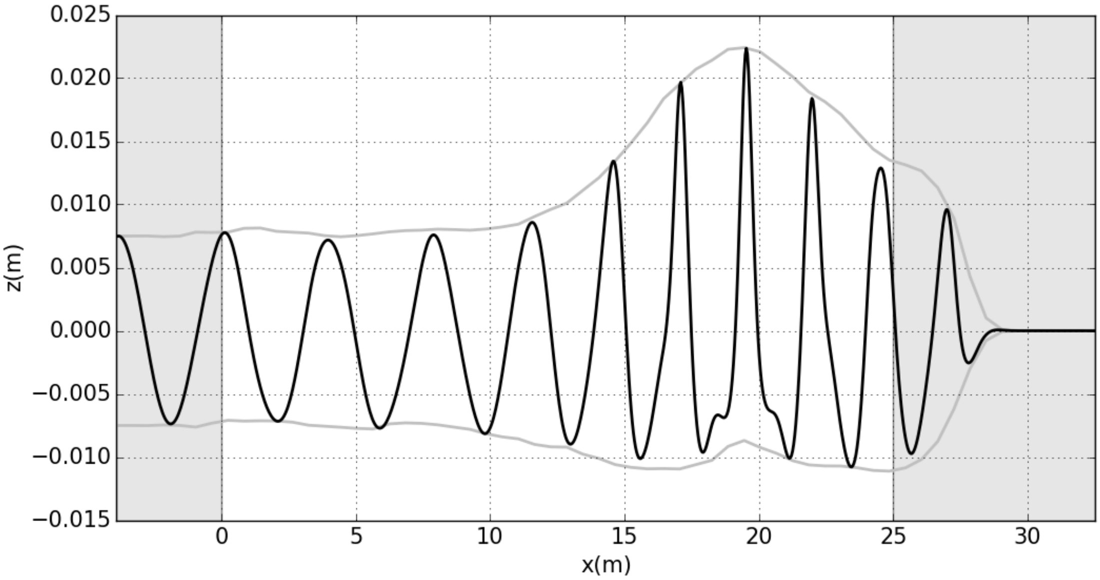

(b) Free surface position at $t = 18$ s (black line) and wave envelope (gray lines) along the centerline of the tank

Figure 3.17: Simulation results for the experiments of Whalin (1971) with $H = 0.015$ m and $T = 2$ s.

The evaluation of derivatives estimated using the RBF-FD method for a representative sinusoidal function allowed identifying the optimal RBF to implement in Misthyc. Then, preliminary work comparing simulation results with experimental measurements of 3D laboratory experiments demonstrated the robustness of the RBF-FD method for wave propagation applications (Raoult, 2017; Raoult et al., 2019). While the initial results are promising, there do exist several limitations to this approach. Two main limitations include the development of instabilities near the domain boundaries and the computational time of this approach, which requires solving the full Laplace BVP in the domain at each time step, and future work will be focused on these issues.

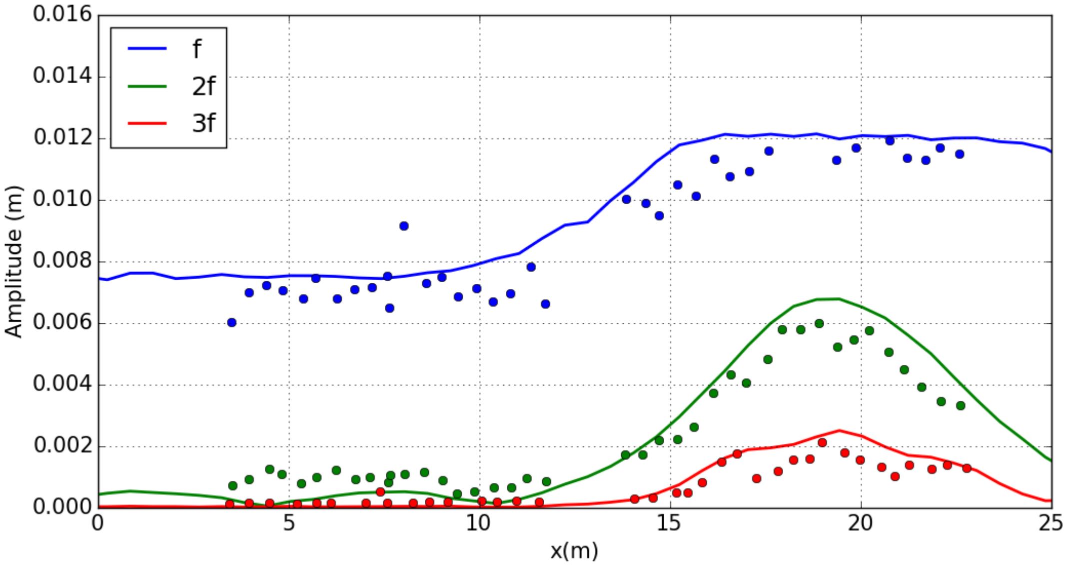

Figure 3.18: Observed (circles) and simulated (lines) spatial evolution of the amplitude of first three harmonics (at frequencies f, $2f$ and $3f$) of the free surface elevation for $T = 2$ s, $H = 0.015$ m of the experiments of Whalin (1971), using a PHS RBF $r^7 + p3$ with $N_{sten} = 21$.

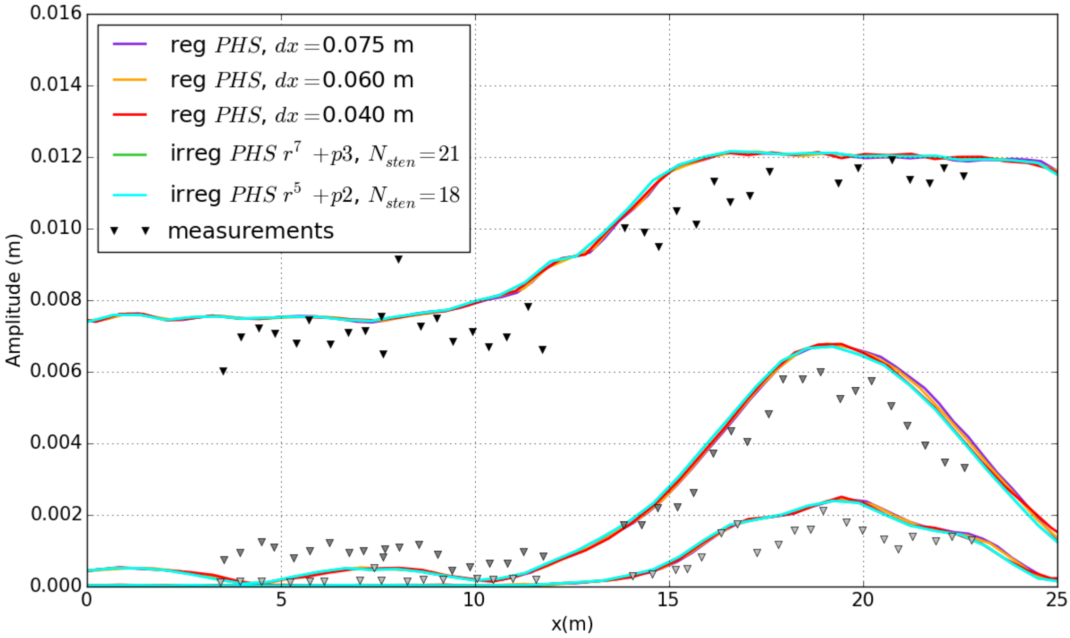

Figure 3.19: Observed (triangles) and simulated (lines) spatial evolution of the amplitude of first three harmonics (at frequencies f, $2f$ and $3f$) of the free surface elevation for $T = 2$ s, $H = 0.015$ m of the experiments of Whalin (1971) for regular and irregular meshes with different node spacing (Table 3.2).

3.6 Simulating wave breaking

Finally, my recent work is focused on parameterizing the effects of wave breaking to extend the application of Misthyc to nearshore wave propagation applications at study sites. This work is being carried out within the France Energies Marines (FEM) - ANR DiMe (Dimensionnement et Météocean) project and the Labex DEPHYMAN project in collaboration with Michel Benoit at the Ecole Centrale Marseille and IRPHE laboratory, and two post-doctoral researchers (Christos Papoutsellis and Bruno Simon) financed by these two projects.

Current research in the field of observations and modeling of wave breaking dynamics demonstrates the complexity of this process and the challenges in integrating the impacts of wave breaking in numerical models. In models that do not simulate directly wave breaking, first, it is necessary to identify the initiation of wave breaking, which is not trivial, and then it is necessary to accurately describe the impacts of the breaking wave on the flow.

Several different methods for taking into account the effects of wave breaking in potential flow theory models have been proposed over the last few decades, but this work has been focused primarily on Boussinesq-type models. Recently, there has been renewed interest in this field with the development of fully nonlinear potential flow and multi-layer non-hydrostatic models that are computationally efficient and thus can be used for coastal applications (e.g. Tissier et al., 2012; Seiffert and Ducrozet, 2018; Filippini et al., 2018).

In these types of models, including the Misthyc model, where overturning waves can not be simulated explicitly, only the effects of wave breaking on the momentum or energy balance can be parameterized. To describe fully wave breaking processes, two-phase DNS (direct numerical simulation) models simulating accurately the air-water interface, air entrainment, and bubble dynamics are necessary to reproduce accurately wave breaking events (Popinet, 2009; Deike et al., 2016; Lubin and Glockner, 2015). However, DNS models are still prohibitively computationally expensive and are therefore not an optimal choice at the temporal (hours to days) and spatial (kilometers) scales necessary for simulating nearshore wave dynamics. Therefore, a range of nearshore wave models (e.g. Boussinesq, SGN, FNPF, multi-layer non-hydrostatic, etc.) have been developed in recent years to seek an optimal compromise between computational efficiency and numerical accuracy in simulating highly nonlinear and dispersive waves as they propagate from intermediate and deep water conditions to the nearshore zone. Thus, incorporating the effects of wave breaking recently has become a topic of renewed interest (e.g. motivating the organization every two years since 2014 of the B'WAVES workshop, including workshops in Bordeaux, France in 2014; Bergen, Norway in 2016; Marseille, France in 2018).

The next two sections present first a review of techniques currently used to parameterize wave breaking in potential flow models, primarily with applications in Boussinesq-type models (section 3.6.1), and then our tests of the selected approaches in fully nonlinear potential flow models based on the Zakharov equations (section 3.6.2).

3.6.1 Current state of the art

In phase-resolving wave propagation models that can be both accurate (representing partially or fully nonlinear and dispersive effects) and computationally efficient at the temporal and spatial scales of nearshore wave propagation, the parameterization of wave breaking processes is necessary. This requires two important steps: (1) the identification of breaking waves, quantified with breaking onset criteria, and (2) the proper dissipation of wave energy (both the magnitude and spatial distribution). In the following two sections, a review of existing approaches used for these two steps is presented.

3.6.1.1 Wave breaking onset criteria

A variety of techniques exist to identify breaking waves, and Barthelemy et al. (2018) divided them into three generic categories: geometric, kinematic, and energetic. The most commonly used criteria are based on geometric properties, such as wave steepness or asymmetry, or kinematic properties such as the crest acceleration or fluid speed relative to the wave phase speed. The third type of approach is based on dynamical criteria, suggesting that the wave energy flux can be used locally to identify unstable, breaking waves within wave groups (overview by Tulin and Landrini, 2000). In shallow water conditions, which will be the focus of the work presented here, the most commonly used criteria include:

- wave steepness (e.g. Deigaard, 1989; Schäffer et al., 1993),
- horizontal crest velocity (e.g. Zelt, 1991),
- free surface vertical velocity (e.g. Kirby et al., 1998; Kennedy et al., 2000),
- wave Froude number or "Relative Trough Froude Number" (RTFN) (e.g. Utku, 1999; Okamoto and Basco, 2006),
- hybrid approaches (e.g. Breaking Celerity Index, D'Alessandro and Tomasicchio, 2008).

There exist a wide variety of approaches used to identify breaking waves because of the difficulty in defining a breaking wave. Depending on the physical processes that are being investigated (i.e. air-sea interactions, bubble entrainment, impacts on structures, etc.), the definition of a breaking wave may vary, and therefore the criteria used to identify the initiation of this process also vary. In addition, depending on the water depth (deep or shallow water breaking) and the type of wave breaking (e.g. spilling, plunging, surging), the physical mechanism causing wave breaking is not the same. Thus, a variety of approaches have been proposed, and no one approach has been demonstrated to be applicable universally (Barthelemy et al., 2018).

Wave steepness The wave steepness criteria is based on the geometrical approach of Deigaard (1989), extended by Schäffer et al. (1993). As waves shoal, the wave front steepens until it eventually becomes unstable and begins to break. The identification of breaking waves can thus be defined with a wave front slope criterion, assuming that non-breaking waves reach a local maximum slope before breaking is initiated. Wave breaking steepness criteria are typically used to identify wave breaking in deep water conditions, while the relative water depth is typically used to define shallow water breaking criteria. However, Miche (1944) developed an empirical relation combining both of these criteria to create criterion applicable in intermediate water depths:

$$\left(\frac{H}{L}\right)_{max} = 0.142 \tanh \frac{2\pi d}{L}. \tag{3.23}$$

Hughes (2004) showed that this formula has a tendency to underestimate wave heights in deep water environments and to overestimate wave heights in shallow water environments. However, this criteria continues to be used as an approximation of the maximum wave steepness. Deigaard (1989) suggested that the maximum wave steepness threshold, or $\tan\phi$, is around 10° in the inner surf zone. However, Schäffer et al. (1993) concluded that this threshold varies significantly in both time and space and that a constant threshold can not be used. The criteria used to initiate wave breaking cannot be used to terminate breaking, and Schäffer et al. (1993) instead proposed a threshold that decays exponentially in time from the wave breaking initiation to termination value. This simple approach requires tuning a number of empirical parameters for each test case to optimize the initiation and termination of wave breaking, and different sets of initiation and termination thresholds have been suggested, ranging from $14 - 32^\circ$ and $7 - 10^\circ$, respectively (Schäffer et al., 1993; Madsen et al., 1997; Sørensen et al., 1998).

Horizontal crest velocity Instead of using a criteria based on the wave shape, a series of other wave breaking criteria were developed based on the kinematic properties of breaking waves. Stating that it is not possible to define a critical wave steepness for all wave conditions, Zelt (1991) instead preferred to define a critical horizontal velocity at the free surface as the wave breaking criterion for solitary waves. When the dimensionless velocity gradient $\frac{\partial u}{\partial x}\sqrt{\frac{h+\eta}{g}}$ exceeded the threshold value of 0.3, waves were considered to be breaking. Other kinematic breaking criteria are based on the ratio of the horizontal fluid velocity at the wave crest u_c and the local wave phase speed c, often using a threshold of $u_c/c \geq 1$ to define the initiation of wave breaking (Kurnia and van Groesen, 2014). More recently, Barthelemy et al. (2018) proposed a dynamical wave breaking onset criterion B_x based on the ratio of the local energy flux to the energy density, normalized by the local crest speed magnitude. At the free surface, this criterion reduces to $B_x = u_c/c$. In their study, focused primarily on deep water waves, they suggest that waves that exceed a threshold value of 0.85 will eventually break, although there may be a time lag between the time that the threshold is exceeded and the initiation of wave breaking, which limits the use of this criterion to define the initiation of wave breaking in numerical models.

Free surface vertical velocity As an alternative to using the horizontal velocity as a wave breaking criteria, the free surface vertical velocity η_t may also be used (Kirby et al., 1998; Kennedy et al., 2000). Kennedy et al. (2000) suggested that using a critical value of η_t as the wave breaking onset criteria ensured that the dissipation is concentrated on the front face of the wave. Again, much like the wave steepness criteria, the thresholds used to initiate and terminate wave breaking are not the same, and an empirical relationship must be used to estimate how this value varies in time. For example, Kennedy et al. (2000) estimate that wave breaking begins when $\eta_t^{(I)} > 0.65\sqrt{gh}$. Then the threshold decreases linearly in time (over a transition time T^*) until wave breaking terminates when $\eta_t^{(F)} < 0.15\sqrt{gh}$. These values were proposed for 1DH domains, and Chen et al. (2000) suggest a smaller initiation threshold of 0.35 for 2D wave fields. The default transition time chosen by the authors is $T^* = 5\sqrt{h/g}$. However, each of these parameters must be considered as a calibration parameter for different wave conditions and different types of mathematical and numerical models. The advantage of this type of wave breaking initiation criterion is that the quantity η_t is already known in models based on the Zakharov equations and thus requires no additional computation.

Wave Froude number This criteria is based on the analogy between a breaking wave and a moving hydraulic jump propagating like a bore. In this case, a breaking wave is treated like a shock and two boundary conditions are required: (1) upstream side: trough, supercritical flow, and (2) downstream side: crest, moving shock celerity (Utku, 1999; Okamoto and Basco, 2006). Therefore, to determine a critical threshold for wave breaking based on this analogy, the wave Froude number or “Relative Trough Froude Number” (RTFN) is calculated as: $\mathrm{RTFN} = Fr_t = \frac{|u_{trough}|+C}{\sqrt{gD}}$, with C the wave phase speed, D the relative length scale calculated as the water depth in the wave trough, and u_{trough} the depth-averaged particle velocity in the wave trough. Okamoto and Basco (2006) suggest that the RTFN must be greater than 1 for all wave motion, and that the value should be larger for breaking waves. The authors make the analogy between the transition from an undular jump to a surface roller jump and the critical limit distinguishing a non-breaking and breaking wave. They conclude that the RTFN should therefore be in the range 1.36-1.60 (Okamoto and Basco, 2006; Kazolea et al., 2014). One drawback to this method is the need to calculate accurately the wave celerity at the crest and in the trough. A hybrid approach is proposed, using a cross-correlation method in deep water conditions and an analytical equation in shallow water conditions to avoid underestimating u_{trough} (Okamoto and Basco, 2006), thus creating a somewhat computationally expensive wave breaking initiation criteria.

Hybrid approaches Finally, recent work has also concentrated on hybrid approaches that make use of more than one existing wave breaking criteria. For example, D’Alessandro and Tomasicchio (2008) proposed the Breaking Celerity Index (BCI) by coupling two of the criteria listed above: (1) the free surface vertical velocity criteria η_t and (2) the RTFN. In their model, wave breaking is initiated when η_t exceeds a threshold defined by: $BCI = \frac{\sqrt{g(h+a)}-u_\alpha}{1.47}$, where u_α is the horizontal velocity at the reference water depth $z = z_\alpha = -0.531h$ (Nwogu, 1993), and the denominator 1.47 is an empirical parameter that appears to depend on the bottom slope (D’Alessandro and Tomasicchio, 2008).

3.6.1.2 Wave breaking energy dissipation

Once the onset of wave breaking has been identified, it is necessary to estimate the impacts of wave breaking on the fluid flow. The energy dissipation caused by breaking can be parameterized using a variety of different methods proposed in the literature:

- free surface pressure term (e.g. Guignard and Grilli, 2001),
- eddy viscosity model (e.g. Heitner and Housner, 1970; Zelt, 1991; Kennedy et al., 2000),
- wave roller model (e.g. Schäffer et al., 1993; Madsen et al., 1997),
- vorticity model (e.g. Svendsen et al., 1996; Veeramony and Svendsen, 1998, 2000), and
- hybrid switching approach (e.g. Boussinesq-type model to NLSWE, Tissier et al., 2012; Kazolea et al., 2014).

These five approaches have been developed and implemented in a variety of different wave propagation models, mostly restricted to Boussinesq or SGN-type models, where dissipation terms are added to the conservation of momentum equations. The majority of the models assume that the geometrical form of and energy dissipated by a breaking wave can be simulated as: (1) a bore, or quasi-steady wave with a roller on the front face that is transported by the wave (Brocchini, 2013), or (2) a hydraulic jump. However, the different types of approaches listed above make different assumptions about the dominant physical processes causing wave breaking, or about the optimal numerical method used to parameterize the effects.

Free surface pressure This technique applies an artificial pressure at the free surface in the dynamic free surface boundary condition to dissipate wave energy in an absorption zone near the domain boundary, as reviewed by Clément (1996) and Grilli and Horrillo (1999). Here, the wave energy is dissipated simply by preventing the waves from overturning, without trying to reproduce accurately the physical processes associated with wave breaking. The artificial pressure term can be applied in a zone extending from the surf zone to the domain boundary, or locally around an identified breaking wave. Guignard and Grilli (2001) developed this technique to simulate spilling breaking waves, assuming that the energy dissipated by wave breaking is equivalent to the energy dissipated by a hydraulic jump with the same geometrical characteristics (following the work of Svendsen et al., 1978; Svendsen and Madsen, 1984). The artificial pressure added at the free surface is assumed to be of the form:

$$p_{bm}(x, \eta, t) = \nu_{b0} S(x) \frac{\partial \Phi}{\partial n} \left(\eta(x, t) \right), \tag{3.24}$$

where $\frac{\partial \Phi}{\partial n}$ is the normal velocity at the free surface, and ν_{b0} is an absorption function. To make a smooth transition in the zone where the pressure term is applied, $S(x)$ is a function varying between 0 and 1 . The absorption function ν_{b0} is determined such that the wave power dissipated by an individual breaking wave P_b is proportional to the power dissipated by a hydraulic jump P_h (following Lamb, 1932) with the same geometrical characteristics, or:

$$P_b = \nu_{b0} \int_{x_l}^{x_r} S(x) \left(\frac{\partial \Phi}{\partial n} \right)^2 d\Gamma, \tag{3.25}$$

$$= \mu P_h = \mu \rho g c \frac{hH^3}{4h_c h_t}, \tag{3.26}$$

where c is the wave phase speed, h is the water depth, and h_c and h_t are the wave crest and trough water depths. The constant of proportionality $\mu = 1.5$ is a free parameter that was calibrated with laboratory experiments by Svendsen et al. (1978). Applying this method requires implementing a wave tracking algorithm to identify breaking waves and calculate a certain number of geometrical (h_c, h_t, extent of breaking region) and kinematic wave properties (c).

Eddy viscosity model This type of wave breaking model assumes that the energy dissipated by a breaking wave can be represented by the formation and propagation of a bore. An artificial viscosity representing an eddy viscosity describes the energy dissipation by assuming that the Reynolds stresses represent the energy transfer and turbulence generated during wave breaking. In Boussinesq-type models, wave breaking is thus integrated in the conservation of momentum equations with a diffusion term of the form $\nu_T(u)_{xx}$ (Brocchini, 2013), where u is the vertically-integrated horizontal velocity. The artificial viscosity is then calculated either as $\nu_T \approx u_* d$, with $u_* = \sqrt{gd}$ (Zelt, 1991; Kennedy et al., 2000; Brocchini, 2013), or from a conservation equation for turbulent kinetic energy and a mixing length hypothesis (Karambas and Koutitas, 1992; Chen et al., 2000).

Representing breaking wave energy dissipation with an eddy viscosity approach is a popular choice because of its simplicity to implement (e.g. Zelt, 1991; Karambas and Koutitas, 1992; Wei et al., 1995; Chen et al., 2000; Musumeci et al., 2005; Roeber et al., 2010), and recent work continues to demonstrate the accuracy of this approach (e.g. Kurnia and van Groesen, 2014). Extended models have also been proposed to add the dissipation mechanism in the conservation of mass equation to integrate vertically the equations only in the potential part of the flow and not in the turbulent region near the free surface (e.g. Cienfuegos et al., 2010; Klonaris et al., 2013).

Applying an eddy viscosity model also requires a wave tracking algorithm to be able to calculate the associated eddy viscosity and to follow the temporal evolution of each breaking wave. The added term is diffusive, which therefore has the additional benefit of reducing the appearance of instabilities related to frequency dispersion or nonlinearities, and this term is often applied using a temporal ramp function (varying from 0 to 1) to progressively introduce and remove the applied viscosity to avoid the appearance of temporal instabilities.

Wave roller model An additional approach is to represent the physical processes during a breaking wave event through the formation of a surface wave roller, as described by Svendsen and Madsen (1984). A wave roller is defined as the mass of recirculating foam that forms during wave breaking when the generated turbulence mixes air and water. This mass of foam is then assumed to be transported passively by the wave in the form of a "roller" (Deigaard, 1989). In this approach, the water column is often divided in two layers of constant horizontal velocity for simplicity. To simulate the effects of a wave roller a convection term is added to the conservation of momentum equations. The convection term represents the dissipation of wave energy (ΔE) corresponding to that dissipated by a hydraulic jump (Schäffer et al., 1993) with the same height as that of the breaking wave H_b: $\Delta E \approx H_b^3$ (Brocchini, 2013).

This approach has been applied widely in Boussinesq-type models (e.g. Schäffer et al., 1993; Madsen et al., 1997). To take into account the effects of the wave roller, an initially uniform horizontal velocity profile is assumed to be non-uniform, following the simplified approach of Madsen (1981), with two layers of constant velocity that depend on the geometry of the wave:

$$u = \begin{cases} c & S - \delta \leq z \leq S \\ u_0 & -h \leq z \leq S - \delta \end{cases}$$

where u_0 is the velocity under the wave, c is the wave phase velocity, δ is the thickness of the wave roller, and h is the water depth.

The impact of the wave roller is then estimated as the difference R between the uniform and non-uniform vertical profile of the horizontal velocity. The horizontal gradient R_x of the term R,

$$R = \delta \left(c - \frac{P}{h} \right)^2 \left(1 - \frac{\delta}{h} \right)^{-1}, \tag{3.27}$$

is added to the conservation of momentum equations, where P is the vertically integrated horizontal velocity. This empirical term depends on the geometrical properties of the wave roller, which vary in space and time, as well as the wave phase speed (estimated as $c = 1.3\sqrt{gh}$ following the experiments of Stive, 1980). One advantage of this approach is that the physical processes of wave breaking are represented. However, an empirical approach is used to calculate the impacts of the physical processes, and the implementation of this model also requires a wave tracking algorithm to estimate the wave characteristics (e.g. phase velocity, roller thickness) and their evolution in time.

Vorticity model The previous approaches assume that the flow can be represented using potential flow theory and that the impacts of wave breaking can be estimated by adding heuristic terms to the Bernoulli equation (or DFSBC) or the conservation of momentum equation. However, it is clear that a breaking wave violates the assumption that the flow is irrotational. Thus another approach for modeling breaking waves is to propose a new model as a function of the stream function $\nabla^2\Psi = \omega$ and not the velocity potential $\nabla^2\Phi = 0$ (Svendsen et al., 1996; Veeramony and Svendsen, 1998), where ω is the vorticity that must be described independently. This method was applied in Boussinesq-type models by expanding the stream function using a power series and searching for a solution at a specified order. The irrotational or potential part of the flow u_p

and the rotational part of the flow u_r associated with the effects of viscosity, are separated and solved for independently. Finally, the mass and momentum conservation equations are coupled with a vorticity transport equation, and the system is closed by specifying the vorticity boundary conditions. The vorticity is zero at the surface and the bottom, to satisfy the boundary conditions of no vorticity outside of the wave roller region and no bottom friction, respectively. In the roller, however, the vorticity has an important role, with a maximum at the limit between the roller and the flow beneath it.

The advantage of this type of model is that the assumption of irrotational flow is fully satisfied, and the rotational part of the flow is treated appropriately. This approach has been used in several wave propagation models (e.g. Veeramony and Svendsen, 2000; Musumeci et al., 2006). However, the model still requires a wave tracking algorithm to identify and follow in time breaking waves and to calculate wave characteristics that enable estimating empirically the vorticity and viscosity associated with wave breaking.

Hybrid switching approach Finally, one of the most recently proposed approaches is to couple a Boussinesq-type model with a Nonlinear Shallow Water (NLSW) equation model to simulate directly the wave energy dissipation associated with wave breaking. Following Zijlema et al. (2011), who developed a multi-layer non-hydrostatic wave propagation model, the wave energy dissipation in this approach is simulated following the assumption that breaking waves can be represented by shock waves. When the dispersive terms are neglected in Boussinesq or SGN-type models, they reduce to the NLSW equations (Tonneli and Petti, 2012; Tissier et al., 2012). Therefore, to simulate wave breaking processes in a Boussinesq-type model, the dispersive terms are neglected locally when a breaking wave is identified, and the wave energy dissipation is estimated naturally by the NLSW equations (e.g. Tissier et al., 2012; Kazolea et al., 2014).

The advantage of this approach is that the wave energy dissipation is estimated automatically and does not require empirical approximations based on wave characteristics. This approach has thus been implemented in a variety of Boussinesq and SGN-type models in recent years (e.g. Tonneli and Petti, 2012; Tissier et al., 2012; Roeber and Cheung, 2012; Kazolea et al., 2014). However, it is still necessary to implement a wave tracking algorithm to identify breaking waves and to specify the spatial extent over which the NLSW equations are applied.

3.6.2 Implementation and validation of wave breaking parameterization

The implementation of a wave breaking parameterization approach must thus include both an onset criteria and a mechanism for dissipating the wave energy. The previous section summarized the state of the art for phase-resolving nearshore wave models. However, it must be noted that the majority of this work has been done in Boussinesq or SGN-type models, or more recently, in multi-layer non-hydrostatic models. The efficiency and accuracy of each approach depends on the model in which it is implemented, therefore emphasizing the interest in testing existing methods in different mathematical models.

The work that we have conducted with two post-doctoral researchers (Christos Papoutsellis and Bruno Simon) is thus concentrated on the choice of the optimal approach to parameterize the impacts of wave breaking in wave propagation models based on the Zakharov equations. Unlike Boussinesq-type models, there is no explicit equation for the conservation of momentum, and thus the effects of wave breaking are incorporated directly in the free surface boundary condition equations.

During the post-doctoral research of Christos Papoutsellis, breaking waves were detected using a criteria based on the velocity of the free surface position, following Kennedy et al. (2000) and Kurnia and van Groesen (2014). This is a natural choice for a model based on the Zakharov equations that calculates η_t at each time step. Then, a dissipative term is activated in the dynamic free surface boundary condition. We hypothesized that the two most appropriate methods to implement in a numerical model solving the fully nonlinear and dispersive Zakharov equations are:

1. an artificial pressure term simulating the wave energy dissipation of an effective hydraulic jump (EHJ), proposed by Guignard and Grilli (2001), and
2. an eddy viscosity method (EVM) proposed by Kurnia and van Groesen (2014), depending on a mixing length parameter, the total water depth, and the temporal gradient of the free surface position.

In the post-doctoral work of Christos Papoutsellis, these two approaches were adapted for the Zakharov equations and implemented in the model of Athanassoulis and Belibassakis (1999), Athanassoulis and Papoutsellis (2015), and Papoutsellis et al. (2018), which is based on the Zakharov equations (like the Misthyc code). This code, called HCMS for Hamiltonian Coupled-Mode System, solves the DtN problem using a coupled mode approach instead of the spectral approach coded in Misthyc (and presented in section 3.2). For more details about this model, see Athanassoulis and Belibassakis (1999), Athanassoulis and Papoutsellis (2015), and Papoutsellis et al. (2018).

First, by evaluating the propagation of dispersive shock waves, the mass and momentum conservation properties and wave energy dissipation of the model were verified for both the eddy viscosity method (EVM) and the effective hydraulic jump (EHJ) approach. This is an important demonstration since the EHJ method was constructed by requiring energy dissipation, while the EVM approach was constructed by requiring momentum conservation. Simulation results of the wave energy dissipation and decrease in wave height for the case of regular waves shoaling and breaking on a beach profile of constant slope (Figure 3.20) and over a barred beach profile (not shown here) show good agreement with the laboratory observations of Ting and Kirby (1994) and Beji and Battjes (1993), respectively (Papoutsellis et al., accepted, 2019).

In the post-doctoral work of Bruno Simon, these two approaches were also being tested in a second fully nonlinear potential flow model that solves exactly the same equations as the Misthyc

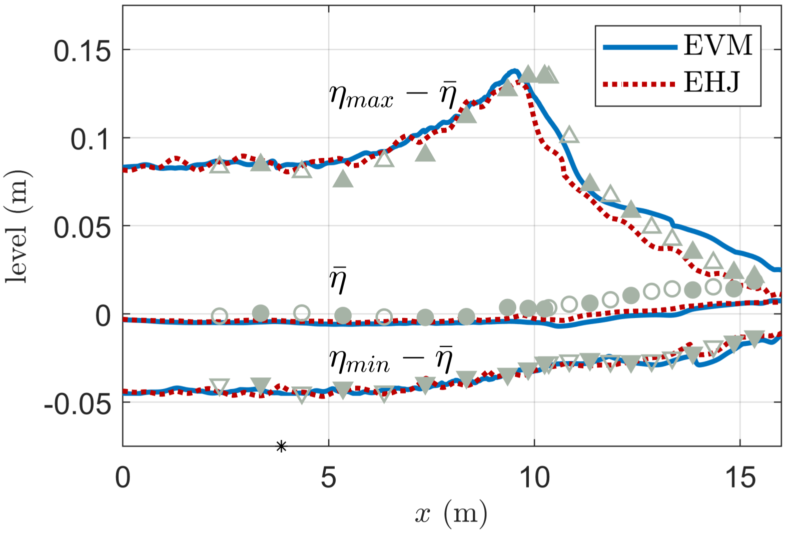

Figure 3.20: Comparison of simulated and measured wave envelope along the wave channel for a spilling breaking wave experiment of Ting and Kirby (1994).

model (Simon et al., submitted, 2019). The primary differences with Misthyc are the use of an iterative solver (GMRES algorithm with Incomplete L-U preconditioning) to solve the Laplace BVP and a third-order Runge Kutta time-marching scheme (Simon et al., 2018). In this work, three different wave breaking initiation criteria were additionally tested, including the criteria tested by Papoutsellis et al. (accepted, 2019), as well as a wave slope criterion, and the new criterion B_x proposed by Barthelemy et al. (2018). The test cases focused on reproducing laboratory experiments of irregular wave propagation and breaking over a barred bathymetry (Beji and Battjes, 1993), or plane beach slopes (Mase and Kirby, 1992; Husrin et al., 2012; Adytia et al., 2018). This work demonstrated the accuracy of all approaches in reproducing well the free surface position, in particular in the shoaling region. In the post-breaking region, differences between the observed and simulated wave shape (e.g. skewness and asymmetry parameters) increase, and work remains to be done to improve these characteristics.

Ongoing tests are focused on validating the conservation of mass and momentum of the proposed approaches, testing the sensitivity of the criteria to the initiation and termination of wave breaking, and evaluating the spatial extent of the application of the wave breaking dissipation term (i.e. along the entire wave or only on the wave face).

3.7 Ongoing work and perspectives

There is a strong need for highly accurate wave propagation models that are capable of simulating wave hydrodynamics in the coastal zone for real applications. The objective of the development of the Misthyc model is to achieve this goal, while maintaining reasonable computational times to enable the use of the model for practical applications. To achieve this goal, there remain certain limitations to overcome, which will be the focus of my research in this field in the next five years, including:

- Validation of the proposed approach for **parameterizing wave breaking dissipation** in the 1DH model and extension of this approach to the **2DH model**, to be able to apply the model to real applications, in particular during the final stages of the FEM-ANR DiMe project (2017-2020);
- **Implementation of a moving shoreline (runup)** to represent accurately wave reflection and absorption at the shoreline, as well as wave setup (e.g. Figure 3.20);
- **Optimization of the model**, in particular regarding the use of an indirect solver to solve the Laplace BVP at each time step;
- **Improvement of lateral boundary treatment** in the RBF-FD method to reduce model instabilities for non-symmetric stencils;
- **Comparison with existing wave propagation models** such as SWASH (multi-layer non-hydrostatic model), BOSZ or FunWave (Boussinesq-type models), etc. to evaluate the accuracy, efficiency, and limitations of the Misthyc model.

These five research goals address some of the current limitations of the model, and my research in the field of modeling wave hydrodynamics will be centered on these axes that are outlined in the following sections.

3.7.1 Parameterizing wave breaking dissipation

Current work in the scientific community is focused on investigating a variety of different approaches, first to identify the initiation of wave breaking, and then to estimate properly the wave dissipation during each individual breaking event. Work in the field is concentrated on using laboratory and field measurements, as well as numerical models to investigate these processes. As mentioned in the previous section, my current work is focused on testing and validating two different methods used to take into account the wave energy dissipation during breaking events. This work is carried out within the ANR-FEM DiMe (2017-2020) and LaBeX DEPHYMAN (2018-2019) projects, in collaboration with Michel Benoit and two post-doctoral researchers, Christos Papoutsellis and Bruno Simon.

The two approaches being evaluated are the application of an artificial pressure at the free surface, following the approach of Guignard and Grilli (2001), and the use of an eddy viscosity model, following Kurnia and van Groesen (2014). Preliminary tests demonstrate that both methods reproduce well both spilling and plunging waves, but several differences between the two methods are being explored, which suggest the use of the eddy viscosity model as the optimal approach.

First, the eddy viscosity model appears more accurate for cases with steeper beach slopes. This effect may be expected given the assumption that the breaking wave characteristics and energy dissipation can be related to that of a hydraulic bore (Guignard and Grilli, 2001), and the calibration coefficient $\mu = 1.5$ was determined from laboratory experiments of waves propagating across a flat bottom and up a gentle (1:35) slope (Svendsen et al., 1978).

Second, the wave energy dissipation mechanisms introduce additional terms in the free surface boundary conditions, which can cause the appearance of instabilities in the model. To avoid this problem, the pressure term is applied smoothly in space (with a bump function), while the eddy viscosity approach is applied smoothly in time with a ramp function.

3.7.2 Implementation of a moving shoreline

In order to simulate properly wave dynamics in the nearshore zone, it will be necessary to implement a moving shoreline in the numerical model. However, the numerical schemes used to resolve the vertical variations of the velocity potential in both the Misthyc and HCMS models are not easily extendable to extremely shallow water and to a moving shoreline approach. In the work of Christos Papoutsellis, in the test cases extending from deep to shallow water conditions (e.g. Figure 3.20), the numerical model becomes unstable when the water depth approaches very small values. Thus far, we have treated the nearshore zone and shoreline using a relaxation zone, and it will be necessary to explore other approaches that will represent properly the wave dynamics, including wave setup, runup, and reflection at the shoreline.

A variety of different methods have been proposed for treating a moving boundary in potential flow and Boussinesq-type models (e.g. moving slot, boundary extrapolation, Lagrangian regridding techniques), and the simplest and most direct method that may be applied in the current formulation follows the approach of Lynett et al. (2002) in extrapolating (e.g. η and $\tilde{\Phi}$) beyond the moving boundary. Using this approach, the shoreline is not restricted to fall on a specified grid point, nor are complex regridding techniques necessary. However, this type of scheme will cause numerical dissipation (Lynett et al., 2002) and will not conserve the Hamiltonian structure of the mathematical model. It will, however, allow tracking the shoreline position and simulation of nearshore dynamics once issues of the stability in the nearshore zone are resolved.

The approach of Lynett et al. (2002) is based on using a threshold δ_{min} for the total water depth $h + \eta$, below which the free surface position η and velocity potential $\tilde{\Phi}$ are extrapolated beyond the wet boundary. They defined the threshold as $\delta_{min} = a_0/50$, where a_0 is the initial wave amplitude. However, this threshold is likely strongly dependent on the given model, and will need to be studied in depth in the Misthyc model, in particular by looking at the convergence of the model as a function of the threshold δ_{min}.

Additional approaches that may be explored in collaboration with researchers in the LHSV include coupling the Misthyc model to a model solving the Navier Stokes equations to resolve fully the wave breaking processes and wave run-up in the (very) nearshore zone. Two possibilities to investigate are coupling Misthyc with a Volume of Fluid (VOF) model, Code Saturne, in collaboration with Jeffrey Harris, or pursuing the post-doctoral research of Jérémie Chicheportiche in coupling Misthyc with a SPH model in collaboration with Damien Violeau. However, these approaches may be unnecessary when considering only the accuracy of reproducing the moving shoreline, since Pedersen (2008) suggest that thin tongue swash and runup dynamics may be simple enough that even the shallow water equations are unnecessarily complicated.

3.7.3 Optimization of the model

During the thesis work of Cécile Raoult, the optimization of the model was achieved by implementing the parallel version of the direct linear solver MUMPS (Amestoy et al., 2001, 2006). In the current version of the Misthyc model, solving the linear system of equations is the process that takes more than 99% of the CPU time at each time step (Raoult, 2017), thus making it the most important step to optimize. Our initial work was focused simply on using the parallelized version of MUMPS, which was optimized by its developers for sparse, symmetric matrices such at the one solved in the 1DH version of the model. The system of equations that is solved in the 2DH version of the model is less sparse and has elements further from the diagonal. In addition, as the matrix size increases rapidly when transitioning from the 1DH to 2DH model, it is necessary to search for other methods, in particular iterative methods, requiring less memory to solve the linear system of equations.

During the Masters internship of D. Tasing (Tasing, 2016), a series of tests were conducted using the Hypre (for "high performance preconditioners") library developed by the National Lawrence Livermore Laboraotry (Falgout and Yang, 2002; Falgout et al., 2004) to explore solving the linear system of equations using an indirect method. A series of different combinations of preconditioners and indirect solvers were tested. The tests demonstrated the efficiency of the GMRES method in solving the matrix, and subsequent work focused on selecting the optimal preconditioner to pair with the GMRES iterative solver. The choice of a preconditioner has a significant impact on the efficiency of the GMRES method, and our tests compared the results obtained using Diagonal scaling, EUCLID, and BoomerAMG approaches (described in detail in HYPRE (2006)). For the case of a matrix with over 600,000 points and nearly 43 million non-zero entries in the matrix, using the ILU-BJ (Incomplete LU factorization - Block Jacobi) preconditioner with GMRES allowed reducing the CPU time by a factor of 25 in comparison with MUMPS (with a threshold of 10^{-5}). The results using the diagonal scaling preconditioner were nearly equivalent, and the conclusion of this work was that the implementation of either of these preconditioners with the GMRES iterative solver would allow optimizing the model CPU time.

These tests were conducted on matrices extracted from the Misthyc code, and current work includes integrating the Hypre library in the Fortran code of Misthyc and validating the accuracy and efficiency of this method in comparison to the MUMPS solver when propagating nonlinear waves during long time simulations. Additional methods that will be tested to optimize the model performance are:

- adapting a different temporal integration scheme, for example by replacing the fourth-order explicit Runge-Kutta scheme with a lower order scheme, or with an iterative approach that requires fewer resolutions of the system of linear equations (Laplace BVP problem, such as an Adams-Moulton or Adams-Bashworth predictor-corrector scheme (Shampine and Gordon, 1975). Finally, implicit methods could also be tested. However, implicit methods have the drawback of losing the Hamiltonian structure of the model, and simplectic methods (Feng, 1986) could be another more appropriate alternative to study.
- parallelizing not only the method used to solve the linear system of equations, but also the entire Misthyc code using domain decomposition. This was not yet implemented since the the pre-processing phase of the model and filling the matrix were shown to require a negligible amount of time for a test case with over 60,000 nodes (3% and $<$1% of the calculation time of one time step, respectively). As the matrix size increases, these calculation times will also increase, and thus work can be done to reduce their (still small) contribution to the total CPU time. These different approaches will be explored during the continued development of the Misthyc model to enable obtaining reasonable calculation times for simulating real applications of nearshore wave propagation.

3.7.4 Improvement of lateral boundary treatment

One well known issue strictly related to the implementation of the RBF-FD method is the treatment of non-symmetric stencils, in particular in the case of the lateral boundaries (Fornberg et al., 2002; Fornberg and Zuev, 2007). Raoult (2017) demonstrated that the errors in estimating derivatives near the boundaries can be one to two orders of magnitude larger than those for interior nodes (Figure 3.21) by distinguishing the errors estimated for three sets of nodes: interior nodes with a centered stencil, asymmetric stencils not located on the boundary (called asymmetric stencil nodes), and boundary nodes with a fully one-sided stencil (Figure 3.21).

Three different types of solutions may be proposed:

- edge enhancement techniques such as including low degree polynomials, node clustering near the boundaries, or Not-a-knot (Nak) and Super Not-a-knot (Snak) methods that allow moving RBF centers outside of the model domain (Fornberg et al., 2002);
- spatial variations in C for IS functions (Fornberg and Zuev, 2007); and
- addition of layers of nodes outside of the boundary, typically called ghost nodes, that allow enforcing both the boundary conditions and the PDE (partial differential equation) at the boundary nodes (e.g. Engsig-Karup et al., 2009).

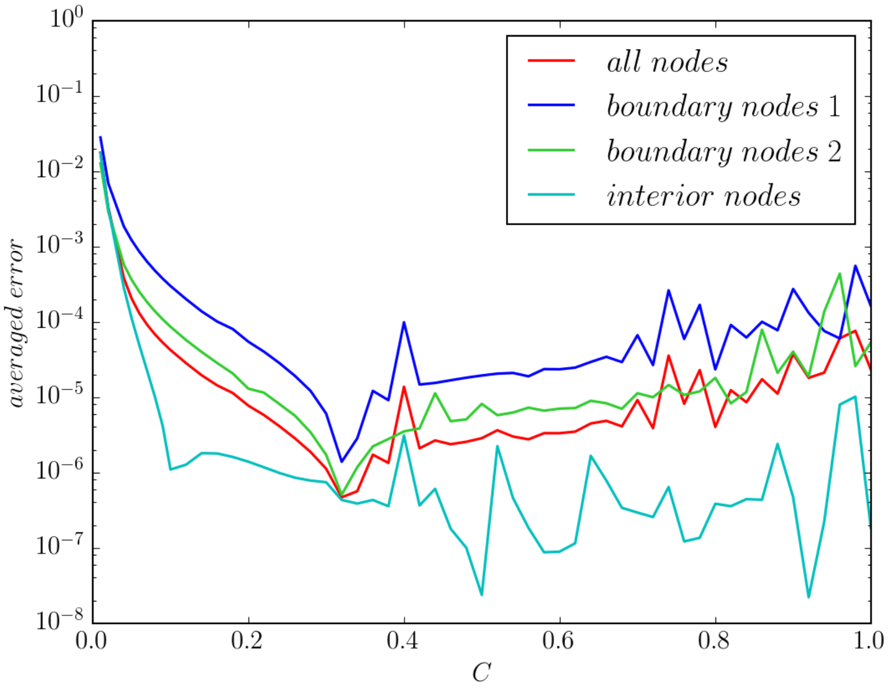

Figure 3.21: Normalized global errors for f_x as a function of the shape parameter C for a representative sinusoidal function (using a multiquadric (MQ) function with an added polynomial of degree 0 and a stencil size $N_{sten} = 21$): $f(x, y) = Acos\left(\frac{2\pi}{L}(x_c os\theta + y\sin\theta)\right)$, with $L = 0.5$ m, $A/L = 0.05$, and $\theta = 20$. The domain extended from $0 \leq x \leq 1,\ 0 \leq y \leq 1$, and was discretized with regularly-spaced nodes with $\Delta x = \Delta y = 0.005$ m ($= L/100$).

Future work will be focused primarily on edge enhancement techniques, in particular the use of a different RBF function or node clustering techniques near the boundaries. Preliminary tests carried out at the end of Cécile Raoult's thesis suggested that these approaches may enable reducing the errors near the model domain boundaries.

3.7.5 Comparison with existing wave propagation models

Finally, it is important to demonstrate the ability of the model to simulate well wave propagation in the nearshore zone in comparison to field observations and to other existing wave models. To demonstrate the accuracy and efficiency of the Misthyc model, it will be important to compare the simulation results to other nonlinear wave propagation models such as Boussinesq or SGN-type models (e.g. BOSZ, FUNWAVE, UHAINA, Roeber et al., 2010; Roeber and Cheung, 2012; Kirby et al., 1998; Shi et al., 2012; Filippini et al., 2018), HOS methods (e.g. HOS-ocean, Ducrozet et al., 2012; Gouin et al., 2016), and multi-layer non-hydrostatic models (e.g. SWASH, Zijlema and Stelling, 2008; Zijlema et al., 2011), including the accuracy of the simulations and the computational time required. These comparisons will be important to demonstrate both the advantages and limitations of the selected modeling approaches in order to define the optimal tools to be used for different modeling applications. Within the ANR-FEM DiMe project, Volker Roeber and I currently participate in the thesis committee of a PhD student Audrey Varing, advised by Jean-François Filipot (FEM). In our ongoing collaborative work, we plan to compare the results of Misthyc and BOSZ (Boussinesq-type wave propagation model (Roeber et al., 2010)). This work will therefore encourage the development of collaborations with researchers working on closely related subjects in this field, both externally and within the LHSV.

Chapter 4

Conclusions

In summary, in the coming years, I will continue to develop two principal research themes: coastal morphological evolution and coastal wave hydrodynamics. Throughout the last decade since completing my PhD, I have centered my work on these two themes, exploring a variety of different approaches spanning observational, experimental, empirical, and numerical work.

The fundamental research questions identified here are centered on improving understanding of the physical processes controlling wave propagation and beach morphological evolution, and improving our ability to model these processes at the desired spatial and temporal scales for a wide range of applications.

The main challenges associated with empirical beach morphological modeling are related to how to simplify the complex dynamics of the nearshore zone to develop models that are capable of efficiently and reliably predicting beach morphological response to wave forcing. I plan to focus on taking into account alongshore sediment transport processes, the interactions between wave forcing and the water (or tide) level, and the inherent uncertainties in this simple modeling approach. This work will continue to be the focus of ongoing collaborations with researchers from the IUEM, as well as with 3 research groups in Japan within the PHC Sakura project. In addition, the extension of the equilibrium shoreline change model is the topic of the PhD thesis of Teddy Chataigner (2018-2020), several Masters internships, and future collaborations currently being initiated with research teams abroad, such as with Camilo Jaramillo Cardona from the University of Cantabria who is working on coupling cross-shore and alongshore sediment transport in medium to long-term morphological models, and Giovanni Coco and Jennifer Montano at the University of Auckland who are working on coupling dune evolution with equilibrium models.

Concerning coastal wave hydrodynamics, my work is focused on the development of a highly accurate nonlinear and dispersive wave propagation model using fully nonlinear potential flow theory. The objective of this project is to develop a highly accurate and efficient wave propagation model that is applicable for practical applications in the coastal zone. The fundamental research questions are centered on the improvement of the representation of complex physical processes such as wave breaking and viscous effects, and on the optimal numerical implementation to solve this system of equations (Zakharov equations plus boundary conditions) for 2D and 3D domains. This work is currently being carried out in the ANR-FEM DiMe project and is part of a long-term collaboration with Michel Benoit, who is now working at the IRPHE. These activities could benefit from ongoing collaborations with colleagues working in the DiMe project, who focus on wave breaking in Boussinesq and spectral wave models, as well as future collaborations with colleagues in the LHSV laboratory, who focus on coupling potential flow and RANS models.

Finally, I plan to continue to develop these two research themes and the links between these two fields of study. In particular, the Misthyc model will be used to simulate wave propagation in the nearshore zone, both by reproducing the hydrodynamics of the laboratory experiments of storm-induced beach erosion discussed in section 2.2.3 and by analyzing the transformation of waves from deep to shallow water at the Porsmilin and Vougot study sites evaluated in section 2.2.4. This work will allow a more in-depth study of the wave hydrodynamics in relation to the observed morphological changes, as well as an analysis of the sensitivity of morphological change models to the wave forcing conditions.

In addition to my research projects described in this manuscript, Appendix A provides an overview of my academic and project responsibilities, and Appendix B presents my curriculum vitae, which includes a detailed summary of my presented and published work. Following my responsibilities as a researcher at the Cerema, I will continue to focus on fundamental research questions in these two fields and also on practical applications to meet operational needs.

Bibliography

D. Adytia, S. Husrin, and Adiwijaya, Kang. Numerical simulation of breaking regular and irregular wave propagation above a sloping bottom. *Journal of Physics: Conference Series*, 1090: 012065, 2018.

Y. Agnon, P. A. Madsen, and H. A. Schäffer. A new approach to high-order Boussinesq models. *J. Fluid Mech.*, 399:319–333, 1999.

P. R. Amestoy, I. S. Duff, J. Koster, and J.-Y. L'Excellent. A fully synchronous multifrontal solver using distributed dynamic scheduling. *SIAM J. of Matrix Anal. and Appl.*, 23(1):15–41, 2001.

P. R. Amestoy, A. Guermouche, J.-Y. L'Excellent, and S. Pralet. Hybrid scheduling for the parallel solution of linear systems. *Parallel Computing*, 32:136–156, 2006.

T. R. Anderson, C. H. Fletcher, M. M. Barbee, L. N. Frazer, and B. M. Romine. Doubling of coastal erosion under rising sea level by mid-century in Hawaii. *Natural Hazards*, 78:75–103, 2015.

S. Andréfouët, M. Claereboudt, P. Matsakis, J. Pagès, and P. Dufour. Typology of atoll rims in Tuamotu Archipelago (French Polynesia) at landscape scale using SPOT HRV images. *Int. J. Remote Sensing*, 22(6):987–1004, 2001.

E. J. Anthony. Sediment-wave parametric characterization of beaches. *J. Coastal Res.*, 14(1): 347–352, 1998.

M. Antuono and A. Colagrossi. The damping of viscous gravity waves. *Wave Motion*, 50:197–209, 2013.

F. Ardhuin, E. Rogers, A. V. Babanin, J.-F. Filipot, R. Magne, A. Roland, A. van der Westhuysen, P. Queffeulou, J.-M. Lefevre, L. Aouf, and F. Collard. Semiempirical dissipation source functions for ocean waves, Part I: Definition, calibration, and validation. *J. Phys. Ocean.*, 40:1917–1941, 2010.

A. Ashton, A. B. Murray, and O. Arnoult. Formation of coastline features by large-scale instabilities induced by high-angle waves. *Nature*, 414:296–300, 2001.

A. D. Ashton and A. B. Murray. High-angle wave instability and emergent shoreline shapes: 1. modeling of sand waves, flying spits, and capes. *Journal of Geophysical Research: Earth Surface*, 111(F4), 2006.

G. A. Athanassoulis and K. A. Belibassakis. A consistent coupled-model theory for the propagation of small-amplitude water waves over variable bathymetry regions. *J. Fluid Mech.*, 389: 275–301, 1999.

G. A. Athanassoulis and C. Papoutsellis. New form of the Hamiltonian equations for the nonlinear water-wave problem, based on a new representation of the DtN operator, and some applications. In *Procedings of the 34th International Conference on Ocean, Offshore and Arctic Engineering*, St John's, Newfoundland, Canada, 2015.

A. Aubanel, N. Marquet, J. M. Colombani, and B. Salvat. Modifications of the shore line in the Society islands (French Polynesia). *Ocean and Coastal Management*, 42:419–438, 1999.

D. G. Aubrey. Seasonal patterns of onshore/offshore sediment movement. *Journal of Geophysical Research: Oceans*, 84(C10):6347–6354, 1979.

R. A. Bagnold. Beach formation by waves: Some model experiments in a wave tank (includes photographs). *Journal of the Institution of Civil Engineers*, 15(1):27–52, 1940.

M. Banno and Y. Kuriyama. Prediction of future shoreline change with sea-level rise and wave climate change at Hasaki, Japan. *Coastal Engineering Proceedings*, 1(34):56, 2014.

G. Barnett. *A Robust RBF-FD Formulation based on Polyharmonic Splines and Polynomials.* PhD thesis, University of Colorado, 2015.

X. Barthelemy, M. L. Banner, W. L. Peirson, F. Fedele, M. Allis, and F. Dias. On a unified breaking onset threshold for gravity waves in deep and intermediate depth water. *J. Fluid Mech.*, 841: 463–488, 2018.

W. N. Bascom. The relationship between sand size and beach-face slope. *Transactions, American Geophysical Union*, 32(6):866–874, 1951.

T. Bayes. LII. An essay towards solving a problem in the doctrine of chances. By the late Rev. Mr. Bayes, F. R. S. communicated by Mr. Price, in a letter to John Canton, A. M. F. R. S. *Philosophical Transactions of the Royal Society of London*, 53:370–418, 1763.

V. Bayona, M. Moscoso, and M. Kindelan. Optimal constant shape parameter for multiquadric based RBF-FD method. *J. Comp. Physics*, 230:7384–7399, 2011.

A. Bayram, M. Larson, H. C. Miller, and N. C. Kraus. Performance of longshore sediment transport formulas evaluated with field data. In *Coastal Engineering 2000*, pages 3114–3127. American Society of Civil Engineers, 2001.

A. Bayram, M. Larson, and H. Hanson. A new formula for the total longshore sediment transport rate. *Coastal Engineering*, 54(9):700 – 710, 2007.

M. Becker, B. Meyssignac, C. Letetrel, W. Llovel, A. Cazenave, and T. Delcroix. Sea level variations at tropical Pacific islands since 1950. *Global and Planetary Change*, 80-81:85–98, 2012.

F. Becq-Girard, P. Forget, and M. Benoit. Non-linear propagation of unidirectional wave fields over varying topography. *Coast. Eng.*, 38:91–113, 1999.

S. Beji and J. A. Battjes. Experimental investigation of wave propagation over a bar. *Coast. Eng.*, 19:151–162, 1993.

K. Belibassakis, G. Athanassoulis, and T. Gerostathis. Directional wave spectrum transformation in the presence of strong depth and current inhomogeneities by means of coupled-mode model. *Ocean Engineering*, 87:84 – 96, 2014.

K. A. Belibassakis and G. A. Athanassoulis. A coupled-mode system with application to nonlinear water waves propagating in finite water depth and in variable bathymetry regions. *Coast. Eng.*, 58:337–350, 2011.

N. A. Berard, R. P. Mulligan, A. M. F. da Silva, and M. Dibajnia. Evaluation of XBeach performance for the erosion of a laboratory sand dune. *Coastal Engineering*, 125:70 – 80, 2017.

J. O. Berger. Bayesian Analysis: A look at today and thoughts of tomorrow. *Journal of the American Statistical Association*, 95(452):1269–1276, 2000.

J. Berkhoff. Computation of combined refraction - diffraction. *Coastal Engineering Proceedings*, 1(13):23, 1972.

A. Bernabeu, R. Medina, and C. Vidal. A morphological model of the beach profile integrating wave and tidal influences. *Marine Geology*, 197(1):95 – 116, 2003.

H. B. Bingham and H. Zhang. On the accuracy of finite-difference solutions for nonlinear water waves. *J. Eng. Math*, 58:211–228, 2007.

E. C. F. Bird. *Sea Level Rise and Coastal Subsidence*, chapter Coastal erosion and rising sea level, pages 87–103. Kluwer Academic Publishers, Dordrecht, the Netherlands, 1996.

E. H. Boak and I. L. Turner. Shoreline definition and detection: A review. *Journal of Coastal Research*, 21(4):688–703, 2005.

A. Bolle, P. Mercelis, D. Roelvink, P. Haerens, and K. Trouw. Application and validation of XBeach for three different field sites. *Coastal Engineering Proceedings*, 1(32):40, 2011.

P. Bonneton, E. Barthelemy, F. Chazel, R. Cienfuegos, D. Lannes, F. Marche, and M. Tissier. Recent advances in Serre–Green Naghdi modelling for wave transformation, breaking and runup processes. *European Journal of Mechanics - B/Fluids*, 30(6):589 – 597, 2011.

F. Bouchette, M. Manna, P. Montalvo, A. Nutz, M. Schuster, and J.-F. Ghienne. Growth of cuspate spits. *Journal of Coastal Research*, pages 47–52, Apr. 2014.

G. Bouvard. Analyse morphodynamique et application d'un modèle d'équilibre de plage en milieu macrotidal. Master's thesis, Institut Universitaire Européen de la Mer – Laboratoire Géosciences Océan, Plouzané, France, 2017.

J. P. Boyd. *Chebyshev and Fourier Spectral Methods: Second Edition, Revised.* Dover Publications, Mineaola, NY, USA, 2001.

A. Bradbury, S. Cope, C. Wilkinson, and T. Mason. Regional patterns of changing beach morphology at a decadal scale. *Journal of Coastal Research*, 65(sp1):452 – 457 – 6, 2013.

O. T. Brenner, E. E. Lentz, C. J. Hapke, R. E. Henderson, K. E. Wilson, and T. R. Nelson. Characterizing storm response and recovery using the beach change envelope: Fire Island, New York. *Geomorphology*, 300:189 – 202, 2018.

M. Brocchini. A reasoned overview on Boussinesq-type models: the interplay between physics, mathematics and numerics. *Proceedings of the Royal Society of London A: Mathematical, Physical and Engineering Sciences*, 469(2160), 2013.

M. Brocchini and N. Dodd. Nonlinear shallow water equation modeling for coastal engineering. *Journal of Waterway, Port, Coastal, and Ocean Engineering*, 134(2):104–120, 2008.

M. B. Brommer and L. M. B. van der Burgh. Sustainable coastal zone management: A concept for forecasting long-term and large-scale coastal evolution. *Journal of Coastal Research*, 2009 (251):181 – 188 – 8, 2009.

P. Bruun. Coastal erosion and development of beach profiles. Technical Memorandum No. 44, U.S. Army Corps of Engineers, Washington, 1954.

P. Bruun. Sea-level rise as a cause of shoreline erosion. *J. Waterways and Harbours Division*, 88 (1-3):117–130, 1962.

H. Burningham and J. French. Understanding coastal change using shoreline trend analysis supported by cluster-based segmentation. *Geomorphology*, 282:131 – 149, 2017.

D. P. Callahan, P. Nielsen, N. Cartwright, M. R. Gourlay, and T. E. Baldock. Atoll lagoon flushing forced by waves. *Coast. Eng.*, 53:691–704, 2006.

B. Castelle, P. Bonneton, H. Dupuis, and N. Sénéchal. Double bar beach dynamics on the high-energy meso-macrotidal French Aquitanian coast: A review. *Marine Geology*, 245(1):141 – 159, 2007.

B. Castelle, V. Marieu, S. Bujan, S. Ferreira, J.-P. Parisot, S. Capo, N. Sénéchal, and T. Chouzenoux. Equilibrium shoreline modelling of a high-energy meso-macrotidal multiple-barred beach. *Marine Geology*, 347:85–94, 2014.

C. Caulet, F. Floc'h, N. L. Dantec, M. Jaud, E. Augereau, F. Ardhuin, and C. Delacourt. Wave setup variations along a cross-shore profile of a macrotidal sandy embayed beach, Porsmilin, Brittany, France. In *Proceedings Coastal Dynamics*, pages 168–179, Helsingor, Denmark, 2017.

P. G. Chamberlain and D. Porter. The modified mild-slope equation. *Journal of Fluid Mechanics*, 291:393–407, 1995.

G. Chapalain, R. Cointe, and A. Temperville. Observed and modeled resonantly interacting progressive water-waves. *Coast. Eng.*, 16:267–300, 1992.

J. R. Chaplin. Developments of Stream-Function wave theory. *Coast. Eng.*, 3:179–205, 1980.

F. Chazel, M. Benoit, A. Ern, and S. Piperno. A double-layer Boussinesq-type model for highly nonlinear and dispersive waves. *Proc. R. Soc. A*, 465:2319–2346, 2009.

Q. Chen, P. A. Madsen, H. A. Schäffer, and D. R. Basco. Wave-current interaction based on an enhanced Boussinesq approach. *Coastal Engineering*, 33(1):11 – 39, 1998.

Q. Chen, J. T. Kirby, R. A. Dalrymple, A. B. Kennedy, and A. Chawla. Boussinesq modeling of wave transformation, breaking, and runup. II: 2D. *Journal of Waterway, Port, Coastal, and Ocean Engineering*, 126(1):48–56, 2000.

M. J. Chern, A. G. L. Borthwick, and R. Eatock Taylor. A pseudospectral σ-transformation model of 2-D nonlinear waves. *J. Fluids Structures*, 13:607–630, 1999.

R. Cienfuegos, E. Barthélemy, and P. Bonneton. Wave-breaking model for Boussinesq-type equations including roller effects in the mass conservation equation. *Journal of waterway, port, coastal, and ocean engineering*, 136(1):10–26, 2010.

D. Clamond and D. Dutykh. Fast accurate computation of the fully non linear solitary surface gravity waves. *Computers & Fluids*, 84:35–38, 2013.

D. Clamond and J. Grue. A fast method for fully nonlinear water-wave computations. *J. Fluid Mech.*, 447:337–355, 2001.

A. Clément. Coupling of two absorbing boundary conditions for 2D time-domaine simulations of free surface gravity waves. *J. Comp. Phys.*, 126:139–151, 1996.

P. Cobelli, A. Maurel, V. Pagneux, and P. Petitjeans. Global measurement of water waves by Fourier Transform Profilometry. *Exp. Fluids*, 46:1037–1047, 2009.

G. Coco, N. Senechal, A. Rejas, K. Bryan, S. Capo, J. Parisot, J. Brown, and J. MacMahan. Beach response to a sequence of extreme storms. *Geomorphology*, 204:493 – 501, 2014.

C. Coelho, R. Silva, F. V. Gomes, and F. T. Pinto. A vulnerability analysis approach for the Portuguese West Coast. *Transactions of the Wessex Institute*, page 12, 2006.

J. A. G. Cooper and S. McLaughlin. Contemporary multidisciplinary approaches to coastal classification and environmental risk analysis. *J. Coast. Res.*, 14(2):512–524, 1998.

N. R. Council. *Managing Coastal Erosion.* The National Academies Press, Washington, DC, 1990.

P. J. Cowell, M. J. F. Stive, A. W. Niedoroda, H. J. de Vriend, D. J. P. Swift, G. M. Kaminsky, and M. Capobianco. The Coastal-Tract (Part 1): A conceptual approach to aggregated modeling of low-order coastal change. *Journal of Coastal Research*, 19(4):812–827, 2003.

W. Craig and C. Sulem. Numerical simulation of gravity waves. *Journal of Computational Physics*, 108(1):73 – 83, 1993.

CREOCEAN. Conséquences de l'élévation du niveau de la mer sur l'atoll de Rangiroa [consequences of sea level rise for the rangiroa atoll]. Report for the Ministry of the Environment No. 42119, CREOCEAN, La Rochelle, France, 1995.

F. D'Alessandro and G. R. Tomasicchio. The BCI criterion for the initiation of breaking process in Boussinesq-type equations wave models. *Coastal Engineering*, 55(12):1174–1184, 2008.

R. A. Dalrymple. Prediction of storm/normal beach profiles. *J. Wat., Port, Coast, Ocean Eng.*, 118: 193–200, 1992.

R. A. Dalrymple and B. D. Rogers. Numerical modeling of water waves with the SPH method. *Coast. Eng.*, 53:141–147, 2006.

C. Daly, F. Floc'h, L. P. Almeida, and R. Almar. Modelling accretion at Nha Trang Beach, Vietnam. In *Proceedings Coastal Dynamics*, pages 1886–1896, Helsingor, Denmark, 2017.

R. C. Daniels, V. M. Gornitz, A. J. Mehta, L. Say-Chong, and R. M. Cushman. Adapting to sea-level rise in the U.S. Southeast: The influence of built infrastructure and biophysical factors on the inundation of coastal areas. Ornl/cdiac-54, Environmental Science Division, U.S. Department of Energy, Oak Ridge, Tennessee, 1992.

M. Davidson and I. Turner. A behavioral template beach profile model for predicting seasonal to interannual shoreline evolution. *Journal of Geophysical Research: Earth Surface*, 114(F1), 2009.

M. Davidson, R. Lewis, and I. Turner. Forecasting seasonal to multi-year shoreline change. *Coastal Engineering*, 57(6):620–629, 2010.

M. Davidson, K. Splinter, and I. Turner. A simple equilibrium model for predicting shoreline change. *Coastal Engineering*, 73:191–202, 2013.

M. A. Davidson, I. L. Turner, K. D. Splinter, and M. D. Harley. Annual prediction of shoreline erosion and subsequent recovery. *Coastal Engineering*, 130:14 – 25, 2017.

R. G. D. Davidson-Arnott. Conceptual model of the effects of sea level rise on sandy coasts. *Journal of Coastal Research*, 216:1166–1172, 2005.

J. L. Davies. A morphogenic approach to world shorelines. *Zeitschrift fur Geomorphologie*, 8: 127–142, 1964.

R. A. Davis and M. O. Hayes. What is a wave-dominated coast? *Marine Geology*, 60(1):313 – 329, 1984.

M. De Carlo. Érosion de plage protégée par des structures immergées lors de tempêtes : Validation du modèle XBeach. Master's thesis, ENSTA ParisTech, 2017.

H. de Vriend, M. Capobianco, T. Chesher, H. de Swart, B. Latteux, and M. Stive. Approaches to long-term modelling of coastal morphology: A review. *Coastal Engineering*, 21(1):225 – 269, 1993.

H. de Vriend, J. Zyserman, J. Nicholson, P. Pechon, J. Roelvink, and H. Southgate. Medium-term 2DH coastal area modelling. *Coastal engineering*, 21(1-3):193–224, 1993.

R. Dean and J. Houston. Determining shoreline response to sea level rise. *Coastal Engineering*, 114:1 – 8, 2016.

R. G. Dean. *Equilibrium beach profiles: US Atlantic and Gulf coasts.* Department of Civil Engineering and College of Marine Studies, University of Delaware, 1977.

R. G. Dean and R. Dalrymple. *Water Wave Mechanics for Engineers and Scientists.* World Scientific Publishing, 1991.

A. Dehouck, H. Dupuis, and N. Sénéchal. Pocket beach hydrodynamics: The example of four macrotidal beaches, Brittany, France. *Marine Geology*, 266(1):1 – 17, 2009.

R. Deigaard. Mathematical modelling of waves in the surf zone. Prog. report 69. ISVA, Technical University of Denmark, Lyngby, Denmark, 1989.

L. Deike, W. K. Melville, and S. Popinet. Air entrainment and bubble statistics in breaking waves. *J. Fluid Mech.*, 801:91–129, 2016.

F. Dias, A. Dyachenko, and V. Zakharov. Theory of weakly damped free-surface flows: A new formulation based on potential flow solutions. *Physics Letters*, A 372:1297–1302, 2008.

W. R. Dickinson. Holocene sea-level record on Funafuti and potential impact of global warming on Central Pacific atolls. *Quaternary Research*, 51:124–132, 1999.

M. Dingemans. Comparison of computations with Boussinesq-like models and laboratory measurements. Mast-G8M technical report, Delft Hydraulics, Delft, The Netherlands, 1994.

M. W. Dingemans. *Water wave propagation over uneven bottoms. Part1 - Linear wave propagation.* World Scientific Publishing, 1997. Advanced Series on Ocean Engineering, Volume 13.

G. Dodet, B. Castelle, G. Masselink, T. Scott, M. Davidson, F. Floc'h, D. Jackson, and S. Suanez. Beach recovery from extreme storm activity during the 2013–14 winter along the Atlantic coast of Europe. *Earth Surface Processes and Landforms*, 44(1):393–401, 2019.

D. G. Dommermuth and D. K. P. Yue. A high-order spectral method for the study of nonlinear gravity waves. *J. Fluid Mech.*, 184:267–288, 1987.

A. V. Dongeren, R. Lowe, A. Pomeroy, D. M. Trang, D. Roelvink, G. Symonds, and R. Ranasinghe. Numerical modeling of low-frequency wave dynamics over a fringing coral reef. *Coastal Engineering*, 73:178 – 190, 2013.

A. Doria, R. T. Guza, W. C. O'Reilly, and M. L. Yates. Observations and modeling of San Diego beaches during El Niño. *Cont. Shelf Res.*, 124:153–164, 2016.

E. Doukakis. Coastal red spots along the western Thermaikos Gulf. In *Proc. 9th Conf. Env. Sci. Tech.*, page 6, Rhodes island, Greece, 2005.

R. N. Dubois. Seasonal changes in beach topography and beach volume in Delaware. *Marine Geology*, 81(1):79 – 96, 1988.

R. N. Dubois. Barrier-beach erosion and rising sea level. *Geology*, 18:1150–1152, 1990.

G. Ducrozet, F. Bonnefoy, D. Le Touzé, and P. Ferrant. 3-D HOS simulations of extreme waves in open seas. *Natural Hazards and Earth System Science*, 7(1):109–122, 2007.

G. Ducrozet, F. Bonnefoy, D. Le Touzé, and P. Ferrant. A modified High-Order Spectral method for wavemaker modeling in a numerical wave tank. *Euro. J. Mecha. B/ Fluids*, 34:19–34, 2012.

D. Dutykh and F. Dias. Viscous potential free-surface flows in a fluid layer of finite depth. *C.R. Acad. Sci. Paris*, 345:113–118, 2007.

A. P. Engsig-Karup, H. B. Bingham, and O. Lindberg. An efficient flexible-order model for 3D nonlinear water waves. *J. Comp. Phys.*, 228:2100–2118, 2009.

EUROSION. Living with coastal erosion in Europe: Sediment and Space for Sustainability, Part IV - a guide to coastal erosion management practices in europe: Lessons learned. Technical Report 27 p, European Commission, 2004.

R. D. Falgout and U. M. Yang. *hypre*: A Library of High Performance Preconditioners. In P. Sloot, A. Hoekstra, C. Tan, and J. Dongarra, editors, *Computational Science — ICCS 2002. ICCS 2002. Lecture Notes in Computer Science*, volume 2331, pages 632–641. Springer, Berlin, Heidelberg, 2002.

R. D. Falgout, J. E. Jones, and U. M. Yang. The design and implementation of *hypre*, a library of parallel high performance preconditioners. In A. M. Bruaset and A. Tveito, editors, *Numerical Solution of Partial Differential Equations on Parallel Computers*, pages 267–294. Springer, 2004.

A. S. Farris and J. H. List. Shoreline change as a proxy for subaerial beach volume change. *J. Coast. Res.*, 23(3):740–748, 2007.

K. Feng. Difference schemes for Hamiltonian formalism and symplectic geometry. *J. Comput. Math.*, 4(3):279–289, 1986.

M. S. Fenster, R. Dolan, and R. A. Morton. Coastal storms and shoreline change: Signal or noise? *Journal of Coastal Research*, 17(3):714–720, 2001.

A. G. Filippini, S. de Brye, V. Perrier, F. Marche, M. Ricchuito, D. Mannes, and P. Bonneton. UHAINA : A parallel high performance unstructured near-shore wave model. In *Procedings XVèmes Journées Nationales Génie Côtier – Génie Civil*, La Rochelle, France, 2018.

C. Fochesato, S. T. Grilli, and F. Dias. Numerical modeling of extreme rogue waves generated by directional energy focusing. *Wave Motion*, 44:395–416, 2007.

M. Ford. Shoreline changes on an urban atoll in the Central Pacific Ocean: Majuro Atoll, Marshall Islands. *Journal of Coastal Research*, 28(1):11–22, 2012.

B. Fornberg. Generation of finite difference formulas on arbitrarily spaced grids. *Mathematics of Computation*, 51(184):699–706, 1988.

B. Fornberg and J. Zuev. The Runge phenomenon and spatially variable shape parameters in RBF interpolation. *Comp. Math. Applic.*, 54:379–398, 2007.

B. Fornberg, T. A. Driscoll, G. Wright, and R. Charles. Observation on the behaviour of radial basis function approximation near boundaries. *Comp. Math. Applic.*, 43:473–490, 2002.

R. Franke. Scattered Data Interpolation: Tests of Some Methods. *Math. Comp*, 38:181–200, 1982.

J. French, A. Payo, B. Murray, J. Orford, M. Eliot, and P. Cowell. Appropriate complexity for the prediction of coastal and estuarine geomorphic behaviour at decadal to centennial scales. *Geomorphology*, 256:3 – 16, 2016.

D. Fructus, D. Clamond, J. Grue, and Ø. Kristiansen. An efficient model for three-dimensional surface wave simulations: Part I: Free space problems. *J. Comp. Phys.*, 205:665–685, 2005.

D. R. Fuhrman and P. A. Madsen. Tsunami generation, propagation, and run-up with a high-order Boussinesq model. *Coast. Eng.*, 56:747–758, 2009.

D. R. Fuhrman, H. B. Bingham, and P. A. Madsen. Nonlinear wave-structure interactions with a high-order Boussinesq model. *Coast. Eng.*, 52:655–672, 2005.

J. C. Galland, N. Goutal, and J.-M. Hervouet. TELEMAC: A new numerical model for solving shallow water equations. *Adv. Water Resources*, 14(3):138–148, 1991.

M. Garcin, M. Yates, G. Le Cozannet, P. Walker, and V. Donato. Sea level rise and coastal morphological changes on tropical islands: example from New Caledonia and French Polynesia (SW Pacific). In *Geophysical Research Abstracts, 13*, 13, page 3504. EGU2011, 2011.

M. Garcin, A. Baills, G. Le Cozannet, T. Bulteau, A.-L. Auboin, and J. Sauter. Pluri-decadal impact of mining activities on coastline mobility of estuaries of New Caledonia (South Pacific). *Journal of Coastal Research*, 65(SIv1):494–499, 2013.

M. Garcin, M. Vendé-Leclerc, P. Maurizot, G. L. Cozannet, B. Robineau, and A. Nicolae-Lerma. Lagoon islets as indicators of recent environmental changes in the South Pacific – the New Caledonian example. *Continental Shelf Research*, 122:120 – 140, 2016.

M. Gervais, D. Pham Van Bang, V. Vidal, M. Yates, and M. Benoit. Protection anti-érosion de plages par utilisation du procédé Géocorail SAS : étude de faisabilité par expérimentation sur modèle réduit. Technical report, Cerema, 2014.

M. Gervais, D. Pham Van Bang, V. Vidal, M. Yates, and M. Benoit. Réduire l'érosion des plages lors des tempêtes grâce à des structures immergées : une étude expérimentale comparative en canal à houle. In *Proc. GCGC*, page 9, Toulon, France, 2016.

E. Goldstein, G. Coco, and N. G. Plant. A review of machine learning applications to coastal sediment transport and morphodynamics. *EarthArXiv online*, page 43, 2018.

V. M. Gornitz, R. C. Daniels, T. W. White, and K. R. Birdwell. The development of a coastal risk assessment database: Vulnerability to sea-level rise in the U.S. Southeast. *J. Coast. Res.*, 12: 327–338, 1994.

V. M. Gornitz, T. M. Beaty, and R. C. Daniels. A coastal hazards data base for the U.S. West Coast. Ornl/cdiac-81, ndp-043c, Oak Ridge National Laboratory, 1997.

M. Gouin, G. Ducrozet, and P. Ferrant. Validation of a nonlinear spectral model for water waves over a variable bathymetry. In *30th International Workshop on Water Waves and Floating Bodies*, Bristol, UK, 4 p., 2015.

M. Gouin, G. Ducrozet, and P. Ferrant. Development and validation of a non-linear spectral model for water waves over variable depth. *Euro. J. Mecha. B/ Fluids*, 57:115–128, 2016.

F. Grasso, H. Michallet, E. Barthélemy, and R. Certain. Physical modeling of intermediate cross-shore beach morphology: Transients and equilibrium states. *Journal of Geophysical Research: Oceans*, 114(C9), 2009.

S. T. Grilli and J. Horrillo. Shoaling of periodic waves over barred-beaches in a fully nonlinear numerical wave tank. *Int. J. Offshore Polar Eng*, 9(4):257–263, 1999.

S. T. Grilli, J. Skourup, and I. A. Svendsen. An efficient boundary element method for nonlinear water waves. *Eng. Anal. Bound. Elem.*, 6(2):97–107, 1989.

S. T. Grilli, P. Guyenne, and F. Dias. A fully non-linear model for three-dimensional overturning waves over an arbitrary bottom. *International Journal for Numerical Methods in Fluids*, 35(7): 829–867, 2001.

D. J. Grimes, N. Cortale, K. Baker, and D. E. McNamara. Nonlinear forecasting of intertidal shoreface evolution. *Chaos: An Interdisciplinary Journal of Nonlinear Science*, 25(10):103116, 2015.

S. Guignard and S. Grilli. Modeling of wave shoaling in a 2D-NWT using a spilling breaker model. In *Proceedings of the 11th ISOPE*, pages 116–123, Stavanger, Norway, 2001.

B. T. Gutierrez, N. G. Plant, and E. R. Thieler. A Bayesian network to predict coastal vulnerability to sea level rise. *Journal of Geophysical Research: Earth Surface*, 116(F2), 2011.

P. Guyenne and D. P. Nicholls. A high-order spectral method for nonlinear water waves over moving bottom topography. *SIAM J. Sci. Comput.*, 30(1):81–101, 2007.

R. J. Hallermeier. A profile zonation for seasonal sand beaches from wave climate. *Coastal Engineering*, 4:253 – 277, 1980. ISSN 0378-3839.

J. L. Hammack. A note on tsunamis: their generation and propagation in an ocean of uniform depth. *J. Fluid Mech.*, 60(4):769–799, 1973.

K. Hamon. Étude de la morphodynamique et du profil d'équilibre d'une plage de poche macrotidale. Master's thesis, Laboratoire Géosciences Océan UMR6538 IUEM/UBO, 2014.

H. Hanson, S. Aarninkhof, M. Capobianco, J. A. Jiménez, M. Larson, R. J. Nicholls, N. G. Plant, H. N. Southgate, H. J. Steetzel, M. J. F. Stive, and H. J. de Vriend. Modelling of coastal evolution on yearly to decadal time scales. *Journal of Coastal Research*, 19(4):790–811, 2003.

C. Hapke and N. Plant. Predicting coastal cliff erosion using a Bayesian probabilistic model. *Mar. Geol.*, 278:140–149, 2010.

C. J. Hapke, D. Reid, and B. Richmond. Rates and trends of coastal change in California and the regional behavior of the beach and cliff system. *Journal of Coastal Research*, pages 603–615, 2009.

C. J. Hapke, N. G. Plant, R. Henderson, W. C. Schwab, and T. R. Nelson. Decoupling processes and scales of shoreline morphodynamics. *Marine Geology*, 381:42 – 53, 2016.

R. L. Hardy. Multiquadric equation of topography and other irregular surfaces. *J. Geophys. Res.*, 76:1905–1915, 1971.

M. D. Harley, I. L. Turner, A. D. Short, and R. Ranasinghe. A reevaluation of coastal embayment rotation: The dominance of cross-shore versus alongshore sediment transport processes, collaroy-narrabeen beach, southeast australia. *Journal of Geophysical Research: Earth Surface*, 116(F4), 2011.

M. D. Harley, I. L. Turner, M. A. Kinsela, J. H. Middleton, P. J. Mumford, K. D. Splinter, M. S. Phillips, J. A. Simmons, D. J. Hanslow, and A. D. Short. Extreme coastal erosion enhanced by anomalous extratropical storm wave direction. *Oceanography and Maritime Engineering*, 7(1): 6033, 2017.

M. L. Harmelin-Vivien and P. Laboute. Catastrophic impact of hurricanes on atoll outer reef slopes in the Tuamotu (French Polynesia). *Coral Reefs*, 5:55–62, 1986.

K. L. Heitner and G. W. Housner. Numerical model for tsunami run-up. *ASCE J. Waterway Harbors Coastal Eng. Div.*, 96:701–719, 1970.

A. Hibma, H. de Vriend, and M. Stive. Numerical modelling of shoal pattern formation in well-mixed elongated estuaries. *Estuarine, Coastal and Shelf Science*, 57(5):981 – 991, 2003.

P. Higuera, J. L. Lara, and I. J. Losada. Realistic wave generation and active wave absorption for Navier-Stokes Application to OpenFOAM®. *Coast. Eng.*, 71:102–118, 2013a.

P. Higuera, J. L. Lara, and I. J. Losada. Simulating coastal engineering processes with OpenFOAM®. *Coast. Eng.*, 71:119–134, 2013b.

J. Hinkel and R. J. T. Klein. Integrating knowledge to asses coastal vulnerability to sea-level rise: The development of the DIVA tool. *Global Environmental Change*, 19:384–395, 2009.

HR Wallingford. CAMELOT (Coastal Area Modelling for Engineering in the LOng Term). Final project report, fd 1001, HR Wallingford, Wallingford, United Kingdom, 2000.

S. A. Hughes. Wave momentum fluw parameter: a descriptor for nearshore waves. *Coastal Engineering*, 51:1067–1084, 2004.

M. D. Hurst, A. Barkwith, M. A. Ellis, C. W. Thomas, and A. B. Murray. Exploring the sensitivities of crenulate bay shorelines to wave climates using a new vector-based one-line model. *Journal of Geophysical Research: Earth Surface*, 120(12):2586–2608, 2015.

S. Husrin, A. Strusińska, and H. Oumeraci. Experimental study on tsunami attenuation by mangrove forest. *Earth, Planets and Space*, 64(10):15, 2012.

HYPRE. Hypre high performance conditioners: Users guide. Crl-code-22295, Center for Applied Scientific Computing, Lawrence Livermore National Laboratory, 2006.

D. L. Inman, M. H. S. Elwany, and S. A. Jenkins. Shorerise and bar-berm profiles on ocean beaches. *J. Geophys. Res.*, 98(C10):18181–18199, 1993.

IPCC. Climate Change 2014: Synthesis Report. Contribution of Working Groups I, II and III to the Fifth Assessment Report of the Intergovernmental Panel on Climate Change. Technical report, IPCC, Geneva, Switzerland, 2014.

B. E. Jaffe and D. M. Rubin. Using nonlinear forecasting to learn the magnitude and phasing of time-varying sediment suspension in the surf zone. *Journal of Geophysical Research: Oceans*, 101(C6):14283–14296, 1996.

J. A. Jiménez, J. Guillén, and A. Falqués. Comment on the article “Morphodynamic classification of sandy beaches in low energetic marine environment" by Gómez-Pujol, L., Orfila, A., Cañellas, B., Alvarez-Ellacuria, A., Méndez, F.J., Medina, R. and Tintoré, J. *Marine Geology*, 242, pp. 235-246, 2007. *Mar. Geol.*, 255:96–101, 2008.

J. A. Jiménez and A. Sánchez-Arcilla. A long-term (decadal scale) evolution model for microtidal barrier systems. *Coastal Engineering*, 51(8):749 – 764, 2004.

M. Kamali Nezhad. *Plages en équilibre morphologique et hydrodynamique associée*. PhD thesis, Océan, Atmosphère. Institut National Polytechnique de Grenoble - INPG„ Grenoble, France, 2004.

M. Kamalinezhad, H. Michallet, and E. Barthélemy. Equilibre morphologique de barres de déferlement: Expériences. In *Proc. GGCGC*, pages 195–202, Compiègne, France, 2004.

J. W. Kamphuis. Alongshore sediment transport rate. *Journal of Waterway, Port, Coastal, and Ocean Engineering*, 117(6):624–640, 1991.

E. J. Kansa. Multiquadrics - A scattered data approximation schem with application to computational fluid-dynamics - II Solution to parabolic, hyperbolic and elliptic partial diffrential equations. *Computers Math. Applic.*, 19:147–161, 1990.

T. Karambas and C. Koutitas. A breaking wave propagation model based on the Boussinesq equations. *Coastal Engineering*, 18(1):1 – 19, 1992.

M. Kazolea, A. I. Delis, and C. E. Synolakis. Numerical treatment of wave breaking on unstructured finite volume approximations for extended Boussinesq-type equations. *Journal of Computational Physics*, 271:281–305, 2014.

A. B. Kennedy and J. D. Fenton. A fully-nonlinear computational method for wave propagation over topography. *Coast. Eng.*, 32:137–161, 1997.

A. B. Kennedy, Q. Chen, J. T. Kirby, and R. A. Dalrymple. Boussinesq modeling of wave transformation, breaking, and runup. I: 1D. *J. Waterway, Port, Coast. and Ocean Eng.*, 126(1):39–47, 2000.

A. B. Kennedy, J. T. Kirby, Q. Chen, and R. A. Dalrymple. Boussinesq-type equations with improved nonlinear performance. *Wave Motion*, 33:225–243, 2001.

J. T. Kirby and R. A. Dalrymple. Propagation of obliquely incident water waves over a trench. *J Fluid Mech.*, 133:47–63, 1983.

J. T. Kirby, G. Wei, Q. Chen, A. B. Kennedy, and R. A. Dalrymple. FUNWAVE 1.0: fully nonlinear Boussinesq wave model - Documentation and user's manual. Technical report, University of Delaware, 1998.

G. Klonaris, C. Memos, and T. Karambas. A Boussinesq-type model including wave-breaking terms in both continuity and momentum equations. *Ocean Engineering*, 57:128 – 140, 2013.

P. D. Komar and D. L. Inman. Longshore sand transport on beaches. *J. Geophys. Res.*, 75:5914–5927, 1970.

D. L. Kriebel and R. G. Dean. Convolution method for time-dependent beach profile response. *J. Waterw. Port Coastal Ocean Eng.*, 119:204–226, 1993.

Y. Kuriyama, M. Banno, and T. Suzuki. Linkages among interannual variations of shoreline, wave and climate at Hasaki, Japan. *Geophysical Research Letters*, 39(6), 2012.

R. Kurnia and E. van Groesen. High order Hamiltonian water wave models with wave-breaking mechanism. *Coastal Eng.*, 93:55–70, 2014.

H. Lamb. *Hydrodynamics.* Cambridge University Press, 1932.

J. L. Lara, N. Garcia, and I. J. Losada. RANS modelling applied to random wave interaction with submerged permeable structures. *Coast. Eng.*, 53:395–417, 2006.

M. Larson and N. C. Kraus. SBEACH: Numerical model for simulating storm-induced beach change. CERC, Technical Report CERC-89-9, U.S. Army Corps of Engineers, Vicksburg, Mississippi, 1989.

M. Larson, H. Hanson, and N. C. Kraus. Analytical solutions of one-line model for shoreline change near coastal structures. *Journal of Waterway, Port, Coastal, and Ocean Engineering*, 123 (4):180–191, 1997.

M. Larson, M. Capobianco, and H. Hanson. Relationship between beach profiles and waves at Duck, North Carolina, determined by canonical correlation analysis. *Mar. Geol.*, 160:275–288, 2000.

E. Lazarus, A. Ashton, A. B. Murray, S. Tebbens, and S. Burroughs. Cumulative versus transient shoreline change: Dependencies on temporal and spatial scale. *Journal of Geophysical Research: Earth Surface*, 116(F2), 2011.

G. Le Cozannet, M. Garcin, M. Yates, D. Idier, and B. Meyssignac. Approaches to evaluate the recent impacts of sea-level rise on shoreline changes. *Earth Science Reviews*, 138:47–60, 2014.

G. Le Cozannet, T. Bulteau, B. Castelle, R. Ranasinghe, G. Wöppelmann, J. Rohmer, N. Bernon, D. Idier, J. Louisor, and D. Salas-Y-Mélia. Quantifying uncertainties of sandy shoreline change projections as sea level rises. *Scientific reports*, 9(1):42, January 2019.

C. Lee and K. D. Suh. Internal generation of waves for time-dependent mild-slope equations. *Coast. Eng.*, 34:35–57, 1998.

G. Lee, R. J. Nicholls, and W. A. Birkemeier. Storm-driven variability of the beach-nearshore profile at Duck, North Carolina, USA, 1981-1991. *Mar. Geol.*, 148:163–177, 1998.

C. Lemos. Calibration d'un modèle empirique d'équilibre de la variation du trait de côte en fonction des données DGPS et de houle. Master's thesis, Institut Universitaire Européen de la Mer – Laboratoire Domaines Océaniques, Plouzané, France, 2016.

C. Lemos, F. Floc'h, M. L. Yates, N. Le Dantec, V. Marieu, K. Hamon, V. Cuq, S. Suanez, and C. Delacourt. Equilibrium modeling of the beach profile on a macrotidal embayed Low Tide Terrace beach. *Ocean Dynamics*, 2018.

G. Lesser, J. Roelvink, J. van Kester, and G. Stelling. Development and validation of a three-dimensional morphological model. *Coastal Engineering*, 51(8):883 – 915, 2004.

B. Li and C. Fleming. A three dimensional multigrid model for fully nonlinear water waves. *Coast. Eng.*, 30:235–258, 1997.

P. W. Limber, P. N. Adams, and A. B. Murray. Modeling large-scale shoreline change caused by complex bathymetry in low-angle wave climates. *Marine Geology*, 383(C):55–64, 2017.

J. H. List and A. S. Farris. Large-scale shoreline response to storms and fair weather. In *Proc. Coastal Sediments '99, Amer. Soc. of Civil Eng. Reston, VA*, pages 1324–1338, 1999.

P.-F. Liu and A. Orfila. Viscous effects on transient long-wave propagation. *J. Fluid Mech.*, 50: 83–92, 2004.

P.-F. Liu, G. Simarro, and A. Orfila. Experimental and numerical investigation of viscous effects on solitary wave propagation in a wave tank. *Coastal Engineering*, 53:181–190, 2006.

P. L. Liu, P. Lin, K.-A. Chang, and T. Sakakiyama. Numerical modeling of wave interaction with porous structures. *J. Waterway Port, Coastal, Ocean Eng.*, 125:322–330, 1999.

J. W. Long and N. G. Plant. Extended Kalman Filter framework for forecasting shoreline evolution. *Geophysical Research Letters*, 39(13), 2012.

I. López, L. Aragonés, Y. Villacampa, and J. C. Serra. Neural network for determining the characteristic points of the bars. *Ocean Engineering*, 136:141 – 151, 2017.

P. Lubin and S. Glockner. Numerical simulations of three-dimensional plunging breaking waves: generation and evolution of aerated vortex filaments. *J. Fluid Mech.*, 767:364–393, 2015.

B. Ludka, R. Guza, W. O'Reilly, and M. Yates. Field evidence of beach profile evolution toward equilibrium. *Journal of Geophysical Research: Oceans*, 120(11):7574–7597, 2015.

P. Lynett, T.-R. Wu, and P. L.-F. Liu. Modeling wave runup with depth-integrated equations. *Coastal Eng.*, 46:89–107, 2002.

Q. W. Ma, G. X. Wu, and R. Eatock Taylor. Finite element simulation of fully non-linear interaction between vertical cylinders and steep waves. Part 1: Methodology and numerical procedure. *Int. J. Numer. Meth. Fluids*, 36:265–285, 2001.

P. A. Madsen. *A Model for a Turbulent Bore.* PhD thesis, Series paper 28. ISVA, Technical University of Denmark, Lyngby, 1981.

P. A. Madsen and H. A. Schäffer. Higher order Boussinesq-type equations for surface gravity waves: derivation and analysis. *Phil. Trans. R. Soc. A*, 356:3123–3181, 1998.

P. A. Madsen and O. R. Sørensen. A new form of the boussinesq equations with improved linear dispersion characteristics. part 2. a slowly-varying bathymetry. *Coastal Engineering*, 18(3):183 – 204, 1992.

P. A. Madsen, O. Sørensen, and H. Schäffer. Surf zone dynamics simulated by a Boussinesq type model. Part I. Model description and cross-shore motion of regular waves. *Coastal Engineering*, 32(4):255–287, 1997.

P. A. Madsen, H. B. Bingham, and H. Liu. A new Boussinesq method for fully nonlinear waves from shallow to deep water. *J. Fluid Mech.*, 462:1–30, 2002.

A. E. Maguire. *Hyrdrodynamics, control and numerical modelling of absorbing wavemakers.* PhD thesis, University of Edinburgh, Edinburgh, Scotland, 2011.

H. Mase and J. T. Kirby. Hybrid frequency-domain kdv equation for random wave transformation. In *Coastal Engineering 1992*, pages 474–487. American Society of Civil Engineers, 1992.

G. Masselink and C. Pattiaratchi. Seasonal changes in beach morphology along the sheltered coastline of Perth, Western Australia. *Marine Geology*, 172(3):243 – 263, 2001.

G. Masselink and A. D. Short. The effect of tide range on beach morphodynamics and morphology: a conceptual beach model. *Journal of Coastal Research*, pages 785–800, 1993.

R. McCall, J. V. T. de Vries, N. Plant, A. V. Dongeren, J. Roelvink, D. Thompson, and A. Reniers. Two-dimensional time dependent hurricane overwash and erosion modeling at Santa Rosa Island. *Coastal Engineering*, 57(7):668 – 683, 2010.

R. McCall, G. Masselink, T. Poate, J. Roelvink, L. Almeida, M. Davidson, and P. Russell. Modelling storm hydrodynamics on gravel beaches with XBeach-G. *Coastal Engineering*, 91:231 – 250, 2014.

S. McLaughlin and J. A. G. Cooper. A multi-scale coastal vulnerability index: A tool for coastal managers? *Environmental Hazards*, 9(3):233–248, 2010.

H. Michallet, F. Grasso, and E. Barthélemy. Long waves and beach profile evolutions. *Journal of Coastal Research*, pages 221–225, 2007.

R. Miche. Mouvements ondulatoires des mers en profondeur constante ou decroissante. Technical report, École Nationale des Ponts et Chaussées, 1944.

J. K. Miller and R. G. Dean. A simple new shoreline change model. *Coastal Engineering*, 51(7): 531–556, 2004.

J. K. Miller and R. G. Dean. Shoreline variability via empirical orthogonal function analysis: Part I temporal and spatial characteristics. *Coastal Engineering*, 54(2):111 – 131, 2007.

E. Monsalve, A. Maurel, V. Pagneux, and P. Petitjeans. Propagation of nonlinear waves passing over submerged step. *Physics Procedia*, 70:863–866, 2015.

R. A. Morton, J. C. Gibeaut, and J. G. Paine. Meso-scale transfer of sand during and after storms: implications for prediction of shoreline movement. *Mar. Geol.*, 126:161–179, 1995.

R. Musumeci, I. A. Svendsen, and J. Veeramony. The flow in the surf zone: a fully nonlinear Boussinesq-type of approach. *Coast. Eng.*, 52:565–598, 2005.

R. E. Musumeci, L. Cavallaro, E. Foti, P. Scandura, and P. Blondeaux. Waves and currents crossing at a right angle: experimental investigation. *J. Geophys. Res.*, 111(7):C07019, 2006.

J. N. Newman and C.-H. Lee. Boundary-Element Methods in offshore structure analysis. *J. Offshore Mech. Arctic Eng.*, 124:81–89, 2002.

R. J. Nicholls and A. C. de la Vega-Leinert. Implications of sea-level rise for Europe's coasts. *Journal of Coastal Research*, 24(2):285–287, 2008.

R. J. Nicholls, P. P. Wong, V. R. Burket, J. Codignotto, J. Hay, R. McLean, S. Ragoonaden, and C. D. Woodroffe. Coastal systems and low-lying areas. In *Climate change 2007: impacts, adaptation and vulnerability. Contribution of Working Group II to the fourth assessment report of the Intergovernmental Panel on Climate Change*, pages 315–356, Cambridge, UK, 2007.

R. J. Nicholls, S. E. Hanson, J. A. Lowe, R. A. Warrick, X. Lu, and A. J. Long. Sea-level scenarios for evaluating coastal impacts. *Wiley Interdisciplinary Reviews: Climate Change*, 5(1):129–150, 2014.

A. W. Niedoroda, C. W. Reed, D. J. P. Swift, H. Arato, and K. Hoyanagi. Modeling shore-normal large-scale coastal evolution. *Mar. Geol.*, 126:181–199, 1995.

S. B. Nimmala, S. C. Yim, and S. T. Grilli. An efficient three-dimensional FNPF numerical wave tank for large-scale wave basin experiment simulation. *Journal of Offshore Mechanics and Arctic Engineering*, 135:021104, 2013.

O. G. Nwogu. Alternative form of Boussinesq equations for nearshore wave propagation. *J. Waterway, Port, Coastal and Ocean Eng.*, 119(6):618–638, 1993.

F. Oehler, G. Coco, M. O. Green, and K. R. Bryan. A data-driven approach to predict suspended-sediment reference concentration under non-breaking waves. *Continental Shelf Research*, 46: 96 – 106, 2012.

T. Okamoto and D. R. Basco. The Relative Trough Froude Number for initiation of wave breaking: Theory, experiments and numerical model confirmation. *Coastal Engineering*, 53(8):675–690, 2006.

H. T. Özkan Haller and S. Brundidge. Equilibrium beach profile concept for Delaware beaches. *J. Wat., Port, Coast, Ocean Eng.*, 133(2):147–160, 2007.

L. Pape, B. Ruessink, M. A. Wiering, and I. L. Turner. Recurrent neural network modeling of nearshore sandbar behavior. *Neural Networks*, 20(4):509 – 518, 2007.

C. Papoutsellis, M. L. Yates, B. Simon, and M. Benoit. Modeling of depth-induced wave breaking in a fully nonlinear free-surface potential flow model. *Coast. Eng.*, accepted, 2019.

C. E. Papoutsellis, A. G. Charalampopoulos, and G. A. Athanassoulis. Implementation of a fully nonlinear Hamiltonian Coupled-Mode Theory, and application to solitary wave problems over bathymetry. *European Journal of Mechanics - B/Fluids*, 72:199–224, 2018.

G. Pedersen. *Modeling runup with depth integrated equation models*, pages 3–41. World Scientific, 2008.

R. Pelnard-Considére. Essai de théorie de l'évolution des formes de rivages en plages de sable et de galets. *La Houille Blanche*, pages 289–301, 1956.

D. Pender and H. Karunarathna. A statistical-process based approach for modelling beach profile variability. *Coastal Engineering*, 81:19 – 29, 2013.

N. G. Plant and K. T. Holland. Prediction and assimilation of surf-zone processes using a Bayesian network: Part I: Forward models. *Coastal Engineering*, 58(1):119 – 130, 2011.

N. G. Plant, R. A. Holman, and M. H. Freilich. A simple model for interannual sandbar behavior. *J. Geophys. Res.*, 104(C7):15755–15776, 1999.

N. G. Plant, E. Robert Thieler, and D. L. Passeri. Coupling centennial-scale shoreline change to sea-level rise and coastal morphology in the Gulf of Mexico using a Bayesian network. *Earth's Future*, 4(5):143–158, 2016.

S. Popinet. An accurate adaptive solver for surface-tension-driven interfacial flows. *J. Comp. Phys.*, 228:5838–5866, 2009.

S. Quartel, A. Kroon, and B. G. Ruessink. Seasonal accretion and erosion patterns on a microtidal sandy beach. *Mar. Geol.*, 250:19–33, 2008.

R. Ranasinghe and C. Pattiaratchi. The seasonal closure of tidal inlets: Wilson Inlet — a case study. *Coastal Engineering*, 37(1):37 – 56, 1999.

R. Ranasinghe, D. Callaghan, and M. J. F. Stive. Estimating coastal recession due to sea level rise: beyond the Bruun rule. *Climatic Change*, 110(3):561–574, Feb 2012.

C. Raoult. *Modélisation numérique non-linéaire et dispersive des vagues en zone côtière.* PhD thesis, Université Paris-Est, Chatou, France, 2017.

C. Raoult, M. Benoit, and M. Yates. Validation of a fully nonlinear and dispersive wave model with laboratory non-breaking experiments. *Coastal Eng.*, 114:194–207, 2016a.

C. Raoult, M. L. Yates, and M. Benoit. Modeling viscous effects in a fully nonlinear and dispersive potential model. In *Proceedings 15èmes Journées de l'Hydrodynamique*, Brest, France, 2016b.

C. Raoult, M. L. Yates, and M. Benoit. Development and validation of a 3D RBF-spectral model for coastal wave simulation. *J. Comp. Phys.*, 378:278–302, 2019.

M. M. Rienecker and J. D. Fenton. A Fourier approximation method for steady water waves. *J. Fluid Mech.*, 104:119–137, 1981.

A. Robinet, D. Idier, B. Castelle, and V. Marieu. A reduced-complexity shoreline change model combining longshore and cross-shore processes: The lx-shore model. *Environmental Modelling & Software*, 109:1 – 16, 2018.

V. Roeber and K. F. Cheung. Boussinesq-type model for energetic breaking waves in fringing reef environments. *Coastal Engineering*, 70(4):1–20, 2012.

V. Roeber, K. F. Cheung, and M. H. Kobayashi. Shock-capturing Boussinesq-type model for nearshore wave processes. *Coastal Engineering*, 57(4):407–423, 2010.

D. Roelvink, A. Reniers, A. van Dongeren, J. van Thiel de Vries, R. McCall, and J. Lescinski. Modelling storm impacts on beaches, dunes and barrier islands. *Coastal Engineering*, 56(11): 1133 – 1152, 2009.

D. Roelvink, J. Roelvink, and A. Reniers. *A Guide to Modeling Coastal Morphology*. Advances in coastal and ocean engineering. World Scientific, 2012. ISBN 9789814304252.

D. Roelvink, R. McCall, S. Mehvar, K. Nederhoff, and A. Dastgheib. Improving predictions of swash dynamics in XBeach: the role of groupiness and incident-band runup. *Coastal Engineering*, 134:103 – 123, 2018.

J. Roelvink and I. Brøker. Cross-shore profile models. *Coastal Engineering*, 21(1):163 – 191, 1993.

J. E. Romate and P. J. Zandbergen. Boundary integral equation formulations for free-surface flow problems in two and three dimensions. *Computational Mechanics*, 4(4):276–282, Jul 1989.

M. Roseau. *Asymptotic Wave Theory*. North-Holland, Amsterdam, Holland, 1976.

I. Safak, J. List, J. Warner, and N. Kumar. Observations and 3D hydrodynamics-based modeling of decadal-scale shoreline change along the Outer Banks, North Carolina. *Coastal Engineering*, 120:78 – 92, 2017.

H. A. Schäffer, P. A. Madsen, and R. Deigaard. A Boussinesq model for waves breaking in shallow water. *Coastal Engineering*, 20(3-4):185–202, 1993.

B. R. Seiffert and G. Ducrozet. Simulation of breaking waves using the high-order spectral method with laboratory experiments: wave-breaking energy dissipation. *Ocean Dynamics*, 68:65–89, 2018.

L. F. Shampine and M. K. Gordon. *Computer solution of ordinary differential equations : the initial value problem*. W.H. Freeman, San Francisco, CA, USA, 1975.

S. Shao. Incompressible SPH simulation of wave breaking and overtopping with turbulence modelling. *Int. J. Numer. Meth. Fluids*, 50:597–621, 2006.

Y.-L. Shao and O. M. Faltinsen. A harmonic polynomial cell (HPC) method for 3D Laplace equation with application in marine hydrodynamics. *J. Comp. Phys.*, 274:312–332, 2014.

J. Shaw, R. B. Taylor, S. Solomon, H. A. Christian, and D. L. Forbes. Potential impacts of global sea-level rise on Canadian coasts. *The Canadian Geographer*, 42(4):365–379, 1998.

C. Sheppard, D. J. Dixon, M. Gourlay, A. Sheppard, and R. Payet. Coral mortality increases wave energy reaching shores protected by reef flats: Examples from the Seychelles. *Estuarine, Coastal and Shelf Science*, 64:223–234, 2005.

F. Shi, J. T. Kirby, J. C. Harris, J. D. Geiman, and S. T. Grilli. A high-order adaptive time-stepping TVD solver for Boussinesq modeling of breaking waves and coastal inundation. *Ocean Modelling*, 43-44:36–51, 2012.

A. D. Short and C. D. Woodroffe. *The coast of Australia.* Cambridge University Press, Melbourne, Australia, 2009.

E. W. Shows. Florida's coastal setback line—an effort to regulate beachfront development. *Coastal Zone Management Journal*, 4(1-2):151–164, 1978.

B. Simon, C. Papoutsellis, M. Benoit, and M. L. Yates. Modélisation du déferlement du à la bathymétrie dans un code de simulation des vagues non-linéaires et dispersives en zone côtière. In *Proc. 16èmes Journée de l'Hydrodynamique*, page 11, Marseille, France, 2018.

B. Simon, C. Papoutsellis, M. Benoit, and M. L. Yates. Comparing methods of modeling depth-induced breaking of irregular waves with a fully nonlinear potential flow approach. *J. Ocean Eng. Mar. Energy*, submitted, 2019.

R. A. Smith. An operator expansion formalism for nonlinear surface waves over variable depth. *J. Fluid Mech.*, 363:333–347, 1998.

R. K. Smith and K. R. Bryan. Monitoring beach face volume with a combination of intermittent profiling and video imagery. *Journal of Coastal Research*, pages 892–898, 2007.

F. E. Snodgrass, K. F. Hasselman, G. R. Miller, W. H. Munk, and W. H. Powers. Propagation of ocean swell across the Pacific. *Philosophical Transactions of the Royal Society of London A: Mathematical, Physical and Engineering Sciences*, 259(1103):431–497, 1966.

O. R. Sørensen, P. A. Madsen, and H. A. Schäffer. Nearshore wave dynamics simulated by Boussinesq type models. In *Proc. of 26th ICCE*, pages 272–285, Copenhagen, Denmark, 1998. ASCE, New York.

H. N. Southgate and A. H. Brampton. Coastal morphology modelling: a guide to model selection and usage. Report sr 570, HR Wallingford, 2001.

K. D. Splinter and M. L. Palmsten. Modeling dune response to an East Coast low. *Marine Geology*, 329-331:46 – 57, 2012.

K. D. Splinter, R. A. Holman, and N. G. Plant. A behavior-oriented dynamic model for sandbar migration and 2DH evolution. *Journal of Geophysical Research: Oceans*, 116(C1), 2011.

K. D. Splinter, I. L. Turner, and M. A. Davidson. How much data is enough? The importance of morphological sampling interval and duration for calibration of empirical shoreline models. *Coastal Engineering*, 77:14 – 27, 2013.

K. D. Splinter, I. L. Turner, M. A. Davidson, P. Barnard, B. Castelle, and J. Oltman-Shay. A generalized equilibrium model for predicting daily to interannual shoreline response. *Journal of Geophysical Research: Earth Surface*, 119(9):1936–1958, 2014.

D. K. Stauble. The use of shoreline change mapping in coastal engineering project assessment. *Journal of Coastal Research*, pages 178–206, 2003.

S. E. Stead. Estimation of gradient from scattered data. *Rocky Mountain J. Math.*, 14:265–280, 1984.

G. Stelling and M. Zijlema. An accurate and efficient finite-difference algorithm for non-hydrostatic free-surface flow with application to wave propagation. *Int. J. Numer. Meth. Fluids*, 43:1–23, 2003.

M. J. F. Stive. Velocity and pressure field of spilling breakers. *Coastal Engineering Proceedings*, 1 (17), 1980.

M. J. F. Stive. How important is global warming for coastal erosion? *Climatic Change*, 64:27–39, 2004.

M. J. F. Stive, S. G. J. Aarninkhof, L. Hamm, H. Hanson, M. Larson, K. M. Wijnberg, R. J. Nicholls, and M. Capobianco. Variability of shore and shoreline evolution. *Coast. Eng.*, 47:211–235, 2002.

D. R. Stoddard. Ecology and morphology of recent coral reefs. *Bio. Rev.*, 44:433–498, 1969.

D. R. Stoddard and F. R. Fosberg. The hoa of Hull Atoll and the problem of hoa. Atoll Research Bulletin No. 394, National Museum of Natural History, Smithsonian Institution, Washington, D. C., USA, 1994.

J. Sutherland, D. Walstra, T. Chesher, L. van Rijn, and H. Southgate. Evaluation of coastal area modelling systems at an estuary mouth. *Coastal Engineering*, 51(2):119 – 142, 2004.

I. Svendsen, P. Madsen, and J. Hansen. Wave characteristics in the surf zone. *Proc. 16th Coastal Engineering Conf.*, pages 520–539, 1978.

I. Svendsen, K. Yu, and J. Veeramony. A Boussinesq breaking wave model with vorticity. In B. L. Edge, editor, *Coastal Engineering 1996*, pages 1192–1204. American Society of Civil Engineers, 1996.

I. A. Svendsen and P. A. Madsen. A turbulent bore on a beach. *J. Fluid Mech.*, 148:73–96, 1984.

R. D. Tasing. Optimisation du code de calcul numérique « Misthyc » pour la propagation des vagues en zone côtière. Master's thesis, Université Pierre et Marie Curie, Paris, France, 2016.

E. R. Thieler and W. W. Danforth. Historical shoreline mapping (I): Improving techniques and reducing positioning errors. *J. Coastal Res.*, 10(3):549–563, 1994.

E. R. Thieler and E. S. Hammar-Klose. National assessment of coastal vulnerability to future sea-level rise: Preliminary results for the U.S. Atlantic Coast. Tech. rep. open-file report 99-953, US Geological Survey, 1999.

Y. Tian and S. Sato. A numerical model on the interaction between nearshore nonlinear waves and strong currents. *Coast. Eng. J.*, 50(4):369–395, 2008.

F. C. K. Ting and J. T. Kirby. Observation of undertow and turbulence in a laboratory surf zone. *Coast. Eng.*, 24:51–80, 1994.

M. Tissier, P. Bonneton, F. Marche, F. Chazel, and D. Lannes. A new approach to handle wave breaking in fully non-linear Boussinesq models. *Coastal Engineering*, 67:54–66, 2012.

M. Tonneli and M. Petti. Shock-capturing Boussinesq model for irregular wave propagation. *Coastal Eng.*, 61:8–19, 2012.

P. Tonnon, L. van Rijn, and D. Walstra. The morphodynamic modelling of tidal sand waves on the shoreface. *Coastal Engineering*, 54(4):279 – 296, 2007.

G. E. Tsekouras, A. Rigos, A. Chatzipavlis, and A. Velegrakis. A Neural-Fuzzy Network based on Hermite polynomials to predict the coastal erosion. In L. Iliadis and C. Jayne, editors, *Engineering Applications of Neural Networks*, pages 195–205, Cham, 2015. Springer International Publishing.

M. P. Tulin and M. Landrini. Breaking waves in the ocean and around ships. In *Twenty-Third Symposium on Naval Hydrodynamics,*, pages 713–745, Office of Naval Research, Bassin d'Essais des Carenes, National Research Council., 2000.

USACE. Shore Protection Manual. Technical report, U.S. Army Corps of Engineers, Vicksburg, Mississippi, 1984.

M. Utku. *The Relative Trough Froude Number: a new wave breaking criteria.* PhD thesis, Dept. of Civil and Environmental Engr., Old Dominion University, Norfolk, Virginia, 1999.

A. Van Dongeren, A. Bolle, D. Roelvink, M. Vousdoukas, T. Plomaritis, J. Williams, C. Armaroli, D. Idier, P. Van Geer, J. Van Thiel De Vries, P. Haerens, R. Taborda, J. Benavente, E. Trifonova, P. Ciavola, Y. Balouin, and P. Eftimova. Micore: dune erosion and overwash model validation with data from nine European field sites. In E. T. AGU, editor, *AGU Fall Meeting*, volume 90(52), pages NH14A–06, San Francisco, United States, 2009.

L. van Rijn, D. Walstra, B. Grasmeijer, J. Sutherland, S. Pan, and J. Sierra. The predictability of cross-shore bed evolution of sandy beaches at the time scale of storms and seasons using process-based profile models. *Coastal Engineering*, 47(3):295 – 327, 2003.

A. van Rooijen, A. Reniers, J. van Thiel de Vries, C. Blenkinsopp, and R. McCall. Modeling swash zone sediment transport at Truc Vert Beach. *Coastal Engineering Proceedings*, 1(33):105, 2012.

A. A. van Rooijen, R. T. McCall, J. S. M. van Thiel de Vries, A. R. van Dongeren, A. J. H. M. Reniers, and J. A. Roelvink. Modeling the effect of wave-vegetation interaction on wave setup. *Journal of Geophysical Research: Oceans*, 121(6):4341–4359, 2016.

J. Veeramony and I. A. Svendsen. A Boussinesq model for breaking waves: comparisons with experiments. In *Coastal Engineering 1998*, pages 258–271. American Society of Civil Engineers, 1998.

J. Veeramony and I. A. Svendsen. The flow in surf-zone waves. *Coastal Engineering*, 39(2):93–122, 2000.

C. L. Vincent and M. J. Briggs. Refraction-Diffraction of Irregular Wave over a Mound. *J. Wat. Port Coast. Ocean Eng*, 115:269–284, 1989.

S. Vitousek, P. L. Barnard, P. Limber, L. Erikson, and B. Cole. A model integrating longshore and cross-shore processes for predicting long-term shoreline response to climate change. *Journal of Geophysical Research: Earth Surface*, 122(4):782–806, 2017.

M. I. Vousdoukas, D. Wziatek, and L. P. Almeida. Coastal vulnerability assessment based on video wave run-up observations at a mesotidal, steep-sloped beach. *Ocean Dynamics*, 62:123–137, Jan. 2012.

P. Wang and N. C. Kraus. Beach profile equilibrium and patterns of wave decay and energy dissipation across the surf zone elucidated in a large-scale laboratory experiment. *Journal of Coastal Research*, 2005(213):522 – 534 – 13, 2005.

Z. Wang, T. Louters, and H. de Vriend. Morphodynamic modelling for a tidal inlet in the Wadden Sea. *Marine Geology*, 126(1):289 – 300, 1995.

A. P. Webb and P. S. Kench. The dynamic response of reef islands to sea-level rise: Evidence from multi-decadal analysis of island change in the Central Pacific. *Global and Planetary Change*, 72:234–246, 2010.

G. Wei, J. T. Kirby, S. T. Grilli, and R. Subramanya. A fully nonlinear Boussinesq model for surface waves: Part I. Highly nonlinear unsteady waves. *J. Fluid Mech.*, 294:71–92, 1995.

B. J. West, K. A. Brueckner, R. S. Janda, M. Milder, and R. L. Milton. A new numerical method for surface hydrodynamics. *J. Geophys. Res.*, 92:11803–11824, 1987.

R. W. Whalin. The limit of applicability of linear wave refraction theory in a convergence zone. Technical report, DTIC Document, 1971.

J. J. Williams, A. R. de Alegría-Arzaburu, R. T. McCall, and A. V. Dongeren. Modelling gravel barrier profile response to combined waves and tides using XBeach: Laboratory and field results. *Coastal Engineering*, 63:62 – 80, 2012.

C. D. Winant, D. L. Inman, and C. E. Nordstrom. Description of seasonal beach changes using empirical eigenfunctions. *J. Geophys. Res.*, 80:1979–1986, 1975.

C. Winter. Meso-scale morphodynamics of the Eider Estuary: Analysis and numerical modelling. *Journal of Coastal Research*, pages 498–503, 2006.

C. Winter. *Observation and Modelling of Morphodynamics in Sandy Coastal Environments.* PhD thesis, University Bremen, Bremen, Germany, 2012.

C. D. Woodroffe. *Coasts: Form, Process and Evolution.* Cambridge University Press, 2002.

L. Wright, A. Short, and M. Green. Short-term changes in the morphodynamic states of beaches and surf zones: an empirical predictive model. *Marine geology*, 62(3-4):339–364, 1985.

L. D. Wright and A. D. Short. Morphodynamic variability of surf zones and beaches: A synthesis. *Mar. Geol.*, 56:93–118, 1984.

G. X. Wu, Q. W. Ma, and R. Eatock Taylor. Numerical simulation of sloshing waves in a 3D tank based on a finite element method. *Appl. Ocean Res.*, 20:337–355, 1998.

M. L. Yates and M. Benoit. Accuracy and efficiency of two numerical methods of solving the potential flow problem for highly nonlinear and dispersive water waves. *Int. J. Numer. Meth. Fluids*, 77:616–640, 2015.

M. L. Yates and G. Le Cozannet. Evaluating european coastal evolution using Bayesian networks. *Nat. Hazards Earth Syst. Sci.*, 12:1173–1177, 2012.

M. L. Yates, R. T. Guza, and W. C. O'Reilly. Equilibrium shoreline response: Observations and modeling. *J. Geophys. Res.*, 114(C09014), 2009a.

M. L. Yates, R. T. Guza, W. C. O'Reilly, and R. J. Seymour. Overview of seasonal sand level changes on southern California beaches. *Shore & Beach*, 77(1):39–46, 2009b.

M. L. Yates, R. T. Guza, W. C. O'Reilly, and R. J. Seymour. Seasonal persistence of a small southern California beach fill. *Coast. Eng.*, 56:559–564, 2009c.

M. L. Yates, R. T. Guza, W. C. O'Reilly, J. E. Hansen, and P. L. Barnard. Equilibrium shoreline response of a high wave energy beach. *J. Geophys. Res.*, 116(C04014), 2011.

M. L. Yates, G. Le Cozannet, M. Garcin, E. Salaï, and P. Walker. Multidecadal atoll shoreline change on Manihi and Manuae, French Polynesia. *J. Coast. Res.*, 29(4):870–882, 2013.

V. E. Zakharov. Stability of periodic waves of finite amplitude on the surface of a deep fluid. *J. Appl. Mech. Tech. Phys.*, 9(2):190–194, 1968.

J. A. Zelt. The run-up of nonbreaking and breaking solitary waves. *Coast. Eng.*, 15:205–246, 1991.

K. Zhang, B. C. Douglas, and S. P. Leatherman. Global warming and coastal erosion. *Climatic Change*, 64, 2004.

B. B. Zhao, R. C. Ertekin, W. Y. Duan, and M. Hayatdavoodi. On the steady solitary-wave solution of the Green-Naghdi equations of different levels. *Wave Motion*, 51:1382–1395, 2014.

L. Zhu, Q. Chen, and X. Wan. Optimization of non-hydrostatic Euler model for water waves. *Coast. Eng.*, 91:191–199, 2014.

M. Zijlema and G. S. Stelling. Further experiences with computing non-hydrostatic free-surface flows involving water waves. *Int. J. Numer. Meth. Fluids*, 48:169–197, 2005.

M. Zijlema and G. S. Stelling. Efficient computation of surf zone waves using the nonlinear shallow water equations with non-hydrostatic pressure. *Coast. Eng.*, 55:780–790, 2008.

M. Zijlema, G. S. Stelling, and P. Smit. SWASH: An operational public domain code for simulating wave fields and rapidly varied flows in coastal waters. *Coast. Eng.*, 58:992–1012, 2011.

N. Zimmermann, K. Trouw, B. De Maerschalck, F. Toro, R. Delgado, T. Verwaest, and F. Mostaert. Scientific support regarding hydrodynamics and sand transport in the coastal zone: Evaluation of XBeach for long term cross-shore modelling. Version 3.0. wl rapporten, 00_072., Flanders Hydraulics Research & IMDC, Antwerp, Belgium, 2015.

Appendix A

Academic and project responsibilities

As a researcher for the Cerema in the Saint-Venant Hydraulics Laboratory, the responsibilities of my position are centered on my research activities and their application for the mission of the Cerema as a public actor. However, I have had a longterm interest in mentoring and teaching and have developed this interest throughout my career. I believe that imparting our knowledge to students during their academic careers is one of the most enriching and important facets of our work as researchers, both through supervising their work via internships, thesis projects, and postdoctoral projects, and directly through teaching.

A.1 Research supervision

Postdoctoral researchers

Christos Papoutsellis (2017-2018): Postdoctoral researcher (12 months, 50%, co-supervision with Michel Benoit, FEM-ANR project DiMe), 6 months IRPHE, Marseille, 6 months LHSV. Integrating the effects of wave breaking in a Hamiltonian Coupled-Mode Theory deterministic, fully nonlinear potential flow wave propagation model for coastal applications.

Bruno Simon (2018-2019): Postdoctoral researcher (18 months, 25%, co-supervision with Michel Benoit, Sergey Gavrilyuk, Olivier Kimmoun, DEPHYMAN Labex project), IRPHE, Marseille. Integrating the effects of wave breaking and optimizing a 3D deterministic, fully nonlinear potential flow wave propagation model.

Mathieu Gervais (2015-2016): Postdoctoral researcher (18 months, 50%, co-supervision with Damien Pham Van Bang, Geocorail project), LHSV. Analysis of laboratory measurements of wave transformation and morphological changes with the goal of mitigating beach erosion in storm conditions with a submerged breakwater.

PhD students

Marc Igigabel (2019-2020): Engineer at the Cerema, LHSV (30%, co-supervision with Youssef Diab (HDR, Laboratoire d'Urbanisme (LAB'URBA)). "Les systèmes de protection contre les submersions marines - Diagnostic, adaptation et gestion" (Coastal protection systems against marine flooding - Diagnostic, adaptation, and management).

Teddy Chataigner (2018-2020): PhD student, LHSV (55%, co-supervision with Nicole Goutal (HDR), Nicolas Le Dantec, financed by grants from the DGA, the Cerema, and the ENPC). Beach morphological changes: integrated empirical modeling of cross-shore and longshore processes.

Cécile Raoult (2014-2017): PhD student, LHSV (50%, co-supervision with Michel Benoit, CIFRE grant). Nonlinear and dispersive numerical modeling of nearshore waves.

Masters and Engineering students

Nicolas Cailler (2019): Masters intern, ENSTA Bretagne (60%, co-supervised with Nicolas Le Dantec), LHSV, Chatou, France. Empirical modeling of beach morphological evolution and shoreline dynamics : sea-level rise climate change impacts.

Corentin Petton (2019): Masters intern, Université de Caen (60%, co-supervised with Nicolas Le Dantec), LHSV, Chatou, France. Empirical modeling of beach morphological evolution and shoreline dynamics : wave climate change impacts.

Alessandro De Carolis (2019): Erasmus intern, University of Cassino (30%, co-supervised with Pablo Tassi), LHSV, Chatou, France. Dune hydraulics.

Matthew Leary (2018): Masters intern, University of Rhode Island (60%, co-supervised with Nicolas Le Dantec and France Floc'h), LHSV, Chatou, France. Extension of an equilibrium beach change model to include alongshore transport processes.

Marine de Carlo (2017): Masters intern, ENSTA (60%, co-supervised with Damien Pham Van Bang), LHSV, Chatou, France. Validating the morphological change model XBeach to simulate submerged breakwater beach erosion reduction experiments.

Gabin Bouvard (2017): Engineering intern, ENTPE (50%, co-supervised with Nicolas Le Dantec and France Floc'h), UBO, Brest, France. Application and calibration of an equilibrium model applied to a beach-dune system at Guisseny beach.

Dimitri Tasing (2016): Masters intern, UPMC (100%), LHSV, Chatou, France. Optimization of the wave propagation model Misthyc.

Christina Ghitui (2016): Masters intern, ENSE3 (Grenoble INP) (20%, co-supervised with Marc Andreevsky and Antoine Joly), LNHE, EDF R&D, Chatou, France. Comparing wave propagation models.

Maria Clara Lemos Rodríguez (2016): Masters intern, IUEM/UBO (30%, co-supervised with

France Floc'h and Nicolas Le Dantec), IUEM/UBO, Brest, France. Predicting shoreline change using equilibrium models: Porsmilin, France.

Pierre Desbrières (2014): First year intern, ENPC (50%, co-supervised with Michel Benoit), LHSV, Chatou, France. Modeling waves in the coastal zone.

Emilie Salaï (2011): Masters intern, Université de Caen Basse Normandie (60% co-supervised with Gonéri Le Cozannet), BRGM, Orléans, France. Multidecadal shoreline change of atolls: Manihi and Scilly.

A.2 Teaching

Sea State, Waves and Coastal Morphodynamics, ENSTA, Master, 12h, 2013-2019

Since 2013, I have participated in the program Master WAPE (Water, Air, Pollution, and Energy) of the University Paris-Saclay (Ecole Polytechnique and ENSTA ParisTech), in partnership with the Master OACOS (Océan, Atmosphère, Climat et Observations Spatiales), co-organized by l'École des Ponts ParisTech, l'Université Pierre et Marie Curie, l'École Normale Supérieure, l'École Polytechnique, and l'ENSTA ParisTech. My participation in this class consists of approximately 12h of classes (theory and practical applications) covering linear wave theory, sea states, the propagation of waves in port and coastal zones, nearshore hydrodynamics, and an introduction to wave models and nonlinear waves.

Travaux Maritimes, ENPC, 2nd year students, 20h, 2016-2019

Since 2016, I have participated in teaching the class "Travaux Maritimes", or Maritime works, at the ENPC as part of the second year of the program "Génie Civil et Construction". For the last two years, I have been responsible for the first module of the course concerning coastal waves and currents, which includes approximately 10h of theoretical courses (covering topics similar to those in the Sea State, Coastal Waves and Morphodynamics course) and 10h of practical sessions focused on an applied project.

Physical processes and modeling of waves in coastal and port zones, LHSV/LNHE training sessions, 6h, 2016, 2019

As part of a series of training sessions concerning the general theme of Environmental Hydraulics, I taught two sessions concerning the dominant physical processes and modeling of waves in coastal zones and ports. This series of courses was designed by members of the LHSV and LNHE (Laboratoire National d'Hydraulique et Environnement) and is destined for students, researchers, and engineers in these laboratories, the MFEE (Mécanique des Fluides, Energie et Environnement) laboratory, and other departments of EDF R&D.

Scientific English, ENS Cachan, 2nd year, 20h, 2012-2013

In 2012-2013, I additionally participated (20h) in teaching a scientific English ("Anglais scientifique") course to second year students at the Ecole Normale Supérieur de Cachan.

The Ocean, UCSD, 2nd/3rd year, 20h, 2008

During my PhD, I was a teaching assistant (20h) for a class entitled "The Ocean", covering marine geology, and physical, biological, and chemical oceanography for second and third year students at the University of California, San Diego.

A.3 Other academic responsabilities

In addition to my role as a teacher and mentor for Masters students, PhD students, and postdoctoral researchers, I acted as an academic supervisor for first year students at the ENPC during their scientific internships abroad (2 students in 2013, 3 students in 2015) in the fields of coastal and marine engineering. I am currently acting as the university's academic tutor for a student from the ENSTA doing a scientific internship at the UPPA and for a student from the ENPC doing a professional internship at EGIS.

In the LHSV, I initiated and have organized since 2016 the "Journée des Doctorants du LHSV" to highlight the work of the PhD students in our laboratory. This day of presentations is important to present the work being carried out in our laboratory to the three member organizations of the laboratory (EDF R&D, Cerema, ENPC) and to encourage interactions between students and researchers within and associated with the laboratory (e.g. LNHE of EDF R&D).

A.4 Project management

2018-2019: *PHC (Programme Hubert Curien) Sakura Project – Predicting decadal-scale shoreline evolution integrating the impacts of climate change,* financed by the Japan Society for the Promotion of Science, the French Ministry for Europe and Foreign Affairs, and the French Ministry of Higher Education, Research and Innovation.
I am the French coordinator of this project that provides financial support for the collaboration developed between a team of French researchers from the LHSV and IUEM/UBO and a team of Japanese researchers at the Port and Airport Research Institute (PARI), Kyoto University, and Toyohashi University of Technology.

2017-2020: *DiMe Project – "Dimensionnement et Meteocean : modélisation et observation des états de mer extrêmes déferlants pour les EMR"*, financed by France Energies Marines ITE ("Institute pour la Transition Energétique") and the ANR ("Agence National de la Recherche").
The main objective of this project is to improve the estimation of large, breaking waves and their

impacts on offshore and nearshore structures. I am the scientific coordinator for the Cerema as a part of the consortium of 18 academic, governmental, and industrial partners working together on this project. Notably, the Cerema is responsible for working on: (1) comparing the ANEMOC and HOMERE wave databases, in particular for large wave events, (2) co-supervising a postdoctoral researcher (22 months) working on improving the parametrization of wave breaking in spectral wave models, and (3) co-supervising a postdoctoral researcher (12 months) working on taking into account the effects of wave breaking in a fully nonlinear and dispersive potential flow wave propagation model. I am overseeing administratively and scientifically the Cerema's participation in the project (6 researchers/engineers from the Cerema) and am personally working on the third research subject listed above.

Appendix B

Curriclum Vitae

Saint Venant Hydraulics Laboratory
6 quai Watier, BP 49
78401 Chatou, France
☎ *(+33) 1 30 87 78 35*
marissa.yates-michelin@cerema.fr

Marissa L. Yates

Education

2009 **PhD Oceanography**, *Scripps Institution of Oceanography, UCSD*, La Jolla, CA, USA,
Seasonal Sand Level Changes on Southern California Beaches :
Observations and Modeling
Thesis director : Dr. Bob Guza.

2003 **B.S. Environmental Engineering**, *MIT*, Cambridge, Massachusetts, USA.

Positions

2011–present **Researcher**, *Saint Venant Hydraulics Laboratory, DTecEMF, Cerema*, Chatou, France.

2017 **Visiting academic**, *Cambridge Coastal Research Unit, Department of Geography, University of Cambridge*, Cambridge, UK.

2010–2011 **Geological engineer**, *Coastal Risks Group, BRGM*, Orléans, France.

2009–2010 **Postdoctoral researcher**, *Scripps Institution of Oceanography*, La Jolla, CA, USA.

2003–2009 **Graduate student researcher**, *Scripps Institution of Oceanography*, La Jolla, CA, USA.

2002 **Research internship, *Research Experience for Undergraduates***,
Horn Point Laboratory, University of Maryland, Cambridge, MD, USA.

2002 **Research internship**, *MIT*, Cambridge, MA, USA.

2001 **Research internship**, *Consorzio Venezia Nuova*, Venice, Italy.

Teaching experience

2016-present **Maritime Works**, *Lecturer*, ENPC, Champs-sur-Marne, France.

2013-present **Sea State, Coastal Waves and Morphodynamics**, *Lecturer*, ENSTA, Palaiseau, France.

2016,2019 **LNHE and LHSV Free surface hydraulics training session : Waves and coastal hydrodynamics classes**, *Lecturer*, EDF R&D, Chatou, France.

2011–2013 **Scientific English**, *Lecturer*, ENS Cachan, Cachan, France.

2007 **The Oceans**, *Teaching assistant*, University of California, San Diego, La Jolla, CA, USA.

2003–2009 **Physics and mathematics tutor (high school level)**, *Breyer's Branches*, Solana Beach, CA, USA.

2002 **Waste Containment and Remediation Technology**, *Teaching assistant*, MIT, Cambridge, MA, USA.

Advising experience

Postdoctoral researchers

2017-2019 **B. Simon**, *IRPHE, Marseille, France*, Integrating the effects of wave breaking and optimizing a 3D deterministic, fully nonlinear potential flow wave propagation model *(co-advised with M. Benoit)*.

2017-2018 **C. Papoutsellis**, *IRPHE, Marseille & LHSV, Chatou, France*, Wave breaking in a fully nonlinear and dispersive potential flow model *(co-advised with M. Benoit)*.

2015 **M. Gervais**, *LHSV, Chatou, France*, Mitigating beach erosion in storm conditions with a submerged breakwater *(co-advised with D. Pham Van Bang)*.

PhD students

2019–2020 **M. Igigabel**, *Cerema, Plouzané, France*, Systems to protect against marine flooding *(PhD based on work experience, co-advised with Y. Diab)*.

2018–2021 **T. Chataigner**, *LHSV, Chatou, France*, Integrating alongshore processes in the beach morphodynamic evolution *(co-advised with N. Le Dantec, N. Goutal)*.

2014–2016 **C. Raoult**, *LHSV, Chatou, France*, Modeling nonlinear waves in the coastal zone *(co-advised with M. Benoit)*.

Masters and engineering students

2019 **N. Cailler**, *LHSV, Chatou, France*, Empirical modeling of beach morphological evolution and shoreline dynamics : sea-level rise impacts *(co-advised with N. Le Dantec)*.

2019 **C. Petton**, *LHSV, Chatou, France*, Empirical modeling of beach morphological evolution and shoreline dynamics : wave climate change impacts *(Masters, co-advised with N. Le Dantec)*.

2018 **M. Leary**, *LHSV, Chatou, France*, Extension of an equilibrium beach change model to include alongshore transport processes *(Masters, co-advised with N. Le Dantec, F. Floc'h)*.

2017 **M. De Carlo**, *LHSV, Chatou, France*, Validating the morphological change model XBeach to simulate submerges breakwater beach erosion reduction experiments *(Masters, co-advised with D. Pham Van Bang)*.

2017 **G. Bouvard**, *UBO, Brest, France*, Application and calibration of an equilibrium model applied to a beach-dune system at Guisseny beach *(Engineer, co-advised with N. Le Dantec, F. Floc'h)*.

2016 **D. Tasing**, *LHSV, Chatou, France*, Optimization of the wave propagation model Misthyc *(Masters)*.

2016 **C. Ghitui**, *LHNE, EDF R&D, Chatou, France*, Comparing wave propagation models *(Masters, co-advised with M. Andreevsky, A. Joly)*.

2016 **M. C. Lemos Rodríguez**, *UBO, Brest, France*, Predicting shoreline change using equilibrium models : Porsmilin, France *(Masters, co-advised with N. Le Dantec, F. Floc'h)*.

2011 **E. Salaï**, *BRGM, Orléans, France*, Multidecadal shoreline change of atolls : Manihi and Scilly *(co-advised with G. Le Cozannet)*.

Undergraduate interns/projects

2019 **ENPC tutor for professional internship**, *M. Queijeiro Rilo*, EGIS.

2019 **ENSTA tutor for scientific internship**, *X. Lastiri*, UPPA.

2013, 2015 **Tutor for internships abroad**, *2-3 students per year*, ENPC.

2014 **Intern, ENPC**, *P. Desbrières*, LHSV, Chatou, France,
Modeling waves in the coastal zone *(co-advised with M. Benoit)*.

Projects

2019 **ISblue**, *Interdisciplinary graduate School for the blue planet : Incoming PhD Student Mobility (2 months) for Jennifer Montano Munoz*, French co-host.

2018-2020 **Programme Hubert Curien (PHC) Sakura**, *Predicting decadal-scale shoreline evolution integrating the impacts of climate change*, French project leader.

2017-2020 **ANR-France Energies Marines (FEM)**, *Modeling and observation of extreme sea states with wave breaking for Renewable Marine Energy applications (DiMe)*, Cerema Scientific coordinator, post-doctoral researcher co-advisor.

2017 **ANR Labex MEC**, *Wave breaking : physical, mathematical and numerical studies (DEPHYMAN)*, Participant, post-doctoral researcher co-advisor.

2015-2016 **Geocorail contract**, *Laboratory experiments of reducing storm-induced beach erosion with submerged strcutres*, Participant, post-doctoral researcher co-advisor.

2011-2015 **National Project EMACOP**, *Marine, Coastal, and Port Energy*, Participant.

2010-2013 **ANR CECILE**, *Coastal Environment Changes Impact of sea LEvel*, Participant.

2009-2014 **FP7 THESEUS**, *Innovative technologies for safer European coasts in a changing climate*, Participant.

Refereed Publications

[1] A. Varing, J.-F. Filipot, S. Grilli, R. Duarte, V. Roeber, and **Yates, M. L.** A new kinematic breaking onset criterion for spilling and plunging breaking waves in shallow water. *Coast. Eng.*, submitted, 2019.

[2] B. Simon, C. Papoutsellis, M. Benoit, and **Yates, M. L.** Comparing methods of modeling depth-induced breaking of irregular waves with a fully nonlinear potential flow approach. *J. Ocean Eng. Mar. Energy*, submitted, 2019.

[3] C. Papoutsellis, **Yates, M. L.**, B. Simon, and M. Benoit. Modeling of depth-induced wave breaking in a fully nonlinear free-surface potential flow model. *Coast. Eng.*, revision submitted, 2019.

[4] C. Raoult, **Yates, M. L.**, and M. Benoit. Development and validation of a 3D RBF-spectral model for coastal wave simulation. *J. Comp. Phys.*, 378 :278–302, 2019.

[5] C. Lemos, F. Floc'h, **Yates, M. L.**, N. Le Dantec, V. Marieu, K. Hamon, V. Cuq, S. Suanez, and C. Delacourt. Equilibrium modeling of the beach profile on a macrotidal embayed low tide terrace beach. *Ocean Dynamics*, 68 :1207–1220, 2018.

[6] M. Benoit, C. Raoult, and **Yates, M. L.** Analysis of the linear version of a highly dispersive potential water wave model using a spectral approach in the vertical. *Wave Motion*, 74C :159–181, 2017.

[7] A. Doria, R. T. Guza, W. C. O'Reilly, and **Yates, M. L.** Observations and modeling of San Diego beaches during El Niño. *Cont. Shelf Res.*, 124 :153–164, 2016.

[8] C. Raoult, M. Benoit, and **Yates, M. L.** Validation of a fully nonlinear and dispersive wave model with laboratory non-breaking experiments. *Coast. Eng.*, 114 :194–207, 2016.

[9] B. Ludka, R. Guza, W. C. O'Reilly, and **Yates, M. L.** Field evidence of beach profile evolution toward equilibrium. *J. Geophys Res.*, 120(11) :7574–7597, 2015.

[10] **Yates, M. L.** and M. Benoit. Accuracy and efficiency of two numerical methods of solving the potential flow problem for highly nonlinear and dispersive water waves. *Intl. J. Num. Meth. Fluids*, 77 :616–640, 2015.

[11] G. Le Cozannet, M. Garcin, **Yates, M.**, D. Idier, and B. Meyssignac. Approaches to evaluate the recent impacts of sea-level rise on shoreline changes. *Earth Science Reviews*, 138 :47–60, 2014.

[12] G. Le Cozannet, M. Garcin, L. Petitjean, A. Cazenave, M. Becker, B. Meyssignac, P. Walker, C. Devilliers, O. Le Brun, S. Lecacheux, A. Baills, T. Bulteau, **Yates, M.**, and G. Wöppelmann. Exploring the relation between sea level rise and shoreline erosion using sea level reconstructions : an example in French Polynesia. *J. Coast. Res.*, SI 65 :2137–2142, 2013.

[13] G. Le Cozannet, M. Garcin, T. Bulteau, **Yates, M. L.**, M. Méndez, A. Baills, D. Idier, and C. Oliveros. An AHP-derived method for mapping the physical vulnerability of coastal areas at regional scales. *Nat. Hazards Earth Syst. Sci.*, 13 :1209–1227, 2013.

[14] **Yates, M. L.**, G. Le Cozannet, M. Garcin, E. Salaï, and P. Walker. Multidecadal atoll shoreline change on Manihi and Manuae, French Polynesia. *J. Coast. Res.*, 29(4) :870–882, 2013.

[15] **Yates, M. L.** and G. Le Cozannet. Evaluating european coastal evolution using bayesian networks. *Nat. Hazards Earth Syst. Sci.*, 12 :1173–1177, 2012.

[16] **Yates, M. L.**, G. Le Cozannet, and N. Lenôtre. Quantifying errors in long-term coastal erosion and inundation hazard assessments. *J. Coast. Res.*, SI 64 :260–264, 2011.

[17] **Yates, M. L.**, R. T. Guza, W. C. O'Reilly, J. E. Hansen, and P. L. Barnard. Equilibrium shoreline response of a high wave energy beach. *J. Geophys. Res.*, 116(C04014), 2011.

[18] **Yates, M. L.**, R. T. Guza, and W. C. O'Reilly. Equilibrium shoreline response : Observations and modeling. *J. Geophys. Res.*, 114(C09014), 2009.

[19] **Yates, M. L.**, R. T. Guza, W. C. O'Reilly, and R. J. Seymour. Overview of seasonal sand level changes on southern California beaches. *Shore & Beach*, 77(1) :39–46, 2009.

[20] **Yates, M. L.**, R. T. Guza, W. C. O'Reilly, and R. J. Seymour. Seasonal persistence of a small southern California beach fill. *Coast. Eng.*, 56 :559–564, 2009.

[21] **Yates, M. L.**, R. T. Guza, R. Gutierrez, and R. Seymour. A technique for eliminating water returns from lidar beach elevation surveys. *J. Atmos. Oc. Tech.*, 25(9) :1671–1682, 2008.

Conference Proceedings

- Simon, B., Papoutsellis, C., Benoit, M., **Yates, M.**, 2018. Modélisation du déferlement du à la bathymétrie dans un code de simulation des vagues non-linéaires et dispersives en zone côtière. Proc. 16èmes Journée de l'Hydrodynamique, Marseille, France, 11p.
- Varing, A., Filipot, J. F., Roeber, V., Duarte, R., **Yates-Michelin, M.**, 2018. A Discussion on the Wave Breaking Criteria of Shallow Water Ocean Waves. Proc. 16èmes Journée de l'Hydrodynamique, Marseille, France, 11p.
- Christie, E. K., Möller, I., Spencer, T., **Yates, M.**, 2018. Modelling Wave Attenuation due to Salt Marsh Vegetation using a Modified SWAN Model. Proc. 36th International Conference on Coastal Engineering, Baltimore, MD, USA, 9p.
- Igigabel, M., **Yates, M.**, 2018. Cost study of coastal protection. Proc. 36th International Conference on Coastal Engineering, Baltimore, MD, USA, 12p.
- Michard, B., Bouland, S., **Yates, M.**, Varing, A., Filipot, J.-F., Sergent, P., 2018. Projet EMACOP : mesures in-situ de houle versus le modèle numérique SWASH sur le site d'Esquibien (Finistère). Proc. XVèmes Journées Nationales Génie Côtier – Génie Civil, La Rochelle, France, 12p.
- Lemos, C., Floc'h, F., **Yates, M.**, Le Dantec, N., Marieu, V., Hamon, K., Cuq, V., Suanez, S., Delacourt, C., 2017. *Equilibrium modeling of the shoreline position on a macrotidal embayed beach*, Proc. Coastal Dyanmics, Helsingør, Denmark, 12p.
- Raoult, C., **Yates, M. L**., Benoit, M., 2016. *Modeling viscous effects in a fully nonlinear and dispersive potential model*, Proc. 15èmes Journées de l'Hydrodynamique, Brest, France, 16p.
- Raoult, C., Benoit, M., **Yates, M. L.**, 2016. *Développement d'un modèle numérique non-linéaire et dispersif pour la propagation des vagues en zone côtière*, Proc. GCGC, Toulon, France, 12p.
- Gervais, M., Pham Van Bang, **Yates, M.**, D., Vidal, V., Benoit, M., 2016. *Réduire l'érosion des plages lors des tempêtes grâce à des structures immergées : une étude expérimentale comparative en canal à houle*, Proc. GCGC, Toulon, France, 9p.
- Gervais, M., Pham Van Bang, D., Vidal, V., **Yates, M.**, Benoit, M., 2015. *Mitigating beach erosion in storm conditions with a submerged breakwater : an experimental study*, Coastal and Maritime Mediterranean Conference, Ferrara, Italie, 5p.
- **Yates, M. L.**, Benoit, M., Raoult, C., 2015. *Fully nonlinear and dispersive of nearshore wave modeling : accuracy and efficiency of two methods of solving the potential flow problem*, Proc. IWWWFB, Bristol, UK, 4p.
- Raoult, C., Benoit, M., **Yates, M. L.**, 2014. *Etude et qualification d'un modèle numérique complètement non-linéaire et dispersif pour les vagues en zone côtière*, Proc. GCGC, Dunkerque, France, 10p.
- Benoit, M., Raoult, C., , **Yates, M. L.**, 2014. *Fully nonlinear and dispersive modeling of surf zone waves : non-breaking tests*, Proc. ICCE, Seoul, South Korea, 10p.
- Benoit, M., **Yates, M. L.**, Chazel, F., 2013. *A comparison of simulation approaches based on the Zakharov equations*, Proc. IWWWFB, Le Croisic, France, 4p.
- **Yates, M. L.**, Benoit, M., 2012. *Modélisation Non-linéaire et Dispersive des Vagues en Zone Côtière : Ètude Comparative de Deux Méthodes de Simulation Précises*, Proc. 13èmes Journées de l'Hydrodynamique, Chatou, France, 13p.
- Le Cozannet, G., Cazenave, A., Garcin, M., Becker, M., Donato, V., Rogel, P., Salas Y Melia, D., Walker, P., Woppelmann, G., **Yates, M.**, 2011. *L'élévation récente du niveau marin et l'érosion côtière : le cas d'îles océaniques du Pacifique*. Geosciences, 14, 92-99.
- Le Cozannet, G., N. Lenôtre, **M. Yates**, P. Nacass, B. Colas, C. Pérherin, C. Peinturier, C. Vanroye, C. Hajji, B. Poupat, C. Azzam, J. Chemitte, and F. Pons, 2010. Climate Change impact, adaptation and associated costs for coastal riske in France. *Littoral 2010, Conference Proceedings*, London, UK, 21-23 September 2010.
- Sanford, L.P., P. Dickhudt, L. Rubiano-Gomez, **M. Yates**, S. Suttles, C.T. Friedrichs, D. Fugte, and H. Romaine, 2005. Variability of suspended particle concentrations, sizes and settling velocities in the Chesapeake Bay turbidity maximum. *In* Flocculation in Natural and Engineered Environmental Systems. I.G. Droppo, G. G. Leppard, P. Liss, and T. Milligan, Eds. Boca Raton, Florida, CRC Press, LLC : 221-236. UMCES Contribution No. 3597.

Conferences

- Raoult, C., **M. L. Yates** (presenter), Benoit, M. A Nonlinear and Dispersive 3D Model for Coastal Waves using Radial Basis Functions, *International Conference on Coastal Engineering*, Baltimore,

MD, USA, 2018.
- De Carlo, M., **M. L. Yates** (presenter), D. Pham Van Bang, M. Gervais, V. Vidal. Evaluating Storm Erosion on Beaches Protected by Submerged Structures with XBeach, *XBeach X Users Conference*, Delft, Netherlands, 2017.
- **Yates, M. L.**, M. Benoit, C. Raoult. Fully nonlinear and dispersive nearshore wave modeling : accuracy and efficiency of two methods of solving the potential flow problem, *IWWWFB*, Bristol, UK, 2015.
- **Yates, M. L.**, M. Benoit. Accurate modeling of nonlinear and dispersive waves in the coastal zone, *WISE*, College Park, MD, USA, 2013.
- **Yates, M. L.**, M. Benoit. Modélisation Non-linéaire et Dispersive des Vagues en Zone Côtière : Étude Comparative de Deux Méthodes de Simulation Précises, *Journées de l'Hydrodynamique*, Chatou, France, 2012.
- **Yates, M. L.**, G. Le Cozannet, N. Lenôtre. Quantifying errors in long-term coastal erosion and inundation hazard assessments.*International Coastal Symposium*, Szczecin, Poland, 2011.
- Le Cozannet, G., N. Lenôtre, **M. Yates** (presenter), P. Nacass, B. Colas, C. Pérherin, C. Peinturier, C. Vanroye, C. Hajji, B. Poupat, C. Azzam, J. Chemitte, F. Pons. Climate change impact, adaptation and associated costs for coastal risks in France. *Littoral 2010*, London, UK, 2010.
- **Yates, M.L.**, J.E. Hanson, W.C. O'Reilly, P.L. Barnard, and R.T. Guza (presenter). Equilibrium Shoreline Change at Ocean Beach, San Francisco, CA. *Ocean Sciences Meeting*, Portland, OR, 2010.
- **Yates, M.L.**, R.T. Guza, R.J. Seymour, W.C. O'Reilly, and A. Young. Alongshore Variability of Shoreline Change and Geologic Factors. *AGU, Fall Meeting*, San Francisco, CA, 2008.
- **Yates, M.L.**, R.T. Guza, W.C. O'Reilly, and R.J. Seymour. Overview of Seasonal Sand Level Changes on Southern California Beaches, *ASBPA National Coastal Conference : Sustainable Shorelines*, Chicago, IL, 2008.
- **Yates, M.L.**, and R.T. Guza. Seasonal Sand Level Changes on Southern California Beaches : Observations and Modeling, *Physical Oceanography Dissertation Symposium*, Honolulu, HI, 2008.
- **Yates, M.L.**, R.T. Guza, R.J. Seymour, and W.C. O'Reilly. Sand Level Changes and Beach Equilibrium Concepts, *International Conference of Coastal Engineering*, Hamburg, Germany, 2008.
- **Yates, M.L.**, R.T. Guza, R.J. Seymour, and W.C. O'Reilly. Seasonal Beach Changes and Equilibrium Concepts. AGU, *Ocean Sciences Meeting*, Orlando, FL, 2008.
- **Yates, M.L.**, R.T. Guza, R.J. Seymour, and W.C. O'Reilly. Seasonal Sand Level and Wave Variability on Southern California Beaches. *California and the World Ocean*, Long Beach, CA, 2006.
- **Yates, M.L.**, R.T. Guza, R.J. Seymour, W.C. O'Reilly, and J.O. Thomas. Seasonal Sand Level and Wave Variability on Southern California Beaches. *International Conference of Coastal Engineering*, San Diego, CA, 2006.
- **Yates, M.L.**, R. Guza, R. Seymour, W. O'Reilly, and R. Gutierrez. Seasonal Changes in Sand Level and Wave Energy on Southern California Beaches. *Ocean Sciences Meeting*, Honolulu, HI, (poster), 2006.
- Madsen, O.S. and **Yates, M.L.**. On Wave Reflection from Beaches. *International Conference of Coastal Engineering*, Lisbon, Portugal, 2004.
- **Yates, M.L.**, Sanford, P. , Dickhudt, P., and Suttles, S. E. Video In Situ Settling Tube Apparatus Characterization of Sediments in the Estuarine Turbidity Maximum Zone of the Chesapeake Bay. *ASLO, Aquatic Sciences*, (poster), 2003.

Seminars

2018	**PARI**, *Port and Airport Research Institute*, Kurihama, Japan.
2017	**CCRU**, *Department of Geography, University of Cambridge*, Cambridge, UK.
2016	**GDR TransNat**, Roscoff, France.
2015	**ANGE Laboratory**, *Université Pierre et Marie Curie*, Paris, France.
2012	**CETMEF**, Compiègne, France.
2011	**LNHE**, *EDF R&D*, Chatou, France.
2009	**BRGM**, Orléans, France.
2009	**L'OCEAN**, *Université Pierre et Marie Curie*, Paris, France.
2008	**COM**, *Université de la Méditerranée*, Marseille, France.
2008	**EPOC**, *Université de Bordeau 1*, Bordeaux, France.

Workshops

2018	**GLADYS workshop**, *CNRS*, Saint Julien en Vercors, France.
2017	**Delft Software Days 2017**, *Deltares*, Delft, The Netherlands.
2016	**B'WAVES 2016**, *University of Bergen*, Bergen, Norway.
2015	**GLADYS-Littoral workshop**, *CNRS*, Allègre-les-Fumades, France.
2015	**Wave propagation in complex media**, Cargèse, Corse, France.
2013	**HYDRALAB Young Researchers Conference on Floating Bodies**, *IFREMER*, Plouzané, France.
2012	**Parallel Computing : MPI**, *IDRIS*, Orsay, France.
2010	**ArcGIS**, *BRGM*, Orléans, France.

Field work

2009	**Imperial Beach Field Experiment**, Imperial Beach, California, USA, Large scale observations of chlorophyll, bacteria, passive tracer and drifter dispersion in the surf zone.
2006	**Huntington Beach Field Experiment**, Huntington Beach, California, USA, Observations of currents and chlorophyll, bacteria, passive tracer and drifter dispersion in the surf zone.
2002	**R/V Cape Henlopen**, Chesapeake Bay, MD, USA, Cruise observations of suspeneded sediments in the turbidity maximum zone of the Chesapeake Bay.

Awards and Honors

2008	American Shore and Beach Preservation Association Educational Award
2007–2008	Achievement Rewards for College Scientists Scholar
2007	California Shore and Beach Preservation Associate Weigel Scholarship
2004–2007	National Defense Science and Engineering Graduate Fellowship
2003–2004	T.R. and Edith Folsom Graduate Fellowship
2003	Outstanding Student Poster Award, ASLO Aquatic Sciences Meeting
2001	Gilbert Winslow Scholarship

Service

Administrative responsabilities

- Interim head of the Cerema LRHE laboratory (since 2018)
- Co-leader of the *Waves and coastal and maritime risks* research group of the LHSV (since 2015)
- Coordinator of the *Journée des doctorants LHSV* (2016-2019)
- Co-contributor to the LHSV website
- Participant in the Work Group : Research and Innovation, Direction technique Eau, mer et fleuves, Cerema

Reviewer

Delaware Sea Grant, Earth Surface, EWTEC, Geo-Marine Letters, Journal of Coastal Research, Journal of Geophysical Research–Earth, Journal of Geophysical Research–Oceans, Journal of Marine Systems, Journal of Waterway, Port, Coastal, and Ocean Engineering, Marine Geology, Ocean Dynamics, Ocean Engineering, Ocean Modelling

Appendix C

Articles: Coastal morphological evolution

C.1 Yates et al. (2013)

Journal of Coastal Research | 29 | 4 | 870–882 | Coconut Creek, Florida | July 2013

www.cerf-jcr.org

Multidecadal Atoll Shoreline Change on Manihi and Manuae, French Polynesia

Marissa L. Yates[†]*, **Gonéri Le Cozannet**[†], **Manuel Garcin**[†], **Emilie Salaï**[‡], and **Patrice Walker**[§]

[†]Bureau de Recherches Géologiques et Minières
3 avenue Claude Guillemin
45060 Orléans, France
marissa.yates-michelin@developpement-durable.gouv.fr

[‡]Université de Caen Basse-Normandie
Esplanade de la Paix
14032 Caen, France

[§]Creocean Zone Technocean
Rue Charles Tellier
17000 La Rochelle, France

ABSTRACT

www.JCRonline.org

Yates, M.L.; Le Cozannet, G.; Garcin, M.; Salai, E., and Walker, P., 2013. Multidecadal atoll shoreline change on Manihi and Manuae, French Polynesia. *Journal of Coastal Research,* 29(4), 870–882. Coconut Creek (Florida), ISSN 0749-0208.

As interest in the impact of sea-level rise on atoll islands increases, this study contributes to the growing database of observations of shoreline changes on South Pacific Islands, where few observations are currently available. Historical aerial photographs and recent satellite images were used to evaluate multidecadal surface area and shoreline changes on two atolls in French Polynesia: Manihi and Manuae. During the 40- to 50-year study period, atoll island surface area primarily increased or remained stable on Manihi and decreased on Manuae. Distinct ocean and lagoon shoreline changes were observed in different geographical regions of each atoll. On Manihi, ocean shoreline accretion rates were larger on the NW rim than the SE rim. On Manuae, atoll islands on the NE rim were eroding on the lagoon side and accreting on the ocean side, whereas islands on the SE rim showed the opposite trend. Sea-level rise is often thought to cause atoll erosion, but in this study, lagoon and ocean shorelines both eroded and accreted over a period when sea-level rise rates were greater than the global mean. Surface area changes related directly to anthropogenic activities were identified on only two of the 47 atoll islands. After completing a classification of the incident wave field, it was hypothesized that waves have an important role in controlling the shoreline change variability. Additional field surveys and *in situ* observations are needed to validate this hypothesis and to understand better island response to changing forcing factors.

ADDITIONAL INDEX WORDS: *Sea-level rise, climate change, erosion, South Pacific.*

INTRODUCTION

Atolls are midocean reef islands that may be highly vulnerable to changes in climatic forcing because of their low-lying morphology and exposure to a variety of ocean conditions. In particular, small islands on the rims of atolls are considered particularly fragile in the face of future sea-level rise (Nicholls *et al*., 2007), and for this reason, several atoll island nations (*e.g*., Tuvalu, Kiribati) have recently received significant attention in both the media and the scientific community (Connell, 2003).

Atolls are annular coral reef islands that form on midocean volcanic hotspots. Darwin proposed the theory that atolls are the result of two processes: subsidence of the foundation (inactive volcano) and upward growth of corals (Darwin, 1842). Initially, a fringing reef develops around the volcano, which progresses to a barrier reef, and eventually to an atoll, with the continued subsidence of the volcanic landmass and the upward growth of the reef. The subsidence is due to isostatic adjustment, lithospheric flexure, or plate migration away from the hotspot forming the volcano (Woodroffe, 2008). The reef growth is dependent on coral polyps that live near the surface of the water and excrete calcium carbonate to form skeletons. The solid base of the coral reef is composed of calcite and dolomite, which originate from coral skeletons, carbonate sediments created from their erosion, and direct precipitation of calcium carbonate from sea water (Ohde *et al*., 2002; Stoddart, 1969). Therefore, the geologic formation and long-term evolution (on scales of hundreds to thousands of years) of atolls is closely related to the relative sea level and the reef growth rate (*e.g*., Pirazzoli and Montaggioni, 1986; Pirazzoli *et al*., 1988; Stoddart, 1990).

Atoll islands are composed primarily of unlithified biodetrital sediments that are eroded from reefs and accumulate on atoll reef flats (Ohde *et al*., 2002). Atoll islands are highly dynamic environments in which the accumulation and retention of sedimentary deposits depends on the island elevation relative to sea level, as well as the tidal range, wind and wave energy and direction, and local currents (Stoddart, 1990). In addition, complex interactions between a variety of other factors

---

DOI: 10.2112/JCOASTRES-D-12-00129.1 received 6 July 2012; accepted in revision 7 September 2012; corrected proofs received 30 January 2013.

*Present address: Laboratoire d'Hydraulique Saint-Venant, Université Paris-Est (Joint research unit: EDF R&D, CETMEF, Ecole des Ponts ParisTech) 6 quai Watier, B.P. 49 78401 Chatou, France; Present affiliation: Centre d'Etudes Techniques Maritimes Et Fluviales (CETMEF).

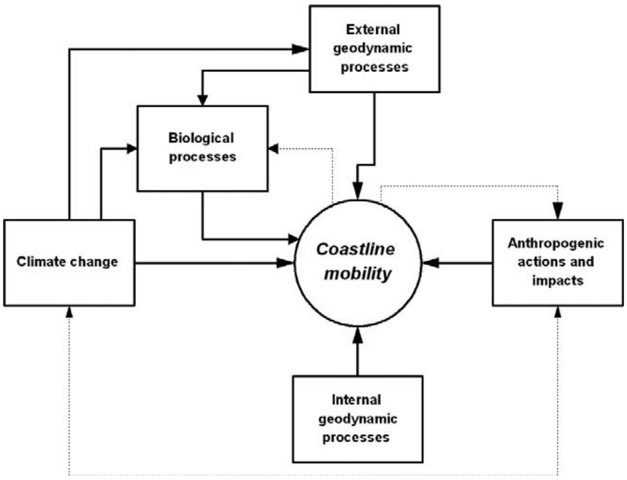

Figure 1. Families of forcing factors that affect coastline mobility, with arrows indicating some of the interactions and feedbacks (from Garcin *et al.*, 2011).

influence the resilience or mobility of island shorelines (Figure 1, Garcin *et al.*, 2011), such as climate change (*e.g.*, wind and wave regimes, precipitation, sea level), internal (*e.g.*, seismic, volcanic activity) and external (sediment fluxes) geodynamic processes, biological processes, and anthropogenic actions and the resultant impacts.

Sea-level rise is commonly perceived to be the most important factor causing the erosion and flooding of atolls (Dickinson, 1999), which may result in their inhabitants becoming the first environmental refugees (Connell, 2003). However, studies of South Pacific Islands have shown that the primary causes of coastal erosion may instead be due to changes in wind and wave patterns (Flood, 1986; Kench *et al.*, 2006), cyclones or tsunamis (Bourrouilh-Le Jan and Talandier, 1985; Dupon, 1984; Harmelin-Vivien, 1994; Stoddart, 1963), or even vertical land movement due to tectonic activity (Ballu *et al.*, 2011). For example, extreme events such as cyclones have been shown to cause both atoll island erosion (Harmelin-Vivien, 1994) and accretion (Maragos, Baines, and Beveridge, 1973), depending on the island sediment composition and exposure to storms (Bayliss-Smith, 1988). Steady waves and cyclones may cause accretion due to the breakup and landward transport of biodetrital reef material, or erosion and flooding due to direct wave impacts, elevated water levels, or strong currents during lagoon flushing. Lagoon flushing is caused by inflow across the reef flat or island overtopping by waves causing an increase in the lagoon water level, which flushes out through atoll passes or channels on the leeward atoll rim (Callaghan *et al.*, 2006). Anthropogenic factors, such as coral and sediment mining, have also been shown to be the primary cause of shoreline erosion on several atolls (Ford, 2012; Xue, 1997). Although anthropogenic impacts may be important on local scales in highly urbanized areas, Salvat *et al.* (2008) suggested that increases in cyclone strength, sea surface temperature, and ocean acidity may be the leading factors affecting atolls in French Polynesia.

There are a limited but growing number of studies evaluating atoll island shoreline changes (Collen, Garton, and Gardner, 2009; Ford, 2012; Kench *et al.*, 2006, and others), and the objective of the current study is to add to this growing database by examining multidecadal island shoreline change on two atolls in French Polynesia. Manihi and Manuae were selected for analysis for three primary reasons: availability of historical aerial photographs allowing a multidecadal shoreline change analysis, minimal human activities, and estimates of elevated sea-level rise rates in this region (see the section “Sea-Level Rise during the Study Period”). In this paper, the remote sensing image analysis and wave classification analysis are described, the shoreline change results for 41 islands on Manihi and six islands on Manuae are presented, and the potential factors causing the observed changes are discussed.

STUDY SITES

Setting

The current study evaluates island evolution on two atolls in French Polynesia: Manihi and Manuae (Figure 2). Manihi (14°25′ S, 145°55′ W) is located at the NW extent of the Tuamotu Islands in the King George Islands, and Manuae, also called Scilly (16°30′ S, 154°40′ W), is located at the NW extent of the Society Islands in the Leeward Islands (Figure 2). The atolls differ in many aspects, including size, geomorphology, exposure to waves, and extent of human development and use.

Manihi has an elongated shape, with major and minor axes of approximately 28 km and 8 km, respectively (Figure 3a). The lagoon has gentler slopes and is less than 30 m deep on the eastern side, but exceeds 30 m depth at the western end near the only deep pass, Tairapa (SHOM, 2007). The tidal range is less than 0.5 m (data from SHOM). More than 60 islands cover the reef flat, ranging in size from 6000 m^2 to approximately 2 km^2. Tourism has developed at Manihi as a result of the construction of an airport and a luxury resort. However, the atoll still has a population of less than 1000 people, who live primarily in the village of Turipaoa. The northern atoll rim is mostly undeveloped, and there is a scattering of homes on the southern atoll rim.

In comparison, Manuae is smaller and nearly circular, with a diameter of approximately 10 km (Figure 3b). Islands exist only on the eastern rim of the atoll, ranging from 0.1 to 1.3 km^2, and the entire western and southern rim is open to the ocean. In this region, Chevalier (1979) observed that the submerged reef flat is covered by only 1–2 m of water. Observations of aligned beachrock sloping toward the lagoon suggest that this part of the atoll rim was once covered in sandy islands that were reworked and eventually entirely eroded by cyclone waves or a tsunami (Barsczus, 1980; Chevalier, 1979; Salvat, 1983).

The lagoon of Manuae is deep, reaching 70 m depth (Venec-Peyre, 1987), but no deep passes exist, and the water exchange between the lagoon and the ocean takes place across the shallow reef flat (Chevalier, 1979). The tidal range is less than 0.3 m (Guilcher *et al.*, 1969). Copra was produced on Manuae in the 1920s, but the plantation is no longer in operation, and in

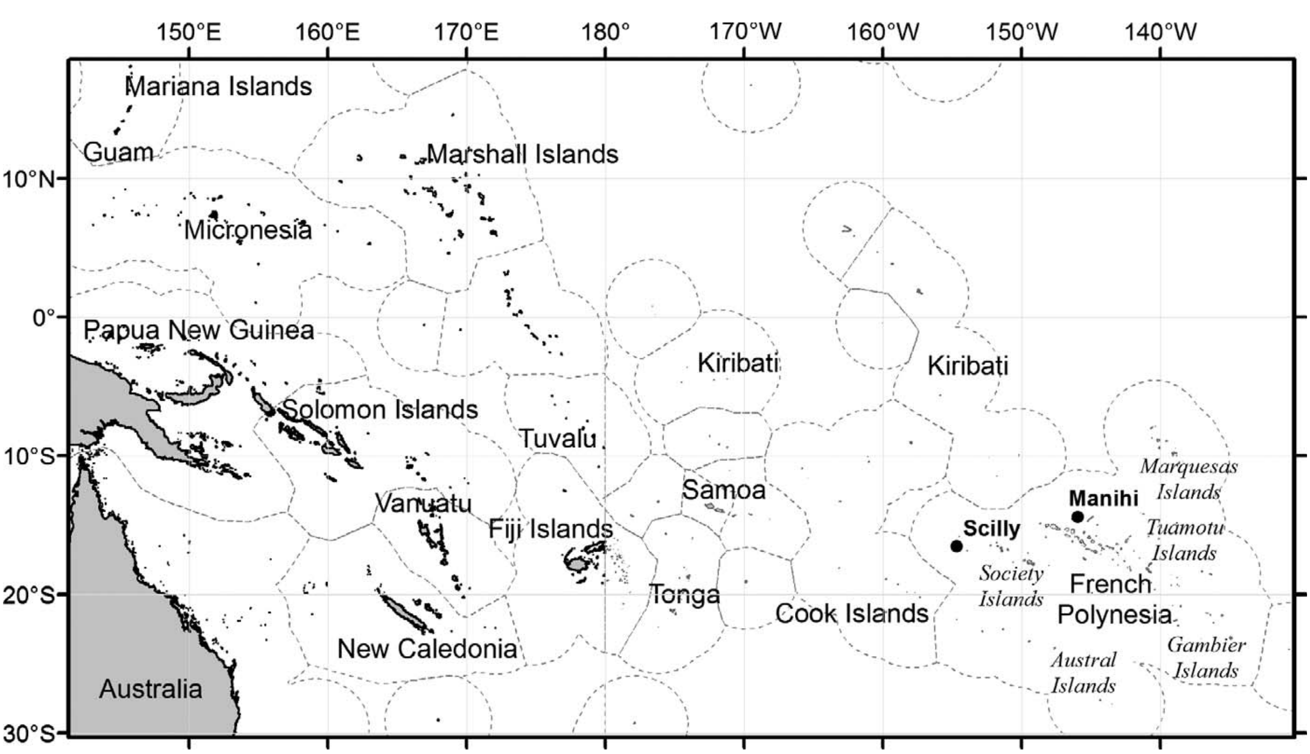

Figure 2. Location of the study sites in the Southern Pacific Ocean: Manihi in the Tuamotu Islands (located to the left of the label) and Manuae in the Society Islands of French Polynesia.

1992, the atoll was designated as a nature reserve. Very few man-made structures were observed on this atoll.

Sea-Level Rise during the Study Period

Global estimates of relative sea-level rise since the beginning of the 20th century indicate a rate of approximately 1.7 ± 0.3 mm/y (Church, White, and Hunter, 2006). High-resolution satellite observations show an accelerated rate of 3.3 ± 0.4 mm/y between 1993 and 2009 (Nicholls and Cazenave, 2010), with significant regional variability primarily due to temperature and salinity variations (Lombard *et al.*, 2005). Satellite observations extending to 2010 show that sea-level rise in the western tropical Pacific was more than three times the global average during this period (Cazenave and Llovel, 2010). However, multidecadal tide gauge records (spanning more than 24 y) on islands within 15° of the equator show peak-to-peak interannual variations of up to ±0.45 m related to the El Niño Southern Oscillation cycle (Church, White, and Hunter, 2006). To investigate multidecadal trends extending beyond the era of satellites, Becker *et al.* (2012) reconstructed sea levels in the Pacific Island Region (between 20°S and 15°N latitude, and 120°E and 135°W longitude) over the 60-year time period from 1950 to 2009 using DRAKKAR model sea surface heights and high-quality, long-term tide gauge measurements. (See Becker *et al.*, 2012; Llovel *et al.*, 2009; and Meyssignac *et al.* 2012 for more details about the reconstruction method.) At Manihi and Manuae, Becker *et al.* (2012) estimate approximately 2.5 and 2.9 mm/y, respectively, of absolute sea-level rise during the last 60 years (Figure 4).

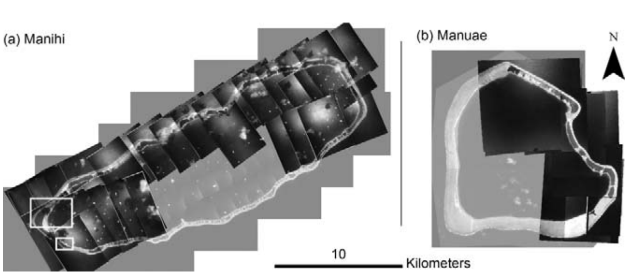

Figure 3. Images of the atolls (a) Manihi and (b) Manuae, showing the historical aerial photographs used in this analysis overlaying the recent aerial photographs and satellite images. The white boxes in (a) indicate the location of the images shown in Figure 9. The southern rim of Manihi was not surveyed in 1961, and the photographs on the western rim of Manuae were not georectified due to the lack of islands.

Becker *et al.* (2012) also caution that local, relative sea-level rise, as felt by the population living on an island, may also be affected by vertical land movements. Direct global positioning system measurements in the Torres Islands showed that subsidence due to tectonic activity nearly doubled the absolute, climate-related sea-level rise (Ballu *et al.*, 2011), but these measurements are not available at Manihi and Manuae. The

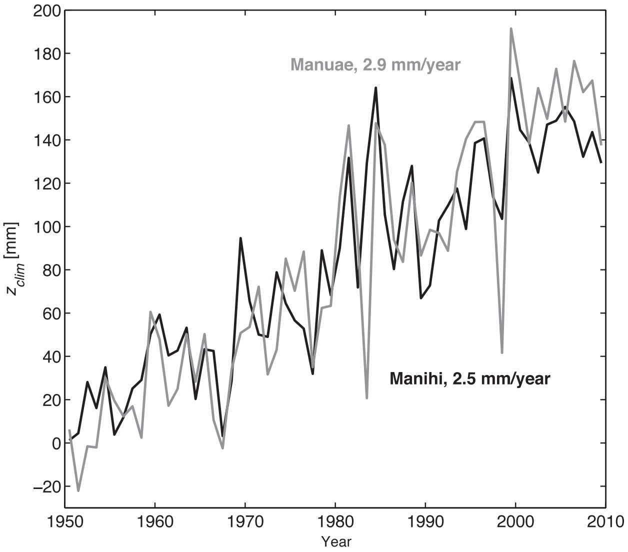

Figure 4. Reconstruction of the climatic component of historic sea-level (z_{clim}) since 1950 (data from the analysis of Becker *et al.*, 2012), indicating the estimated linear sea-level rise trends at Manihi (black) and Manuae (gray).

lack of current hotspots or high volcanic islands in the Tuamotu Islands (Pirazzoli and Montaggioni, 1986), as well as the estimated age (50–60 million years old) of the seamount upon which Manihi formed (Pirazzoli and Montaggioni, 1985), suggest that volcano-isostatic equilibrium and relative vertical stability were likely reached long ago. In comparison, the Society Islands are relatively young, and assuming a constant drift rate of the Pacific Plate, Pirazzoli and Montaggioni (1985) and Barsczus (1980) estimated that the seamount forming the base of Manuae is approximately 5 to 6.5 million years old. Pirazzoli and Montaggioni (1985) concluded that volcano-isostatic phenomena are likely still active near Manuae, estimating a subsidence rate of approximately 0.05 mm/y in the Leeward Islands. Therefore, rates of vertical land movement are assumed to be negligible in comparison with absolute sea-level rise for these two atolls.

Wind and Wave Climate

French Polynesia is primarily exposed to cyclonic waves (originating in the west), trade waves (originating in the east), and southern swell. Two general types of waves are distinguished: seasonal waves that rarely exceed 3 m significant wave height, and cyclone waves that can reach up to 12 m significant wave height (Des Garets, 2005). Swell in this region of French Polynesia usually originates in the SW, in the Southern Ocean or just E of New Zealand, or in the N to NW, in the North Pacific Ocean (Des Garets, 2005).

The atolls of Manihi and Manuae are exposed to different wave conditions given their geographic locations. Manuae is isolated and is exposed to waves originating from all directions, whereas Manihi is shielded from waves originating from the south by the presence of a string of atolls located directly to the south in the Tuamotu Islands (Figure 2). In addition, Manuae is located in a region that is more frequently affected by cyclones than Manihi (Larrue and Chiron, 2010). During the cyclone seasons from 1969/1970 to 2006/2007, twice as many cyclones passed within a 400-km radius of Manuae than Manihi, with 20 and 10 cyclones, respectively (data from the Australian Bureau of Meteorology, 2011).

Table 1. *Image data.*

Atoll	Date	Data source	Image resolution (m)	Scan resolution* (m)
Manihi	1961	Aerial photographs	1 (1:20,000)	0.5
	2001	Aerial photographs	0.5 (1:15,000)	—
Manuae	1955	Aerial photographs	2 (1:40,000)	1
	2008	*Quickbird* satellite images	0.5–0.6	—

* For paper photographs.

METHODS

Image Analysis

Multidecadal shoreline and land surface area changes were examined using historical and recent aerial photographs and recent satellite images (see Table 1; data provided by the Service of Urbanization of French Polynesia). The scanned images were georectified and georeferenced using ArcGIS software. Owing to the lack of conventional permanent reference points (*e.g.*, survey datum points, Thieler and Danforth, 1994), secondary reference points were used to georectify the photographs. Secondary reference (or control) points are features that are stable and clearly identifiable in the historical and recent images, such as corners of buildings, ends of jetties, road intersections, *etc*. (Crowell, Leatherman, and Buckley, 1991). On Manihi and Manuae, very few permanent buildings or roads were located in both sets of images (only in the village of Turipaoa on Manihi). Therefore, natural geomorphological features, including distinctly shaped beach rock outcrops (on the ocean and lagoon side of the atoll rim) and lagoon coral pinnacles, were used to georectify the historical photographs, assuming that these distinct features have not changed significantly. Errors induced by changes in these geomorphological features contribute to the root-mean-square error of each georectified image. In total, 49 photographs of Manihi and 12 photographs of Manuae (Figure 3) were georectified in ArcGIS using second-order polynomials with an average of 32 secondary reference points in each photograph, resulting in root-mean-square errors of 1 to 4 m for each photograph.

Shoreline and surface area changes were estimated by measuring the movement of the vegetation limit between two survey dates (Table 1, following Ford, 2012; Webb and Kench 2010; and others). Thieler and Danforth (1994) suggest that the vegetation limit may be used as an indicator of shoreline position, especially when historical records of more commonly used proxies, such as the mean high water line or evidence of the wet/dry or high tide line (Crowell, Leatherman, and Buckley, 1991), are not available for long-term analyses. This proxy is particularly adapted to evaluating multidecadal changes (Ford, 2012; Garcin *et al.*, 2008), since it is a rather stable indicator of shoreline changes that typically vary on the scale of months to years instead of the higher-frequency changes measured by other proxies (Hoeke, Zarillo, and Synder, 2001). Ford (2012) also pointed out the drawback to using the vegetation limit as a proxy for the shoreline position, noting that the beach width or volume may change without causing a change in the vegetation limit.

To identify the seaward vegetation limit for each island, overlapping aerial photographs were superposed (Figure 3), and the highest quality images (with high color contrast and no cloud cover) were used to digitalize manually the vegetation limit. The repeatability of the method was evaluated and will be discussed in the "Shoreline Change Uncertainties" section. A portion of the southern rim of Manihi was not photographed during the aerial flight in 1961 (Figure 3); therefore, estimates of island change were not calculated in this region.

With the digitalized shorelines, two different measures of island changes were analyzed: surface area and shoreline position. Surface area changes were calculated as the difference between the digitalized polygons using the ET GeoWizards toolbox in ArcGIS. Shoreline change was calculated using the Digital Shoreline Analysis System (Thieler *et al.*, 2009) in ArcGIS, on transects with 100-m alongshore spacing. The average change in shoreline position was calculated for the ocean and lagoon shore of each island, following Webb and Kench (2010). Surface area changes estimate the net change in vegetated land area, while the two measures of shoreline change distinguish between ocean and lagoon erosion and accretion processes.

Wave Analysis

In order to examine the wave exposure of Manihi and Manuae, data were obtained from the hindcast wave model WaveWatch III, run by IFREMER (with 0.25° spatial resolution in a zone around French Polynesia, during the period from 1997 to 2011, Ardhuin *et al.*, 2010). While this time period is short for evaluating interannual variability or calculating extreme event statistics, it allows a preliminary evaluation of the differences in the annual wave fields affecting the two atolls.

To quantify the wave field, two model points were extracted at Manihi (located off the NW and SE shores, at –14.35°N, 146.05°W and –14.45°N, 145.85°W, respectively), and one model point was extracted near Manuae (located to the E, at –16.55°N, –153.3°E). Manuae is located 150 km to the west of the high spatial resolution model domain, thus the closest model grid point was selected for the analysis. The modeled wave field at this point is assumed to be representative of the wave field observed at Manuae, since the atoll is isolated and no obstructions exist between the atoll and the model output location.

Clustering algorithms are a classic approach used to identify the dominant wave classes in wave time series (Butel, Dupuis, and Bonneton, 2002). A variety of different methods are available, and here, a K-means algorithm is used to distinguish the dominant wave classes by their significant wave height, peak period, and mean wave direction, as in Le Cozannet *et al.* (2011). The number of wave classes (15) was chosen empirically, as a compromise between resolving too many distinct wave events (thus making the interpretation difficult) and isolating the most important observed classes. These wave classes may then be regrouped into well-known wave modes (*e.g.*, trade waves, southern swell) based on the analysis of the physical characteristics and seasonality of the wave classes.

Shoreline Change Uncertainties

Errors in estimated shoreline change arise from a variety of different sources: image resolution, aerial photograph georectification, and shoreline digitalization. Taking into account the scale of the photographs and the scan resolution, the images have a resolution of between 1 and 2 m *per* pixel (see Table 1). Average shoreline change errors resulting from the identification of the shoreline using different photographs (*i.e.,* errors associated with the image georectification) and the interpretation of the shoreline location by different users, were 0.5 m and 1 m, respectively. Taking into account the digitalization, pixel size, and georectification errors, average shoreline changes of less than 5 m were not considered significant and were interpreted as stable shorelines.

RESULTS

The islands on Manihi were generally stable or increasing in surface area (Figure 5), while the islands on Manuae were generally eroding or decreasing in surface area (Figure 6). In addition, within each atoll, island shoreline change rates showed distinct ocean and lagoon shoreline trends depending on their geographic location.

Manihi Surface Area and Shoreline Changes

In total, only two small islands on Manihi (4%) decreased in surface area between 1961 and 2001, while approximately 29% of the islands were stable, and 67% increased in surface area (Figure 5a). The islands on the NW rim of the atoll increased in surface area, while the islands on the SE atoll rim either increased in surface area or remained in dynamic equilibrium.

The estimated lagoon (R_{LAGOON}) and ocean (R_{OCEAN}) shoreline change rates (Figure 7a) also show distinct trends on the NW and SE atoll rims (zones separated schematically by the black line in Figure 5a). Less than half of the islands on the SE rim have significant (larger than the estimated errors) ocean or lagoon shoreline change rates, and the observed trends are relatively small (triangles, Figure 7a). In comparison, islands on the NW rim have ocean shoreline accretion rates that are up to twice as large (open circles, Figure 7a). No distinct trends in lagoon shoreline changes were observed.

Evidence of these distinct trends in surface area and shoreline change is seen in two examples of islands on the NW and SE atoll rims (Figure 5). In Figure 5b, shoreline accretion is observed on the ocean side of the island, particularly on the E end, where a small island increased in size and eventually became attached to the neighboring island. In comparison, in Figure 5c, three small islands on the SE rim showed little or no net change during the 40-year period.

Manuae Surface Area and Shoreline Changes

Unlike Manihi, the majority of the islands on Manuae (five out of six) decreased in surface area between 1955 and 2008 (Figure 6a). However, the erosion occurred on different sides of the islands depending on their geographic location (zones

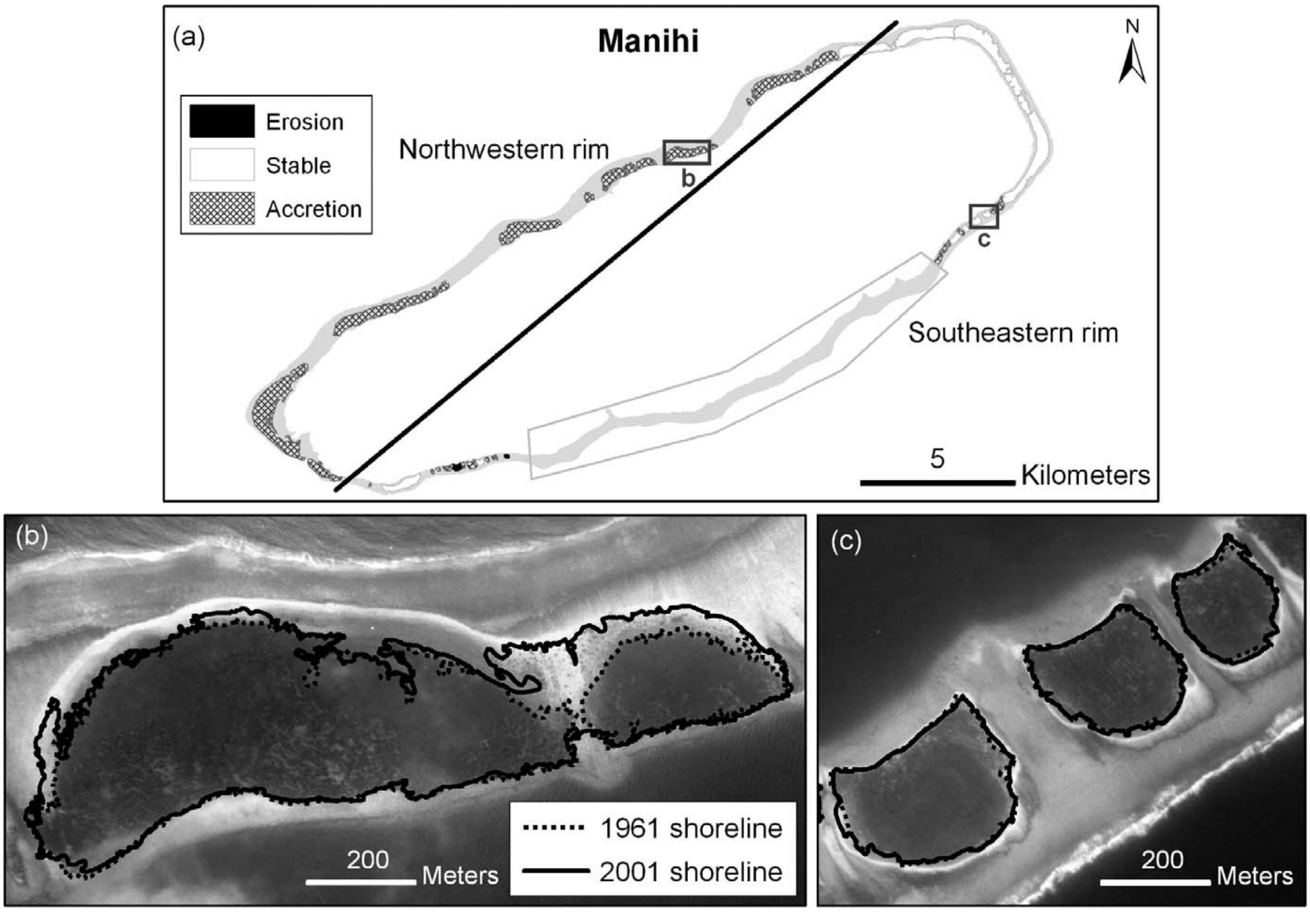

Figure 5. Observed changes on Manihi: (a) surface area changes for each island, and examples of 1961 (dotted line) and 2001 (solid line) shorelines, overlaid on the historical aerial photographs for islands on the (b) northern and (c) southern atoll rims. The lettered boxes in (a) indicate the location of insets (b) and (c).

separated schematically with the black line in Figure 6a). Three of the four islands located on the NE rim of Manuae experienced ocean shoreline accretion and lagoon shoreline erosion (diamonds, Figure 7b), whereas the fourth island near the schematic transition zone did not have shoreline change trends larger than the estimated errors. On the SE atoll rim, both islands experienced ocean shoreline erosion and lagoon shoreline accretion (asterisks, Figure 7b).

Figure 6b shows an example of an island with an eroding lagoon shoreline on the NE rim of Manuae, with losses extending up to 100 m in some locations. The ocean shoreline of this island remained stable on the southern end, while accretion was observed along the central and northern portion. In addition, the ocean shoreline is rather uniform in comparison with the highly variable structure of the eroding lagoon shoreline. In Figure 6c, small lagoon shoreline accretion and ocean shoreline erosion trends were observed on the southernmost island.

Wave Classification

Northern and southern Manihi and Manuae are exposed to different wave fields with average annual wave energy fluxes (during the period 1997–2011) of 5.7, 5.8, and 21.9 kW/m of wave crest, respectively. Using the K-means algorithm described in the “Methods” section, the wave classifications of the three wave time series show differences in the dominant direction of incoming wave energy (Figure 8).

The N rim of Manihi is exposed to the open ocean and is thus affected by waves arriving from the N and NE (Figure 8a). Waves arriving from the N are usually rather weak, with the exception of infrequent, energetic storms and cyclones (Créocéan, 1995). The majority of these waves classes have a mean wave height of 1 m or less, while the wave class corresponding to northern storms and cyclones has a mean significant wave height of 2.9 m (and a percentage annual occurrence of 0.4%).

The two wave time series at Manihi show a high percentage annual occurrence of trade waves, which are especially dominant on the southern side of Manihi (Figures 8a and b). Owing to the shielding of the southern rim of Manihi from southern waves caused by the presence of an atoll “barrier” to the south in the Tuamotu Islands (Figure 2), the rim is

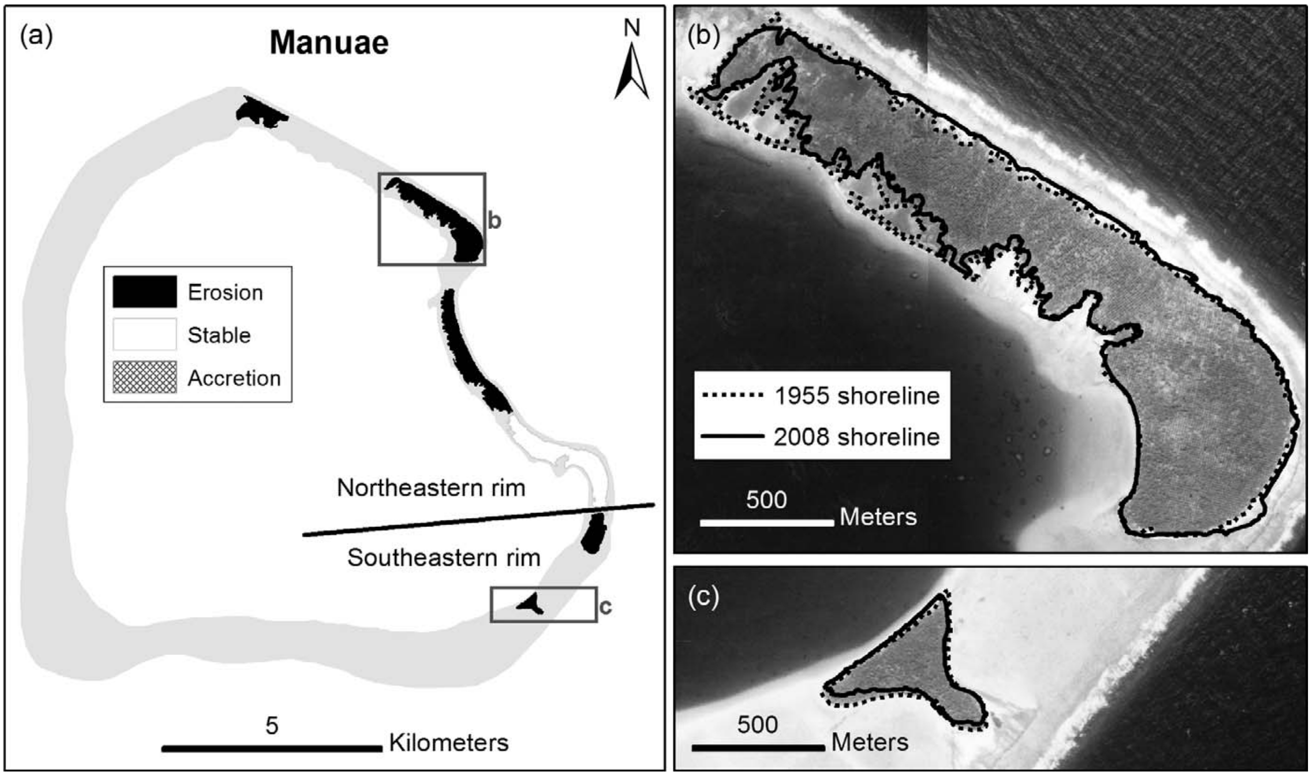

Figure 6. Observed changes on Manuae: (a) surface area changes for each island, and examples of 1955 (dotted line) and 2008 (solid line) shorelines, overlaid on the historical aerial photographs for islands on the (b) NE and (c) SE atoll rims. The lettered boxes in (a) indicate the location of insets (b) and (c).

primarily exposed to waves originating from the east, created by the trade winds.

In contrast, Manuae is an isolated atoll that is directly affected by waves arriving from all directions (Figure 8c, Table 2), with a total wave energy flux nearly four times as large as that observed at Manihi. The wave classification shows that southern waves (excluding SE waves) occur during 39% of the year and represent 46% of the incoming wave energy flux affecting the atoll. The next most important wave modes are the trade waves and SE waves (21% and 20% annual occurrence, respectively). Long period swell and large waves also arrive from north and west of Manuae, but waves originating in the south and east dominate the annual occurrence and wave energy flux of the atoll (Table 2).

DISCUSSION

During the study period, the islands on Manihi were relatively stable or showed an increase in surface area, whereas the islands on Manuae generally decreased in surface area. In addition, within each atoll, ocean and lagoon shoreline changes varied in different geographic regions. The accumulation of sediments on islands is determined by a variety of factors such as waves and cyclones, currents, reef-building organism distribution, and the reef geometry and size (Gourlay, 1988; Stoddart, 1969), as well as anthropogenic activities and sea-level rise. Together these factors cause changes in island shoreline position and total surface area. The complexity of the coastal environment and a lack of data prevent a quantitative analysis of the influence of these factors but allow a qualitative analysis of their relative importance to understand better the causes of the observed multidecadal island evolution.

Shoreline Response to Forcing Factors

Anthropogenic Activities

Human activities, in the form of sediment dredging, agriculture, pearl farming, tourism, and construction of buildings and protective shoreline structures may all have direct and indirect impacts on island sediment budgets and shoreline change (Aubanel *et al*., 1999; Ford, 2012). Only two islands on Manihi show evidence of direct shoreline modification: the first as a result of the construction of a port and the stabilization of the shoreline in the village (Figures 9a and b), and the second as a result of the construction of an airport runway (Figures 9c and d). In both cases, the total island area increased because of land reclamation. However, the indirect impacts of human activities on atoll island surface area and shoreline changes (*i.e.,* changes in sediment supply and transport patterns resulting from sediment mining, dredging, reef health, *etc*.) were unable to be evaluated.

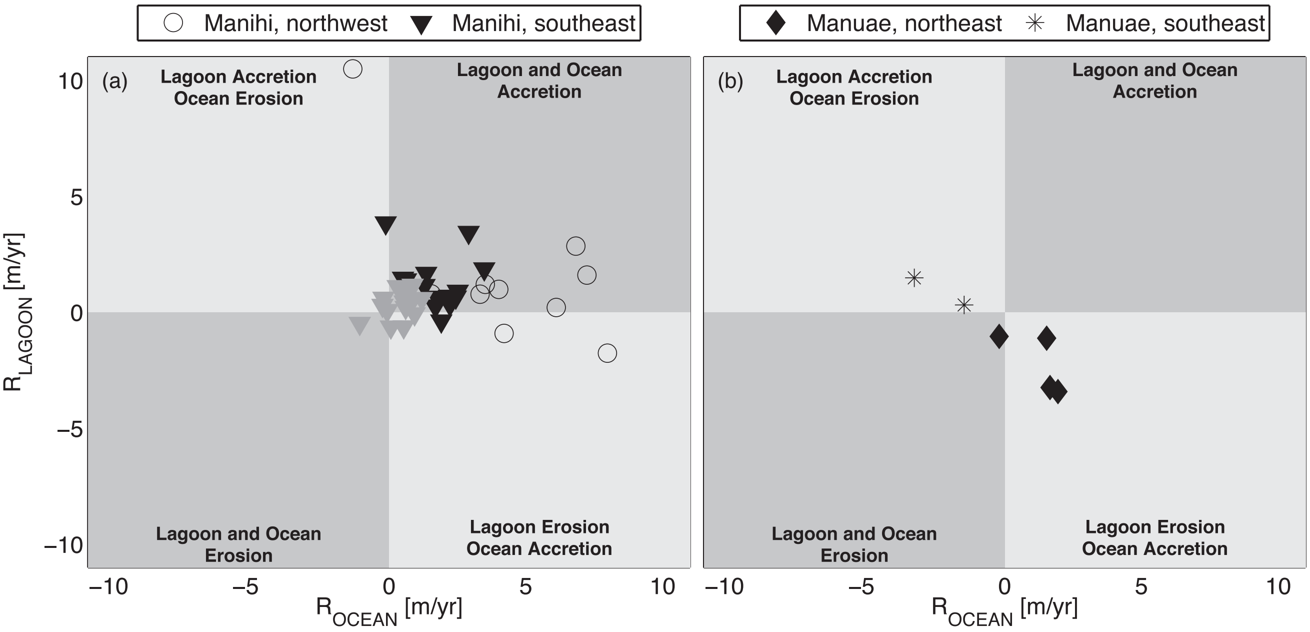

Figure 7. Observed ocean (R_{OCEAN}) and lagoon (R_{LAGOON}) shoreline change rates on (a) Manihi and (b) Manuae. The gray points correspond to islands showing no significant (above the limit of estimated errors) lagoon and ocean shoreline changes. The point shape (see legends) identifies the island's geographical location on the two atolls, as defined by the black lines in Figures 5a and 6a.

Sea-Level Rise

Sea-level rise is hypothesized to cause ocean shoreline erosion and possible loss or lagoonward "rollover" of islands in atoll environments (Dickinson, 1999). In addition to increasing the water level relative to the beach, sea-level rise may also increase the water depth over the adjacent reef and therefore leave the atoll ocean shorelines exposed to higher wave energy (Sheppard *et al*., 2005). Many studies use the Bruun Rule (Bruun, 1962) to estimate shoreline retreat, but the Bruun Rule states that sea-level rise results only in shoreline erosion. However, in this study, no islands on Manihi and only two islands on Manuae demonstrated ocean shoreline erosion trends larger than the estimated errors (Figure 7). While sea-level rise likely has an important role in governing the long-term shoreline accretion and erosion of these atoll islands, it is unable to explain the observed variability in shoreline change rates. In addition, these observations suggest that, during the study period, Manihi and Manuae have been resilient to sea-level rise rates that are greater than the global mean.

Cyclones and Waves

Island exposure to waves provides an attractive and simple explanation for the observed morphology, sedimentary character, and distribution of atoll islands (Kench *et al*., 2006). While average annual wave energy fluxes affecting the northern and southern rims of Manihi are very similar, differences in exposure to steady waves and extreme events may play an important role in controlling shoreline changes.

Incoming waves breaking across the reef provide energy that may break up the reef and transport bioclastic sediments landward. The impacts of cyclones may increase the sediment transport potential (Harmelin-Vivien and Laboute, 1986), contributing to larger shoreline accretion on the NW rim of Manihi. Large wave events directly affecting the northern atoll rim may also have indirect impacts on the southern atoll rim *via* lagoon flushing, as observed on the nearby atoll Manihiki (Callaghan *et al*., 2006). At Manihi, lagoon flushing can only occur through the one narrow pass, Tairapa, or through the frequent, narrow channels between islands on the SE rim (*e.g*., Figures 3 and 5c), which are common features on atolls exposed to hurricanes (Stoddart and Fosberg, 1994). Field surveys, such as that of Callaghan *et al*. (2006), with additional measurements of morphological changes or anecdotal evidence from past events, are necessary to validate such a hypothesis.

At Manuae, the large wave energy flux suggests a high potential for sediment transport on the ocean shoreline of the southern and eastern atoll rims. In contrast, waves from the NW do not account for a large fraction of the total wave energy flux, but storms originating from this direction may cause both elevated sea levels and wave propagation over the western reef flat and across the lagoon. Waves propagating across the lagoon may cause subsequent erosion on the lagoon shoreline of the eastern rim, as evidenced by the lagoon shoreline erosion observed on the NE rim (Figure 7b). Finally, following the classification of Tuamotu atoll rims developed by Andréfouët *et al*. (2001), the dominance of submerged areas on the SE atoll rim (Figure 3b) is suggestive of recurring erosion from southern swell, as observed on the

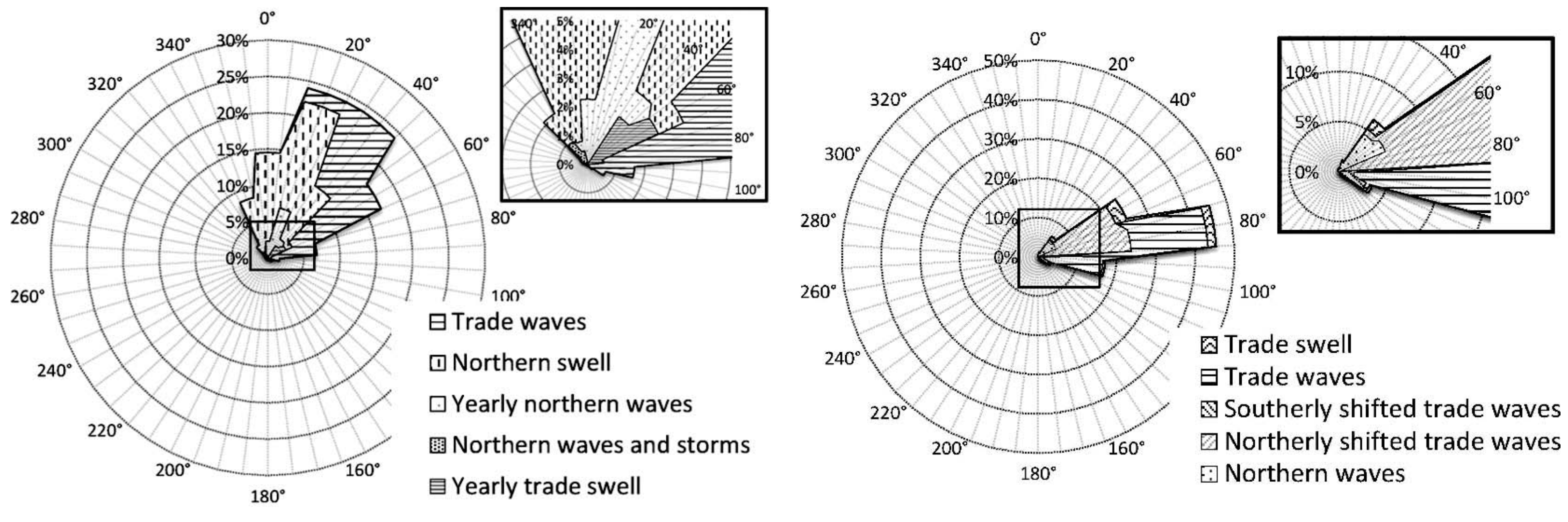

(a) North Manihi

(b) South Manihi

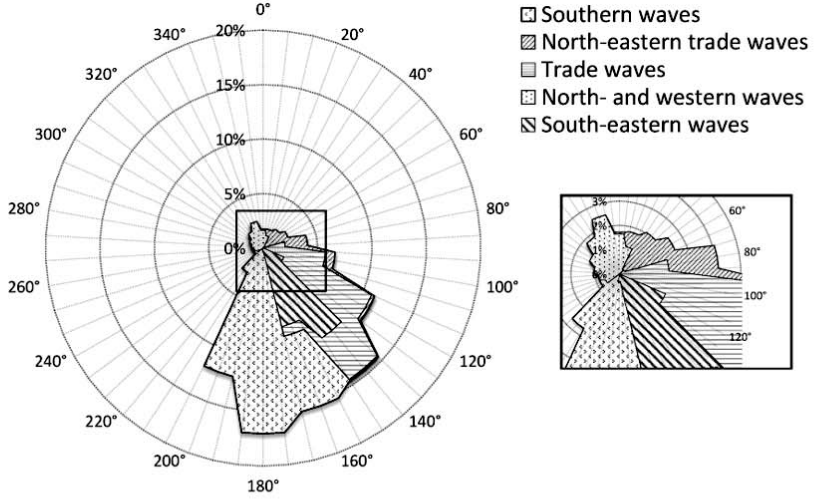

(c) Manuae

Figure 8. Wave roses of the three wave time series ouputs from WaveWatch III model outputs between 1997 and 2011 (Ardhuin *et al.*, 2010), showing the percentage annual occurrence (radial coordinate) and direction (angular coordinate) of the five dominant wave modes at each location. (Note the difference in the radial axis scales.)

Table 2. *Wave classes identified by a K-means algorithm for the 1997–2011 wave time series at Manuae, grouped by wave mode.*

Wave class	Season	Origin	Hs (m)	T (s)	D (degrees)	Occurrence (%)
N and W	Humid	NW	2.1	9.5	316	1.9
N and W	Humid	NNW	1.7	17.6	331	2.4
N and W	Humid	W	1.7	13.9	272	2.8
N and W	Humid	N	1.5	14.3	357	4.1
Summer E	Humid	ENE	1.5	11.5	53	4.6
Summer E	Humid	E	1.6	16.5	78	3.4
Trade (E)	Annual	ESE	1.7	8.6	107	7.7
Trade (E)	Annual	ESE	1.7	12.9	110	8.9
Trade (E)	Mostly dry	SE	2.3	8.9	139	5.8
SE	Mostly dry	SE	2.0	15.1	141	7.9
SE	Mostly dry	SSE	1.6	11.4	150	11.7
S	Mostly dry	S	1.6	11.5	193	8.6
S	Mostly dry	S	1.9	13.8	170	13.0
S	Mostly dry	S	2.0	14.3	199	11.1
S	Mostly dry	S	2.1	16.9	182	6.2

SE atoll rim (*e.g.*, Figure 6c). As at Manihi, field surveys measuring the local ocean and lagoon wave field and currents, as well as morphological changes, are needed to validate such hypotheses.

Biological Factors

Very few data exist concerning the health of reefs at Manihi and Manuae, and the impact of biological factors on sediment budgets was unable to be evaluated in this study. It is,

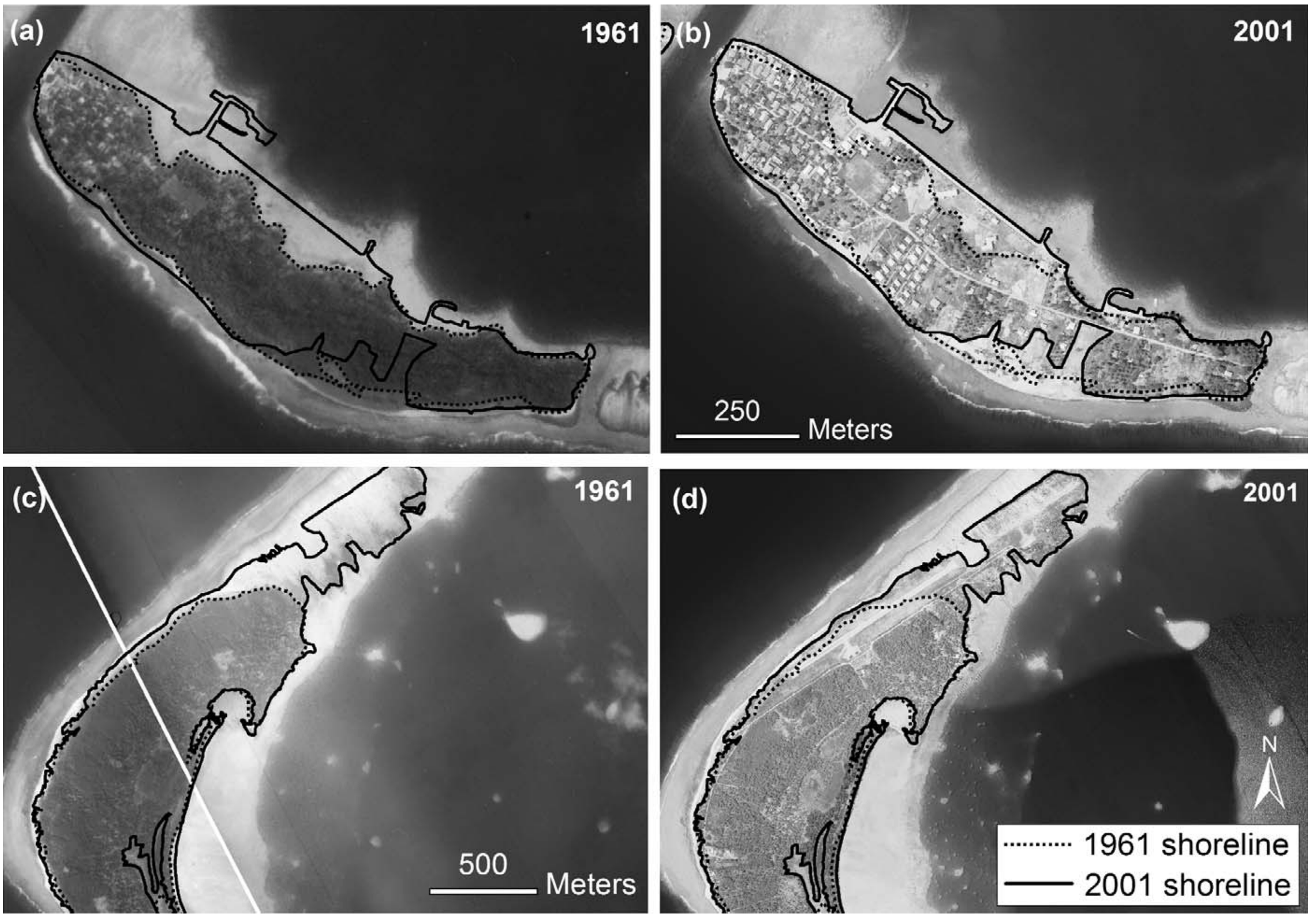

Figure 9. Observed island shoreline changes on Manihi caused directly by human activities: (top) the enlargement of the town of Turipaoa and the construction of a port and (bottom) the construction of an airport runway. The location of the insets is shown by the boxes in Figure 3a.

however, important to note that atoll islands depend on nearby, offshore reefs as a primarily source of carbonate sediments (Stoddart, 1969). A variety of stresses, such as the introduction of nonnative species and direct damage to reefs from tropical cyclones, coral mining, and fishing, as well as changes in sea level, sea surface temperature, salinity, ocean acidity, water quality, and turbidity, (Mimura *et al*., 2007), may directly damage reefs or cause coral bleaching (the loss of symbiotic algae and/or pigments) (Nicholls *et al*., 2007) and eventual mortality.

Study Limitations

The study results are based on the analysis of remote sensing images, which provide snapshots of the islands at two different periods in time. It is unlikely that island shoreline changes were homogeneous during the 40 to 50-year study period as a result of variations in the wave field and episodic extreme events that may have caused large changes in short time periods (Harmelin-Vivien, 1994; Maragos, Baines, and Beveridge, 1973). Ballu *et al*. (2011), Bayliss-Smith (1988), Stoddart (1990), and others also emphasize that there may be an offset between the time scale of processes affecting the shoreline position and the time scale of shoreline changes.

In addition, the high costs associated with *in situ* measurements prevented ground truthing of the observed shoreline and surface area changes. These limitations, and the uncertainties inherent in the image analysis (discussed in the "Methods" sections) suggest that these observations of shoreline and surface area changes must be interpreted with caution. However, owing to the paucity of available observations of multidecadal island surface area and shoreline changes, it is important to make use of existing data as a first step in studying atoll island changes. Future studies can build on these results with the availability of more frequent remote sensing observations and *in situ* measurements of wave conditions and morphological changes.

Future Changes to Forcing Factors

Attempts to predict future atoll evolution are restricted by the limited, but increasing number of measurements of historical atoll island shoreline changes, as well as limited understanding of the principal factors causing these changes, and how these factors evolve in time. Many studies try to predict future coastal change with simple conceptual models such as the Bruun Rule. However, this model has not been adequately verified with observations (Cooper and Pilkey, 2004), and the basic model assumptions are generally not satisfied in coral reef island environments (Cowell and Kench, 2001). Instead, Pilkey and Cooper (2004) recommend making predictions based on observations of past changes combined with expertise regarding the local context and expectations of future change.

This study estimates historical shoreline changes on islands on Manihi and Manuae. However, one must take caution before extrapolating these historic trends to predict future shoreline changes because of limited knowledge of how the forcing factors may change. Increased human pressure, as already observed on some highly developed atolls (*e.g*., Tuvalu; Connell, 2003), may enhance anthropogenic impacts, while climate change may affect wind and wave regimes (including cyclones) or cause an acceleration of sea-level rise (Nicholls and Cazenave, 2010), disrupting the existing shoreline change dynamics.

CONCLUSIONS

Analysis of historical and recent aerial photographs and recent satellite images shows distinct island shoreline and surface area changes on the atolls Manihi and Manuae. The islands on Manihi were primarily stable or increasing in surface area, whereas the islands on Manuae primarily decreased in surface area. Each atoll was divided geographically into two regions showing distinct ocean and lagoon shoreline change trends. Islands on the NW rim of Manihi showed larger ocean shoreline accretion rates than those on the SE rim, and no overall lagoon shoreline change trends were observed. Islands on the NE rim of Manuae experienced lagoon shoreline erosion and ocean shoreline accretion, while the opposite trend was observed for islands on the SE rim. An analysis of the wave climate affecting the two atolls shows that the annual energy flux at Manuae is nearly four times greater than that at Manihi. Trade waves are an important source of energy on both atolls, but the largest wave events impact the northern rim of Manihi and the southern rim of Manuae.

Although many studies suggest that atoll islands are eroding as a result of sea-level rise, this work supports the hypothesis, in agreement with the results of Webb and Kench (2010), that recent rates of climate-induced sea-level rise are not the primary factor controlling shoreline change variability in these environments at this time. The observations in this study suggest that atoll islands have persisted over multidecadal time scales with sea-level rise rates of approximately 3 mm/y during the last 60 years (a rate significantly higher than the global mean).

The observed island shoreline change variability is hypothesized to be related to the variability in wave exposure. While the northern and southern rims of Manihi are exposed to similar annual average wave energy fluxes, the northern rim of Manihi is exposed to infrequent, large wave events that may contribute to the enhanced ocean shoreline accretion rates observed there. On Manuae, the exposure of the eastern rim lagoon shoreline to waves propagating across the interior of the lagoon may explain the observed erosion trends, while the southern rim's constant exposure to intense southern swell may explain the observed ocean shoreline erosion. However, detailed observations of nearshore waves, currents, and morphological changes are needed to validate these hypotheses.

This study contributes to the growing body of knowledge of atoll island shoreline changes with multidecadal observations on the atolls of Manihi and Manuae. However, with predictions of future changes in waves, cyclone intensity, sea-level rise, sea surface temperature, and human-induced pressure, one must be cautious when extrapolating observations of historical shoreline change to predict future shoreline change. Continued and additional surveying of atoll islands and their response to varied forcing conditions is crucial for improving understanding of historical changes and for predicting future change.

ACKNOWLEDGMENTS

The work presented in this article was supported by the French National Research Agency (ANR) through the CEP-2009 program [project "Coastal Environmental Changes: Impact of sea Level rise" (CECILE) under grant number ANR-09-CEP-001-01]. With the assistance of Aude Nachbaur, the aerial photographs and satellite images were provided by the Service of Urbanization (SAU) of French Polynesia (Emilie Nowak, Didier Lequeux, Emmanuel Des Garets). The wave hindcast data from WaveWatch III are available from IFREMER. We thank Anny Cazenave, Mélanie Becker, and Benoît Meyssignac of the LEGOS laboratory for providing and aiding in the interpretation of the sea-level rise reconstruction data, as well as Rodrigo Pedreros for insight regarding the interpretation of the wave and geomorphology data. Finally, we would like to thank the anonymous reviewers for their insightful comments and suggestions to improve this paper.

LITERATURE CITED

Andréfouët, S.; Claereboudt, M.; Matsakis, P.; Pagès, J., and Dufour, P., 2001. Typology of atoll rims in Tuamotu Archipelago (French Polynesia) at landscape scale using SPOT HRV images. *International Journal of Remote Sensing*, 22(6), 987–1004.

Ardhuin, F.; Rogers, E.; Babanin, A.V.; Filipot, J.F.; Magne, R.; Roland, A.; van der Westhuysen, A.; Queffeulou, P.; Lefevre, J.M.; Aouf, L., and Collard, F., 2010. Semiempirical dissipation source functions for ocean waves, part I: definition, calibration, and validation. *Journal of Physical Oceanography*, 40, 1917–1941. doi: 10.1175/2010JPO4324.1.

Aubanel, A.; Marquet, N.; Colombani, J.M., and Salvat, B., 1999. Modifications of the shore line in the Society islands (French Polynesia). *Ocean and Coastal Management*, 42, 419–438.

Australian Bureau of Meteorology, 2012. *Tropical Cyclone Information for the Southern Hemisphere.* http://www.bom.gov.au/cgi-bin/silo/cyclones_sh.cgi.

Ballu, V.; Bouin, M.-N.; Siméoni, P.; Crawford, W.C.; Calmant, S.; Boré, J.M.; Kanas, T., and Pelletier, B., 2011. Comparing the role of absolute sea-level rise and vertical tectonic motions in coastal flooding, Torres Islands (Vanuatu). *Proceedings of the National Academy of Sciences, USA*, 108, 13019–13022. doi: 10.1073/pnas.1102842108.

Barsczus, H.G., 1980. Evaluation de l'age de l'atoll de Scilly (Manuae), Archipel de la Société—Iles-Sous-Le-Vent. *Notes and documents de geophysique*. no. 1980/29, Observatoire de Géophysique Palatai. Papeete, Tahiti: Centre Orstom de Tahiti, Polynésie Française.

Bayliss-Smith, T.P., 1988. The role of hurricanes in the development of reef islands, Ontang Java Atoll, Solomon Islands. *The Geographical Journal*, 154(3), 377–391.

Becker, M.; Meyssignac, B.; Letetrel, C.; Llovel, W.; Cazenave, A., and Delcroix, T., 2012. Sea level variations at tropical Pacific islands since 1950. *Global and Planetary Change*, 80–81, 85–98. doi: 10.1016/j.gloplacha.2011.09.004.

Bourrouilh-Le Jan, F.G. and Talandier, J., 1985. Sédimentation et fracturation de haute énergie en milieu récifal: tsunamis, ouragans et cyclones et leurs effets sur la sédimentologie et la géomorphologie d'un atoll: motu et hoa, à Rangirao, Tuamotu, Pacifique SE. *Marine Geology*, 67, 263–333.

Bruun, P., 1962. Sea-level rise as a cause of shoreline erosion. *Journal of the Waterways and Harbor Division*, 88(1–3), 117–130.

Butel, R.; Dupuis, H., and Bonneton, P., 2002. Spatial variability of wave conditions on the French Atlantic coast using in-situ data. *Journal of Coastal Research*, 36, 96–108.

Callaghan, D.P.; Nielsen, P.; Cartwright, N.; Gourlay, M.R. and Baldock, T.E., 2006. Atoll lagoon flushing forced by waves. *Coastal Engineering*, 53, 691–704.

Cazenave, A. and Llovel, W., 2010. Contemporary sea level rise. *Annual Review of the Marine Sciences*, 2, 145–173. doi: 10.1146/annurev-marine-120308–081105.

Chevalier, J.P., 1979. Géomorphologie et coraux in Scilly, atoll de l'archipel de la Société, Polynésie Française, Bull. No. 1. *Muséum National Histoire Naturelle, École Pratique des Hautes Études*, p. 31–33.

Church, J.A.; White, N.J., and Hunter, J.R., 2006. Sea-level rise at tropical Pacific and Indian Ocean islands. *Global and Planetary Change*, 53, 155–168.

Collen, J.D.; Garton, D.W., and Gardner, J.P.A., 2009. Shoreline changes and sediment redistribution at Palmyra Atoll (Equatorial Pacific Ocean): 1874–present. *Journal of Coastal Research*, 25(3), 711–722.

Connell, J., 2003. Losing ground? Tuvalu, the greenhouse effect and the garbage can. *Asia Pacific Viewpoint*, 44(2), 89–107.

Cooper, J.A.G. and Pilkey, O.H., 2004. Sea-level rise and shoreline retreat: time to abandon the Bruun Rule. *Global and Planetary Change*, 43, 157–171.

Cowell, P.J. and Kench, P.S., 2001. The morphological response of atoll islands to sea-level rise. Part 1: modifications to the shoreface translation model. *In:* Healy, T.R. (ed.), *International Coastal Symposium 2000: Challenges for the 21st Century in Coastal Sciences, Engineering, and Environment,* Journal of Coastal Research, Special Issue No. 34, pp. 633–644.

Créocéan, 1995. Conséquences de l'élévation du niveau de la mer sur l'atoll de Rangiroa [consequences of sea level rise for the Rangiroa Atoll]. *Report for the Ministry of the Environment No. 42119*. La Rochelle, France: Créocéan.

Crowell, M.; Leatherman, S.P., and Buckley, M.K., 1991. Historical shoreline change: error analysis and mapping accuracy. *Journal of Coastal Research*, 7(3), 839–852.

Darwin, C.R., 1842. *The Structure and Distribution of Coral Reefs. Being the First Part of the Geology of the Voyage of the Beagle, under the Command of Capt. Fitzroy, R.N. during the Years 1832 to 1836*. London: Smith Elder.

Des Garets, E., 2005. Bilan des connaissances sur les surcotes marines en polynésie. *Rapport BRGM/RP-55038-FR.* Orleans, France: Bureau des Recherches Géologiques et Minières.

Dickinson, W.R., 1999. Holocene sea-level record on Funafuti and potential impact of global warming on Central Pacific atolls. *Quaternary Research*, 51, 124–132.

Dupon, J.F., 1984. Where the exception confirms the rule: the cyclones of 1982–1983 in French Polynesia. *Disasters*, 8(1), 34–47.

Flood, P.G., 1986. Sensitivity of coral cays to climatic variations, southern Great Barrier Reef, Australia. *Coral Reefs*, 5, 13–18.

Ford, M., 2012. Shoreline changes on an urban atoll in the Central Pacific Ocean: Majuro Atoll, Marshall Islands. *Journal of Coastal Research*, 28(1), 11–22.

Garcin, M.; Desprats, J.F.; Fontaine, M.; Pedreros, R.; Attanayake, N.; Fernando, S.; Siriwardana, C.H.E.R.; De Silva, U., and Poisson, B., 2008. Integrated approach for coastal hazards and risks in Sri Lanka. *Natural Hazards and Earth System Sciences*, 8, 577–586.

Garcin, M.; Yates, M.; Le Cozannet, G.; Walker, P., and Donato, V., 2011. Sea level rise and coastal morphological changes on tropical islands: example from New Caledonia and French Polynesia (SW Pacific). *In: Geophysical Research Abstracts, 13*. EGU2011, 13, p. 3504.

Gourlay, M.R., 1988. Coral cays: products of wave action and geological processes in a biogenic environment. *In:* Choat, J.H.; Barnes, D.; Borowitzka, M.A., Coll, J.C.; Davies, P.J.; Flood, P.; Hatcher, B.G.; Hopley, D.; Hutchings, P.A.; Kinsey, D.; Orme, G.R.; Pichon, M.; Sale, P.F.; Sammarco, P.; Wallace, C.C.; Wilkinson, C.; Wolanski, E., and Bellwood, O. (eds.), *Proceedings of the 6th International Coral Reef Symposium*, volume 2 (Townsville, Australia, ICRS), pp. 491–496.

Guilcher, A.; Berthois, L.; Doumenge, F.; Michel, A.; Saint-Requier, A., and Arnold, R., 1969. *Les Récifs et Lagons Coralliens de Mopelia et de Bora-Bora (îles de la Société: et quelques autres récifs et lagons de comparaison (Tahiti, Scilly, Tuamotu occidentales); morphologie, sédimentologie, fonctionnement hydrologique*. Paris: Orstom.

Harmelin-Vivien, M.L., 1994. The effects of storms and cyclones on coral reefs: a review. *In:* Finkl, C.W. (ed.), *Coastal Hazards: Perception, Susceptibility and Mitigation,* Journal of Coastal Research, Special Issue No. 12, pp. 211–231.

Harmelin-Vivien, M.L. and Laboute, P., 1986. Catastrophic impact of hurricanes on atoll outer reef slopes in the Tuamotu (French Polynesia). *Coral Reefs*, 5, 55–62.

Hoeke, R.K.; Zarillo, G.A. and Synder, M., 2001. *A GIS Based Tool for Extracting Shoreline Positions from Aerial Imagery (BeachTools)*. *ERDC/CHL CHETN-IV-37*. Washington, DC: U.S. Army Corps of Engineers.

Kench, P.S.; Brander, R.W.; Parnell, K.E., and McLean, R.F., 2006. Wave energy gradients across a Maldivian atoll: implications for island geomorphology. *Geomorphology*, 81, 1–17. doi: 10.1130/G21066.1.

Larrue, S. and Chiron, T., 2010. Les îles de Polynésie française face à l'aéa cyclonique. *Vertigo*, 10(3), 22 p.

Le Cozannet, G.; Lecacheux, S.; Delvallee, E.; Desamaut, N.; Oliveros, C., and Pedreros, R., 2011. Teleconnection pattern influence on sea-wave climate in the Bay of Biscay. *Journal of Climate*, 24, 641–652. doi: 10.1175/2010JCLI3589.1.

Llovel, W.; Cazenave, A.; Rogel, P.; Lombard, A., and Nguyen, A.B., 2009. Two-dimensional reconstruction of past sea level (1950–2003) from tide gauge data and an Ocean General Circulation Model. *Climate Past*, 5, 217–227.

Lombard, A.; Cazenave, A.; Le Traon, P.Y., and Ishii, M., 2005. Contribution of thermal expansion to present-day sea-level change revisited. *Global and Planetary Change*, 47, 1–16.

Maragos, J.E.; Baines, G.B.K., and Beveridge, P.J., 1973. Tropical cyclone Bebe creates a new land formation on Funafuti Atoll. *Science*, 21(4105), 1161–1164. doi: 10.1126/science.181.4105.1161.

Meyssignac, B.; Becker, M.; Llovel, W., and Cazenave, A., 2012. An assessment of two-dimensional past sea level reconstructions over 1950–2009 based on tide gauge data and different input sea level grids. *Surveys in Geophysics*, 33, 945–972.

Mimura, N.; Nurse, L.; McLean, R.F.; Agard, J.; Briguglio, L.; Lefale, P.; Payet, R., and Sem, G., 2007. Small islands. *In:* Parry, M.L.; Canziani, O.F.; Palutikof, J.P.; van der Linder, P.J., and Hanson, C.E. (eds.), *Climate Change 2007: Impacts, Adaptation and Vulnerability.* Contribution of Working Group II to the Fourth Assessment Report of the Intergovernmental Panel on Climate Change. Cambridge, UK: Cambridge University Press, pp. 687–716.

Nicholls, R.J. and Cazenave, A., 2010. Sea-level rise and its impact on coastal zones. *Science*, 328(1517). doi: 10.1126/science.1185782.

Nicholls, R.J.; Wong, P.P.; Burket, V.R.; Codignotto, J.; Hay, J.; McLean, R.; Ragoonaden, S., and Woodroffe, C.D., 2007. Coastal systems and low-lying areas. *In:* Parry, M.L.; Canziani, O.F.; Palutikof, J.P.; van der Linder, P.J., and Hanson, C.E. (eds.), *Climate Change 2007: Impacts, Adaptation and Vulnerability.* Contribution of Working Group II to the Fourth Assessment Report of the Intergovernmental Panel on Climate Change. Cambridge, UK: Cambridge University Press, pp. 315–356.

Ohde, S.; Greaves, M.; Masuzawa, T.; Buckley, H.A.; Van Woesik, R.; Wilson, P.A.; Pirazzoli, P.A., and Elderfield, H., 2002. The chronology of Funafuti Atoll: revisiting an old friend. *Proceedings: Mathematical, Physical and Engineering Sciences*, 458(2025), 2289–2306.

Pilkey, O.H. and Cooper, J.A.G., 2004. Society and sea level rise. *Science*, 303, 1781–1782.

Pirazzoli, P.A. and Montaggioni, L.F., 1985. Lithospheric deformation in French Polynesia (Pacific Ocean) as deduced from Quaternary shorelines. *In:* Gabrie, C.; Toffart, J. L., and Salvat, B. (eds.), *Proceedings of the 5th International Coral Reef Congress*, volume 3 (Tahiti, French Polynesia, ICRS), pp. 195–200.

Pirazzoli, P.A. and Montaggioni, L.F., 1986. Late holocene sea-level changes in the Northwest Tuamotu Islands, French Polynesia. *Quaternary Research*, 25, 350–368.

Pirazzoli, P.A.; Montaggioni, L.F.; Salvat, B., and Faure, G., 1988. Late holocene sea level indicators from twelve atolls in the central and eastern Tuamotus (Pacific Ocean). *Coral Reefs*, 7, 57–68.

Salvat, B., 1983. La faune benthique du lagon de l'atoll de Scilly, archipel de la Société. *Journal de la Société des Océanistes*, 77(39), 5–15.

Salvat, B.; Aubanel, A.; Adjeroud, M.; Bouisset, P.; Calmet, D.; Chancerelle, Y.; Cochennec, N.; Davies, N.; Fougerousse, A.; Galzin, R.; Lagouy, E.; Lo, C.; Monier, C.; Ponsonnet, C.; Remoissenet, G.; Schneider, D.; Stein, A.; Tatarata, M., and Villiers, L., 2008. Le suivi de l'état des récifs coralliens de Polynésie Française et leur récente évolution. *Revue d'Ecologie de la Terre et de la Vie*, 63(1–2), 145–177.

Sheppard, C.; Dixon, D.J.; Gourlay, M.; Sheppard, A., and Payet, R., 2005. Coral mortality increases wave energy reaching shores protected by reef flats: examples from the Seychelles. *Estuarine, Coastal and Shelf Science*, 64, 223–234.

Stoddart, D.R., 1963. Effects of Hurricane Hattie on the British Honduras reefs and cays, October 30–31, 1961. *Atoll Research Bulletin No*. 95, Washington, DC: The Pacific Science Board, National Academy of Sciences, National Research Council.

Stoddart, D.R., 1969. Ecology and morphology of recent coral reefs. *Biological Reviews*, 44, 433–498.

Stoddart, D.R., 1990. Coral reefs and islands and predicted sea-level rise. *Progress in Physical Geography*, 14(4), 521–536.

Stoddart, D.R. and Fosberg, F.R., 1994. The hoa of Hull Atoll and the problem of hoa. *Atoll Research Bulletin No. 394*. Washington, DC: National Museum of Natural History: Smithsonian Institution.

Thieler, E.R. and Danforth, W.W., 1994. Historical shoreline mapping (I): improving techniques and reducing positioning errors. *Journal of Coastal Research*, 10(3), 549–563.

Thieler, E.R.; Himmelstoss, E.A.; Zichichi, J.L. and Ergul, A., 2009. Digital shoreline analysis system (DSAS) version 4.0—an arcgis extension for calculating shoreline change. *Technical Report Open-File Report 2008-1278*. Reston, Virginia: U.S. Geological Survey.

Venec-Peyre, M.T., 1987. Boring foraminifera in French Polynesian coral reefs. *Coral Reefs*, 5, 205–212.

Webb, A.P. and Kench, P.S., 2010. The dynamic response of reef islands to sea-level rise: evidence from multi-decadal analysis of island change in the Central Pacific. *Global and Planetary Change*, 72, 234–246.

Woodroffe, C.D., 2008. Reef-island topography and the vulnerability of atolls to sea-level rise. *Global and Planetary Change*, 62, 77–96.

Xue, C., 1997. Coastal erosion and management of Vaitupu Island, Tuvalu. *Technical report 243*. SOPAC.

□ RÉSUMÉ □

Une analyse de la mobilité du trait de côte au cours des cinquantaines dernières années a été réalisée sur deux atolls de Polynésie Franaise (Pacifique Sud): Manihi (Nord-ouest de l'archipel des Tuamotus) et Manuae (Est de l'archipel des îles de la Société). La mobilité de la limite de végétation permanente a été extraite de photographies aériennes anciennes de 1955 ou 1961 et d'images satellites à haute résolution acquises dans les années 2000. Cette analyse a nécessité le géoréférencement des photographies aériennes puis la digitalisation des limites successives de la végétation permanente. La ligne de végétation permanente a été utilisée comme marqueur des mouvements de basse fréquence du trait de côte (*i.e.*, échelles de temps pluri-décennales). En effet, elle demeure aisément identifiable aussi bien sur les images anciennes que récentes tout en s'émancipant des variations à haute fréquence (marée, surcote *etc.*) et des difficultés de pointage de certains marqueurs sur les photographies anciennes. Les incertitudes liées au géoréférencement et à la digitalisation du trait de côte ont été évaluées et conduisent à ne considérer que des mouvements supérieurs à 5m sur la durée considérée. Dans de trés nombreux îlots (*motu*), des changements de plus grande ampleur sont observés et sont de fait sont considérés comme significatifs. Ils indiquent une tendance générale à l'érosion à Manuae et à l'accrétion à Manihi. Cependant, au sein d'un même atoll, nous observons une grande variabilité des évolutions des limites de végétation des motu : ainsi, la plupart des motu sont en accrétion côté lagon et côté océan à Manihi, toutefois, certains sont en érosion côté océan, côté lagon ou bien des deux côtés. Dans ces deux atolls peu anthropisés, les aménagements ne modifient la ligne de rivage que dans deux des 47 motu étudiés (quarante-et-un à Manihi, six à Manuae). Selon Becker *et al*. (2012), l'élévation du niveau marin, dans cette partie du Pacifique, a été supérieure à la moyenne globale depuis 60 ans. Des études antérieures suggèrent que l'élévation du niveau marin induit une érosion des îlots notamment sur leur face océanique. Ces effets n'apparaissent pas dominants dans les deux atolls étudiés. Au contraire, la tendance d'évolution du trait de côte obsevée n'est pas homogène sur l'ensemble des îlots et ne semble donc pas liée à la remontée du niveau marin. En revanche, l'analyse des climats de vagues sur ces deux atolls ainsi que des relations entre la position des motu au sein de l'atoll et l'évolution des traits de côte suggèrent que leur mobilité est dominée, au cours des cinquante dernières années, par les effets des vagues.

C.2 Lemos et al. (2018)

Ocean Dynamics (2018) 68:1207–1220
https://doi.org/10.1007/s10236-018-1185-1

Equilibrium modeling of the beach profile on a macrotidal embayed low tide terrace beach

Clara Lemos[1,2] · France Floc'h[1,2] · Marissa Yates[3,4] · Nicolas Le Dantec[1,2,4] · Vincent Marieu[5] · Klervi Hamon[1,2] · Véronique Cuq[2,6] · Serge Suanez[2,6] · Christophe Delacourt[1,2]

Received: 15 October 2017 / Accepted: 12 June 2018 / Published online: 30 June 2018

Abstract

Eleven-year long time series of monthly beach profile surveys and hourly incident wave conditions are analyzed for a macrotidal Low Tide Terrace beach. The lower intertidal zone of the beach has a pluriannual cycle, whereas the upper beach profile has a predominantly seasonal cycle. An equilibrium model is applied to study the variation of the contour elevation positions in the intertidal zone as a function of the wave energy, wave power, and water level. When forcing the model with wave energy, the predictive ability of the equilibrium model is around 60% in the upper intertidal zone but decreases to 40% in the lower intertidal zone. Using wave power increases the predictive ability up to 70% in both the upper and lower intertidal zones. However, changes around the inflection point are not well predicted. The equilibrium model is then extended to take into account the effects of the tide level. The initial results do not show an increase in the predictive capacity of the model, but do allow the model free parameters to represent more accurately the values expected in a macrotidal environment. This allows comparing the empirical model calibration in different tidal environment. The interpretation of the model free parameter variation across the intertidal zone highlights the behavior of the different zones along the intertidal beach profile. This contributes to a global interpretation of the four model parameters for beaches with different tidal ranges, and therefore to a global model applicable at a wide variety sites.

Keywords Equilibrium model · Macrotidal · Intertidal profile · Low tide terrace · Cross-shore processes

1 Introduction

Predicting the temporal variability of shoreline position in response to hydrodynamic forcing (waves and tides) is of primordial interest to coastal scientists, engineers, and beach managers. Shoreline positions along sandy coasts vary over a range of temporal and spatial scales in response to a wide range of physical processes (Stive et al. 2002; Masselink et al. 2016; Suanez et al. 2015). On short timescales ranging from hours to days, individual storms causing variations in the wave energy arriving at the coast may be the dominant process impacting shoreline change and sediment transport processes. At these timescales, cross-shore processes often dominate observed beach changes (e.g., Davidson and Turner 2009; Yates et al. 2009; Hansen and Barnard 2010; Castelle et al. 2014). Understanding beach profile response to energetic waves and subsequent calm periods is crucial, especially as rising seas encroach upon coastal infrastructure and climate change may modify storm frequency and intensity (Stocker 2014; Ludka et al. 2015).

This article is part of the Topical Collection on the *8th International conference on Coastal Dynamics, Helsingør, Denmark, 12–16 June 2017*

Responsible Editor: Aart Kroon

✉ France Floc'h
france.floch@univ-brest.fr

[1] Geoscience Ocean - UMR 6538, Université de Bretagne Occidentale, Brest, France

[2] Institut Universitaire Européen de la Mer, rue Dumont d'Urville, 29280 Plouzané, France

[3] Saint-Venant Laboratory for Hydraulics (ENPC, EDF R&D, Cerema), Université Paris-Est, Margny-Les-Compiègne, France

[4] Cerema, Technical Departement of Water, Sea and Rivers, 29280 Plouzané, France

[5] EPOC - OASU, URM 5805, Site de Talence, Université Bordeaux 1, Talence, France

[6] CNRS, UMR LETG 6554, Université de Bretagne Occidentale, Brest, France

Beach profile response to hydrodynamic forcing has long been studied. Previous works (Bruun 1954; Dean 1977, 1991) demonstrated that beaches tend to form equilibrium profiles in response to constant wave forcing, and these studies developed empirical functions to describe the observed equilibrium profile shapes. Furthermore, Wright et al. (1985) showed that with varying wave conditions, instantaneous beach profiles are also function of the state of the beach. These concepts have been used in a variety of empirical models to study shoreline position changes on timescales of days to years on sandy beaches dominated by cross-shore processes (e.g., Miller and Dean 2004; Davidson and Turner 2009; Yates et al. 2009, 2011; Davidson et al. 2010, 2013; Castelle et al. 2014; Ludka et al. 2015). These models simulate shoreline variations as a function of wave conditions and the previous shoreline position. Yet, shoreline position models need extensive historical observations, are calibrated for each specific site, and have been applied primarily on microtidal beaches (Yates et al. 2009; Splinter et al. 2014; Ludka et al. 2015). Results on such beaches show that when cross-shore processes are dominant, the model performs well with an efficiency of approximately 80% (e.g., Yates et al. (2009) and Ludka et al. (2015) or Splinter et al. (2014), when the model is forced with the wave energy or Dean number, respectively). Recently, Castelle et al. (2014) suggested that equilibrium shoreline models can be extended and applied to a range of elevation contours in the intertidal zone to evaluate the effect of wave energy at different altitudes along the intertidal beach profile, with an efficiency between 55 and 65% depending on the altitude in the intertidal zone (between Mean Sea Level (MSL) and Highest Astronomical Tide (HAT)).

Macrotidal environments experience different wave conditions and hydrodynamic processes depending on the elevation in the intertidal zone. This complicates the understanding of beach morphodynamics due to temporal variations in the (1) the impacts of wave-driven processes across the intertidal zone and (2) the wave energy dissipation over the subtidal zone. At low tide, waves are highly dissipated over the foreshore zone, and the wave energy reaching the beach may be significantly lower than the offshore wave energy. This dissipation is less important at high tide, and the wave energy reaching the upper intertidal zone of the beach may be comparable to the offshore wave energy. During a tidal cycle, the position of the swash, surf, and shoaling zones shift with the tide both vertically (in altitude) and horizontally (along the intertidal profile), causing the intertidal beach profile to be impacted by different hydrodynamic processes during different phases of the tidal cycle (Masselink and Short 1993). The most sediment transport occurs in the surf and swash zones (e.g., Kroon and Masselink 2002; Masselink et al. 2006; Price and Ruessink 2008). Therefore, the use of a simple equilibrium model to study shoreline position changes on macrotidal beaches may highlight the differences in sediment transport in each of these zones.

In macrotidal environments, a typical beach profile experiencing strong morphodynamic variability over the intertidal zone is the Low Tide Terrace profile as defined in Masselink and Short (1993). A Low Tide Terrace (LTT) profile is a compound profile consisting of a reflective zone on the upper beach and a dissipative zone on the lower beach. LTT profiles appear for low dimensionless fall velocity ($\Omega < 2$) and strong Relative Tide Range ($h/Hs > 7$) (Masselink and Short 1993). Many observations of beach profile changes show that the magnitude varies significantly along the cross-shore profile, caused by large variations in the local beach slope (Miles and Russell 2004; Qi et al. 2010; Almeida et al. 2018). In fact, Miles and Russell (2004) suggest that the dynamics of a LTT beach exhibit characteristics of both dissipative and reflective sites. In addition, Miles and Russell (2004) show that with an increase in the beach slope and a corresponding decrease in the surf zone width, the upper part of the beach is more dynamic and reactive than the lower part, with sediment transport rates that can be one order of magnitude larger.

Empirical models have been shown to predict well the variations observed in the upper intertidal zone of reflective (Yates et al. 2009), dissipative (Splinter et al. 2014), or barred dissipative (Castelle et al. 2014) beaches, but have never been tested on LTT beaches. The application of an equilibrium model at multiple elevation contours along the intertidal beach profile may improve our understanding of LTT beach behavior, and allow a more detailed study of the link between physical processes and the free parameters required in empirical models. Improvements in understanding these parameters contribute to generalized expressions of the model constants.

This paper investigates the ability of an empirical model (based on Yates et al. (2009) and Castelle et al. (2014) to predict the pluriannual morphodynamics of the intertidal zone in a macrotidal environment (i.e., a sandy LTT beach) driven by cross-shore processes, by exploring changes in cross-shore position of a range of elevation contours. This study proposes a new approach to take into account the effects of changing water levels (e.g., tidal effects) by defining a vertical threshold within which the wave energy may cause changes in the cross-shore position of a given altitude, considering that most changes occur in the surf and swash zones. First, the study site and morphological and hydrodynamic data are described (Section 2). Then, the extension of an existing equilibrium shoreline change model (Yates et al. 2009; Castelle et al. 2014) to take into account the effect of the instantaneous water level is described in Section 3, and the results are presented when the model is forced with the wave energy or wave power (Section 4). Finally, the accuracy and erosion/accretion rates of empirical equilibrium models applied on beaches with different tidal ranges are compared (Section 5).

2 Study site and data

2.1 Study site

This study focuses on a macrotidal embayed beach (Porsmilin beach), located in western Brittany (France) on the Iroise sea coastline (Fig. 1). Porsmilin beach is an embayed barrier beach flanked by cliffs to the East and West, and backed by colmated brackish water marshes to the North. The intertidal zone is 200 m wide and 200 m long (Fig. 2) and the median sediment grain size (d50) is 320 μm. It is bounded (to the East and West) by headlands and bedrock, which extend offshore and obstruct the alongshore sediment transport generated in the surf zone. The alongshore sediment flux is assumed negligible since the shoreline does not exhibit rotational behavior (Floc'h et al. 2016). According to the Masselink and Short (1993) classification, Porsmilin beach is a Low Tide Terrace beach. The primarily cross-shore dominant morphological processes (Dehouck et al. 2009) make this sandy beach an ideal site to study cross-shore variations along the intertidal profile using an empirical equilibrium model (Yates et al. 2009). Because of the large tidal range at Porsmilin beach (between 3.5 and 7 m), the evolution of the upper and lower intertidal zone vary significantly for the same incident wave conditions. Biannual bathymetric surveys acquired from 2009 to 2018 show that the subtidal bathymetry of the foreshore steadily increases, without occurence of sandbars.

Due to its orientation in the Iroise Sea (Fig. 2), Porsmilin beach is mainly impacted by southwest waves that have peak periods between 8 and 10 s. The Iroise Sea is a highly energetic, wave-dominated environment, and 1 and 10 year significant wave height return periods are 11.3 and 14.5 m (in 110 m water depth at the West of Ouessant Island) (Dehouck et al. 2009). The tide is semi-diurnal and symmetric, with a mean spring tidal range of 5.7 m and a mean spring tidal current of 0.4 m/s in Bertheaume Bay (SHOM 1994), where Porsmilin beach is located. Along this rocky coastline, wave propagation is considerably affected by refraction and diffraction processes generated by the local bathymetry, including the wide continental shelf, offshore shoals and islands (Ouessant Island, Molene archipielago), and local headlands. Hence, oceanic swells that reach the shoreline have a quasi-normal incident angle and already have dissipated a large amount of energy, resulting in moderate wave energy conditions at Porsmilin beach. Wave conditions are calculated using the WaveWatch III (WWIII) numerical model, by selecting the output point closest to Porsmilin Beach, approximately 2 km offshore in 20 m water depth. Between 2002 and 2014, the annual mean

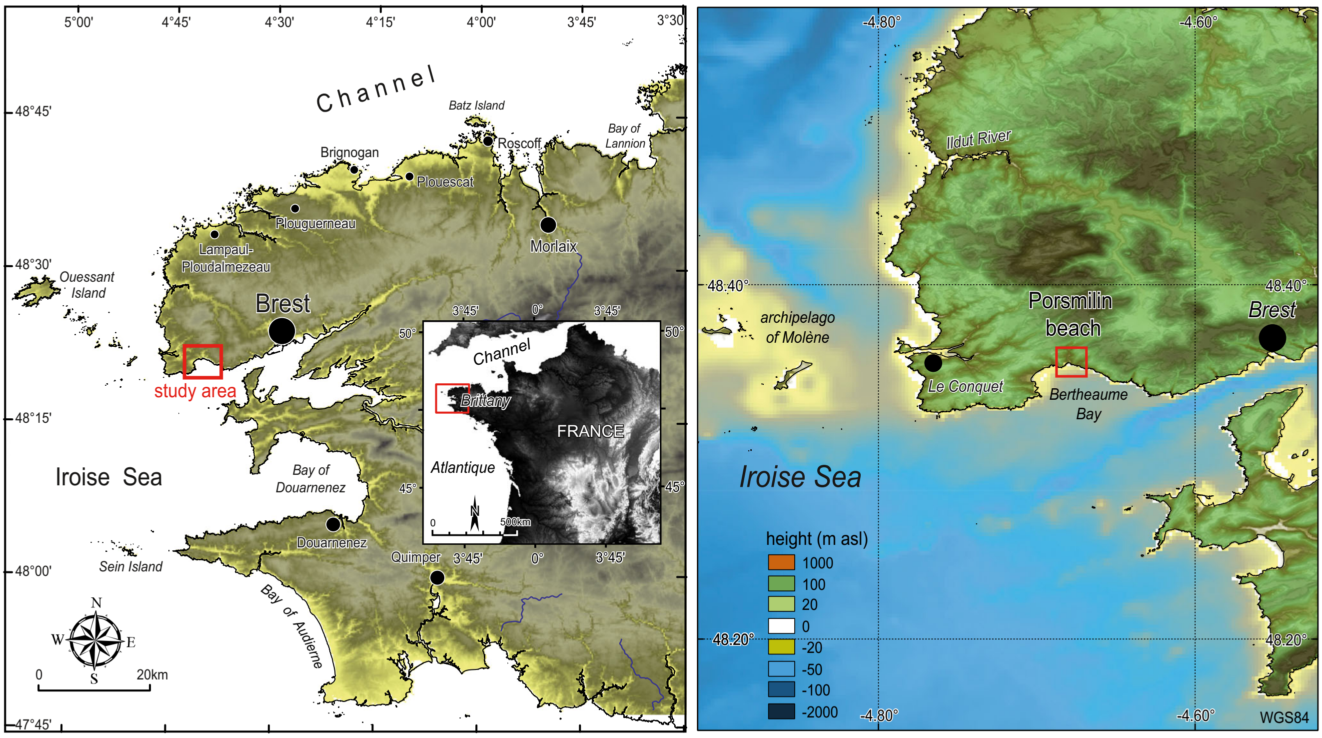

Fig. 1 Maps of NW France showing the location of the Porsmilin beach

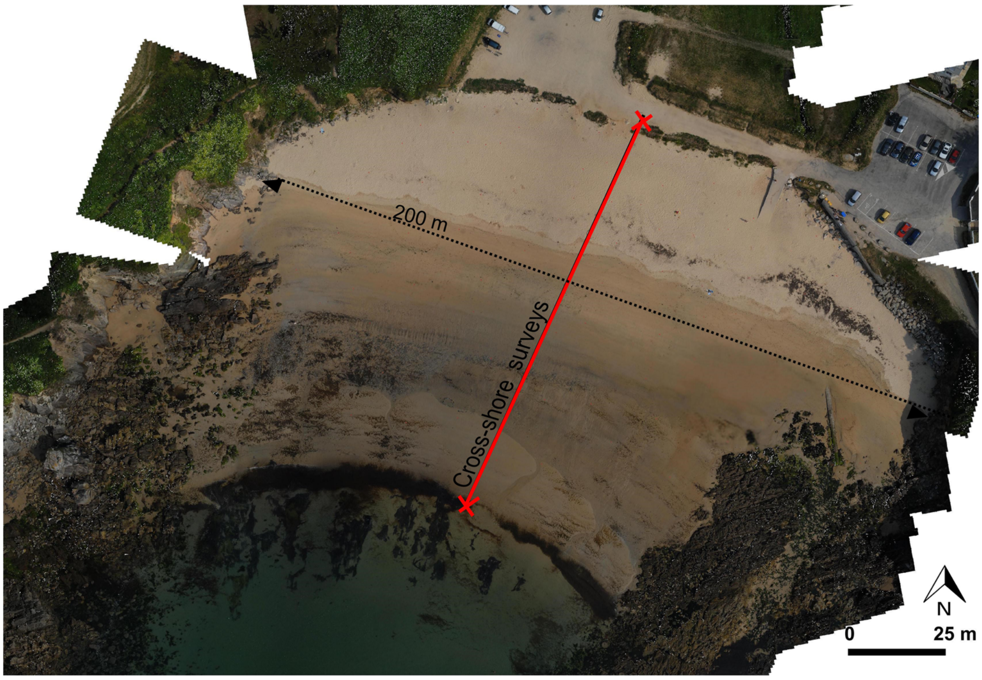

Fig. 2 Planview of the morphological characteristics of the Porsmilin beach

significant wave height was 0.76 m, and the seasonal means in autumn, winter, and spring were 0.7, 1.08, and 0.7 m respectively.

2.2 Beach profiles surveys

Monthly cross-shore surveys were completed from January 2003 to January 2014 (Figs. 2 and 3) with a Differential Global Positioning System (DGPS) RTK (referenced to the French topographic datum IGN69). During this period, 174 profiles of beach sand levels were measured along a single cross-shore transect with 1 m horizontal resolution. Along each profile, the data is then interpolated to a 0.1 m horizontal resolution. Depending on the tide level during the survey, each cross-shore profile has a different length, with 152 profiles extending vertically over the entire intertidal zone from − 1.0 to 4.1 m (IGN69).

As a LTT beach, the intertidal beach profile can be divided into two main parts: (1) a reflective zone from the Mean High Water Spring (MHWS) level (3.4 m IGN69) up to the Mean High Water Neap (MHWN) level (1.6 m IGN69) with a mean slope of 0.08 and (2) a dissipative zone below the MHWN level with a mean slope of 0.02. The MHWN level therefore corresponds to an inflection

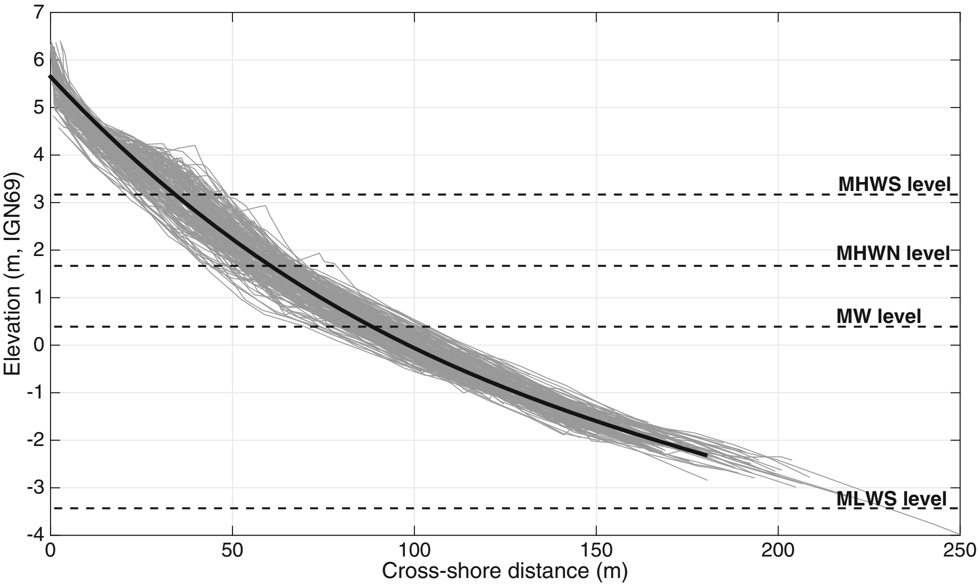

Fig. 3 Cross-shore profiles at Porsmilin from January 2003 to January 2014, indicating the mean beach profile (red), as well as the Mean High Water Spring (MHWS), Mean High Water Neap (MHWN), and Mean Water (MW) levels

point along the intertidal beach profile. In order to study the behavior of different parts of the intertidal beach profile, the temporal evolution of the cross-shore position of three specific elevation contours, MHWS, MHWN, and the Mean Water (MW, 0.4 m IGN69) levels, are shown (Fig. 4). The upper intertidal zone of the beach (represented by the MHWS elevation) shows a mainly seasonal behavior, with erosion during winter, rapid recovery during early spring, and slow accretion during late spring and summer. From 2003 to 2006, the upper part of the beach accreted rapidly at a rate of about 5 m/year. Then, the mean position of the MHWS level remained stable from 2006 to 2010, before experiencing a small erosional trend of 1 m/year from 2010 to 2014, but still not reaching the most eroded measured profile of 2003 (or after the extreme event of winter 2013/2014 (Blaise et al. 2015)). Moving lower down the profile, the inflection point (MHWN) shows a clear pluriannual cycle of about 3 or 4 years: from 2003 to 2005, MHWN progrades, and from 2005 to 2007 it retreats, coming back to the same position as in 2003. The same cycle occurs from 2007 to 2011 and from 2011 to 2014, with smaller amplitude changes and a net accretion trend (1.7 m/year from 2008 to 2014). The lower intertidal zone of the beach represented by the MW level shows mixed behavior, with a pluriannual cycle before 2008 and a more seasonal cycle after 2008. Contrary to the upper intertidal zone or MHWN level, erosion occurs during summer and accretion during winter. From 2010 to 2014, the MW elevation tends to prograde by 2 m/year. This preliminary analysis of three individual contour elevations shows the importance of evaluating the whole intertidal profile instead of focusing on a single contour elevation: overall, the upper intertidal zone erodes slightly, while the middle and the lower intertidal zones accrete.

2.3 Wave and tide data

Hourly wave conditions in 20 m water depth from the numerical model WWIII are used from January 2002 to January 2014 (*NorGas* configuration until 2008, then *NorGas-UG* configuration at the grid point 4° 40.66′ W, 48° 33 N, Tolman (1991)). The WWIII model outputs were compared to observations collected by an Acoustic Doppler Current Profiler (ADCP) deployed during two field experiments (25 November to 31 December 2013, and 24 September to 8 November 2014) at the same coordinates in 20 m water depth. The linear fit between the modeled (Hs_{wwIII}) and measured (Hs_{ADCP}) wave heights confirm the model's skill, with a correlation coefficient of 0.88 and a slope of 1.6 (Fig. 5). It is noted that the larger Hs values (> 1.5 m) are underpredicted by WWIII.

The mean period (Tm) and significant wave height (Hs) from WWIII are not linearly related. Therefore, in order to consider the impacts of both the wave height and wave period variability in the empirical model, wave energy and wave power (taking into the effects of the wave period) are tested to force the model. The mean period (Tm) data is only available between January 2008 and January 2014, which

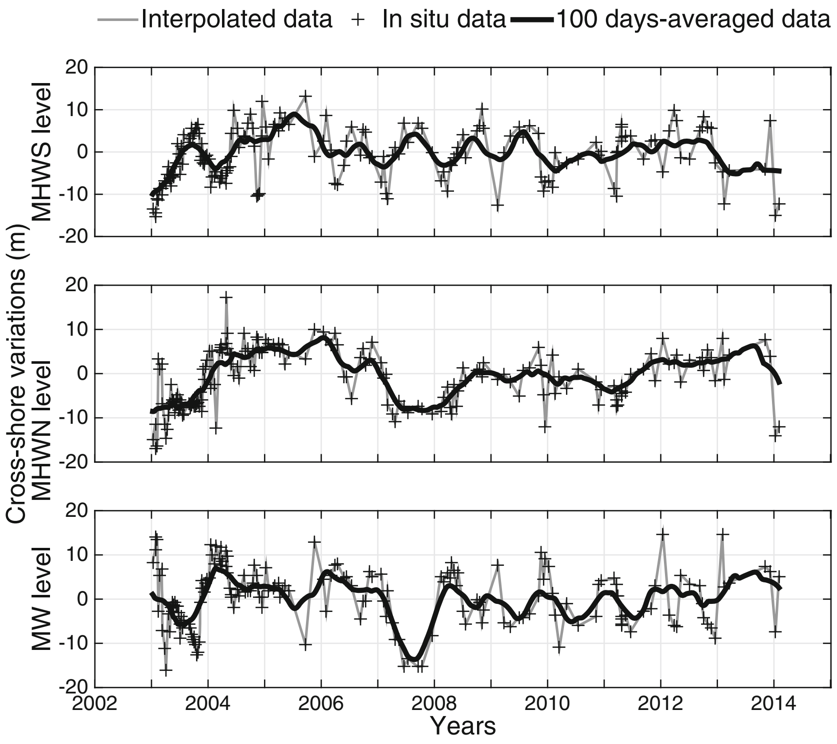

Fig. 4 From top to bottom Temporal evolution of the cross-shore position of the MHWS, MHWN, and MW levels from the in situ data (black crosses), interpolated data (gray line) and 100-day averaged data (thick black line)

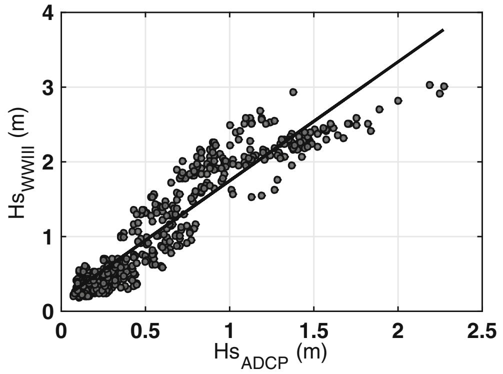

Fig. 5 Scatter diagram of the significant wave height from the numerical model WWIII (Hs_{WWIII}) and significant wave height from an ADCP (Hs_{ADCP}) located near the considered WWIII node, showing the linear regression (black line, y = 1.6x + 0.2) with a correlation coefficient of 0.88

corresponds to 66 beach profiles. Finally, hourly estimates of the tide level (2002 to 2014) from the SHOM (National Hydrographic Service) are used from the grid point 4° 49.48 W, 48° 38.29 N.

3 Equilibrium model

3.1 Model description

An equilibrium shoreline model (Yates et al. 2009; Castelle et al. 2014) is applied at discrete elevations along the intertidal beach profile, ranging from − 1.0 to 4.1 m (every 0.1 m). The model simulates temporal changes of the cross-shore position of each elevation contour using an equilibrium approach based on the theory that a beach adapts to form an equilibrium profile in response to given wave conditions (Wright et al. 1985). The rate at which the beach evolves towards equilibrium is a function of both the intensity of the wave forcing (e.g., wave energy or power) and the disequilibrium between the current and equilibrium conditions (defined as a function of the current contour position S), which causes the beach to erode or accrete. In this study, the model developed by Yates et al. (2009) is used for predicting changes in the cross-shore position (dS/dt), which depend on both the wave energy (E) and the wave energy disequilibrium (ΔE):

$$dS/dt = C^{\pm} E^{1/2} \Delta E \tag{1}$$

with

$$\Delta E = E - E_{\mathrm{eq}}(S) \tag{2}$$

where $C^{\pm}$ are rate change coefficients for accretion (C^{+} for $\Delta E < 0$) and erosion (C^{-} for $\Delta E > 0$). The equilibrium wave energy (E_{eq}) is defined as a linear function of the cross-shore position $E_{\mathrm{eq}}(S) = aS + b$ (a and b are constants for a given elevation). Since the mean wave period has been shown to have significant impacts on the intertidal zone beach morphodynamics (Floc'h et al. 2016), model tests will also include replacing the wave energy with the wave power in Eq. 1. The model developed in Yates et al. (2009) has four free parameters: a and b determining the equilibrium energy for each cross-shore position, and $C^{\pm}$ the accretion and erosion coefficients. Here, following Castelle et al. (2014), a fifth free parameter, d, is added to reduce the dependence of the model on the initial cross-shore position. This parameter represents a deviation of the mean position that is used to initiate the timeseries. A simulated annealing (Barth and Wunsch 1990) algorithm is used to obtain the five free model parameters by minimizing the root-mean-squared error (RMSE) between the model and observations. The number of profiles used to calibrate the model at each of the selected elevations varies from 152 to 174. The number of iterations is 700,000, with a minimum number of loops of 400. In the simulated annealing algorithm, the range of free parameter values in which the optimization occurs has to be defined for each parameter. In previous studies conducted in micro- and mesotidal environements, the equilibrium function E_{eq} is always a negative linear function of the cross-shore position, leading to a negative slope a for every considered altitude. This indicates that erosion always occurs for high wave energy and accretion for low wave energy. To define the range of free parameter values a required for the optimization, the observed accretion/erosion rate is analyzed across the cross-shore profile. When plotting erosion/accretion rate as a function of the cross-shore position and the incident wave energy at different elevation contours and fitting the linear equilibrium function (Fig. 6), the slope is negative on the upper intertidal zone of the beach (close to − 0.1 m^2/m), close to 0 at the inflection point, and positive on the lower intertidal zone of the beach (close to 0.1 m^2/m). From these fits, one can deduce that at the inflection point, the cross-shore position of the elevation contours does not depend on the wave energy and that on the lower intertidal zone of the beach, accretion occurs for strong wave energy events and erosion for low wave energy events (i.e., the opposite of the trend observed on the upper intertidal zone of the beach). In order to verify these preliminary results, the simulated annealing algorithm searches for the five parameters over ranges that span negative and positive values: − 0.5 to − 0.5 m^2/m for a, − 2 to 2 m^2 for b, and − 12 to 12 m.day^{-1}/m^3 for the accretion and erosion coefficients $C^{\pm}$.

3.2 Including tidal water level fluctuations

One important question is how to relate the model free parameters to physical processes (e.g., realistic erosion and

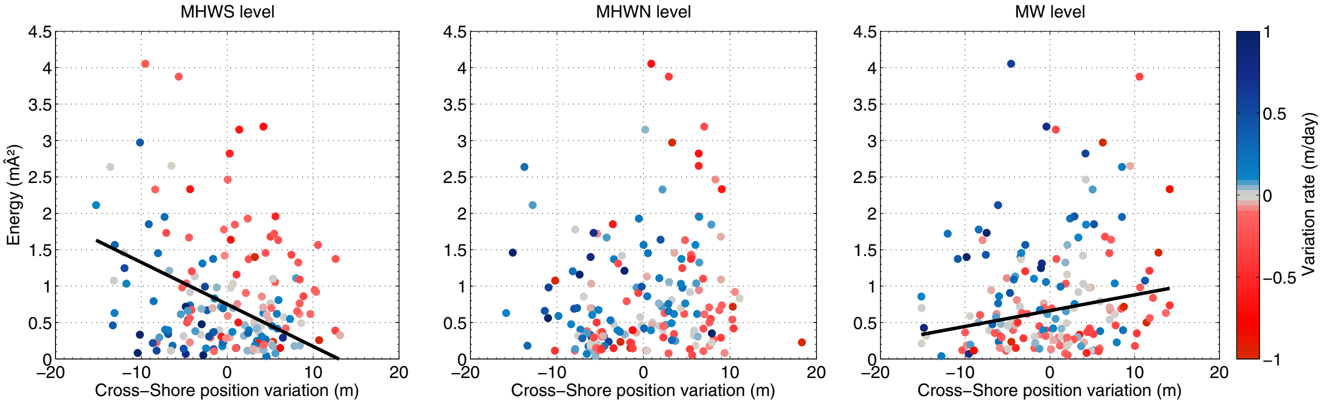

Fig. 6 Erosion (red)/accretion (blue) rate as a function of the to cross-shore position and wave energy (m^2) for: Left MHWS, Center MHWN and Right MW levels; linear equilibrium functions are fitted for variation rates included in [– 0.05; 0.05] m/day (black lines)

accretion rates $C^{\pm}$) when at some altitudes, wave energy only impacts the zone 5% of the time in reality, whereas changes are simulated 100% of the time in the model. Thus, it is important to take into account the tide level when predicting beach morphological changes, especially on meso- and macrotidal beaches. Here, a new approach is proposed in the empirical model by allowing the cross-shore position of the modeled elevation contour to evolve only when it is in the surf or swash zones. This approach requires defining the extent of the surf and swash zones. The upper limit of the swash zone is defined as the vertical runup extent. Many authors have tried to define a generalized formula for the runup level, taking into account the beach slope and/or wave parameters (Guza and Thornton 1982; Holman and Sallenger 1985; King et al. 1990; Stockdon et al. 2006; Senechal et al. 2011; Suanez et al. 2015; Didier et al. 2017). For LTT beach profiles, Caulet et al. (2017) and Almeida et al. (2018) have shown common formula (e.g., Holman and Sallenger 1985; King et al. 1990; Stockdon et al. 2006) underestimate the run up level and do not represent well its temporal and spatial variability. A good approximation of the maximum limit of the runup extent seems to be the significant wave height (Caulet et al. 2017). At the offshore side of the active sediment transport zone, the surf zone offshore extent is often defined proportional to the ratio of significant wave height and water depth (Galvin 1972). The maximum water depth where the breaking occurs on Porsmilin beach corresponds to twice the significant wave height (Dehouck et al. 2009).

In the equilibrium model, a vertical threshold L is defined to determine the spatial extent and therefore the time periods during which the incident wave field causes significant sediment transport around the given elevation contour $Z0$ (see Fig. 7). First, L is chosen as a function of significant wave height: L is taken equal to significant wave height above the observed still water level (maximum runup as upper limit, as described above) and to twice the significant wave height below this elevation (surf zone limit as lower limit). Second, in order to evaluate the impact of this threshold on the model parameters, L is assumed symmetric about the water level $Z0$ for simplicity and a series of sensitivity tests are conducted, with $L = 0.5$, 1, 1.5, 2, 2.5, and 3 m. In the model, the difference between the simulated elevation contour ($Z0$, Fig. 7a) and the instantaneous still water level (hourly tidal predictions obtained from the SHOM data) is calculated and compared to this threshold. If the absolute value of this difference is greater than L, then the simulated shoreline position is not modified (blue zones, Fig. 7b). In this study, for each simulation, the model skill was evaluated with the

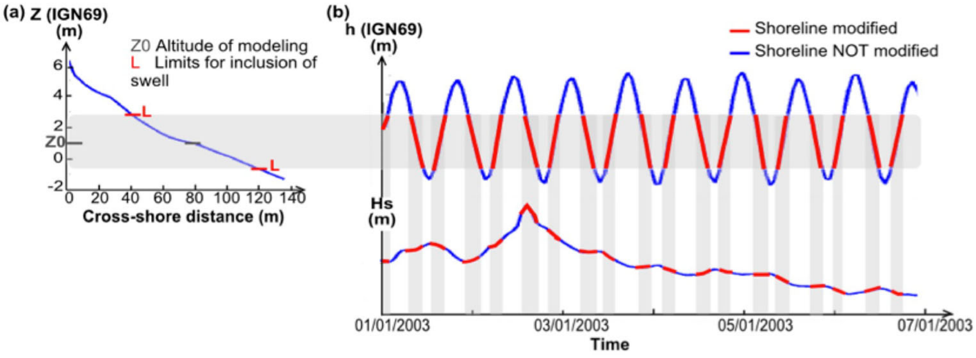

Fig. 7 Diagram showing how the water level is taken into account in the equilibrium mode: **a** beach profile with the selected elevation contour $Z0$ and modeling threshold L, and **b** tide level determining the time periods (red) when the model takes into account the wave forcing to simulate change in the contour elevation cross-shore position

R-squared coefficient (of determination) denoted *R*2, and the root-mean-squared error (RMSE) between the modeled and observed cross-shore position.

4 Results

4.1 Data analysis

In order to explain the observed elevation contour behavior, the main modes describing the beach evolution are extracted from an EOF (Empirical Orthogonal Function) analysis of the detrended profile evolution timeseries (Aubrey 1979; Aubrey et al. 1980; Larson et al. 2003; Karunarathna et al. 2012). This analysis demonstrates that two principal modes describe 64% of the cross-shore variability (Hamon 2014). The first EOF represents 36% of the beach variation, showing variations in the upper intertidal zone, with a seasonal berm appearing at the MHWS level during summer, persisting through autumn, and then disappearing progressively in winter and spring (e.g., along the cross-shore profile between 10 and 60 m, Fig. 8). A fft (fast fourier transform) analysis of the first temporal mode associated with this spatial mode shows peaks at seasonal frequencies similar to those of the significant wave height. The second EOF represents 28% of the morphological changes showing variations along the profile between the MHWN level down to the lower intertidal zone of the beach (e.g., between 50 and 100 m, Fig. 8). The fft analysis associated temporal mode shows a peak period at 3.8 years and only small seasonal components. The temporal variability of this mode is slightly correlated (29%) to the pluriannual behavior of the lower part of the beach, shown in Fig. 3. Preliminary comparisons show that this variability does not seem to be related to the wave climate or other global climate factors (e.g., NAO, ENSO, or WEPA indices, Gouirand and Moron 2003; Treguer et al. 2014; Castelle et al. 2017)

4.2 Empirical model application

During the investigated period, the wave energy at Porsmilin beach varied seasonally. Between 2003 and 2014, the winters of 2006, 2008, and 2010 were the most energetic (Fig. 8), and the winters of 2008, 2010, and 2014 showed maxima in the wave power. These time periods also show large changes in contour position (e.g., Fig. 4), suggesting the importance of the intensity and/or frequency of storms during these winters. To test the accuracy of the empirical equilibrium model in reproducing contour elevation changes, the model was applied along the intertidal beach profile, and Fig. 9 shows the model results when the model is forced with the wave energy. Colored lines show the cross-shore positions of different altitudes vs time. Black crosses correspond to the in situ data acquired at MHWS, MHWN, and MW levels. The thin black lines show the empirical model results for these specific altitudes. Figure 10 compares the predictive ability (RMSE) of the empirical model when forced with wave energy or wave

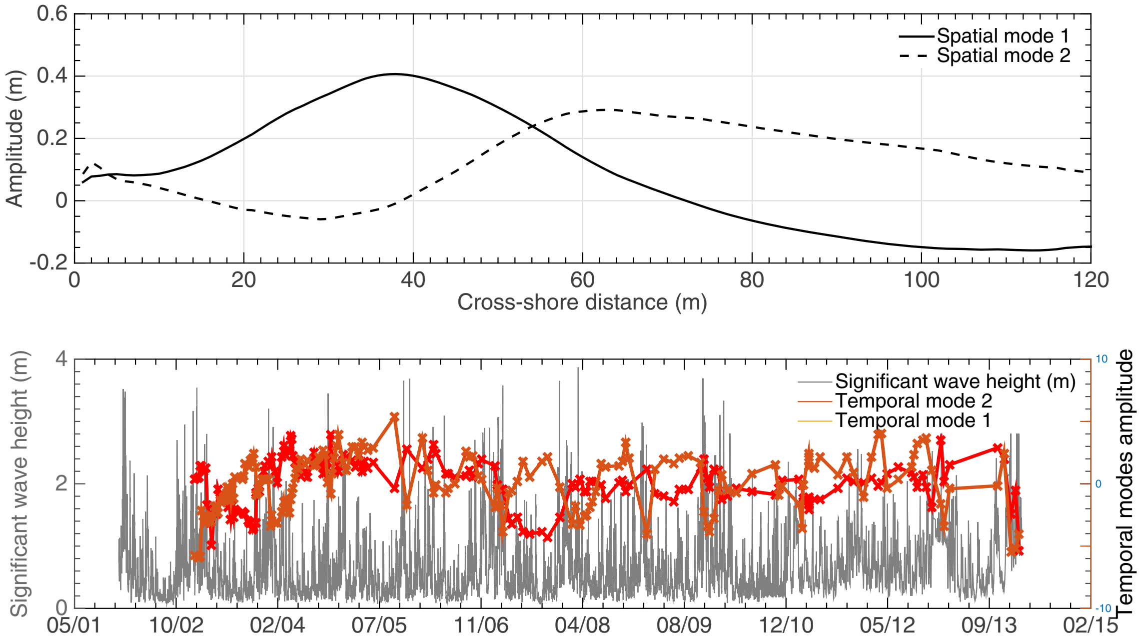

Fig. 8 Empirical Orthogonal Functions (EOF) analyses from 2002 to 2014: Top Two main spatial modes amplitudes vs cross-shore distance from the top of the beach; Bottom Significant wave height (Hs) from WWIII *Norgas* and *Norgas-UG* configuration (gray) and the temporal intensity of the first (orange) and second (red) modes

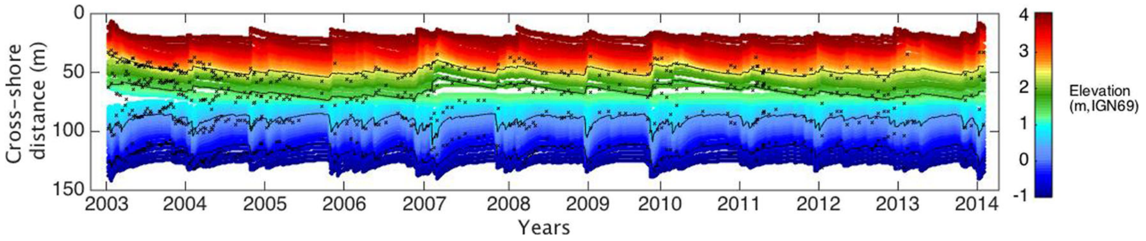

Fig. 9 Empirical model results forced by the wave energy for altitudes from − 1 m up to 4.1 m (IGN69) every 0.1 m (colored lines), in situ data for MW, MHWN, and MHWS levels (black crosses), and the corresponding empirical model results (black thin lines)

power. For the wave power, only the period 2008–2014 is considered (due to lack of wave period data before 2008). For the wave energy, the predictive ability of the model is similar is considering the period 2008–2014 or the entire set of observations from 2002–2014. The model using the wave energy reproduces well the variation of the cross-shore position at seasonal and weekly scales on the upper intertidal zone of the beach, down to an elevation (Z) of approximately 2.2 m with an $R^2 > 0.5$ (Fig. 10). The best predictive ability of the model, with $R^2 = 0.6$, is observed at 3.4 m elevation (MHWS). The correlation coefficient decreases to its minimum (10%) at the inflection point and then increases up to 40% in the lower intertidal zone of the beach. The model reproduces well the seasonal component on the lower intertidal zone of the beach but not the observed pluriannual cycle. Hence, the inflection point behavior is not captured by the empirical model. The predictive ability is improved if the model is forced with the wave power: slightly in the upper intertidal zone (70%) and strongly in the lower intertidal zone (70%), but no improvement occurs at the inflection point (Fig. 9). Thus, taking into account the wave period appears more important in predicting the lower intertidal zone morphodynamics than the upper intertidal zone morphodynamics where the significant wave height is sufficient to explain 60% of the variability. The significant wave height explains 40% of the lower intertidal zone morphodynamics while the mean period explains an additional 30%. The pluriannual cycle (3.8 years) and the inflection point behavior remain poorly reproduced.

Looking more closely at the model's predictive ability on short time scales, erosion is generally well reproduced in the upper intertidal zone, including the periods of significant erosion during the winters of 2006/2007 and 2013/2014 (Fig. 11). The performance of the model decreases during periods of accretion, when the contour position change rate is smaller, but the cumulative accretion may still be large. Inversely, in the lower intertidal zone, accretion is well reproduced and erosion is underestimated.

The free parameter a is negative as expected, above the MHWN level (inflection point) with values between − 0.25 m^2/m and 0 m^2/m (Fig. 12). Its value is quite constant (− 0.2 m^2/m) between MHWS and MHWN levels. At the inflection point, the slope sign changes rapidly to a positive value, of about 0.2 m^2/m, which remains constant for altitudes below 1.4 m IGN69. The free parameter b remains between 1 and 2 m^2 (Fig. 12). The erosion (C^-) and accretion (C^+) coefficients increase from − 0.5 to 0 m day^{-1} m^{-3} at the inflection point (Fig. 12). At 1.0 m IGN69, they increase suddenly to 0.5 m day^{-1} m^{-3} and remain nearly constant for altitudes below 1.0 m IGN69. Thus, the erosion and accretion rate coefficients also change sign crossing the inflection point.

4.3 Effects of water level

In order to simulate more realistically the contour elevation changes on a macrotidal beach, the water level is taken into account as described in Section 3.2. Since wave period data are only available after 2008, this adaptation is tested with the model based on the wave energy in order to use the whole dataset. The model takes into account the

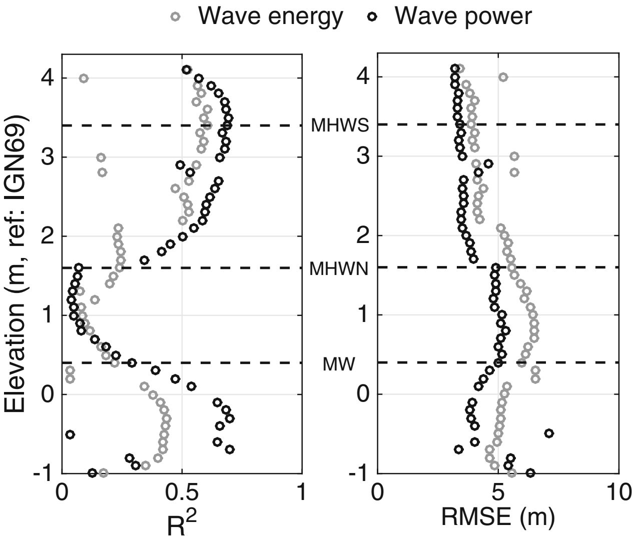

Fig. 10 Predictive ability when the model is forced with wave energy (Hs^2) or wave power (Hs^2×Tm): (left) correlation coefficient between model results and in situ data R^2, and (right) corresponding root mean square error (RMSE) in meters

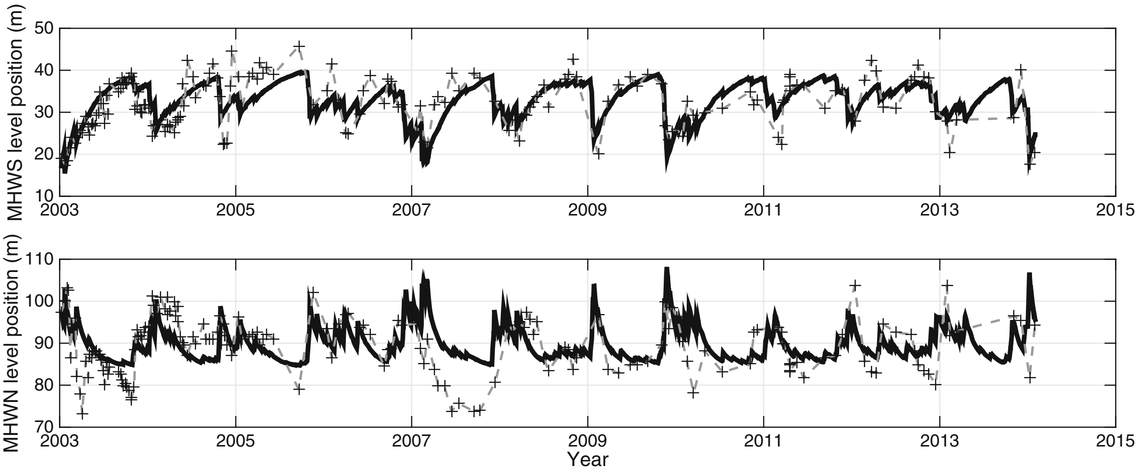

Fig. 11 Temporal variability of the cross-shore position from in situ data (black crosses and gray dashed line) and from the empirical model (black line) at: Top MHWS and bottom MHWN levels

effects of the water level for six symmetric thresholds (L) ranging from 0.5 to 3.0 m, every 0.5 m, and for a varying threshold L that depends on the significant wave height. The first important conclusion is that the model's predictive ability remains the same when applying the effect of the tide level, independent of the threshold L (bottom right plot in Fig. 13). The model is therefore able to reproduce the same morphological changes even if the percentage of wave conditions for which morphological changes are simulated is decreased. For example, for $L = 3$ m, this percentage is almost 100% for elevations between 0 and 1 m, but it decreases to 80% for elevations between 3.5 and 4 m, because the water level will be in the range [tide level ± 3 m] only 80% of the time. This percentage decreases for decreasing L. For $L = 0.5$ m, the maximum percentage of wave conditions taken into account to model the morphodynamical evolution of an altitude is only 20%. The consequence of this threshold L is a reduction of the time period when the cross-shore position evolves in the model. The threshold has no impact on the optimal linear equilibrium function, which does not depend on the duration of the beach response, hence the parameters a and b (Fig. 13). However, the threshold L strongly impacts the rate coefficients that depend on the duration of the beach response. The values of $C^{\pm}$ increase with a decrease in the time period during which the elevation contour movement is simulated, i.e., for decreasing values of L. For $L = 0.5$ m, the most dynamic part of the beach (MHWS and MW levels) reaches a variation rate of ± 4 m day^{-1} m^{-3}. When L is allowed to vary temporally proportional to the significant wave height, the results are similar to those obtained with $L = 0.5$ m for C^{+} and $L = 3$ m for C^{-}.

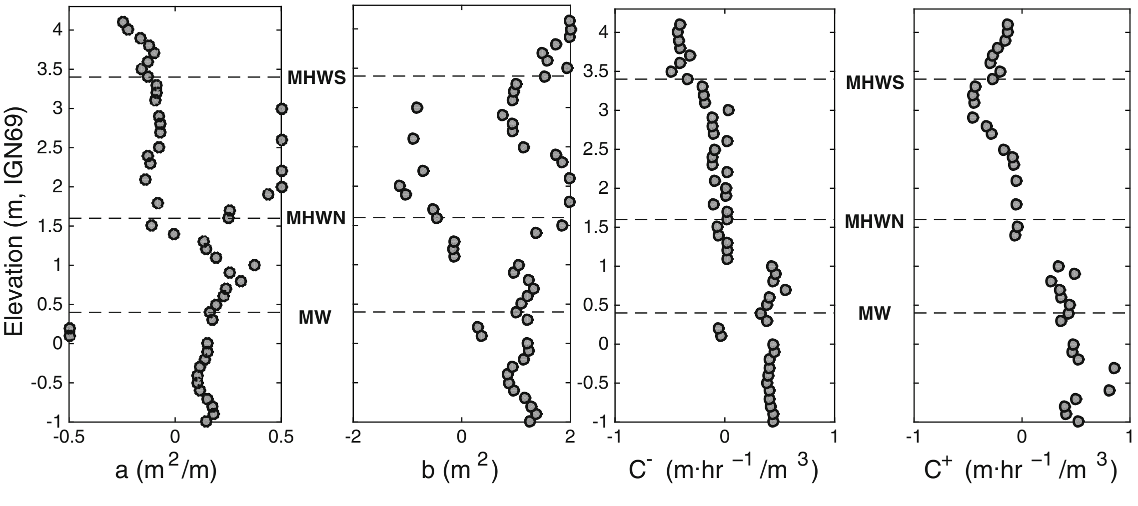

Fig. 12 Four free parameters of Eq. 1 (using Hs^2 as wave energy) determined using simulated annealing to optimize the prediction of the cross-shore position S using Eq. 1

Fig. 13 Four free parameters of Eq. 1 (using wave energy) determined using the simulated annealing to optimize the prediction of the cross-shore position S using Eq. 1 and the associated predictive ability (R^2) considering the effects of water level via different thresholds L, ranging from 0.5 to 3 m, each 0.5 m, and for a threshold L varying proportional to the significant wave height

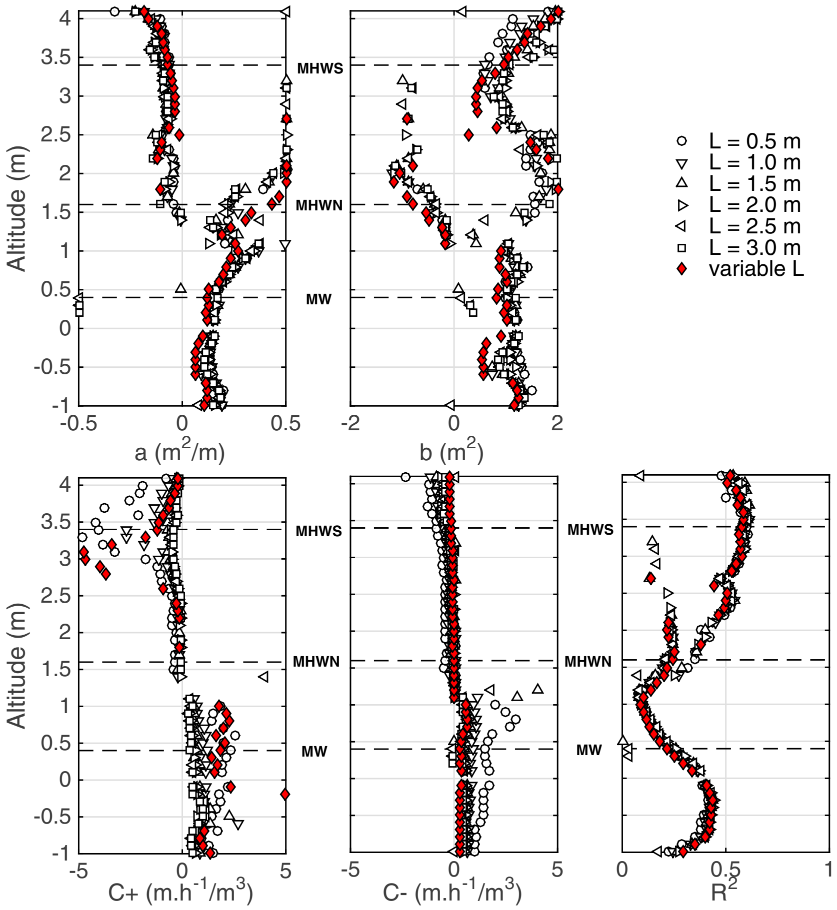

5 Discussion

5.1 Empirical model application

This study applied an empirical equilibrium model in a macrotidal environment for the first time. The model is calibrated for a range of altitudes over the intertidal zone from − 1.0 to 4.1 m IGN69 (French Geographic Datum). The efficiency of the empirical model forced by wave energy is 60% around the MHWS and 40% around the MW level on a macrotidal beach. This study shows that the empirical model developed by Yates et al. (2009) and Castelle et al. (2014) is able to predict contour elevation variations in different tidal regimes on the upper intertidal zone of the beach. This model is able to predict the variation of the shoreline on a microtidal beach with a higher efficiency of 90% (Yates et al. 2009, 2011; Ludka et al. 2015) and on a mesotidal beach with an efficiency around 70% (Castelle et al. 2014). At Porsmilin beach, where the mean wave period was shown to have an important role in beach morphodynamics in previous studies, forcing the equilibrium model with the wave power improved the predictive ability in the upper intertidal zone of the beach from 60 to 70% and in the lower intertidal zone from 40 to 70%.

Porsmilin beach is classified as a LTT beach (Masselink and Short 1993) with a reflective upper intertidal zone and a dissipative lower intertidal zone. At the inflection point in between, the slope changes rapidly (near the MHWN level). At Porsmilin, this is observed with mean slopes of 0.08 and 0.02 above and below MHWN. The behavior of each zone is different as suggested by Miles and Russell (2004). However, contrary to their observations, the lower part of the beach exhibits significant morphological changes, comparable to what is observed in the upper intertidal zone. Above MHWN, high (low) incident conditions are related to strong erosion (accretion), and 60% of the variability is related to the significant wave height. Below MHWN, the equilibrium function is inverted compared to the literature on meso- and microtidal environments (Yates et al. 2009; 2011; Castelle et al. 2014; Ludka et al. 2015): high (low) incident energy leads to accretion (erosion). This may be expected if one considers that the erosion of the upper intertidal zone of the beach leads to a transport to the lower intertidal zone. Since the wave power is more important at high tide than at low tide (less dissipation over the shelf), the erosion in the upper intertidal zone could lead to an accretion in the lower intertidal zone. However, one must note that the cross-shore elevation contours on the upper and lower intertidal zone of the beach are not clearly correlated and thus the sediment exchanges between the upper and lower intertidal zone of the beach are not as simple as suggested. The significant wave height explains only 40% of the variability in the lower intertidal zone and the mean wave period improves the predictions by nearly 30%. This demonstrates the importance of the mean wave period in the lower intertidal zone morphodynamics and shows the different behavior of the dissipative and the reflective zones. Contrary to the rest of the beach, the zone around the inflection point is reproduced poorly by the empirical equilibrium model. First, this region represented by the MHWN level is shown to have a cross-shore position that does not depend on the wave energy ($a \sim 0$). In addition, no seasonal cycle is observed but a strong pluriannual component exists with a caracteristic period of 3–4 years and a net trend of accretion, which is not reproduced by the empirical equilibrium model, suggesting that the forcing responsible for this pluriannual cycle is neither the significant wave height nor the mean period. This variability does not seem to be related to the wave climate or other global climate factors (Gouirand and Moron 2003; Treguer et al. 2014; Castelle et al. 2017), and more investigations are needed to fully understand the beach dynamics on these timescales.

Considering shorter time scales, erosion processes are represented better than the accretion processes in the upper intertidal zone, and, on the contrary, accretion processes are well reproduced in the lower intertidal zone, but erosion is underestimated (Fig. 11). Accretion in the upper intertidal zone and erosion in the lower intertidal zone occur for low incident wave energy. To improve the model's predictive ability above 70%, the low incident energy morphological response needs to be reproduced better. For low incident wave energy, the equilibrium position fixed by the linear equilibrium function (and the fixed parameter a and b) seems to underestimate the real position that can be reached at the considered elevation. The beach reacts quicker than the model to the incident wave energy and the upper (lower) part of the beach progrades (retreats) more rapidly than in the model. The linear equilibrium function may not be a good hypothesis for low energy conditions, where the equilibrium position does not reproduce well the maximum (minimum) position observed on the upper (lower) part of the beach. A function allowing for a varying slope a as a function of the incident wave energy could be used, with a smaller slope for low energy conditions, but more studies are needed of low energy accretionary processes to understand better the beach morphodynamical response.

5.2 Water level and comparison with other study sites

To take into account the effects of varying water levels, the tide level is used in order to determine the time period during which waves impact the intertidal beach morphology. This leads to considering shorter periods of variation, thus larger variation rates. In order to be able to compare study sites located in different tidal environments, a threshold L is proposed to take into account the water level in a range about the astronomical tide level. This threshold is defined between the maximum vertical runup observed on the study site and the breaking point depth (i.e., the extent of the surf and swash zones). Either a realistic threshold is considered, following the variation of significant wave height ($L = Hs$ to model the maximum runup according to previous study on LTT beaches (Caulet et al. 2017; Almeida et al. 2018) and $L = 2Hs$ considering the breaking index observed on this study site (Dehouck et al. 2009)) or a constant, symmetric threshold is considered to study the sensitivity of the free parameters to the threshold L.

The empirical model converges to the same predicted cross-shore position independent of the threshold L. Thus, the efficiency of the model is the same, and the parameters a and b do not change (the linear equilibrium function remains unchanged). Only the coefficients C^+ and C^- (accretion/erosion rates) change depending on the water level threshold L, since the erosion and accretion rate coefficients depend strongly on the duration of wave impact. On the upper and lower limits of the beach, the model simulates contour elevation changes as little as 20% of the time, leading to the largest increases in the rate change coefficients, as would be expected.

Without this threshold, the rate coefficients were in the range $[-0.5; 0.5]$ m day^{-1} m^{-3}. In the literature, the rate coefficients are of the magnitude 4 m day^{-1} m^{-3} in a microtidal environment (Torrey Pines (Yates et al. 2009)) and were in the range $[-3; 3]$ m day^{-1} m^{-3} in a mesotidal environment (Truc Vert (Castelle et al. 2014)). Whereas the vertical evolution of the free parameters a and b are similar between the different study sites, the magnitude of the change coefficients are different, with a minimum value in the macrotidal environment. However, the dynamics at Porsmilin have been shown to be quite rapid (Floc'h et al. 2016), expecting rate coefficients at least as large as on other study sites. Introducing the tide level effects in the model via the threshold L leads to larger rate coefficient for smaller thresholds. For L larger than 1.0 m, the magnitude of $C^{\pm}$ remains small. For $L = 1.0$ m, the magnitude of $C^{\pm}$ reaches the range $[-3; 3]$ m day^{-1} m^{-3}, as in Castelle et al. (2014). The most dynamic zone appears to be the MHWS level and between the MW and MHWN level. C^+ increases more than C^- at MHWS level and C^- increases more than C^+ between MW and MHWN levels. The C^+ and C^- coefficients allow considering different adaptation velocities related to accretion or erosion process, but comparing their magnitudes is not straightforward because of the $\sqrt{E}$ factor in Eq. 1, which is larger when considering C^- than C^+. C^+ has an important role when the incident energy is lower than the equilibrium energy, which indicates accretion and erosion above and below the MHWN level, respectively (mean inflection point observed on this LTT beach). The accretion in the upper intertidal zone is more localized about the MHWS level while the erosion in the lower intertidal zone seems to be spread over a large spatial extent. When the threshold L varies as a function of the significant wave height, the results are similar to those obtained with $L = 0.5$ m for C^+ coefficients, which corresponds to the observed mean significant wave height at Porsmilin. C^- becomes important when the incident wave energy is larger than the equilibrium energy, which indicates erosion and accretion above and below the MHWN level, respectively. The accretion in the lower intertidal zone seems to be localized just below the mean inflection point, when the slope a reaches its maximum positive value (0.8–1 m IGN69). For the C^- coefficients, the results are similar to those obtained with $L = 3$ m, suggesting that the majority of the beach is impacted during larger storms (erosion events) and that the storms with large Hs control the magnitude of the erosion rate change coefficients.

6 Conclusion

This study assesses the predictions of pluriannual morphological evolution of the intertidal zone on a Low Tide Terrace (LTT) beach (Masselink and Short 1993) using an empirical equilibrium model. The model shows a good predicitve ability in the upper intertidal zone (60%) where the sediment dynamics depend on the waves energy, while the lower intertidal zone changes are reproduced at only 40%. The contours near the inflection point are poorly reproduced by the model. Using the wave power instead of the wave energy improves the predictive ability mostly in the dissipative (lower intertidal) zone, where the significant wave height explains 40% of the lower intertidal zone morphodynamics while the mean period explains about 30%. The observed pluriannual cycle and the inflection point behavior remain poorly reproduced. The extension of the model to take into account the effects of the water level during the tidal cycle does not change the model's predictive ability. However, this extension does improve the physical interpretation of the estimated erosion and accretion coefficients and allows a comparison to other study sites with different tidal ranges. Our results confirm that the upper zone of the reflective section, which corresponds to the swash zone during high tide of spring tide, shows large fluctuations occurring in phase with significant wave height. As typically observed in macrotidal environment, this is indeed the tidal stage with largest significant wave height (less dissipation). Our study provides new insights on the dissipative section. Generally much wider than the reflective section, the entire dissipative section shows fluctuations of the same magnitude as the reflective section. Still, morphological response of the beach in low incident energy conditions is underestimated and the model needs to be improved to address this configuration.

Funding information This work was supported by the Labex-MER funded by the Agence Nationale de la Recherche under the program Investissements d'avenir with the reference ANR-10-LABX-19-01, the lab Géosciences Océan UMR6538 and the Pôle Image of IUEM. The long-term measurements were successively supported by the ANR COCORISCO (2010-CEPL-001-01), the SOERE trait de cte and the NSO Dynalit in the frame of the IR ILICO.

References

Almeida LP, Almar R, Marchesiello P, Blenkinsopp C, Martins K, Sénéchal N, Floc'h F, Bergsma E, Benshila R, Caulet C, Biausque M, Duong TH, Le Thanh B, Nguyen TV (2018) Tide control on the swash dynamics of a steep beach with low-tide terrace. Mar Geol xx (accepted with minor revision)

Aubrey DG (1979) Seasonal patterns of onshore/offshore sediment movement. J Geophys Res Oceans 84(C10):6347

Aubrey DG, Inman DL, Winant CD (1980) The statistical prediction of beach changes in southern California. J Geophys Res Oceans 85(C6):3264

Barth N, Wunsch C (1990) Oceanographic experiment design by simulated annealing. J Phys Oceanogr 20:1249

Blaise E, Suanez S, Stéphan P, Fichaut B, David L, Cuq V, Autret R, Houron J, Rouan M, Floc'h F et al (2015) Bilan des tempêtes de lÕhiver 2013–2014 sur la dynamique de recul du trait de côte en Bretagne. Géomorphologie: Relief, Processus, Environnement 21(3):267

Bruun P (1954) Coastal erosion and development of beach profiles. 44 (Technical Memorandum - U.S. Army Corps of Engineers. Washington D. C.)

Castelle B, Marieu V, Bujan S, Ferreira S, Parisot JP, Capo S, Sénéchal N, Chouzenoux T (2014) Equilibrium shoreline modelling of a high-energy meso-macrotidal multiple-barred beach. Mar Geol 347:85

Castelle B, Dodet G, Masselink G, Scott T (2017) A new climate index controlling winter wave activity along the Atlantic coast of Europe: The West Europe Pressure Anomaly. Geophys Res Lett 44(3):1384

Caulet C, Floc'h F, Le Dantec N, Augereau E, Ardhuin F, Delacourt C (2017) Wave setup variations along a cross-shore profile of a sandy pocket beach, Porsmilin, Brittany, France. In: Coastal dynamics, copenhague, danemark, 12–16 juin

Davidson M, Turner I (2009) A behavioral template beach profile model for predicting seasonal to interannual shoreline evolution. J Geophys Res Earth Surf 114(F1):1:21

Davidson M, Lewis R, Turner I (2010) Forecasting seasonal to multiyear shoreline change. Coast Eng 57(6):620

Davidson M, Splinter K, Turner I (2013) A simple equilibrium model for predicting shoreline change. Coast Eng 73:191

Dean RG (1977) Equilibrium beach profiles: US Atlantic And Gulf coasts (Department of Civil Engineering and College of Marine Studies, University of Delaware)

Dean RG (1991) Equilibrium beach profiles: characteristics and applications. J Coast Res 7(1):53–84

Dehouck A, Dupuis H, Sénéchal N (2009) Pocket beach hydrodynamics: The example of four macrotidal beaches, Brittany, France. Mar Geol 266(1):1

Didier D, Bernatchez P, Augereau E, Caulet C, Dumont D, Bismuth E, Cormier L, Floc'h F, Delacourt C (2017) LiDAR validation of a video-derived beachface topography on a tidal flat. Remote Sens 9(8):826

Floc'h F, Le Dantec N, Lemos C, Cancouët R, Sous D, Petitjean L, Bouchette F, Ardhuin F, Suanez S, Delacourt C (2016) Morphological response of a macrotidal embayed beach, Porsmilin, France. J Coast Res 75(sp1):373

Galvin C (1972) Wave breaking in shallow water. In: Meyer (ed) Waves on Beaches and Resulting Sediment Transport, pp 413–456

Gouirand I, Moron V (2003) Variability of the impact of El Niño–southern oscillation on sea-level pressure anomalies over the North Atlantic in January to March (1874–1996). Int J Climatol 23(13):1549

Guza R, Thornton EB (1982) Swash oscillations on a natural beach. J Geophys Res Oceans 87(C1):483

Hamon K (2014) Étude de la morphodynamique et du profil d'équilibre d'une plage de poche macrotidale. Master's thesis, Laboratoire Géosciences Océan UMR6538 IUEM/UBO

Hansen JE, Barnard PL (2010) Sub-weekly to interannual variability of a high-energy shoreline. Coast Eng 57(11):959

Holman RA, Sallenger A (1985) Setup and swash on a natural beach. J Geophys Res Oceans 90(C1):945

Karunarathna H, Horrillo-Caraballo JM, Ranasinghe R, Short AD, Reeve DE (2012) An analysis of the cross-shore beach morphodynamics of a sandy and a composite gravel beach. Mar Geol 299:33

King B, Blackley M, Carr A, Hardcastle P (1990) Observations of wave-induced set-up on a natural beach. J Geophys Res Oceans 95(C12):22289

Kroon A, Masselink G (2002) Morphodynamics of intertidal bar morphology on a macrotidal beach under low-energy wave conditions, North Lincolnshire, England. Mar Geol 190(3-4): 591

Larson M, Capobianco M, Jansen H, Rózyński G, Southgate HN, Stive M, Wijnberg KM, Hulscher S (2003) Analysis and modeling of field data on coastal morphological evolution over yearly and decadal time scales. Part 1: Background and linear techniques. J Coast Res:760–775

Ludka B, Guza R, O'Reilly W, Yates M (2015) Field evidence of beach profile evolution toward equilibrium. J Geophys Res Oceans 120(11):7574

Masselink G, Short AD (1993) The effect of tide range on beach morphodynamics and morphology: a conceptual beach model. J Coast Res 9(3):785–800

Masselink G, Kroon A, Davidson-Arnott R (2006) Morphodynamics of intertidal bars in wave-dominated coastal settings' review. Geomorphology 73(1-2):33

Masselink G, Castelle B, Scott T, Dodet G, Suanez S, Jackson D, Floc'h F (2016) Extreme wave activity during 2013/2014 winter and morphological impacts along the Atlantic coast of Europe. Geophys Res Lett 43(5):2135

Miles JR, Russell PE (2004) Dynamics of a reflective beach with a low tide terrace. Cont Shelf Res 24(11):1219

Miller JK, Dean RG (2004) A simple new shoreline change model. Coast Eng 51(7):531

Price T, Ruessink B (2008) Morphodynamic zone variability on a microtidal barred beach. Mar Geol 251(1-2):98

Qi H, Cai F, Lei G, Cao H, Shi F (2010) The response of three main beach types to tropical storms in South China. Mar Geol 275(1–4):244

Senechal N, Coco G, Bryan KR, Holman RA (2011) Wave runup during extreme storm conditions. J Geophys Res Oceans 116(C7):1:13

SHOM (1994) Courants de mare de la cte ouest de bretagne de goulven penmarch. Tech. rep. SHOM

Splinter KD, Turner IL, Davidson MA, Barnard P, Castelle B, Oltman-Shay J (2014) A generalized equilibrium model for predicting daily to interannual shoreline response. J Geophys Res Earth Surf 119(9):1936

Stive MJ, Aarninkhof SG, Hamm L, Hanson H, Larson M, Wijnberg KM, Nicholls RJ, Capobianco M (2002) Variability of shore and shoreline evolution. Coast Eng 47(2):211

Stockdon HF, Holman RA, Howd PA, Sallenger AH Jr (2006) Empirical parameterization of setup, swash, and runup. Coast Eng 53(7):573

Stocker T (2014) Climate change 2013: the physical science basis: Working Group I contribution to the Fifth assessment report of the Intergovernmental Panel on Climate Change, Cambridge University Press, Cambridge

Suanez S, Cancouët R, Floc'h F, Blaise E, Ardhuin F, Filipot JF, Cariolet JM, Delacourt C (2015) Observations and predictions of wave runup, extreme water levels, and medium-term dune erosion during storm conditions. Journal of Marine Science and Engineering 3(3):674

Tolman HL (1991) A third-generation model for wind waves on slowly varying, unsteady, and inhomogeneous depths and currents. J Phys Oceanogr 21(6):782

Treguer P, Goberville E, Barrier N, L'Helguen S, Morin P, Bozec Y, Rimmelin-Maury P, Czamanski M, Grossteffan E, Cariou T et al (2014) Large and local-scale influences on physical and chemical characteristics of coastal waters of Western Europe during winter. J Mar Syst 139:79

Wright L, Short A, Green M (1985) Short-term changes in the morphodynamic states of beaches and surf zones: an empirical predictive model. Mar Geol 62(3-4):339

Yates M, Guza R, O'Reilly W (2009) Equilibrium shoreline response: Observations and modeling. J Geophys Res Oceans 114(C9):1:16

Yates M, Guza R, O'Reilly W, Hansen J, Barnard P (2011) Equilibrium shoreline response of a high wave energy beach. J Geophys Res Oceans 116(C4):1:13

Appendix D

Articles: Coastal wave hydrodynamics

D.1 Yates and Benoit (2015)

INTERNATIONAL JOURNAL FOR NUMERICAL METHODS IN FLUIDS
Int. J. Numer. Meth. Fluids 2015; **77**:616–640
DOI: 10.1002/fld.3992

Accuracy and efficiency of two numerical methods of solving the potential flow problem for highly nonlinear and dispersive water waves

Marissa L. Yates[1,2,*,†] and Michel Benoit[1,3]

[1] *Saint-Venant Hydraulics Laboratory, Université Paris-Est (joint research unit EDF R&D, Cerema, ENPC), 6 quai Watier, BP 49, 78401 Chatou, France*
[2] *Centre for Studies and Expertise on Risks, Environment, Mobility, and Urban and Country Planning (Cerema), 134 rue de Beauvais, CS 60039, Margny Les Compiègne, France*
[3] *EDF Research and Development (EDF R&D), 6 quai Watier, BP 49, 78401 Chatou, France*

SUMMARY

The accuracy and efficiency of two methods of resolving the exact potential flow problem for nonlinear waves are compared using three different one horizontal dimension (1DH) test cases. The two model approaches use high-order finite difference schemes in the horizontal dimension and differ in the resolution of the vertical dimension. The first model uses high-order finite difference schemes also in the vertical, while the second model applies a spectral approach. The convergence, accuracy, and efficiency of the two models are demonstrated as a function of the temporal, horizontal, and vertical resolutions for the following: (1) the propagation of regular nonlinear waves in a periodic domain; (2) the motion of nonlinear standing waves in a domain with fully reflective boundaries; and (3) the propagation and shoaling of a train of waves on a slope. The spectral model approach converges more rapidly as a function of the vertical resolution. In addition, with equivalent vertical resolution, the spectral model approach shows enhanced accuracy and efficiency in the parameter range used for practical model applications. Copyright © 2015 John Wiley & Sons, Ltd.

Received 11 June 2014; Revised 21 October 2014; Accepted 24 November 2014

KEY WORDS: finite difference; spectral; marine hydrodynamics; nonlinear dynamics; free surface; partial differential equations

1. INTRODUCTION

Accurate and efficient models of nonlinear wave propagation are necessary for coastal and ocean engineers to simulate a variety of coastal processes including shoreline processes, wave interactions with coastal structures, wave energy conversion devices, and even the propagation of tsunamis. Until recently, the majority of wave engineering studies, including the wave energy conversion industry, continued to use linear wave models because of the need to model large spatial domains without prohibitive computational costs [1]. However, in the nearshore region, it is necessary to model the nonlinear and dispersive characteristics of waves, as well as wave interactions with variable bathymetry, to model accurately wave transformation processes.

A growing number of models exist to fulfill this need, ranging from computationally intensive CFD models resolving the full Navier–Stokes equations to Boussinesq or Serre-type models that simplify the vertical structure of the dynamics and are only partially nonlinear and/or dispersive. The use of the Reynolds-averaged Navier–Stokes equations with a turbulence closure scheme enables modeling the complete dynamics of wave propagation and wave interactions with structures

---

[*] Correspondence to: Marissa L. Yates, Saint-Venant Hydraulics Laboratory, Université Paris-Est, 6 quai Watier, B.P. 49, 78401 Chatou, France.
[†] E-mail: marissa.yates-michelin@cerema.fr

(e.g., [2–4]). However, the domain size and resolution are limited by the computational cost, preventing the use of such models for practical applications in the coastal zone. In addition, the numerical methods used in these codes often are unable to propagate accurately free surface waves over long distances without a reduction in the wave phase speed or height because of the presence of numerical diffusion.

By neglecting viscosity and assuming irrotational flow thereby restricting the application of the model to non-breaking waves, the Navier–Stokes equations can be reduced to a fully nonlinear potential flow problem requiring the resolution of the Laplace problem in the fluid domain. A commonly applied strategy for resolving this problem is the use of the boundary integral equations, in which the resolution of the Laplace equation in the interior of the fluid domain is projected onto the boundary surface of the fluid volume (e.g., [5, 6]). Additional proposed methods include projection to a fixed level in the fluid using pseudo-spectral methods [7] to treat the nonlinear free surface boundary conditions (e.g., [8, 9]), or simplification of the vertical variability using a polynomial expansion in the vertical with Boussinesq-type methods (e.g., [10–13]).

Recent work on the direct numerical simulation of the 3D Laplace equation uses finite element [14, 15] and finite difference [16–18] approaches. Bingham and Zhang [17] argue that the resolution of the exact Laplace problem may be ideal when studying nonlinear wave–body interactions because of the relative simplicity of this approach in comparison with more mathematically complex projection methods. In addition, this allows going beyond second-order accurate methods to apply higher-order schemes. Based on the work of [19] and [20], they suggest that it is optimal to use fourth-order finite difference schemes in linear and nonlinear wave models.

In this paper, a fully nonlinear potential flow theory model is developed based on the resolution of the Zakharov equations [21], which express the temporal evolution of the free surface elevation η and free surface velocity potential $\tilde{\phi}$ as a function of these two variables and the vertical velocity at the free surface $\tilde{w}$. The principal difficulty in resolving this system of equations is to calculate the free surface vertical velocity $\tilde{w}$ as a function of $(\eta, \tilde{\phi})$, a problem commonly called 'Dirichlet-to-Neumann' or DtN. When considering flat bottomed, rectangular domains, spectral methods are an attractive and efficient method for solving the DtN problem. The high-order spectral method introduced in [7] and [8] is widely used in such conditions. However, for irregularly shaped domains with variable bottom elevation, this spectral approach is more complicated to apply, although some efforts were made by [22] and [23]. References [24] and [25] introduced another approach based on the expansion of the DtN operator as a sum of global convolution terms and local integrals. An efficient iterative algorithm was developed because of the rapid decay in space of the integral kernels. In this work, two different approaches to resolving the potential in the vertical will be tested: a high-order finite difference approach and a spectral approach.

The mathematical and numerical models are presented (Section 2) before a series of three test cases (Section 3) are used to evaluate the convergence properties, accuracy, and efficiency of the models as a function of the temporal, horizontal, and vertical resolutions: (1) propagation of a regular nonlinear wave in a periodic domain; (2) motion of regular standing waves in a domain with fully reflective boundaries; and (3) propagation and shoaling of a train of waves on a beach. The performance of the two model approaches is compared for each test case, before concluding with a discussion (Section 4) of the optimal model configuration.

2. MODEL DESCRIPTION

2.1. Mathematical model

The flow dynamics of a homogeneous and inviscid fluid of constant density are governed by the Euler equations. By assuming that the flow is irrotational, the velocity vector $\underline{u} \equiv (u, v, w)$ in the fluid domain can be expressed as the gradient of the velocity potential, $\phi(\underline{x}, z, t)$, such that $\underline{u} = (\nabla\phi, \phi_z)^T$, where $\underline{x} \equiv (x, y)$ and $\nabla\phi \equiv \left(\phi_x, \phi_y\right)^T$. In the following, partial derivatives are denoted as $f_\alpha \equiv \frac{\partial f}{\partial \alpha}$, where $\alpha = x, y, z$ or t.

DOI: 10.1002/fld

The velocity potential $\phi(\underline{x}, z, t)$ must then satisfy the Laplace equation in the fluid domain:

$$\nabla^2\phi + \phi_{zz} = 0. \tag{1}$$

To resolve ϕ, the Laplace equation is supplemented by boundary conditions at the free surface, bottom, and lateral boundaries. Here, an impermeable and fixed bottom is considered with $z = -h(\underline{x})$. By assuming continuity of the fluid from the bottom to the free surface $\eta(\underline{x}, t)$ (i.e., non-overturning free surface), and by setting the atmospheric pressure equal to 0 at the free surface, the kinematic and dynamic free surface boundary conditions (at $z = \eta(\underline{x}, t)$) are respectively:

$$\eta_t + \nabla\phi \cdot \nabla\eta - \phi_z = 0, \tag{2}$$

$$\phi_t + \frac{1}{2}(\nabla\phi)^2 + g\eta = 0, \tag{3}$$

where g is the gravitational constant. The bottom boundary condition (at $z = -h(\underline{x})$) restricting flow perpendicular to the bottom is:

$$\nabla\phi \cdot \nabla h + \phi_z = 0. \tag{4}$$

In addition, Dirichlet or Neumann boundary conditions are applied at the lateral boundaries. For the test cases simulated in this study, either periodic lateral boundary conditions or impermeable vertical walls (i.e., $\nabla\phi \cdot \underline{n} = 0$ where $\underline{n}$ is the normal vector at the boundary) are applied.

After defining the velocity potential at the free surface as $\tilde{\phi}(\underline{x}, t) \equiv \phi(\underline{x}, \eta(\underline{x}, t), t)$, the Zakharov equations [21] are derived by rewriting (2) and (3) as a function of the free surface potential $\tilde{\phi}$:

$$\eta_t = -\nabla\eta \cdot \nabla\tilde{\phi} + \tilde{w}(1 + (\nabla\eta)^2), \tag{5}$$

$$\tilde{\phi}_t = -g\eta - \frac{1}{2}\left(\nabla\tilde{\phi}\right)^2 + \frac{1}{2}\tilde{w}^2(1 + (\nabla\eta)^2), \tag{6}$$

where $\tilde{w}(\underline{x}, t)$ is the vertical velocity at the free surface defined by:

$$\tilde{w}(\underline{x}, t) = \phi_z(\underline{x}, \eta(\underline{x}, t), t). \tag{7}$$

After resolving the DtN problem by calculating $\tilde{w}(\underline{x}, t)$ from $(\eta(\underline{x}, t), \tilde{\phi}(\underline{x}, t))$, Equations (5) and (6) model the temporal evolution of the free surface elevation η and the free surface velocity potential $\tilde{\phi}$.

With the objective of modeling arbitrarily shaped domains and bottom profiles, the DtN problem is solved by computing the velocity potential solution of the boundary value problem (BVP), consisting of the Laplace Equation (1) in the fluid domain with a kinematic boundary condition applied at the bottom (4), a Dirichlet boundary condition applied at the free surface $\phi(\underline{x}, z = \eta(\underline{x}, t), t) = \tilde{\phi}(\underline{x}, t)$, and lateral boundary conditions specified for each test case. Once ϕ is known throughout the fluid domain, $\tilde{w}(\underline{x}, t)$ can be calculated with (7).

2.2. Numerical model

The objective of this paper is to evaluate two methods of resolving the DtN problem in the vertical. The numerical methods used to resolve (5) and (6) are described for one horizontal dimension, x, which is discretized by N_X points in the domain.

2.2.1. General modeling strategy. The numerical simulation of the mathematical model requires three main components: (1) a temporal scheme to advance η and $\tilde{\phi}$ in time; (2) a method to compute the horizontal gradient and Laplacian operators; and (3) a technique for resolving the Laplace BVP for ϕ at each time step.

The classical explicit, four-step, fourth-order Runge–Kutta scheme (RK4) with a constant time step is applied. This scheme has sufficient accuracy for the current study, but higher order RK schemes and/or RK schemes with an adaptive time step (e.g., [26]) could also be implemented. For the considered system of (Hamiltonian) equations, a symplectic scheme could also be used (e.g., [27]), as such a scheme should lead to better energy conservation. The selection of an optimal temporal scheme will be considered more in future work.

Horizontal gradients and Laplacian operators are calculated using high-order finite difference approximations with regular or irregular point distribution. Unless otherwise specified, first and second order derivatives in x are approximated using fourth-order schemes following the method of [28]. In the test cases described here, the lateral boundary conditions are either periodic or vertical reflective walls, where $\frac{\partial \phi}{\partial n} = 0$. To maintain fourth-order accuracy of horizontal spatial derivatives in the latter case, the stencil size increases for all decentered finite difference schemes for second order derivatives near the boundaries.

Finally, two model approaches (named Model A and Model B) are used to solve the Laplace BVP problem. Both methods use high-order finite difference approximations to compute horizontal derivatives. In the vertical, Model A uses a finite difference approximation as well, while Model B uses a spectral approach. The same boundary conditions are applied in each case. Although tests by [18] showed improved accuracy using ghost points at the domain boundaries to impose both the boundary condition and the Laplace BVP, this method is not applied in the comparisons here. The models are described in further detail in the following sections.

2.2.2. Model A: high-order finite difference approach. In the first approach, the entire fluid domain is discretized, and high-order finite difference schemes are used to resolve both the horizontal and vertical spatial derivatives (based on the work of [17], [18], and [29]). The vertical domain is transformed to σ-coordinates to simplify the resolution of the system of equations by creating a fixed rectangular domain, with σ varying from 0 at the bottom to 1 at the free surface:

$$\sigma(x,z,t) = \frac{z + h(x)}{\eta(x,t) + h(x)} = \frac{z + h(x)}{d(x,t)}. \tag{8}$$

The total water depth is defined as $d(x,t) = \eta(x,t) + h(x)$. With this coordinate transformation, Equations (1) and (4) can be rewritten as a function of σ and resolved at each point in the fluid domain once the lateral and surface boundary conditions are specified (see [17] for details).

The vertical domain is discretized with N_Z points, creating $N_L = N_Z - 1$ layers of fluid. At each time step, a system of $N_X N_Z$ linear equations must be solved to determine the potential $\phi(x,\sigma)$ in the entire fluid domain. Then, the free surface vertical velocity is calculated as:

$$\tilde{w} = \phi_z\big|_{z=\eta} = \frac{1}{d}\phi_\sigma\big|_{\sigma=1}, \tag{9}$$

and Equations (5) and (6) can be stepped forward in time.

The model convergence is tested as a function of N_X, N_Z, and the vertical distribution of points for the case of a linear wave, following [17] and [18]. For a wave with $kh \sim 4$ ($L = 1$ m, $h = 0.64$ m), the modeled free surface vertical velocity is calculated at time $t = 0$ and compared to the analytical solution. The error is evaluated as:

$$\text{Error} = \frac{||\tilde{w} - \tilde{w}_{exact}||}{||\tilde{w}_{exact}||}, \tag{10}$$

where $\tilde{w}_{exact}$ is the analytical solution calculated with linear wave theory, and $||\cdot||$ is the L2 norm $\left(||x|| = \sqrt{\sum_{i=1}^{n} x_n^2}\right)$. The tests of three different vertical distributions of points, that is, linear distribution, roots of the Chebyshev–Gauss–Lobatto (CGL) polynomials, and roots of the Legendre–Gauss–Lobatto (LGL) polynomials, show that the model convergence is improved with inhomogeneous point spacing, with a higher density of points near the free surface (Figure 1a–b). The differences in model convergence and errors in the free surface vertical velocity are nearly identical using the CGL or LGL discretizations, except for at small values of N_Z. For this test case, the CGL discretization produces smaller errors for $N_Z \leqslant 8$, while the LGL discretization produces smaller errors for $8 < N_Z < 15$, and the differences in errors are of the order 10^{-4} and 10^{-5},

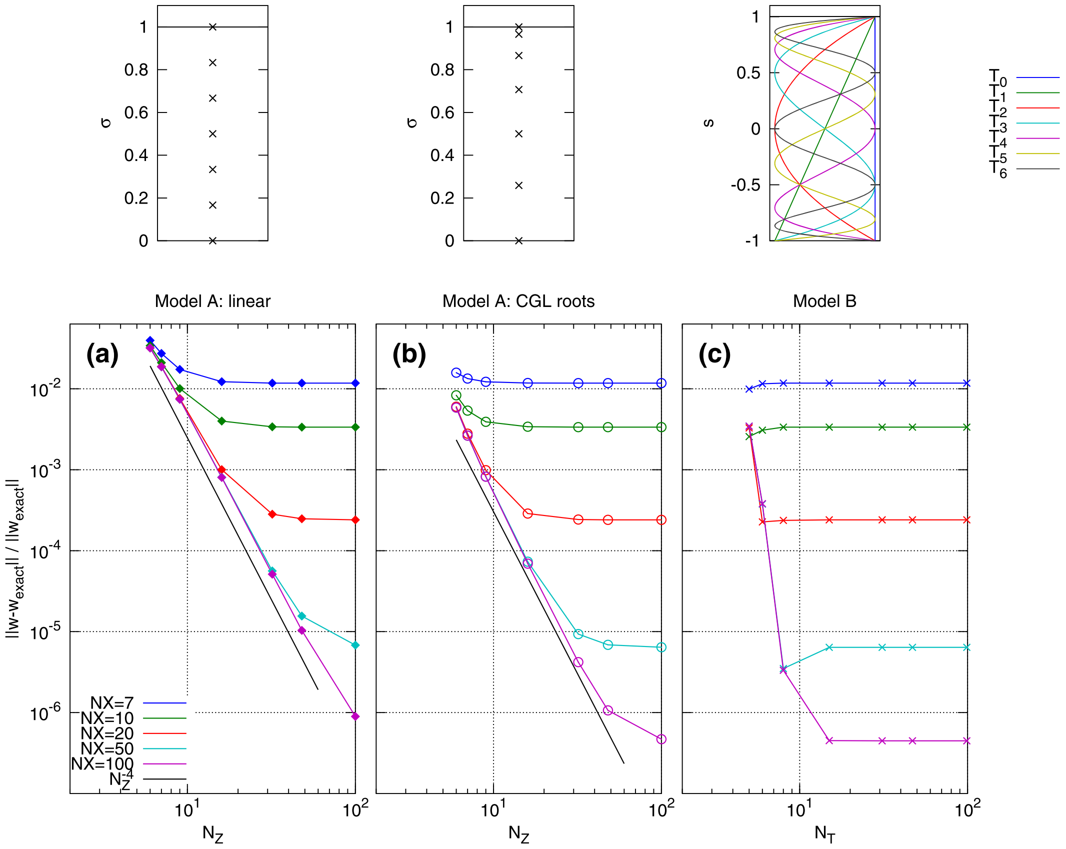

Figure 1. Convergence of the vertical velocity at the free surface $\tilde{w}$ for Models A and B, for a linear wave with $kh \sim 4$. The convergence is evaluated as a function of N_X, N_Z, and the vertical resolution: (a) Model A: linear distribution, (b) Model A: roots of Chebyshev–Gauss–Lobatto (CGL) polynomials, and (c) Model B: spectral method. In the top row, examples of both of the vertical point distributions are shown for Model A (with $N_Z = 7$), and of the Chebyshev polynomials for Model B (with $N_T = 6$).

respectively. Given these differences and the conclusions of [18] showing that the CGL discretization produced the best balance between accuracy in dispersion and internal kinematics, a vertical distribution of points using the roots of CGL polynomials will be used for the test cases shown hereafter for Model A.

2.2.3. Model B: spectral approach. The second approach is inspired by the work of [30] and uses a spectral Chebyshev-tau approach to resolve ϕ in the vertical. The development of the numerical model is comprised of three steps, whose main features are outlined next for the case of fully reflective lateral boundary conditions.

The first step consists of transforming the fluid domain into a rectangular domain, with the vertical coordinate s varying from -1 at the bottom to 1 at the free surface:

$$s(x,z,t) = \frac{2z + h^-(x,t)}{h^+(x,t)}, \tag{11}$$

where $h^+(x,t) = h(x) + \eta(x,t)$ and $h^-(x,t) = h(x) - \eta(x,t)$. The velocity potential, expressed as $\phi(x,z,t) = \varphi(x,s,t)$, must satisfy the Laplace Equation (1) in the fluid domain, the bottom boundary condition (4), the free surface Dirichlet condition, and the impermeability condition at the lateral boundaries (denoted $x = x_b$), which become:

$$\varphi_{xx} + 2s_x\varphi_{xs} + \left(s_x^2 + s_z^2\right)\varphi_{ss} + s_{xx}\varphi_s = 0 \quad \text{in the fluid domain,} \tag{12}$$

$$h^+h_x\varphi_x + 2\left(1 + h_x^2\right)\varphi_s = 0 \quad \text{for } s = -1, \tag{13}$$

$$\varphi(x,1) = \tilde{\phi}(x) \quad \text{for } s = 1, \tag{14}$$

$$\varphi_x + s_x\varphi_s = 0 \quad \text{for } x = x_b. \tag{15}$$

In the second step, the spectral approach is introduced to approximate the velocity potential as a linear combination of base functions of the vertical s coordinate. Similar to [30], Chebyshev polynomials of the first kind, denoted $T_n(x)$ (where $n = 0, 1, 2, ...$ indicates the order of the polynomial), are used because they are easy to calculate and form a basis of orthogonal functions over the range $[-1, 1]$ (e.g., Figure 1c, top). Furthermore, they converge rapidly and have a large convergence domain. The velocity potential is then approximated as:

$$\varphi(x,s) \simeq \varphi_{N_T}(x,s) = \sum_{n=0}^{N_T} a_n(x)T_n(s), \tag{16}$$

where N_T is the highest order Chebyshev polynomial used in the approximation, and $a_n(x)$ are a set of $N_T + 1$ coefficients that must be determined at each point in x. A series of equations for the unknown coefficients $a_n(x)$ and their spatial derivatives $a_n'(x) \equiv \frac{da_n}{dx}$, $a_n''(x) \equiv \frac{d^2a_n}{dx^2}$ are derived by inserting (16) in (12)–(15). The resultant system of equations depends on s, $T_n(s)$, $T_n'(s) \equiv \frac{dT_n}{ds}$ and $T_n''(s) \equiv \frac{d^2T_n}{ds^2}$.

The third step is to apply the Chebyshev-tau method, a variant of the Galerkin method (e.g., [31]), to the Laplace Equation (12) and the Neumann lateral boundary condition (15). The inner product of two arbitrary functions $f(s)$ and $g(s)$ is defined over $[-1, 1]$ as:

$$< f, g > \equiv \int_{-1}^{1} \frac{f(s)g(s)}{\sqrt{1-s^2}} ds. \tag{17}$$

From the orthogonality relation verified by the Chebyshev polynomials,

$$< T_n, T_p > = \begin{cases} 0 & \text{if} \quad n \neq p, \\ \pi & \text{if} \quad n = p = 0, \\ \frac{\pi}{2} & \text{if} \quad n = p \neq 0. \end{cases} \tag{18}$$

The following operator is applied to the arbitrary function $f(s)$:

$$< f >_p \equiv \frac{2}{\pi C_p} < f, T_p >, \quad \text{with} \begin{cases} C_0 = 2, \\ C_p = 1 \quad \text{for } p > 0. \end{cases} \tag{19}$$

The orthonormality relation of the T_n polynomials is then $< T_n >_p = \delta_{np}$, where δ_{np} is the Kronecker delta. Using the Galerkin method, the operator $< . >_p$ is applied to (12) for $p = 0, 1, ..., N_T$:

$$a_p''(x) + \sum_{n=0}^{N_T} C_{pn}a_n'(x) + \sum_{n=0}^{N_T} D_{pn}a_n(x) = 0, p = 0, 1, ..., N_T, \tag{20}$$

with $C_{pn} \equiv (m_{011}B_{p01n} + m_{111}B_{p11n})/m_{020}$ and $D_{pn} \equiv (m_{002}B_{p02n} + m_{102}B_{p12n} + m_{202}B_{p22n} + m_{001}B_{p01n} + m_{101}B_{p11n})/m_{020}$. The terms m_{ijk} depend only on $h^+(x)$, $h^-(x)$ and their spatial derivates (see Equations (21)–(28) in [30]), as well as:

$$B_{pikn} \equiv < s^i \frac{\partial^k T_n}{\partial s^k}(s) >_p . \tag{21}$$

DOI: 10.1002/fld

The coefficients B_{pikn} are constant and can be calculated analytically once at the beginning of each simulation.

By applying the same procedure to the impermeable lateral boundary condition, (15) becomes:

$$2a'_p(x) + \sum_{n=0}^{N_T} C_{pn} a_n(x) = 0, p = 0, 1, ..., N_T. \tag{22}$$

At each point in x, there are $N_T + 1$ unknown coefficients $a_n(x)$ for $n = 0, 1, ..., N_T$. Therefore, using this method to derive (20) and (22) with $p = 0, 1, ..., N_T - 2$ provides $N_T - 1$ equations for both the interior and lateral boundary points. These equations are supplemented by the two boundary conditions at the bottom (13) and free surface (14), which become respectively:

$$\sum_{n=0}^{N_T} \left[(-1)^n h^+ h_x a'_n(x) + (-1)^{n-1} 2n^2 \left(1 + h_x^2\right) a_n(x)\right] = 0, \tag{23}$$

$$\sum_{n=0}^{N_T} a_n(x) = \tilde{\phi}(x). \tag{24}$$

In contrast to [30], spatial derivates of $a_n(x)$ are computed with high-order finite difference formulas (fourth order). Thus, a system of $N_X(N_T + 1)$ linear equations must be solved for the coefficients $a_n(x_i)$ for $i = 1, ..., N_X$.

Once the $a_n(x_i)$ are determined, the vertical velocity at the free surface $\tilde{w}$ is

$$\tilde{w}(x_i) = \phi_s s_z\big|_{s=1} = \frac{2}{h^+(x_i)} \sum_{n=0}^{N_T} a_n(x_i) n^2, \tag{25}$$

and Equations (5) and (6) can be stepped forward in time.

The convergence of Model B is then tested as a function of N_X and N_T for the same linear wave test shown in section 2.2.2 for Model A. As expected, the normalized errors in the calculated free surface vertical velocity converge faster for Model B than for Model A (Figure 1).

2.3. *Numerical resolution of the linear system of equations*

Each time the DtN problem is solved (at each sub-step of the RK4 scheme), a system of $N_X(N + 1)$ linear equations must be resolved. For Model A, $N = N_L$, the number of layers in the vertical, and for Model B, $N = N_T$, the maximum order Chebyshev polynomial. The corresponding matrices are sparse, and to optimize the memory use and efficiency of the model, only the nonzero entries are stored (in vector format). The direct solver MUMPS ("MUltifrontal Massively Parallel Solver", v4.10.0) [32, 33] is applied in the Fortran code using the default settings. A direct (exact) solver was selected to avoid residual errors associated with iterative solvers, but it may be replaced by an iterative solver to increase the efficiency of the model.

3. TEST CASES

In this study, three different test cases will be used to demonstrate the properties of convergence, accuracy, and efficiency of Models A and B as a function of the horizontal, vertical, and temporal resolutions. In addition, the two models will be compared with the objective of determining the most efficient approach to implement in future work.

3.1. *Regular nonlinear wave*

3.1.1. Description of the test case. The first test case investigates the resolution of the DtN problem and the temporal evolution of a regular, nonlinear wave of permanent form in a uniform depth periodic domain. The wave does not deform when propagating in uniform depth. Therefore, the

DOI: 10.1002/fld

wave characteristics should remain identical to the initial conditions after an integer number of wave periods.

The reference solution used to create the initial conditions is calculated using a Fourier series approximation of the stream function method, based on the work of [34] and [35]. This method is capable of calculating highly accurate solutions for highly nonlinear waves in uniform, arbitrary depth, with or without an homogeneous ambient current. STREAM_HT, a Fortran code developed at EDF R&D (Chatou, France) based on this method, is used to approximate the initial free surface position η and velocity potential $\tilde{\phi}$ to the 20th order. A wave with wavelength $L = 64$ m and wave height $H = 6.4$ m is calculated in a water depth $h = 64$ m. The wave steepness is $H/L = 0.1$ (or $ka = kH/2 = \pi/10$), and the relative water depth is $h/L = 1$ (or $kh = 2\pi$). The model domain has periodic boundary conditions, and the length of the domain L_x is the wavelength of a single wave (i.e., $L_x = L$).

3.1.2. Resolving the DtN problem as a function of N_X and N. Before evaluating the model behavior as a function of time, the convergence of the two approaches is investigated as a function of the horizontal ($N_X = L/\Delta x$) and vertical (N) resolutions. For these tests, N_X ranges from 24 to 256, and N ranges from 5 to 100 for Model A and from 2 to 100 for Model B. For both models, at least six points/nodes in the vertical (i.e., $N = 5$) are needed to reach the target fourth-order accuracy with irregular spacing of points/nodes.

In addition to calculating the initial conditions, STREAM_HT is used to calculate the free surface vertical velocity $\tilde{w}$, which is then compared with the values estimated by resolving the DtN problem with the two model approaches. As in Section 2.2.2, the normalized error is calculated as $||\tilde{w} - \tilde{w}_{STREAM}||/||\tilde{w}_{STREAM}||$, where $\tilde{w}_{STREAM}$ is the reference solution calculated using STREAM_HT.

For a fixed horizontal resolution N_X, the normalized error of the free surface vertical velocity decreases with an increase in the vertical resolution N, and both models converge to the same minimum for large values of N (Figure 2). While the decrease in error is monotonic for Model A, Model B reaches a minimum at intermediate values of N ($N = 10 - 15$, for the range of $N_X = 48 - 512$), before converging to a constant value for larger N. The cause of these minima is unknown. More importantly, Model B converges more rapidly than Model A, as shown for

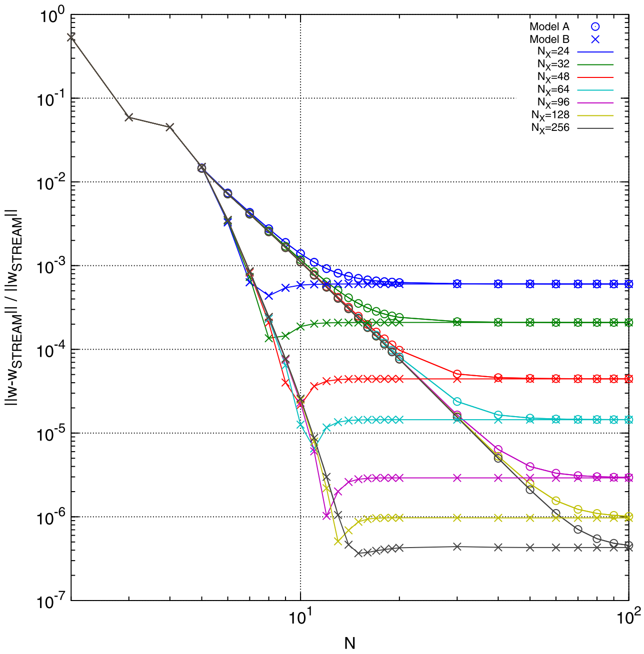

Figure 2. Convergence of the free surface vertical velocity $\tilde{w}$ for a regular nonlinear wave with wave steepness $H/L = 0.1$ ($ka = \pi/10$) and relative water depth $h/L = 1$ ($kh = 2\pi$). Convergence of Models A and B is plotted as a function of the vertical resolution N for a range of horizontal resolutions N_X.

DOI: 10.1002/fld

$N_X = 128$ in Figure 3 in (a) log–log and (b) log–linear space. The convergence of Model A is algebraic, and the error decreases as N^{-k}, with a rate of convergence $k \approx 3.8$ (slightly lower than expected for a fourth-order finite difference scheme). Model B exhibits exponential convergence, as expected from the spectral approach used in the vertical direction. The convergence rate is geometric, and the error decreases as $exp(-qN)$ with $q \approx 1.26$.

In addition, a second test evaluated the convergence of the maximum absolute error in free surface velocity (maximum of $|\tilde{w} - \tilde{w}_{STREAM}|$) to compare qualitatively with the simulation results obtained

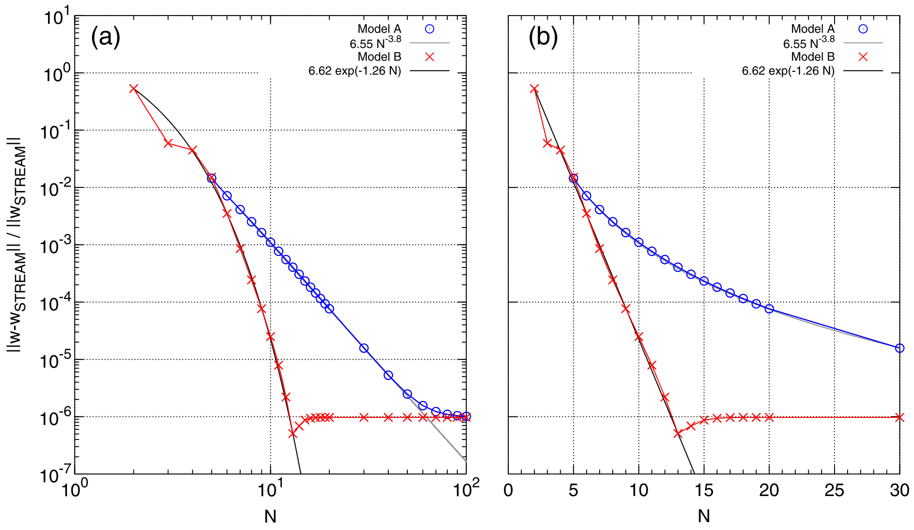

Figure 3. Convergence of Models A and B when resolving the free surface vertical velocity $\tilde{w}$ for a nonlinear wave with wave steepness $H/L = 0.1$ ($ka = \pi/10$) and relative water depth $h/L = 1$ ($kh = 2\pi$), for a representative case with $N_X = 128$. Model A converges linearly, and Model B converges geometrically as a function of the vertical resolution N, as shown in (a) log–log and (b) log–linear space.

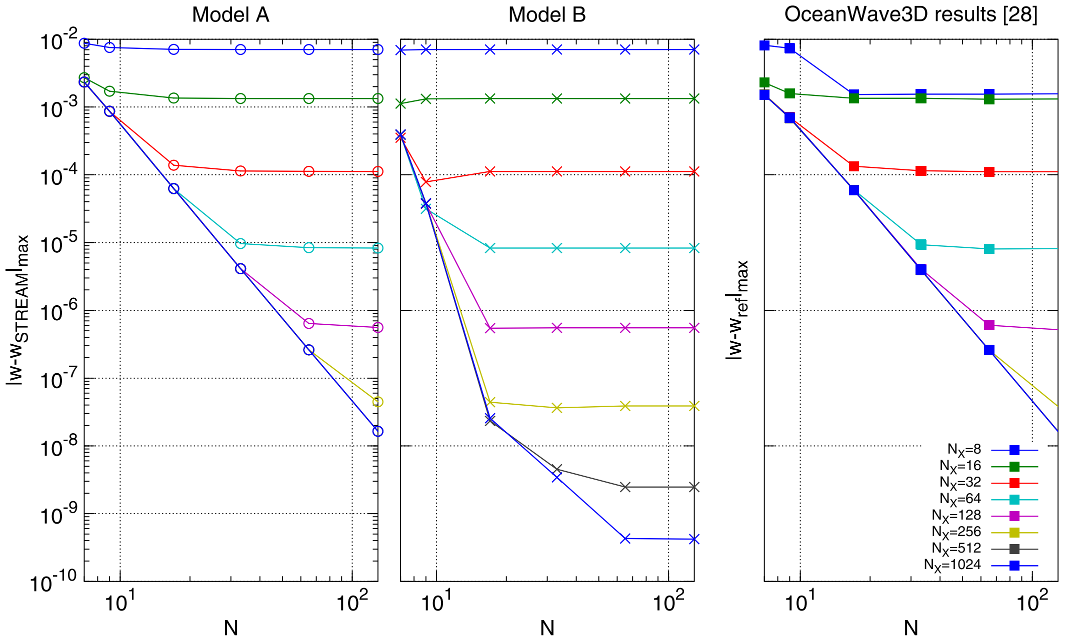

Figure 4. Convergence of the maximum of the vertical velocity error $|\tilde{w} - \tilde{w}_{STREAM}|$ for a nonlinear wave with wave steepness $H/L \approx 0.0955$ ($ka = 0.3$) and relative water depth $h/L = 1$ ($kh = 2\pi$), for (a) Model A, (b) Model B, and (c) OceanWave3D (data digitized from Figure 3 of [29]).

in [29] with the model OceanWave3D. A new reference solution was calculated using STREAM_HT for the wave specified in [29], with wave steepness $H/L \approx 0.0955$ ($ka = 0.3$) and relative water depth $h/L = 1$. Here, $h = 1$ m to compare the absolute errors obtained with Models A and B with the results of [29]. As expected, Model A and OceanWave3D show nearly identical convergence of the maximum vertical velocity errors as a function of N_X and N (Figure 4), with differences only noticeable for $N_X = 8$ and $N > 10$, where OceanWave3D performs better than Model A. To test the cause of this difference, Model A was rerun using ghost points at the bottom of the domain to enforce both the resolution of the Laplace BVP and the bottom boundary condition (as shown by [18]), but this did not change the results obtained with Model A. The reason for this difference is unknown and may be caused by the different methods used to solve the linear system of equations

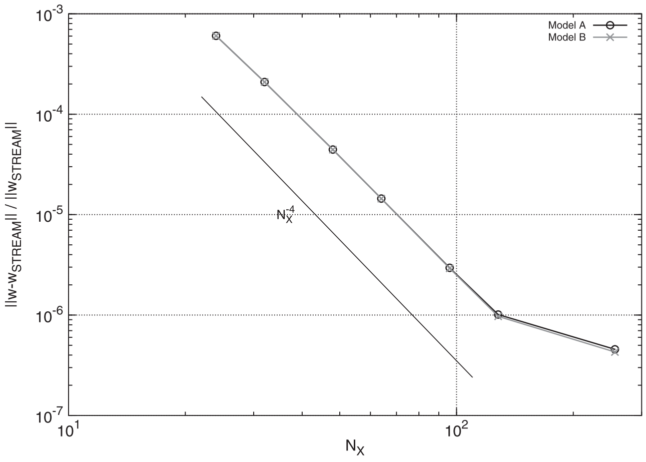

Figure 5. Convergence of the free surface vertical velocity $\tilde{w}$ for a regular nonlinear wave with wave steepness $H/L = 0.1$ ($ka = \pi/10$) and relative water depth $h/L = 1$ ($kh = 2\pi$). Convergence is shown as a function of the horizontal domain resolution N_X (for a fixed vertical resolution $N = 100$).

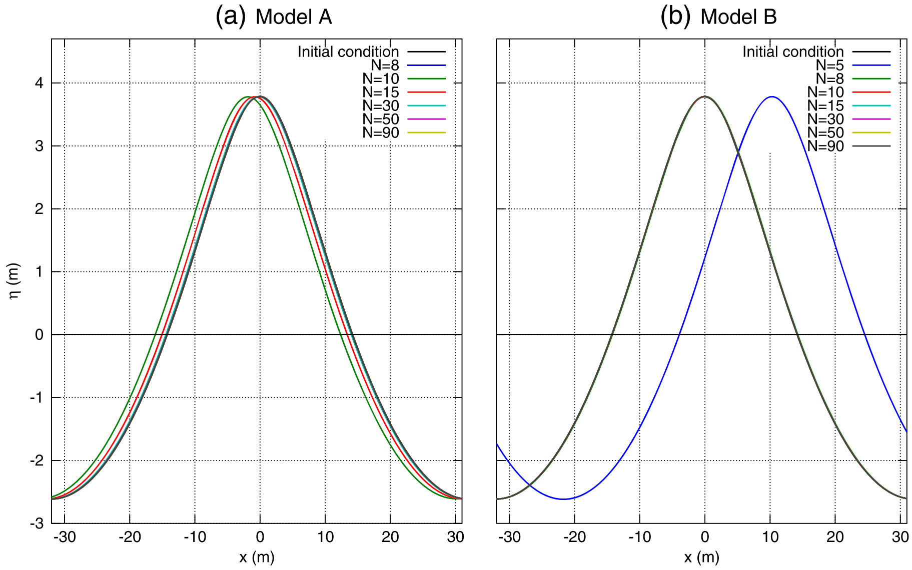

Figure 6. (a) Model A and (b) Model B profiles of the regular nonlinear wave free surface position at the initial time step ($t = 0$, solution given by STREAM_HT) for $N_X = 64$ and after 25 wave periods ($N_{time} = 100$) for a range of vertical resolutions $N = 5 - 90$.

(the direct solver MUMPS for Model A, and a preconditioned iterative method, the generalized minimal residual [GMRES] for OceanWave3D).

Finally, as a function of the horizontal resolution, both models show an algebraic convergence rate proportional to approximately N_X^{-4} (Figure 5).

3.1.3. Propagation errors as a function of N_X, N, and N_{time}. The subsequent tests study the influence of the horizontal resolution N_X, the vertical resolution N, and the number of time steps per wave period N_{time} on the errors after propagating the wave for 25 wave periods. The results are evaluated as a function of the Courant–Friedrichs–Lewy (CFL) number, which is defined here as CFL $\equiv \frac{C\Delta t}{\Delta x}$. With the wave phase speed $C = L/T$, $\Delta x = L/N_X$, and $\Delta t = T/N_{time}$, the CFL number becomes the ratio of the horizontal resolution to the number of time steps per wave period, or CFL $= N_X/N_{time}$.

Simulations with low vertical resolution are unable to model accurately the wave phase speed, and phase differences are visible after propagating the wave for 25 wave periods (Figure 6, for CFL $= 0.64, N_X = 64, N_{time} = 100$). To calculate the phase shift, a second-order polynomial was fit to the three points around the maximum free surface elevation to interpolate the position and magnitude of the maximum free surface position. The phase shift rapidly decreases with increasing vertical resolution, even with an increase in the CFL number. In the midrange of values of vertical resolution N, the phase differences are generally larger for Model A than for Model B, and for the lowest (e.g., $N = 5$) and highest values of N, the phase shifts are approximately the same (Figure 7). Both for models, the phase shifts reach an approximately constant value for large N, and both the phase shift and the value of N at which this plateau is reached depend on the CFL number.

In addition to the appearance of a phase shift, the maximum free surface elevation differs from the initial value during the 25 wave period simulation (Figure 8). The largest differences between the reference solution and the simulated values occur for low vertical resolution simulations (e.g., $N \leqslant 10$ for Models A and B in Figure 8a and b, respectively). For larger values of N, these differences converge to a constant value, which is dependent on the horizontal resolution or CFL number. As a function of the horizontal resolution, the errors in the maximum free surface position generally decrease with increasing horizontal resolution, and exceptions to this trend may be related to the interpolation method (fitting a polynomial to three points) used.

When both the horizontal N_X and vertical N resolutions are instead held constant, errors in the maximum free surface position generally increase with increasing CFL number (Figure 8c–d). However, no clear trends are observed as a function of the number of time steps per wave period N_{time} (in the parameter range tested) for either model.

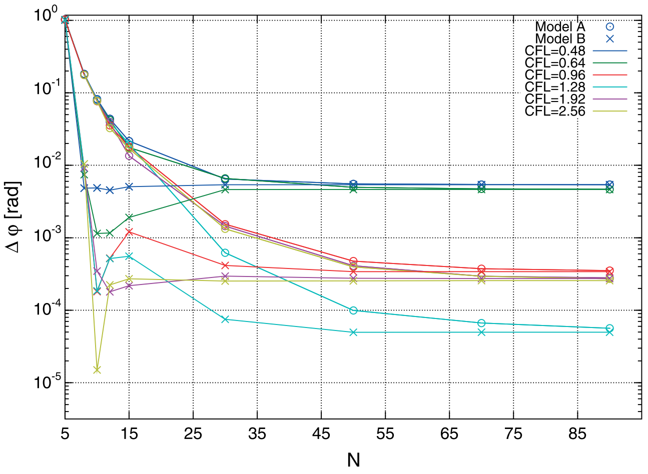

Figure 7. Regular nonlinear wave phase shift after 25 wave periods for $N_{time} = 100$, as a function of the vertical resolution N and CFL number.

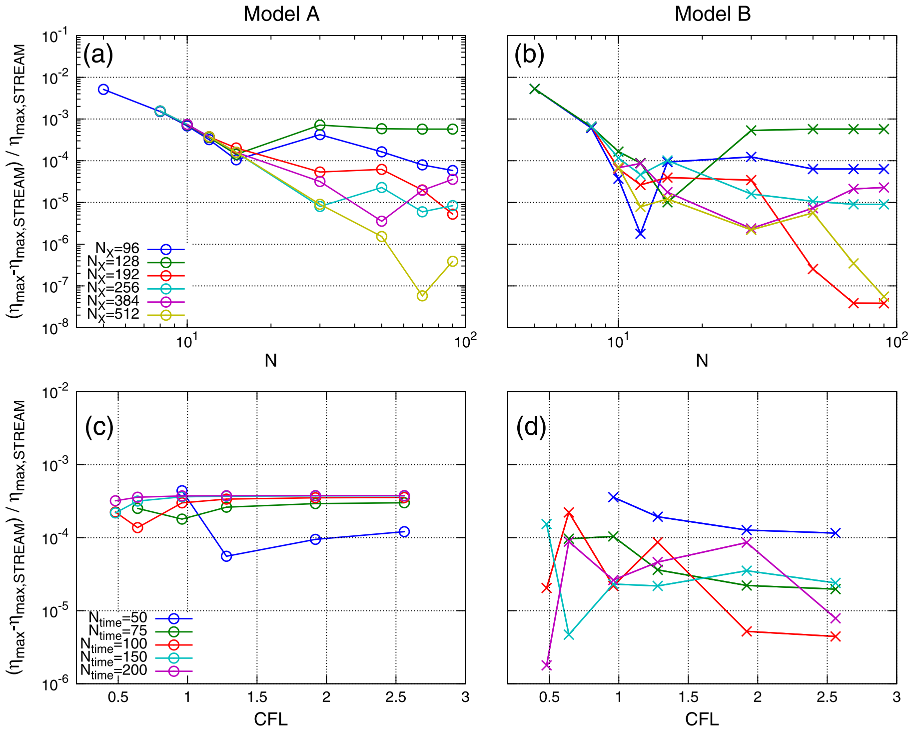

Figure 8. Normalized difference between the regular nonlinear wave simulated maximum free surface elevation and reference solution during the entire 25 wave period simulation: (a, b) for fixed $N_{time} = 100$, as a function of the vertical resolution N and horizontal resolution N_X, and (c, d) for fixed $N = 12$, as a function of the CFL number and number of time steps per wave period N_{time}.

The total energy error is calculated for several different vertical resolutions N and for a range of CFL numbers. The error is defined as the root mean square (rms) error at the end of the simulation period:

$$\text{Error}(t_i) = \sqrt{\frac{1}{N_X} \sum_{k=1}^{N_X} \left(\frac{Y(x_k, t_i) - Y_{ref}(x_k)}{Y_{ref}(x_k)} \right)^2}, \tag{26}$$

where $t_i = T_{end}$ =25 wave periods, Y is the total energy, and Y_{ref} is the total energy at time $t = 0$. For Models A and B, the total energy errors vary as a function of N_X and N_{time}, but this variability is nearly constant for $N \geqslant 8$ (e.g., Figure 9 for $N = 8$), with only small increases for $N < 8$.

With N_{time} held constant, the energy errors decrease with an increase in horizontal resolution, even though the CFL number also increases. With N_X held constant, the total energy error decreases slightly with an increase in the number of time steps per wave period N_{time} and converges to a constant value for CFL <1. The two models show very similar energy errors for this test case, with the exception that Model B remains more stable for higher horizontal resolution simulations.

In conclusion, an optimal value for the vertical resolution appears to be in the range of $7 < N < 15$. In this range, both the phase and the maximum free surface elevation differ little from the initial conditions after 25 wave periods. Larger values of N improve the results minimally, yet are much more computationally expensive. The errors in total energy support this conclusion and further suggest that increasing the horizontal resolution N_X allows larger gains in accuracy than increasing only the number of time steps per wave period N_{time} (or decreasing the CFL number).

3.1.4. Computational effort for a given level of accuracy. Finally, the computational efficiency of the two models was evaluated as a function of a desired level of accuracy at the end of the 25 wave period simulations. Here, the CFL number was held constant (CFL = 1.28), and the horizontal N_X

DOI: 10.1002/fld

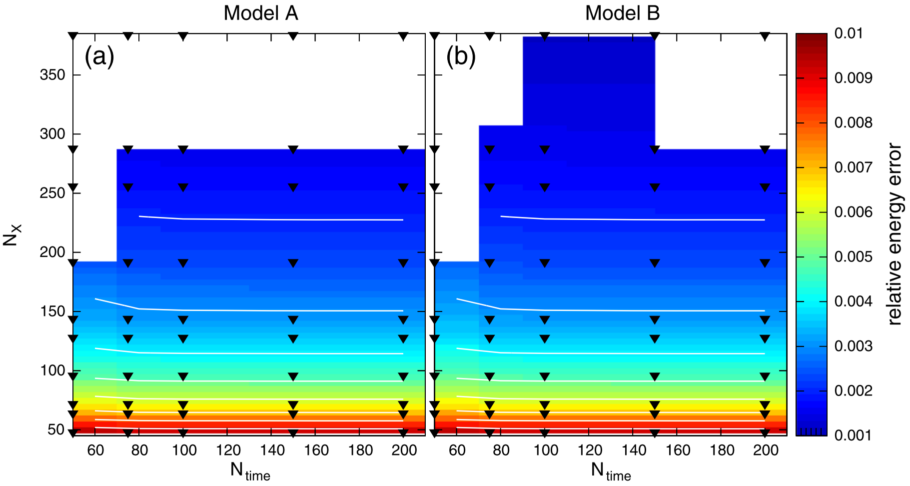

Figure 9. Regular nonlinear wave total energy conservation errors for (a) Model A and (b) Model B, as a function of the number of time steps per wave period N_{time} and the horizontal resolution N_X, for a fixed vertical resolution $N = 8$. The black triangles are the data points used to grid the data, and triangles in regions with no color indicate that the simulations were unstable and stopped before reaching 25 wave periods. The white curves are contour lines at intervals of 0.001.

Table I. Regular nonlinear wave test case with a constant CFL number (CFL = 1.28), the horizontal (N_X) and vertical (N) resolutions needed for Model A and Model B to obtain a given level of accuracy in the energy error.

Model A			Model B		
Energy error	N_X	N	Energy error	N_X	N
7.3×10^{-3}	64	8	7.3×10^{-3}	64	5
4.7×10^{-3}	96	8	4.5×10^{-3}	96	5
3.5×10^{-3}	128	8	3.3×10^{-3}	128	5
2.3×10^{-3}	192	8	2.3×10^{-3}	192	8
1.7×10^{-3}	256	8	1.7×10^{-3}	256	8

and vertical N discretizations needed to obtain a given level of accuracy of the energy error were recorded (Table I). The difference in computational effort required by the two models to obtain a specified level of accuracy in the energy error depends on the both the discretization of the domain and the optimization of each model. Here, Model B is more efficient than Model A, requiring less computational effort to obtain the same level of accuracy in energy errors (Figure 10) for this test case.

3.2. Nonlinear standing wave

3.2.1. Description of the test case. The second test case investigates the motion of a nonlinear standing wave in a domain with fully reflective lateral boundaries. After an integer number of wave periods, the wave characteristics should remain identical to those of the initial condition.

The initial conditions are calculated using the Fourier method of [36], which was developed for calculating highly accurate time-dependent two-dimensional solutions of standing gravity waves of finite amplitude in uniform water depth. This method is capable of calculating accurate solutions of the free surface elevation and velocity potential at any instant in time by representing the velocity potential with a truncated Fourier series and by using an implicit form of the free surface elevation. STREAM_TJ, a Fortran code developed in the Saint-Venant Hydraulics Laboratory (Chatou, France) using the method of [36], is used to approximate the initial conditions to the

DOI: 10.1002/fld

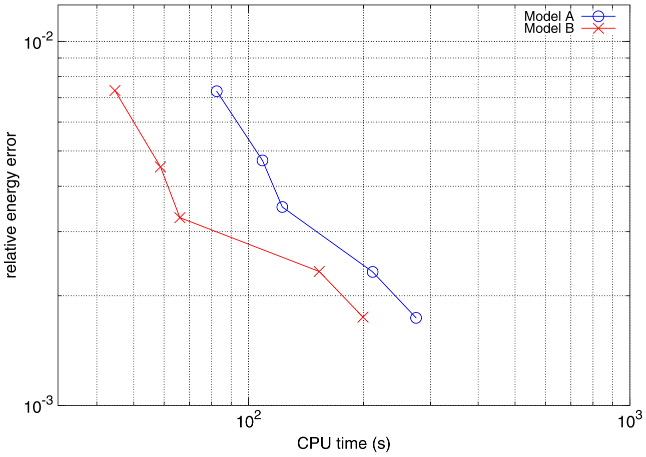

Figure 10. Computational effort required to obtain thresholds of energy errors for the case of a regular nonlinear wave with a constant CFL number (CFL=1.28). See Table I for the corresponding values of horizontal N_X and vertical N resolutions.

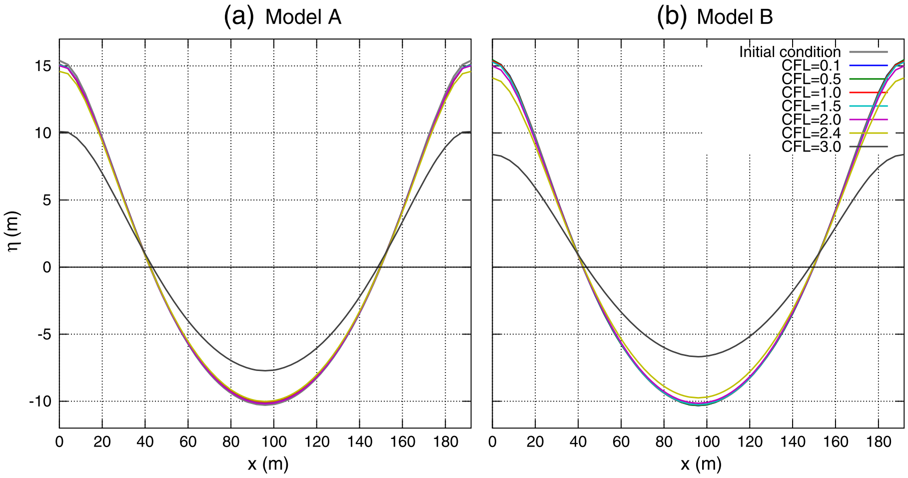

Figure 11. (a) Model A and (b) Model B standing wave free surface position η after 100 wave periods for range of CFL numbers with horizontal resolution $L/\Delta x = 48$.

14th order. A wave with wavelength $L = 192$ m, relative water depth $kh = 3$, and wave steepness $ka = 0.42$ is calculated using STREAM_TJ. These values were selected for comparison with the results of [36], and they represent a nonlinear wave that is approximately 66% of the maximum wave height for $kh = 3$. By specifying the wavelength and non-dimensional depth and wave steepness, the water depth and wave height are $h \approx 91.6732$ m and $H \approx 25.6685$ m, respectively.

For a wave with wavelength L, the length of the domain L_x must be a multiple of the half wavelength $L/2$, and in this case, the domain length is $L_x = L = 192$ m. The initial condition is imposed as the displacement of the free surface η (Figure 11), with no fluid velocity in the domain.

For the following tests, the vertical resolution is held constant with $N = 7$, and the errors and stability of the models are evaluated as a function of the horizontal resolution N_X and number of time steps per wave period N_{time}. This value of N is selected as a good compromise between model accuracy and efficiency. Five regularly spaced grids are tested with a horizontal resolution $L/\Delta x$ ranging from 24 to 96.

3.2.2. Errors as a function of N_X and N_{time}. Errors in the free surface elevation η are evaluated as a function of the CFL number, which is defined using the wave phase velocity $C = L/T$, and can

DOI: 10.1002/fld

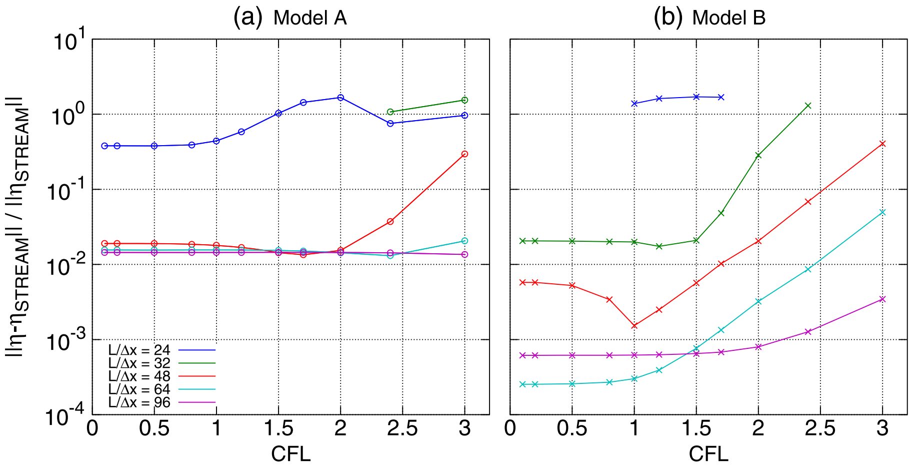

Figure 12. Standing wave free surface position η error after 100 wave periods for (a) Model A and (b) Model B as a function of the CFL number and horizontal grid spacing.

be rewritten as CFL $= N_X/N_{time}$, as for the previous test case. For high CFL number simulations, errors in the free surface elevation η are visible after propagating the wave for 100 wave periods with both models (e.g., $L/\Delta x = 48$, Figure 11). The free surface position differs from the initial conditions primarily because of changes in the wave amplitude, while the wave period remains relatively constant.

Quantification of these errors ($||\eta - \eta_{STREAM}||/||\eta_{STREAM}||$) after 100 wave periods shows that they primarily increase with increasing CFL number and decreasing horizontal resolution (Figure 12). Model B generally produces smaller errors than Model A, with the exception of the grid with coarsest horizontal resolution. For Model A, one exception to the trend is for $L/\Delta x = 32$, where the simulations have higher free surface position errors than the simulations with coarser horizontal resolution ($L/\Delta x = 24$). These simulations are unstable in time for low CFL numbers (approximately CFL < 2.4). For Model B, the horizontal resolution that produces the smallest errors at the lowest CFL numbers ($L/\Delta x = 64$) is not the finest grid.

These anomalies appear to be associated with a transfer of energy from low frequency wave numbers to high frequency wave numbers in both Models A and B (e.g., Model B, Figure 13). The initial wave spectra (Figure 13a) are nearly superimposed for the first 12 wave numbers that are present in all horizontal grids ($L/\Delta x = 24 - 96$). The evolution in time of the initial spectra shows the growth of nodal amplitudes at the high wave number end of the spectrum. For some cases (e.g., $L/\Delta x = 24$ for Model B, Figure 13b), the energy at high wave numbers continues to grow, eventually causing the simulation to become unstable. For other cases (e.g., $L/\Delta x = 48 - 96$ for Model B, Figure 13c–d), the energy at high wave numbers increases but then remains relatively stable (with variations in time) during the length of the current simulations. Similar to the $L/\Delta x = 24$ case for Model B, the $L/\Delta x = 32$ case of Model A also becomes unstable in time at low CFL numbers. However, it is unclear why this occurs for the horizontal grid $L/\Delta x = 32$, whereas this phenomenon is not observed for the coarsest horizontal grid ($L/\Delta x = 24$).

Finally, total energy errors calculated using (26) decrease with increasing horizontal resolution and generally increase with increasing CFL number (Figure 14). For small CFL number simulations, Model B generally has smaller energy errors than Model A. For each horizontal resolution tested, Model A and B errors converge to the same values at large CFL numbers for nearly all horizontal grids, as well as at low CFL numbers for $L/\Delta x = 48$ and $L/\Delta x = 64$. The precise CFL number at which they converge depends on the horizontal resolution and increases with increasing horizontal resolution. For a fixed horizontal resolution, the convergence of the energy errors is proportional to approximately N_{time}^{-4}, as expected for a fourth-order RK4 temporal integration scheme.

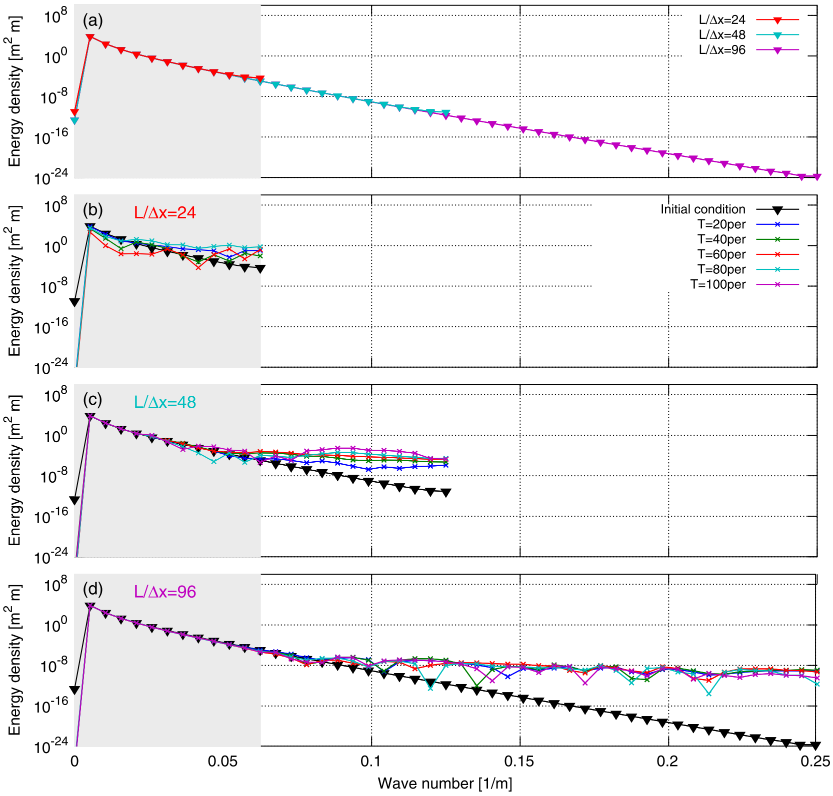

Figure 13. Energy density spectra of (a) the initial conditions created by STREAM_TJ (accurate to the 14th order) for three different horizontal grids, and the temporal evolution of the spectra as a function of the number of periods of wave simulation for Model B with (b) $L/\Delta x = 24$, (c) $L/\Delta x = 48$, and (d) $L/\Delta x = 96$. The gray shaded zone indicates the first 12 spectral components that are common between all of the simulations.

3.3. *Transformation of a train of waves on a slope*

3.3.1. Description of the test case. The last test case evaluates the ability of the two approaches to model the propagation and shoaling of waves in a variable depth domain with impermeable lateral boundaries, following [37]. The test case was proposed by [38], when the authors demonstrated the performance of a highly accurate nonlinear potential flow model that applied a local polynomial approximation of arbitrary order. [37] used the [38] model to find highly accurate reference solutions (after ensuring convergence) for validation of a Boussinesq-type model. Their results will be used here to validate qualitatively the model performance before further tests evaluate the convergence and error evolution of Models A and B.

A train of waves are propagated up a slope (Figure 15a), and the bathymetry in the model domain is defined as:

$$\frac{h}{h1} = \frac{h_{min}}{h_1} + \left(1 - \frac{h_{min}}{h_1}\right)\left[\frac{1}{\cosh(\tan(\pi x/2L_1))}\right], \quad x \leqslant L_1 \tag{27}$$

$$\frac{h}{h_1} = \frac{h_{min}}{h_1}, \quad L_1 < x \leqslant 2L_1 \tag{28}$$

where $h_{min}/h_1 = 0.2$, and $L_1 = 50h_1$ ($h_1 = 1$ m was chosen here). The initial free surface position is defined as a train of waves with decreasing wave amplitude in the x direction:

$$\frac{\eta}{h1} = \frac{a_I}{h_1}\left[\frac{\cos(2\pi N_w x/L_1)}{\cosh(\tan(\pi x/2L_1))}\right], \quad x \leqslant L_1 \tag{29}$$

DOI: 10.1002/fld

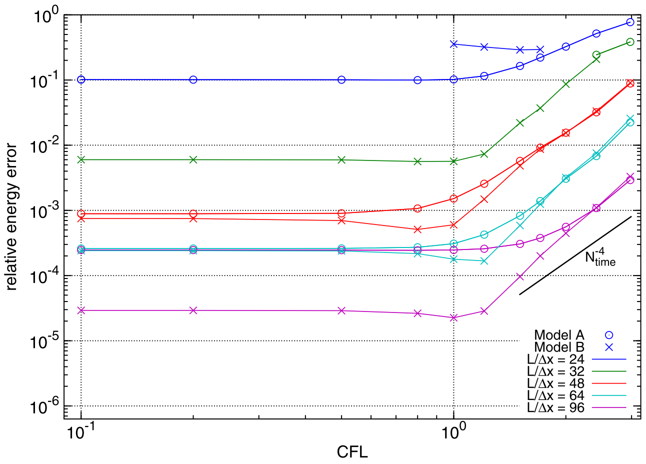

Figure 14. Standing wave total energy error as a function of the CFL number and horizontal grid spacing for Models A and B (with fixed vertical resolution, $N = 7$).

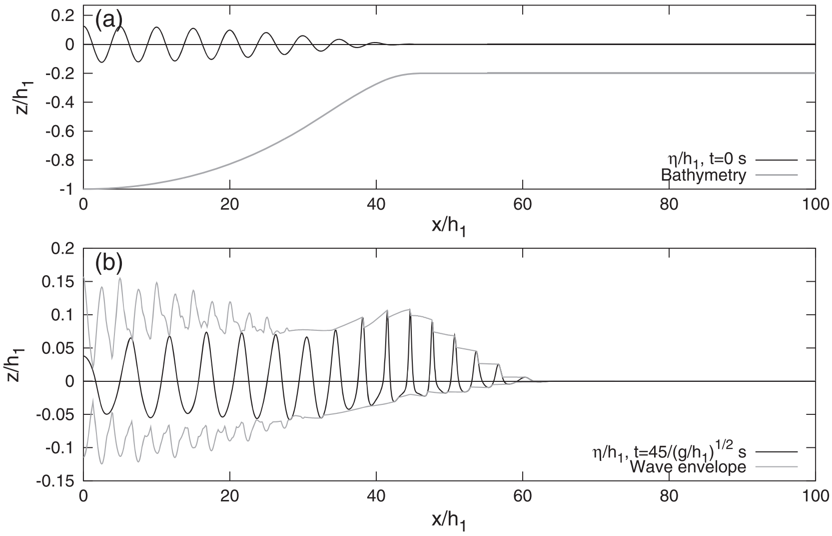

Figure 15. (a) Bathymetry and free surface initial position for $a_I/h_1 = 0.125$, following [37]. (b) Example wave envelope and free surface position at the end of the simulation time.

$$\frac{\eta}{h_1} = 0, \quad L_1 < x \leqslant 2L_1 \tag{30}$$

where $N_w = 10$ is the number of waves (the initial wavelength is thus $L = L_1/N_w$), and a_I/h_1 is the initial wave amplitude. There is no initial fluid velocity in the domain. Kennedy *et al.* [37] completed three tests in which the initial relative wave amplitude varied, and the most nonlinear case with $a_I/h_1 = 0.125$ is shown here (Figure 15a).

With these initial conditions, the system was allowed to evolve in time until the shoaling waves nearly reached the breaking point. Kennedy *et al.* [37] stopped the computations at time T when the waves were judged to be near the breaking point, with $T\sqrt{g/h_1} = 45$, or $T = 14.36$ s, for this test case. At each position, the envelope of crests and troughs (the maximum and minimum elevations recorded during the simulations, e.g., Figure 15b) is calculated for comparison with the results obtained with the model of [38]. The results of these simulations were not available in numerical format, so they were digitalized from the curves in Figure 9 of [37].

DOI: 10.1002/fld

Table II. Regularly spaced horizontal grids for the test case propagating a train of waves on a slope.

Grid	Number of points	Δx (m)
R2	741	0.1
R3	1481	0.05
R4	3701	0.02
R5	7201	0.01
R6	14801	0.005
R7	37001	0.002

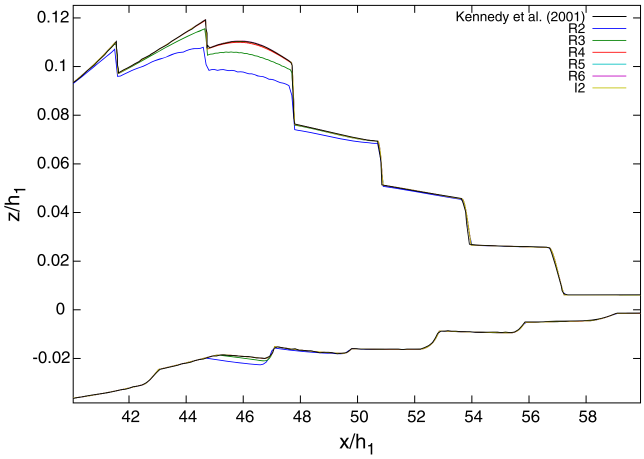

Figure 16. Model A simulation wave envelopes for different horizontal grid spacings (see Tables II and III for details) and constant CFL $\approx$ 0.63 compared with the results of [37]. Model B simulation wave envelopes (not shown for clarity) are nearly identical.

3.3.2. Convergence as a function of N_X and N_{time}. In this section, the vertical resolution is held constant with $N = 7$, and the convergence of the two model approaches is evaluated as a function of the horizontal grid size Δx and the time step Δt.

The simulation results approach those of [37] as Δx and Δt decrease (see Table II for details of the horizontal resolution of each test, denoted R2–R7). A visual comparison demonstrates the convergence of the models with increasing horizontal resolution and number of time steps for a constant CFL number $\approx$ 0.63 (e.g., Figure 16 for Model A, results are similar for Model B and are therefore not shown for clarity). Here, the CFL number is based on the long wave speed in the deepest part of the domain, with CFL $= \sqrt{gh_1}(\Delta t/\Delta x)$. A range of CFL numbers were selected, and the time step Δt for each simulation was calculated to approximate the preselected CFL number with an integer number of time steps to achieve a total simulation time of $T = 14.36$ s.

The relative variations of fluid volume and total mechanical energy are then compared as a function of the CFL number (Figure 17) to evaluate quantitatively the convergence as a function of Δx and Δt. Model A is unable to simulate the propagation of the wave train in simulations with the highest horizontal resolution (R7, with $\Delta x/h_1 = 0.002$). The simulation duration increases with decreasing CFL number, but none of the tests remain stable for the entire simulation period because of the appearance and rapid growth of instabilities at high wavenumbers. Model B remains stable for all of the tested simulations but appears to be more constrained by the CFL number than Model A. The maximum attainable CFL number increases with increasing model resolution (Figure 17b, d).

DOI: 10.1002/fld

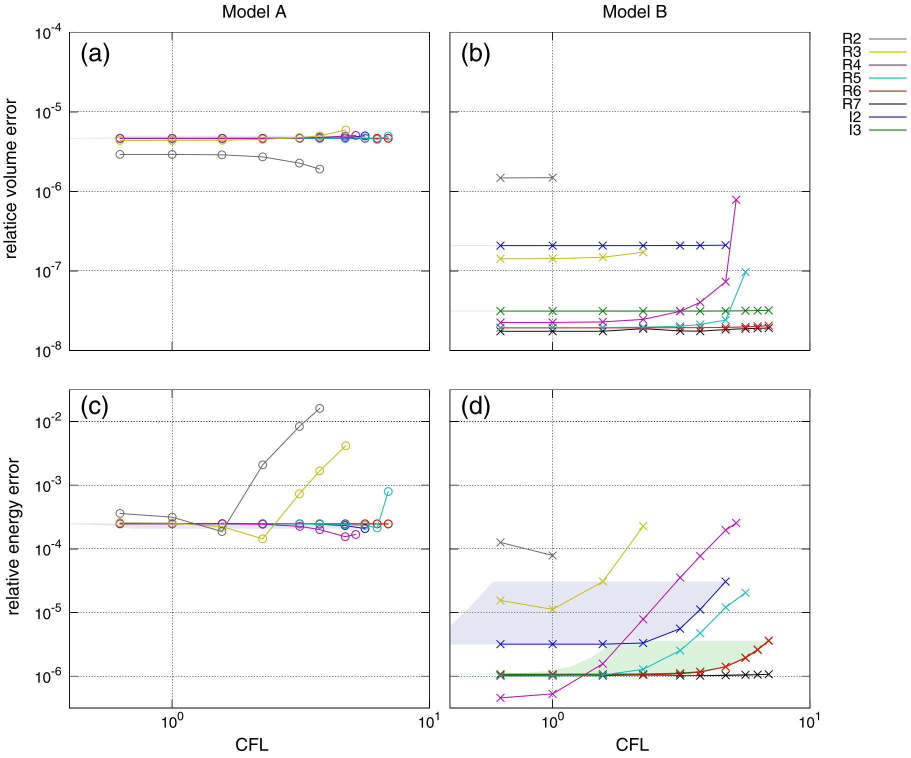

Figure 17. (a–b) Volume and (c–d) energy errors for Model A (left) and Model B (right) as a function of the CFL number and horizontal grid spacing (see Tables II and III for details). The shading indicates the maximum and minimum CFL defined for the irregularly spaced horizontal grids I2 and I3, as explained in section 3.3.3.

For Model A, the volume errors are relatively constant as a function of CFL number. The energy errors are also relatively constant for low CFL numbers and generally increase with increasing CFL number for the coarser horizontal resolution grids (Figure 17a, c). Model B has stable or increasing errors in volume and energy conservation with an increase in CFL number, as expected (Figure 17b, d).

Both models converge to minimum errors for small CFL numbers. Model A converges to minimum errors that are nearly constant, independent of the horizontal grid spacing (for the range of values tested). Model B, however, converges to lower errors for simulations with increased horizontal grid resolution with the exception of the energy error for grid R4. Finally, Model B is more accurate than Model A, with volume and energy conservation errors that are more than an order of magnitude smaller for grids finer than R2.

3.3.3. Irregular horizontal grid spacing. In the previous section, the horizontal grid spacing was uniform, but irregular grid spacing may be used to decrease the simulation time while minimizing the errors. Two irregularly spaced grids are tested (denoted I2 and I3), with low resolution in the uniform-depth far left and right extremes of the domain, and high resolution at the top of the slope where wave shoaling and nonlinear interactions with the bottom are most important (Figure 15a, Table III). For both models, the results are visually indistinguishable with those obtained with grids R5–R7 (Figure 16).

To compare the volume and energy errors with those obtained when using regularly spaced horizontal grids, the CFL number in Figure 17 (solid lines) was defined using the minimum grid spacing ($\Delta x = 0.0125$ m for I2, and $\Delta x = 0.005$ m for I3). To account for the variability in horizontal grid spacing, the minimum CFL number was also calculated using the maximum grid spacing ($\Delta x = 0.1$ m for I2, and $\Delta x = 0.02$ m for I3), as indicated by the shaded zone between the maximum and minimum CFL numbers in Figure 17. If decreasing the grid spacing in the zones

Table III. Irregularly spaced horizontal grids for the test case propagating a train of waves on a slope.

GRID I2		GRID I3	
x	Δx (m)	x	Δx (m)
0 m $< x <$ 35 m	0.05	0 m $< x <$ 20 m	0.02
35 m $< x <$ 40 m	0.025	20 m $< x <$ 35 m	0.01
40 m $< x <$ 48 m	0.0125	35 m $< x <$ 50 m	0.005
48 m $< x <$ 58 m	0.025	50 m $< x <$ 60 m	0.01
58 m $< x <$ 62 m	0.05	60 m $< x <$ 74 m	0.02
62 m $< x <$ 100 m	0.1		

far from the slope has no impact on the model results, irregularly spaced grid I2 errors should be between those of regularly spaced grids R4 and R5, and I3 errors should be equivalent to those of R6.

Similar to the regularly spaced grids, the volume errors for Models A and B are nearly constant as a function of the CFL number, and Model B errors are at least one order of magnitude smaller than those of Model A (Figure 17a–b). For Model A, the errors appear equivalent to those obtained with regularly spaced grids R4–R6. For Model B, the I2 volume errors are slightly larger than the errors obtained for R3 with small CFL numbers. However, they do not increase for large CFL numbers and the simulations remain stable for larger CFL numbers ($2 < \text{CFL} < 4.7$). Similarly, I3 volume errors are slightly larger than those of R4 and R5 for small CFL numbers, but they do not increase and the simulations remain stable for larger CFL numbers ($\text{CFL} > 4.5$).

The energy errors for Model A remain constant as a function of CFL number, while the Model B energy errors increase as a function of CFL number for $\text{CFL} > 1.5$. However, Model B energy errors are at least one to two orders of magnitude smaller than Model A errors (Figure 17c–d). For Model A, these errors are equivalent to those obtained with regularly spaced grids R5 and R6. For Model B, the I2 energy errors at low CFL numbers are between those obtained with grids R3 and R4, and for $\text{CFL} > 2$, these errors are between those obtained with grids R4 and R5. The I3 energy errors are equivalent to those obtained with grid R6.

The CPU time (discussed in more detail in Section 3.3.5) of the simulations with irregularly spaced grids is equivalent to the CPU time of a regularly spaced grid with the same number of points. The I2 simulation time falls between that of grids R3 and R4, while the I3 simulation time is equivalent to that of grid R5. Visual comparison of the R3–R4 and I2 free surface position envelopes in Figure 16 and quantitative comparison of the volume and energy errors for Model B in Figure 17b, d show that gains in accuracy and efficiency can be made by using irregularly spaced grids. For these two tests, the transition between different grid sizes varied by a factor of two. The sensitivity of the model to further increases in this factor was not evaluated here but will be a topic of future work with irregular grids in two horizontal dimensions.

3.3.4. Convergence as a function of the vertical resolution N. Finally, the model convergence also depends strongly on the vertical resolution N, which was held constant in the previous tests (Sections 3.3.2 and 3.3.3). The convergence is evaluated for the irregularly spaced grids I2 and I3 using time steps of $\Delta t = 0.005$ s and $\Delta t = 0.002$ s, respectively (CFL$\approx$ 1.25, based on the definition using the minimum grid spacing). These time steps were selected to maintain a constant CFL number and to maximize the efficiency of the simulations. Because an analytical solution is unavailable for comparison, the wave envelope errors for each model are calculated as the rms difference of the simulated wave envelope with $N = [3, 19]$ and the simulated wave envelope with $N = 20$. For $N = 20$, the maximum and rms difference between the wave envelopes of Models A and B are on the order of 10^{-5} and 10^{-6}, respectively. For Model A, $N = 5$ (i.e., $N_Z = 6$) is the minimum value tested to maintain vertical spatial derivatives with fourth-order accuracy.

DOI: 10.1002/fld

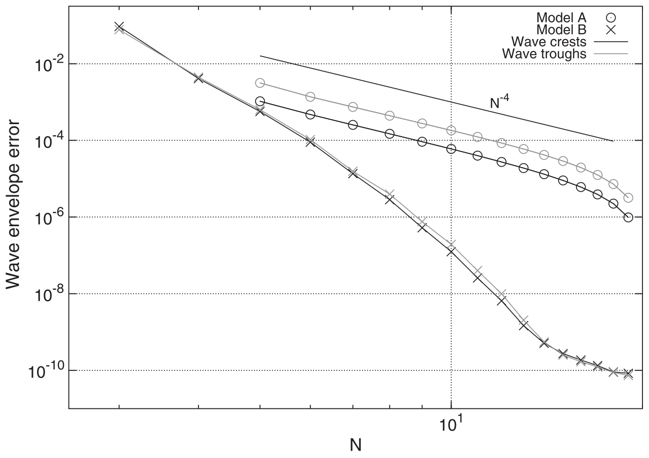

Figure 18. Convergence of the wave envelope RMSE as a function of the vertical resolution N, using $N = 20$ as the reference solution for the horizontal grid I3 (similar results for grid I2).

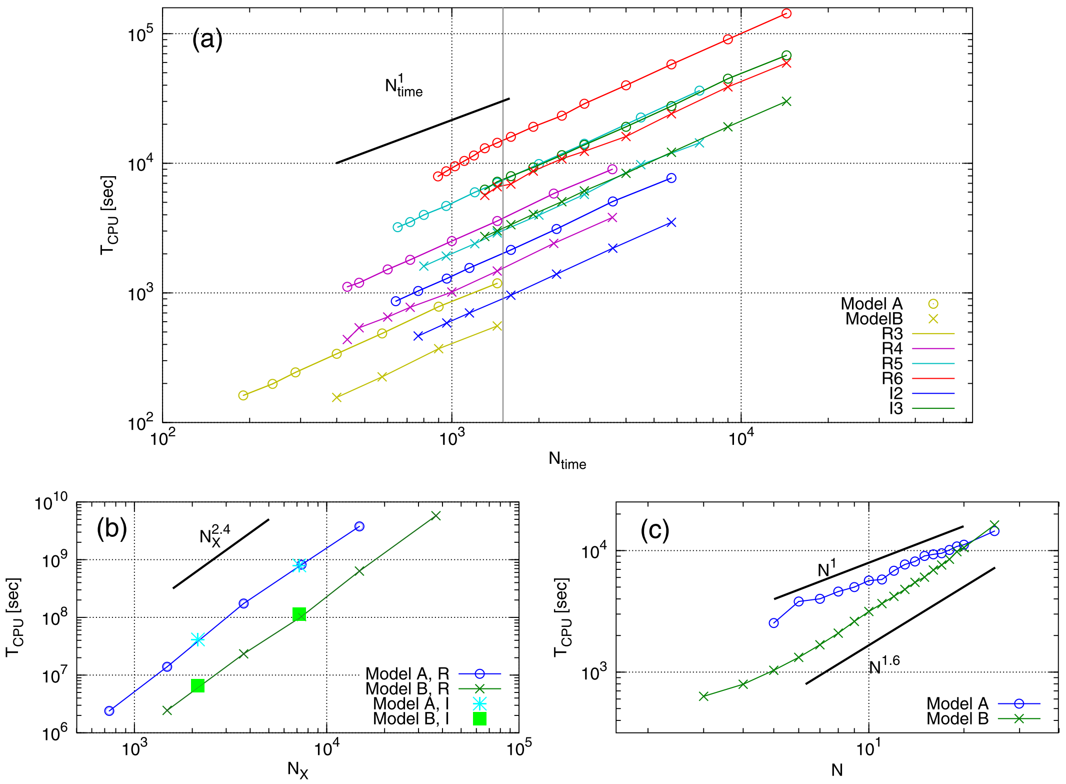

Figure 19. CPU time T_{CPU} as a function of (a) the number of time steps per wave period N_{time}, with constant $N = 7$, (b) the horizontal resolution N_X, with constant $N_{time} = 1500$ (vertical gray line in (a)) for regularly (R) and irregularly (I) spaced grids, and (c) the vertical resolution N for irregularly spaced grid I2 (similar results for grid I3) for Models A and B. The thick black lines indicate the general trends for each parameter plotted.

The wave envelope errors converge more rapidly with Model B than with Model A (Figure 18), with differences of one to three orders of magnitude for $N > 6$. For the same vertical resolution, Model B simulation results more rapidly approach the simulation results obtained for higher values of N.

DOI: 10.1002/fld

3.3.5. CPU time. To further compare the performance of Models A and B, the CPU time trends were evaluated as a function of the number of time steps N_{time} and the horizontal N_X and vertical N resolutions:

$$T_{CPU} = f\,(N, N_X, N_{time}) = N^{\alpha} N_X^{\beta} N_{time}^{\gamma}. \tag{31}$$

All simulations shown here were run on Intel Xeon E5620 (Intel Corporation, Santa Clara, California, USA) 2.4 GHz processor. Because the measured CPU time depends on the machine, only the trends will be discussed here.

As expected, the CPU time is linearly proportional, $\gamma = 1$, to the number of time steps per wave period N_{time} for both models when the vertical resolution is held constant ($N = 7$, Figure 19a). The computation time also increases with increasing horizontal resolution, and for the test cases shown here with $N = 7$, Model B is more efficient than Model A by a factor of approximately two. To evaluate the CPU time as a function of the horizontal resolution, the vertical resolution and number of time steps are then held constant with $N = 7$ and $N_{time} = 1500$. Because the CPU time is a linear function of N_{time}, it is linearly interpolated at $N_{time} = 1500$ (vertical line in Figure 19a) for each horizontal grid. For Models A and B, the CPU time is proportional to the horizontal resolution N_X to the power $\beta = 2.4$ (Figure 19b), which is dependent on the chosen direct solver and its optimization. Further improvements in CPU time may be made with the use of an iterative solver, which will be considered in future work. Finally, the CPU time was evaluated as a function of the vertical resolution N for a constant horizontal resolution (grid I2) and number of time steps $N_{time} = 2872$ (CFL ≈ 1.25). The CPU time increases linearly ($\alpha = 1$) for Model A and slightly more rapidly with $\alpha = 1.6$ for Model B. This difference is caused by the different methods used to resolve the potential in the vertical. Finally, for $N < 20$, Model B is more efficient, while Model A becomes more efficient for $N > 20$.

4. DISCUSSION

The three test cases presented here highlight the numerical properties of the two model approaches and identify differences between the two approaches of resolving the velocity potential in the vertical. The first two academic test cases are compared with reference solutions calculated using high-order Fourier methods. In the third test case simulating waves shoaling on a beach (in the non-breaking limit), the solutions are qualitatively compared with the reference solution of [37], after which the convergence properties, accuracy, and efficiency of the models were evaluated.

4.1. Optimal vertical resolution

This analysis suggests that the optimal vertical resolution for practical applications, which is a compromise between accuracy and efficiency, is approximately $7 < N < 15$ for both models.

The first test case shows that Model B converges more rapidly than Model A. Model B exhibits exponential (geometric) convergence with N, while Model A has algebraic convergence, with decreases in errors approximately proportional to N^{-4} (for fourth-order finite difference schemes). The results of the second and third test cases confirm that Model B converges more rapidly than Model A and is more accurate when equivalent values of N are compared. Therefore, while obtaining highly accurate results, it is possible to reduce the size of the linear system of equations and increase the simulation efficiency by using Model B.

4.2. Optimal CFL number range

As expected, the optimal CFL number is approximately 1 (Figures 12, 16, and 17) for tests with sufficient horizontal grid resolution. The CPU time is optimized, and the free surface elevation, total energy, and volume errors are approximately equal to those obtained in simulations with lower CFL numbers. For simulations with irregularly-spaced grids, the optimal CFL number may be slightly higher than for simulations with regularly-spaced grids (Figure 17), but a precise definition of the CFL number is not straightforward because of the variability in Δx.

4.3. *Stability of the time marching scheme*

Numerical tests of the model stability demonstrate slightly different behavior for Models A and B. For a given horizontal resolution, Model A generally remains stable at higher CFL numbers than Model B. However, Model A often develops instabilities during simulations with high horizontal resolution, whereas Model B remains stable.

Both models demonstrate the appearance of some anomalies in model errors as a function of horizontal resolution or CFL number, as discussed in Section 3.2.2. For the standing wave test case, some simulations with coarse horizontal resolution became unstable, as shown by the loss of energy at low wave numbers and the growth in energy at high wave numbers of the free surface position energy spectra.

4.4. *Optimal model approach*

Model B demonstrates more rapid convergence and lower errors as a function of the vertical resolution N, as well as generally smaller errors in the phase shift, free surface position, total energy, and volume. While some exceptions exist primarily for high CFL number or low vertical resolution simulations, Model B shows improved accuracy for simulations within the optimal range of parameter values for physical applications.

When comparing model efficiency for the third test case, the CPU time of Model A is proportional to N^1, $N_X^{2.4}$, and N_{time}^1, while the CPU time of Model B is proportional to $N^{1.6}$, $N_X^{2.4}$, and N_{time}^1. Although the CPU time of Model B increases more rapidly as a function of the vertical resolution N, it remains below the CPU time of Model A in the range of N recommended for physical applications ($7 < N < 15$). [29] recently demonstrated the enhanced efficiency of a high-order spectral method in both the horizontal and vertical dimensions, in comparison with the finite difference approach of [18]. Here, these results are extended to consider the case when a high-order finite difference approach is used in the horizontal dimension, while a spectral method is used only in the vertical dimension.

Finally, in the third test case, the model accuracy and efficiency were also improved by using irregularly spaced horizontal grids with finer resolution in the shoaling region, in comparison with regularly spaced grids with the same value N_X. In physical applications where a particular zone of interest can be defined (e.g., with increased wave–wave or wave–bathymetry interactions), increasing the horizontal resolution only in these zones can optimize the model accuracy and efficiency.

5. CONCLUSIONS

Three test cases demonstrate the numerical properties of two approaches to solving the fully nonlinear potential flow problem in 1DH (x, z) domains with non-breaking waves. By comparing with reference solutions, these simulations confirm the convergence properties of the two models and demonstrate their ability to resolve accurately and propagate highly nonlinear waves.

Comparison of the convergence properties, model propagation errors, and CPU time of the two approaches to resolving the potential in the vertical confirms the improved accuracy and efficiency of the Model B spectral method (exponential convergence), in comparison with the Model A fourth-order finite difference schemes (algebraic convergence).

Current work includes further model validation in comparison with wave tank experiments for regular and irregular nonlinear waves. Future work includes the optimization and extension of the Model B approach to 2DH domains to validate and apply the model in coastal settings, in particular with the inclusion of wave breaking dissipation.

ACKNOWLEDGEMENTS

We would like to thank Christophe Denis (EDF R&D) for his help in implementing the direct linear solver MUMPS, as well as Pierre Desbrières (ENPC) for his help in running several test case simulations.

REFERENCES

1. Maguire AE. Hyrdrodynamics, control and numerical modelling of absorbing wavemakers. *Ph.D. Thesis*, Edinburgh, Scotland, 2011.
2. Liu PLF, Lin P, Chang K-A, Sakakiyama T. Numerical modeling of wave interaction with porous structures. *Journal of Waterway Port Coastal and Ocean Engineering-ASCE* 1999; **125**:322–330.
3. Lara JL, Garcia N, Losada IJ. RANS modelling applied to random wave interaction with submerged permeable structures. *Coastal Engineering* 2006; **53**:395–417.
4. Shao S. Incompressible SPH simulation of wave breaking and overtopping with turbulence modelling. *International Journal for Numerical Methods in Fluids* 2006; **50**:597–621.
5. Grilli ST, Skourup J, Svendsen IA. An efficient boundary element method for nonlinear water waves. *Engineering Analysis with Boundary Elements* 1989; **6**(2):97–107.
6. Newman JN, Lee C-H. Boundary-element methods in offshore structure analysis. *Journal of Offshore Mechanics and Arctic Engineering* 2002; **124**:81–89.
7. West BJ, Brueckner KA, Janda RS, Milder M, Milton RL. A new numerical method for surface hydrodynamics. *Journal of Geophysical Research* 1987; **92**:11803–11824.
8. Dommermuth DG, Yue DKP. A high-order spectral method for the study of nonlinear gravity waves. *Journal of Fluid Mechanics* 1987; **184**:267–288.
9. Chern MJ, Borthwick AGL, Taylor RE. A pseudospectral σ-transformation model of 2-D nonlinear waves. *Journal of Fluids and Structures* 1999; **13**:607–630.
10. Agnon Y, Madsen PA, Schäffer HA. A new approach to high-order Boussinesq models. *Journal of Fluid Mechanics* 1999; **399**:319–333.
11. Madsen PA, Bingham HB, Liu H. A new Boussinesq method for fully nonlinear waves from shallow to deep water. *Journal of Fluid Mechanics* 2002; **462**:1–30.
12. Fuhrman DR, Bingham HB, Madsen PA. Nonlinear wave–structure interactions with a high-order Boussinesq model. *Coastal Engineering* 2005; **52**:655–672.
13. Chazel F, Benoit M, Ern A, Piperno S. A double-layer Boussinesq-type model for highly nonlinear and dispersive waves. *Proceedings of the Royal Society* 2009; **465**:2319–2346.
14. Wu GX, Ma QW, Taylor RE. Numerical simulation of sloshing waves in a 3D tank based on a finite element method. *Applied Ocean Research* 1998; **20**:337–355.
15. Ma QW, Wu GX, Taylor RE. Finite element simulation of fully non-linear interaction between vertical cylinders and steep waves. Part 1: methodology and numerical procedure. *International Journal for Numerical Methods in Fluids* 2001; **36**:265–285.
16. Li B, Fleming C. A three dimensional multigrid model for fully nonlinear water waves. *Coastal Engineering* 1997; **30**:235–258.
17. Bingham HB, Zhang H. On the accuracy of finite-difference solutions for nonlinear water waves. *Journal of Engineering Mathematics* 2007; **58**:211–228.
18. Engsig-Karup A P, Bingham H B, Lindberg O. An efficient flexible-order model for 3D nonlinear water waves. *Journal of Computational Physics* 2009; **228**:2100–2118.
19. Kreiss H.-O., Oliger J. Comparison of accurate methods for the integration of hyperbolic equations. *Telus XXIV* 1972; **3**:199–215.
20. Fuhrman D R, Bingham H B. Numerical solution of fully non-linear and highly dispersive Boussinesq equations in two horizontal dimensions. *International Journal for Numerical Methods in Fluids* 2004; **44**:231–255.
21. Zakharov V E. Stability of periodic waves of finite amplitude on the surface of a deep fluid. *Journal of Applied Mechanics and Technical Physics* 1968; **9**(2):190–194.
22. Smith R A. An operator expansion formalism for nonlinear surface waves over variable depth. *Journal of Fluid Mechanics* 1998; **363**:333–347.
23. Guyenne P, Nicholls D P. A high-order spectral method for nonlinear water waves over moving bottom topography. *SIAM Journal on Scientific Computing* 2007; **30**(1):81–101.
24. Clamond D, Grue J. A fast method for fully nonlinear water-wave computations. *Journal of Fluid Mechanics* 2001; **447**:337–355.
25. Fructus D, Clamond D, Grue J, Kristiansen Ø.. An efficient model for three-dimensional surface wave simulations: Part I: free space problems. *Journal of Computational Physics* 2005; **205**:665–685.
26. Clamond D, Fructus D, Grue J. A note on time integrators in water-wave simulations. *Journal of Engineering Mathematics* 2007; **58**:149–156.
27. Dias F, Bridges TJ. The numerical computation of freely propagating time-dependent irrotational water waves. *Fluid Dynamics Research* 2006; **38**:803–830.
28. Fornberg B. Generation of finite difference formulas on arbitrarily spaced grids. *Mathematics of Computation* 1988; **51**(184):699–706.
29. Ducrozet G, Bingham HB, Engsig-Karup AP, Bonnefoy F, Ferrant P. A comparative study of two fast nonlinear free-surface water wave models. *International Journal for Numerical Methods in Fluids* 2012; **69**(11):1818–1834.
30. Tian Y, Sato S. A numerical model on the interaction between nearshore nonlinear waves and strong currents. *Coastal Engineering* 2008; **50**(4):369–395.
31. Boyd JP. *Chebyshev and Fourier Spectral Methods: Second Edition, Revised*. Dover Publications: Mineaola, NY, USA, 2001.

32. Amestoy PR, Duff IS, Koster J, L'Excellent J-Y. A fully synchronous multifrontal solver using distributes dynamic scheduling. *SIAM Journal on Matrix Analysis and Applications* 2001; **23**(1):15–41.
33. Amestoy P R, Guermouche A, L'Excellent J.-Y., Pralet S. Hybrid scheduling for the parallel solution of linear systems. *Parallel Computing* 2006; **32**:136–156.
34. Chaplin J R. Developments of stream-function wave theory. *Coastal Engineering* 1980; **3**:179–205.
35. Rienecker M M, Fenton J D. A Fourier approximation method for steady water waves. *Journal of Fluid Mechanics* 1981; **104**:119–137.
36. Tsai C.-P., Jeng D.-S. Numerical Fourier solutions of standing waves in finite water depth. *Applied Ocean Research* 1994; **16**:185–193.
37. Kennedy A B, Kirby J T, Chen Q, Dalrymple R A. Boussinesq-type equations with improved nonlinear performance. *Wave Motion* 2001; **33**:225–243.
38. Kennedy A B, Fenton J D. A fully-nonlinear computational method for wave propagation over topography. *Coastal Engineering* 1997; **32**:137–161.

D.2 Raoult et al. (2019)

Journal of Computational Physics 378 (2019) 278–302

Contents lists available at ScienceDirect

Journal of Computational Physics

www.elsevier.com/locate/jcp

Development and validation of a 3D RBF-spectral model for coastal wave simulation

Cécile Raoult [a,b,*], Michel Benoit [c], Marissa L. Yates [a,d]

[a] *Université Paris-Est, Saint-Venant Hydraulics Laboratory (ENPC, EDF R&D, Cerema), 6 quai Watier, BP 49, 78401 Chatou, France*
[b] *EDF R&D, Laboratoire National d'Hydraulique et Environnement, 6 quai Watier, BP 49, 78401 Chatou, France*
[c] *Aix Marseille Univ, CNRS, Centrale Marseille, Institut de Recherche sur les Phénomènes Hors Equilibre (IRPHE), UMR 7342, 49 rue Frédéric Joliot-Curie, BP 146, 13384 Marseille Cedex 13, France*
[d] *Cerema, Tech. Dept. Water, Sea and Rivers, 134 rue de Beauvais, CS 60039, 60280 Margny-les-Compiègne, France*

ARTICLE INFO

Article history:
Received 28 February 2018
Received in revised form 1 November 2018
Accepted 1 November 2018
Available online 7 November 2018

Keywords:
Nonlinear
Dispersive
Water waves
Potential theory
Zakharov equations
Radial Basis Functions

ABSTRACT

With the objective of simulating wave propagation in the nearshore zone for engineering-scale applications, a two dimensional (2DV) model based on the Euler–Zakharov equations [73,54] is extended to three dimensions (3D). To maintain the flexibility of the approach with the goal of applying the model to irregularly shaped domains, the horizontal plane is discretized with scattered nodes. The horizontal derivatives are then estimated using the Radial Basis Function-Finite Difference (RBF-FD) method, while a spectral approach is used in the vertical dimension. A sensitivity analysis examined the robustness of the RBF-FD approach as a function of RBF parameters when estimating the derivatives of a representative function. For a targeted stencil size between 20 and 30 nodes, Piecewise-Smooth (PS) polyharmonic spline (PHS) functions are recommended, avoiding the use of Infinitely-Smooth (IS) RBFs, which are less appropriate for the desired applications because of their dependence on a shape parameter. Comparisons of simulation results to observations from two wave basin experiments show that nonlinear effects induced by complex bottom bathymetries are reproduced well by the model with the recommended RBF approach, validating the use of this method for 3D simulations of wave propagation.

1. Introduction

Accurate wave propagation models are required for a wide range of coastal management and engineering applications, including the design of coastal structures and the evaluation of coastal risks. In the nearshore zone, nonlinear and dispersive effects, characterized by the wave steepness and relative water depth, respectively, can be particularly important. The wave steepness $\epsilon = kH/2$ and relative wave height H/h (where H, k, and h are the characteristic local wave height, wave number, and water depth, respectively) increase significantly as waves shoal in shallow water and approach the breaking point. The relative water depth $\mu = kh$ is often large in deep and intermediate water, or for the shorter waves in the sea state, indicating the importance of dispersive effects. Wave propagation models thus need to capture properly nonlinear and dispersive effects to simulate accurately offshore and coastal engineering problems. Two-dimensional cross-

---

[*] Corresponding author.
E-mail addresses: cecile.raoult@gmail.com (C. Raoult), benoit@irphe.univ-mrs.fr (M. Benoit), marissa.yates-michelin@cerema.fr (M.L. Yates).

https://doi.org/10.1016/j.jcp.2018.11.002

shore (2DV) wave models can be used as a preliminary step in coastal studies, but 3D models are needed to capture fully the effects of alongshore bathymetric variations, variable wave incidence, the presence of coastal or harbor structures, etc.

A wide variety of mathematical models exist to simulate nearshore wave propagation, and Yates and Benoit [74] and Benoit et al. [12] chose to develop a 2DV fully nonlinear and dispersive potential flow model based on the Euler–Zakharov equations as a compromise between accuracy, mathematical complexity, and computational time. A variety of other approaches exist, and recent non-exhaustive reviews are summarized by Raoult et al. [54] and Gouin et al. [41], for example. The chosen approach, based on fully nonlinear potential flow (FNPF) theory, requires solving the Laplace boundary value problem (BVP), which is implemented numerically in the model using a spectral approach in the vertical direction [59] and finite difference schemes in the horizontal direction. The nonlinear and dispersive capacities of the 2DV version of the model were demonstrated in Yates and Benoit [74,73] and Raoult et al. [54]. The accuracy of a similar approach using the Chebyshev–Tau method in the vertical and a Fourier collocation method in the horizontal was demonstrated in Christiansen et al. [17].

Extending 2DV modeling approaches to 3D increases significantly the number of numerical challenges to overcome, including but not limited to the computational time, domain geometry, and boundary condition specification or far-field representation. Therefore, a variety of different numerical approaches have been used to solve the 3D FNPF problem by reducing the dimension of the problem (e.g. boundary element [56,42,30,52] or High-Order Spectral (HOS) methods [21,22]), discretizing the whole domain but taking local derivatives only (e.g. finite element [71] or finite difference schemes [24]), or searching for fast numerical methods for solving the Laplace problem (e.g. integral equations [40] or coupled modes [11]), each approach having its own advantages and disadvantages.

A number of 3D Numerical Wave Tanks (NWTs) have been developed using high-order Boundary Element Methods (BEM) [56,42,30,52], which are an efficient and accurate approach for solving the Laplace BVP by reducing the dimensionality of the discretized problem. However, standard BEM techniques yield nonsymmetric and fully populated matrices that require fast solution methods (e.g. fast multipole algorithm [53]) or advanced numerical implementations (e.g. pre-corrected Fast Fourier Transform methods [72]) to avoid becoming computationally prohibitively expensive to solve. This is especially the case for simulating irregular nonlinear waves that span a wide range of wavelengths, thus requiring fine grids.

In the literature, two other methods have been used to extend 2DV approaches to 3D with Finite Element Methods (FEM) (e.g. 2DV [70] to 3D [71]) or finite difference schemes (e.g. 2DV [13] to 3D [24]). These approaches require discretizing the entire fluid domain, but the only non-zero elements in the coefficient matrix are the neighboring points (with the number of points depending on the chosen order of the numerical scheme). While the full 3D Laplace problem still must be solved at each time step, recent work has improved the numerical efficiency of such codes (e.g. using preconditioned defect correction methods in 2DV [17] or in 3D in the *OceanWave3D* code [23]) that may then be used for coastal and offshore engineering applications.

Another even more computationally efficient approach uses the HOS method (e.g. Dommermuth and Yue [20], West et al. [63], Craig and Sulem [19]), which is based on a Taylor series expansion of the velocity potential about a reference water level (often the mean water line). This approach was originally developed for unbounded domains and then for finite depth cases, with periodic lateral boundary conditions. Ducrozet et al. [21,22] developed an open-source model, *HOS-ocean*, which is an extension of this method to take into account the generation and propagation of regular and irregular, multidirectional waves. Recently, *HOS-ocean* was also extended to simulate wave propagation over variable bottom bathymetries by Gouin et al. [41].

Additional approaches for solving the BVP include a fast Laplace equation solver using integral equations and an iterative solution procedure that converges rapidly (in 2DV [18] and then 3D [40]), or a fully dispersive coupled-mode model (in 2DV [10] and then 3D [11]).

Here, the objective is to extend the two dimensional model developed by Yates and Benoit [73] and Raoult et al. [54] to three dimensions, maintaining the efficient and accurate spectral approach used in the vertical. The 2DV code used finite difference schemes to estimate horizontal derivatives. This approach is still applicable in two horizontal dimensions for simple domain geometries that can be discretized by regular meshes. However, the model cannot then be applied easily to complex domains. Therefore, to overcome these limitations, a meshless approach based on Radial Basis Functions (RBF) is implemented in the code and tested to propagate highly nonlinear and dispersive waves. The RBF method has been used extensively in other fields of research for a variety of physical and engineering problems, including, for example, diffusion [61,16], radiative transport [50], combustion [48], shallow-water models [77,44], and flow simulations using the Navier–Stokes equations [57]. Here, the RBF method is applied to evaluate its capacity to simulate accurately nonlinear wave propagation.

This paper presents a brief literature review of RBF methods (Section 2), before describing the mathematical model and its numerical implementation in the code (Section 3), focusing on the RBF Finite Difference (RBF-FD) method used to estimate the horizontal derivatives. A sensitivity analysis then evaluates the accuracy and stability of the RBF-FD method as a function of the RBF parameters for a representative test function (Section 4). These tests help to identify the optimal method parameters for simulating waves. Then, the 3D version of the model is validated by simulating two sets of experiments conducted in wave basins with variable bathymetries (Section 5). Finally, an analysis of the advantages and disadvantages of using the RBF-FD approach to simulate nonlinear wave propagation is summarized, including propositions for future work (Section 6).

Table 1
Summary of commonly used RBFs describing the function, the constraints on the free parameters, and the regularity of the function (PS stands for Piecewise-Smooth and IS for Infinitely-Smooth).

Name (Acronyme)	Function $\psi(r)$	Condition	Regularity
Polyharmonic Spline (PHS)	r^m	m odd integer	PS
Thin Plate Spline (TPS)	$r^m \log r$	m even integer	PS
Multiquadric (MQ)	$\sqrt{r^2+C^2}$	$C > 0$	IS
Inverse Multiquadric (IMQ)	$\frac{1}{\sqrt{r^2+C^2}}$	$C > 0$	IS
Inverse Quadratic (IQ)	$\frac{1}{r^2+C^2}$	$C > 0$	IS
Gaussian (GA)	e^{-r^2/C^2}	$C > 0$	IS

2. Brief review of RBF methods

RBFs were first introduced by Hardy [43] for interpolating surfaces. A function $\tilde{f}(\underline{x})$ is sought to approximate a given function $f(\underline{x})$, for which the values f_i $(i = 1, ..., N)$ are known for a given set of N data points $\underline{x}_i$ $(i = 1, ..., N)$ using a set of basis functions $\psi_i(\underline{x})$ $(i = 1, ..., N)$:

$$\tilde{f}(\underline{x}) \approx \sum_{i=1}^{N} \lambda_i \, \psi_i(\underline{x}), \tag{1}$$

with $\underline{x} = (x, y)$. The interpolation coefficients λ_i are determined by solving the set of linear equations obtained by enforcing the interpolation conditions: $\tilde{f}(\underline{x}_i) = f_i$ for $i = 1$ to N. For one-dimensional data, a variety of different basis functions (independent of the data points) lead to non-singular linear systems as long as the N data points are distinct (i.e. Fourier and polynomials series). However, this property is no longer guaranteed when the problem is extended to two dimensions [66]. Hardy [43] proposed using a basis of functions composed of a single radial function $\psi(r)$ centered at each data point: $\psi_i(\underline{x}) = \psi(||\underline{x} - \underline{x}_i||)$ $(i = 1, ..., N)$.

The initial work of Hardy [43] used the multiquadric (MQ) radial function $\psi(r) = \sqrt{r^2 + C^2}$, with r the radial distance from the center $\underline{x}_i$ to node $\underline{x}$ and C a strictly positive shape parameter to obtain a continuously differentiable basis function (even when $r = 0$), where C controls the narrowness of the RBF. A wide variety of radial functions may be used. In a study of scattered data interpolation, Franke [39] tested 29 interpolation methods for six different test functions. The results showed that MQ functions were among the most accurate, together with inverse multiquadric (IMQ) and thin plate spline (TPS) functions (Table 1).

Overall, the RBF method demonstrated good results for spatial interpolation. Therefore the approach was tested further for estimating derivatives in domains with scattered nodes. Stead [58] compared the errors obtained in estimating partial derivatives when using MQ or weighted least square quadratic approximate interpolants. Since RBF interpolants do not have polynomial precision (except when polynomial terms are added), the author recommended using the MQ interpolant for surfaces with significant curvature. Later, Kansa [45] was the first to use the MQ function to solve partial differential equations (PDEs), namely a Poisson equation, with a collocation method. The coefficients of the RBF approximation of the solution are found by solving the linear system obtained by applying the differential operators to the interpolant for the interior nodes and boundary conditions to the interpolant for the boundary nodes. The resulting matrix is not symmetric and is not proven to be unisolvent. Several improvements to this approach were made, by recovering the symmetry of the matrix using Hermite interpolation to modify the basis functions [25], or by imposing both the PDE and the boundary conditions at boundary nodes to increase the constraints where errors are larger [27].

Many different functions can be used in the RBF approach, and as shown in the preliminary study by Franke [39], the results are sensitive to the choice of function. The most commonly used functions (Table 1) can be broken into two families: piecewise-smooth (PS) and infinitely-smooth (IS) functions.

For IS-RBFs (with a shape parameter C), the interpolation system will not be singular if the scattered nodes are distinct. PS-RBFs do not depend on a shape parameter, but they present a singularity at the origin. To ensure the unique solvability of the linear system, the interpolant has to be modified by including polynomial terms, requiring additional constraints for the linear system to be well-posed. In this case, the non-singularity of the matrix becomes more restrictive since it requires that the nodes are not only distinct but are also unisolvent in the appended polynomial space [31].

Global vs. local methods. The RBF method was first introduced as a global method, in which estimates at each node depend on all nodes in the domain, leading to a full coefficient matrix. When the matrix becomes too large, it often becomes ill-conditioned. The interpolation coefficients (λ_i, Eq. (1)) become oscillatory with large magnitudes that may lead to a poor interpolation because of numerical cancellations. In this case, the size of the matrix can be reduced by considering smaller domains using domain decomposition algorithms [8,65,76]. In the limit, one can instead use a local approach by defining stencils centered at each node of the domain and including only the $N_{sten} - 1$ nearest neighbors (for a total of N_{sten} nodes in each stencil) in the estimation of the function (Eq. (1)). Tolstykh and Shirobokov [60] were the first to consider this method to estimate derivatives with a RBF-FD approach, followed shortly by Wright [66] and Shu et al. [57]. Wright and

Fornberg [67] improved the accuracy of this method by including a linear combination of derivatives of the function at the surrounding nodes. The local method has the advantage of reducing considerably the computational time in comparison to the global method, as well as being parallelized easily. The construction of approximate formulas for the derivatives using RBF interpolants, also called the RBF-FD method, will be presented in more detail in Section 3.3.

However, even when using local methods, the matrix may become ill-conditioned for IS-RBFs when $C \to \infty$ (i.e. in the limit of flat basis functions). Several specific algorithms have been developed to obtain accurate results even for large values of C (i.e. Contour Padé [35], RBF-QR [34], RBF-GA [38] or more recently the RBF-RA algorithm [68]). Using a stable algorithm not only improves the derivative estimation accuracy by allowing the use of larger values of C, but also makes the choice of optimal C less critical. Nevertheless, the algorithms may be difficult to adapt to a specific mathematical model or the modified RBFs may have much more complicated expressions.

PS vs. IS functions. The choice of RBF to obtain the most accurate estimates is not straightforward, and some trade-offs must be considered when using IS or PS functions. Errors when using either family of functions in the RBF method depend on the specific choice of the radial function (e.g. Table 1), the mesh resolution and spacing, and the stencil size N_{sten}. Two main characteristics differentiate these two families of functions: (1) the type of convergence as a function of the node spacing, and (2) the dependency on a shape parameter C.

When using global RBF methods, IS-RBFs have spectral convergence, while PS-RBFs have only algebraic convergence, which often leads to a preference for IS-RBFs [31]. However, when using local RBF methods (i.e. RBF-FD method), the spectral accuracy of IS-RBFs is lost, minimizing their advantage over PS-RBFs with respect to convergence. Additionally, stagnation errors exist. One type of PS-RBFs, PHS, require the addition of a polynomial (with M terms) to the interpolant to guarantee the unisolvency of the system. The PHS RBFs then have a convergence rate corresponding to the degree of the added polynomial. For complex applications, Barnett [3] and Bayona et al. [7] recommended an added polynomial of degree such that there are approximately twice as many RBFs as polynomial terms in the interpolant (i.e. $N_{sten} \approx 2M$).

With IS-RBFs, the estimation error depends strongly on the value of the shape parameter C: for small values of C, the error is generally high, decreasing with an increase in C. A minimum is often reached for an intermediate value of $C = C_{opt}$ (called the optimal value of C in the following). When C is increased beyond this optimal value, the error increases and large oscillations may be observed as the matrix becomes ill-conditioned. The matrix may already become ill-conditioned for values of C smaller than C_{opt}: in this case, the minimal error is just at the limit of ill-conditioning. In the limit of $C \to \infty$, Fornberg et al. [37] showed that when the interpolant limit is finite, it tends to a multivariate polynomial. Finding C_{opt} is a difficult task. For global methods, there is no existing mathematical theory to determine the optimal choice of C. Often, this choice is based on the inter-node spacing for convenience. However, based on a series of tests, Carlson and Foley [15] and then Rippa [55] concluded that the optimal value of C depends on the shape of the interpolated function and not on the node positions or spacing. When the RBF method is used to interpolate data, the value of C is chosen by cross-validation methods. For example, Rippa [55] developed a method based on the minimization of a cost function calculated as the error between the interpolant and the desired function. Fasshauer and Zhang [26] adapted this algorithm for the resolution of PDEs with RBF pseudospectral methods. For RBF-FD, Bayona et al. [4] derived an expression of the estimated error as a function of C, showing that C_{opt} depends on the shape of the function and its derivatives. They also showed that it is independent of the node spacing at first order, but can vary with node locations in 2D. Given an expression of the estimated error, Bayona et al. [5] proposed an algorithm to find the optimal value of C. However, this requires first estimating the derivatives at each point with another less accurate method (since the values of the derivative of the function are necessary to compute the error estimates), before re-estimating the derivatives with the RBF-FD method and newly obtained optimal value of C.

The selection of an optimal or even “good” value for the shape parameter C can be challenging. Thus, RBFs without shape parameters, such as PHS, recently have become more attractive, noting furthermore that they produce relatively well-conditioned matrices [4,29].

For more details on RBF methods and numerous application examples, see the recently published book of Fornberg and Flyer [31].

3. Model description

3.1. Mathematical model

The fluid domain is delimited in the vertical by the free surface at $z = \eta(\underline{x}, t)$ and the bottom at $z = -h(\underline{x})$, with the vertical axis z pointing upwards and the origin at the still water level. The fluid is accelerated by gravity $\underline{g}$. At the free surface, the atmospheric pressure is assumed uniform and constant in time (chosen to be 0 by convention), and surface tension is neglected. Potential flow theory is adopted by further considering the irrotational flow of an inviscid and homogeneous fluid of constant density. The kinematics of the fluid are obtained from the velocity potential $\Phi(\underline{x}, z, t)$ such that $\underline{v} = (u, v, w) = (\nabla\Phi, \Phi_z)$, where $\nabla f \equiv (f_x, f_y)$ is the horizontal gradient operator, and partial derivatives are denoted with subscripts.

If the free surface is assumed to be single-valued in $\underline{x}$ (no overturning waves), the evolutions of $\eta(\underline{x}, t)$ and $\tilde{\Phi}(\underline{x}, t) \equiv \Phi(\underline{x}, z = \eta(\underline{x}, t), t)$ are governed by the nonlinear kinematic and dynamic free surface boundary conditions, expressed as functions of free surface quantities only [75]:

$$\eta_t = -\nabla\eta.\nabla\tilde{\Phi} + \tilde{w}\left(1+(\nabla\eta)^2\right), \tag{2}$$

$$\tilde{\Phi}_t = -g\eta - \frac{1}{2}(\nabla\tilde{\Phi})^2 + \frac{1}{2}\tilde{w}^2\left(1+(\nabla\eta)^2\right), \tag{3}$$

where $\tilde{w}(\underline{x},t) \equiv \Phi_z|_{z=\eta(\underline{x},t)}$ is the vertical velocity at the free surface.

To integrate these equations in time, $\tilde{w}$ is determined from η and $\tilde{\Phi}$ by solving the Laplace BVP for the velocity potential Φ in the entire domain (Laplace equation) supplemented by the free surface and bottom boundary conditions (BCs):

$$\nabla^2\Phi + \Phi_{zz} = 0, \; -h(\underline{x}) \le z \le \eta(\underline{x},t), \tag{4}$$

$$\Phi = \tilde{\Phi}(\underline{x},t), \; z = \eta(\underline{x},t), \tag{5}$$

$$\nabla\Phi\cdot\nabla h + \Phi_z = 0, \; z = -h(\underline{x}). \tag{6}$$

At the lateral boundaries, periodic, Dirichlet or Neumann BCs are imposed to close the problem.

The Laplace BVP is solved using a spectral approach in the vertical dimension following the work of Tian and Sato [59]. The method is described for the case of a single horizontal dimension (i.e. $\underline{x} = x$) in Yates and Benoit [73] and Raoult et al. [54]. The extension to two horizontal dimensions is quite straightforward, and only the main steps are presented here.

First, a change of the vertical coordinate from $z \in [-h(\underline{x}), \eta(\underline{x},t)]$ to $s \in [-1,1]$ is made to project the time-varying domain to a constant height domain extending from the bottom at $s=-1$ to the free surface at $s=+1$:

$$s(\underline{x},z,t) = \frac{2z + h^-(\underline{x},t)}{h^+(\underline{x},t)}, \tag{7}$$

where $h^+(\underline{x},t) \equiv h(\underline{x}) + \eta(\underline{x},t)$ and $h^-(\underline{x},t) \equiv h(\underline{x}) - \eta(\underline{x},t)$.

The BVP is then reformulated in the transformed space $(\underline{x},s)$ for $\Phi(\underline{x},z,t) \equiv \varphi(\underline{x},s(\underline{x},z,t),t)$.

Second, the vertical variation of the velocity potential is approximated by a linear combination of Chebyshev polynomials of the first kind, $T_n(s)$:

$$\varphi(\underline{x},s) \approx \sum_{n=0}^{N_T} a_n(\underline{x}) T_n(s), \tag{8}$$

where $n = 0, 1, 2, \ldots$ indicates the order of the polynomial, and N_T is the maximum order of the Chebyshev polynomials. These polynomials are easy to compute, form an orthogonal basis over the range $[-1,1]$, and converge rapidly over a large domain. Yates and Benoit [73] and Raoult et al. [54] have shown that values of N_T smaller than 10 (typically in the range $[5,8]$) are sufficient to obtain high accuracy for a variety of 2DV nonlinear wave propagation test cases.

The approximation Eq. (8) is then introduced in the BVP, and a Chebyshev–Tau method [14] is applied to eliminate the dependence on the vertical coordinate s. The Laplace equation (4) is projected on polynomials T_p for p ranging from 0 to $N_T - 2$, supplemented by the boundary conditions, Eq. (5) and (6), respectively. For nodes located on a lateral boundary, the Laplace equation (4) is replaced, either by a Neumann condition for an impermeable boundary $\nabla\Phi.\underline{n}_{lat} = 0$ (where $\underline{n}_{lat}$ is the unit normal vector at the lateral wall) or by a Dirichlet condition for wave generation, imposing the velocity potential from linear theory (generally supplemented with a relaxation zone). The final set of equations is a linear system for the $a_n(\underline{x})$, which depends only on $\underline{x}$ at a given time:

$$\left\{\begin{array}{lll}
a_{p,xx} + a_{p,yy} + \displaystyle\sum_{n=0}^{N_T} C^x_{pn}\, a_{n,x} + \sum_{n=0}^{N_T} C^y_{pn}\, a_{n,y} + \sum_{n=0}^{N_T} D_{pn} a_n = 0 & \text{for } p = 0, ..N_T - 2 & \text{(a)} \\
\displaystyle\sum_{n=0}^{N_T} a_n = \tilde{\Phi}(\underline{x},t) & & \text{(b)} \\
h^+ h_x \displaystyle\sum_{n=0}^{N_T} (-1)^n a_{n,x} + h^+ h_y \sum_{n=0}^{N_T} (-1)^n a_{n,y} + & & \\
\qquad 2\,(1 + h_x^2 + h_y^2) \displaystyle\sum_{n=0}^{N_T} (-1)^{n-1} n^2 a_n = 0 & & \text{(c)}
\end{array}\right. \tag{9}$$

where

$$C^x_{pn} = (m_{0101} B_{p01n} + m_{1101} B_{p11n})/m_{0220}, \tag{10}$$

$$C^y_{pn} = (m_{0011} B_{p01n} + m_{1011} B_{p11n})/m_{0220}, \tag{11}$$

$$D_{pn} = (m_{0002} B_{p02n} - m_{1002} B_{p12n} + m_{2002} B_{p22n} + m_{0001} B_{p01n} + m_{1001} B_{p11n})/m_{0220}. \tag{12}$$

The m_{ijkl} terms depend only on h^+, h^-, and their spatial derivatives (up to order two). The expressions for these terms are shown in Appendix A. The B_{pikn} terms are introduced to express the projection of the terms $s^i \frac{d^k T_n}{ds^k}$ on the polynomial T_p, and they can be determined analytically as a function of n and p (see Appendix B). These terms are constant and can be computed once at the beginning of each simulation, after N_T is chosen.

For each node $\underline{x}$, $N_T + 1$ unknown coefficients a_n in Eq. (8) must be determined. With the RBF-FD method, the horizontal spatial derivatives of the a_n coefficients are approximated as linear combinations of the values in the vicinity of the node considered, leading to a set of coupled linear equations.

Once the $a_n(\underline{x})$ coefficients are determined, the vertical velocity at the free surface $\tilde{w}(\underline{x})$ is obtained readily from:

$$\tilde{w}(\underline{x}) = \Phi_z(\underline{x}, z = \eta) = s_z\, \varphi_s(s = +1) \approx \frac{2}{h^+(\underline{x})} \sum_{n=1}^{N_T} a_n(\underline{x})\, n^2 \tag{13}$$

The vertical velocity can then be used to evaluate the right hand side of Eq. (2) and Eq. (3), required by the numerical scheme to integrate in time.

3.2. Numerical implementation

A classical, explicit fourth-order Runge Kutta (RK4) scheme with a constant time step is used to integrate Eq. (2) and Eq. (3) in time. At each sub-step of the RK4 scheme, the Laplace BVP is solved. The domain is discretized with $NPXY$ nodes in the horizontal (x, y)-plane, and N_T is the maximum order of the Chebyshev polynomials in Eq. (8). Horizontal derivatives are approximated with the local RBF-FD method (described in section 3.3) using a stencil consisting of a fixed number of neighboring nodes. Therefore, for nodes far from the boundaries, the stencil dimensions are symmetric, while they become asymmetric at and near the boundaries. The effect of this asymmetry will be studied further in section 4. The RBF-FD method is chosen for its ease of implementation, with an algorithm similar to finite difference methods, and for its flexibility with scattered nodes enabling the simulation of complicated domain geometries and the possibility of local refinement. The linear system corresponding to the Laplace BVP is composed of $NPXY(N_T + 1)$ equations for the coefficients $a_n(\underline{x}_i)$, with $n = 0, \ldots, N_T$ and $i = 1, \ldots, NPXY$. The associated matrix is sparse, and the system is currently solved using the direct solver MUMPS ("MUltifrontal Massively Parallel Solver", v4.10.0) [1,2], using the default settings.

3.3. RBF-FD method

3.3.1. Theoretical background

Similar to finite difference methods, applying a linear differential operator $\mathscr{L}$ to a given function f at $\underline{x}_1$ is expressed as a linear combination of the values of the function f at the nodes in the stencil:

$$\mathscr{L} f(\underline{x}_1) \approx \sum_{i=1}^{N_{sten}} \alpha_i^{\mathscr{L}}\, f(\underline{x}_i). \tag{14}$$

The stencil is composed of the node itself and its $N_{sten} - 1$ nearest neighbors $(\underline{x}_2, \underline{x}_3, \ldots, \underline{x}_{N_{sten}})$.

The weights $\alpha_i^{\mathscr{L}}$, for $i = 1$ to N_{sten}, are determined by requiring the approximation in Eq. (14) to be satisfied by the set of radial functions centered at each node of the stencil $\psi_i(\underline{x}) \equiv \psi(||\underline{x} - \underline{x}_i||)$, $i \in [1, N_{sten}]$. This leads to the resolution of a linear set of N_{sten} equations for N_{sten} unknowns, which can be written as:

$$\begin{bmatrix} \psi(||\underline{x}_1 - \underline{x}_1||) & \cdots & \psi(||\underline{x}_{N_{sten}} - \underline{x}_1||) \\ \psi(||\underline{x}_1 - \underline{x}_2||) & \cdots & \psi(||\underline{x}_{N_{sten}} - \underline{x}_2||) \\ \vdots & \vdots & \ddots & \vdots \\ \psi(||\underline{x}_1 - \underline{x}_{N_{sten}}||) & \cdots & \psi(||\underline{x}_{N_{sten}} - \underline{x}_{N_{sten}}||) \end{bmatrix} \begin{bmatrix} \alpha_1^{\mathscr{L}} \\ \vdots \\ \alpha_{N_{sten}}^{\mathscr{L}} \end{bmatrix} = \begin{bmatrix} \mathscr{L}\psi(||\underline{x} - \underline{x}_1||)(\underline{x}_1) \\ \vdots \\ \mathscr{L}\psi(||\underline{x} - \underline{x}_{N_{sten}}||)(\underline{x}_1) \end{bmatrix} \tag{15}$$

As mentioned in the introduction, several different forms of RBF $\psi(r)$ can be used (Table 1).

To improve the accuracy of the estimation, especially at the boundaries of the domain [36], the RBF can be supplemented with a polynomial of degree l: $\sum_{j=1}^{M} b_j p_j(\underline{x})$, where $p_j(\underline{x})_{j=1}^{M}$ is a basis of polynomials up to degree l in $\mathbb{R}^2$ and $M = \binom{l+2}{2}$. In this case, M additional constraints minimizing the far-field growth must be enforced to close the system:

$$\sum_{i=1}^{N_{sten}} \lambda_i p_j(\underline{x}_i - \underline{x}_1) = 0 \quad j = 1, 2, 3 \ldots, M. \tag{16}$$

Finally, the system to be solved to obtain the $\alpha_i^{\mathscr{L}}$ coefficients becomes:

$$\begin{bmatrix} \Gamma & P \\ P^T & 0 \end{bmatrix} \begin{bmatrix} \underline{\alpha} \\ \underline{\beta} \end{bmatrix} = \begin{bmatrix} \mathscr{L}\underline{\psi} \\ \mathscr{L}\underline{p} \end{bmatrix} \tag{17}$$

where Γ is the matrix of ψ in the left hand side of Eq. (15), P is a $M \times N_{sten}$ matrix formed by the p_j, $j = 1, \ldots, M$ basis of polynomials up to degree l in $\mathbb{R}^2$, and $\underline{\beta}$ and $\mathscr{L}\underline{p}$ are the $M \times 1$ vectors formed by β_i and $\mathscr{L}p_i(\underline{x}_1)$.

The application of the method depends on the non-singularity of the matrix $\begin{bmatrix} \Gamma & P \\ P^T & 0 \end{bmatrix}$. The matrix Γ is guaranteed non singular for IS-RBFs provided that the nodes are distinct. For PS-RBFs Γ is no longer guaranteed to be nonsingular, and a polynomial of degree l must be added to ensure that the system is uniquely solvable [66]. Barnett [3] showed that for PHS of the form r^m, the degree l of the added polynomial must satisfy $l \geq (m-1)/2$. The addition of a polynomial also requires the use of an unisolvent set of nodes [66].

3.3.2. Numerical implementation

The weights $\alpha_i^{\mathscr{L}}$ must be calculated at all nodes in the domain for each differential operator $\mathscr{L}$ required for the discretization of the PDEs. In the present model, first and second-order derivatives in the two horizontal dimensions are calculated. At each node $\underline{x}$ of the horizontal mesh, the following steps are carried out. First, the $N_{sten} - 1$ nearest neighbors of the selected node are identified. The size of the stencil and the degree of the augmented polynomial are defined at the beginning of the simulation and are constant for all nodes. Then, the linear system Eq. (17) is solved by completing a LU decomposition. The weights are computed once at the beginning of the simulation and are subsequently used to estimate all spatial derivatives in the model, including, but not limited to, the free surface elevation η, the free surface potential $\tilde{\Phi}$, the water depth h, and the a_n coefficients.

The implementation of the RBF-FD method is first tested to evaluate its accuracy in approximating spatial derivatives of a representative wave function (Section 4), and then it is applied for the simulation of wave tank experiments with variable bathymetries (Section 5).

4. Accuracy of the RBF-FD derivative estimates

4.1. Method

A series of tests were conducted to evaluate the capabilities and limitations of the RBF-FD method in estimating first and second-order spatial derivatives. These tests evaluate the impact of several parameters such as the RBF type, the value of the shape parameter C in the case of IS-RBFs, the degree of the added polynomial, and the stencil size N_{sten}. Previous work (e.g. Franke [39], Stead [58]) has tested different types of RBFs (Table 1) to evaluate the interpolation and derivate estimate accuracy. However, these functions were usually chosen arbitrarily, with more or less complex spatial variations. When simulating ocean wave propagation, the free surface generally has oscillatory variations, thus a sinusoidal function is chosen here as a basic representative model:

$$f(x, y) = A \cos\left(\frac{2\pi}{L}(x\cos\theta + y\sin\theta)\right), \tag{18}$$

where $L = 0.5$ m is the characteristic length of variation (or wavelength), A is the wave amplitude such that $A/L = 0.05$, and $\theta = 20°$ is the direction of wave propagation with respect to the x axis. The domain is defined as $0 \leq x \leq 1$ m and $0 \leq y \leq 1$ m and is discretized with a regular set of nodes with node spacing $\Delta x = \Delta y = 0.05$ m $(= L/100)$. First and second-order derivatives in both horizontal dimensions are estimated with the RBF-FD method and compared to the analytical values (denoted Lf_{theo} hereafter). The accuracy of the estimation is evaluated by calculating the normalized averaged error for all N nodes in the domain:

$$RMS\ Error = \sqrt{\frac{\sum_{i=1}^{N}(Lf(\underline{x}_i) - Lf_{theo}(\underline{x}_i))^2}{\sum_{i=1}^{N}(Lf_{theo}(\underline{x}_i))^2}} \tag{19}$$

Globally, errors are larger closer to the boundaries, and more particularly when the stencil is one-sided in the direction of the derivative (i.e. for $x = 0$ m and $x = +1$ m for x-derivatives, and $y = 0$ m and $y = +1$ m for y-derivatives). Two subsets of nodes are then defined, based on the asymmetry of the stencil: the interior nodes with a centered stencil (such as node A in Fig. 1) and the boundary nodes with asymmetric or one-sided stencils (such as nodes B and C in Fig. 1). In the following, the global averaged error Eq. (19) is shown except when the error behavior differs for the two node sets and is analyzed separately.

From the series of tests carried out to study the sensitivity of the method's accuracy to the chosen parameters, one initial question arises: "Which RBF is optimal?". The values of the other parameters will then depend on this choice. For IS-RBFs, which depend on a shape parameter, the accuracy of the method was evaluated as a function of the:

- IS-RBF function: MQ, IMQ, IQ and GA (see Table 1),
- variation of the shape parameter in the range $C \in [0, 30]$ m,
- inclusion of an added polynomial up to degree 2, and

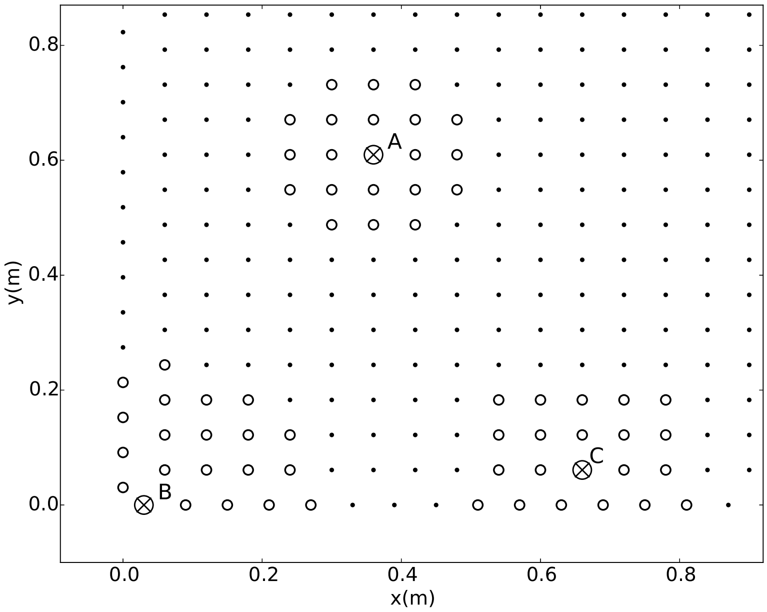

Fig. 1. Example of three stencils of $N_{sten} = 21$ nodes, for a node A in the interior of the domain (symmetric stencil), and nodes B and C on or close to the boundaries (asymmetric stencil).

- stencil size for $N_{sten} = 5, 13$ and 21, corresponding to the optimal thresholds defined by Bayona et al. [4] for regular node sets.

For PS-RBFs (not depending on a shape parameter), the accuracy of the method was evaluated as a function of the:

- PS-RBF function: one TPS function $\psi(r) = r^4 \log r$ to have at least the continuity of the second-order derivatives, and two PHS functions $\psi(r) = r^5$ and $\psi(r) = r^7$,
- inclusion of an added polynomial up to degree 5, (in the following, the shorthand form $r^5 + p3$ is used to denote the PHS r^5 with an added polynomial of degree 3), and
- stencil size in the range $N_{sten} \in [9, 56]$.

4.2. Results

4.2.1. Sensitivity to the shape parameter C

In Fig. 2, the global averaged error for the four IS-RBFs is plotted as a function of the shape parameter C for the first-order (f_x, f_y) and second-order (f_{xx}, f_{yy}) derivatives. For IS-RBFs, the derivative estimate accuracy depends strongly on C. The four RBFs display the same general behavior as a function of C: large errors for small values of C that decrease with an increase in C, and the development of oscillations when C exceeds an unknown threshold (depending on the RBF). These oscillations appear when the coefficient matrix (Eq. (17)) becomes ill-conditioned. The optimal value of C for which the error is minimum (denoted C_{opt}) depends on the RBF and derivative estimated, and is therefore not known a priori (as previously stated in Section 2). First and second-order derivatives in x reach a minimum for $C \approx 0.42$ m, whereas the matrix becomes ill-conditioned for the first and second-order derivatives in y before a minimum is observed. It can be inferred that the optimal value of C for derivatives in y is larger than for derivatives in x for this particular function and value of θ. The choice of the value of C is thus a compromise between optimizing the accuracy of the solution and reaching the limit of an ill-conditioned matrix. The accuracy of the estimation could be improved by allowing the shape parameter to vary with the RBF center (i.e. Kansa and Carlson [46], Kansa and Hon [47]), which produces larger variations in the matrix coefficients, thus reducing the condition number. Bayona et al. [6] developed an algorithm for the RBF-FD method to find the C_{opt} for each node, but it is an inefficient approach in the current model since it requires estimating the derivatives twice. Finally, C_{opt} depends on the function whose derivatives are estimated, suggesting that different coefficients would need to be calculated for each variable. In addition, some variables in the model (η, $\tilde{\Phi}$, ...) are time dependent, requiring the coefficients to be a function of time as well. To increase the accuracy, a simpler approach was tested by normalizing the stencil, or transforming the local support to a unit circle, following the work of Shu et al. [57]. This was expected to reduce the difference in accuracy between interior nodes (with centered stencils) and boundary nodes (with asymmetric stencils), allowing the use of larger values of C for nodes with asymmetric stencils. However, tests with normalized stencils did not improve significantly the RBF accuracy (results not shown here).

The errors for the three PS-RBFs do not depend on a shape parameter and are therefore constant as a function of C (Fig. 2). For PS-RBFs, the errors decrease when the degree of r increases, and $\psi(r) = r^7$ produces the smallest errors for

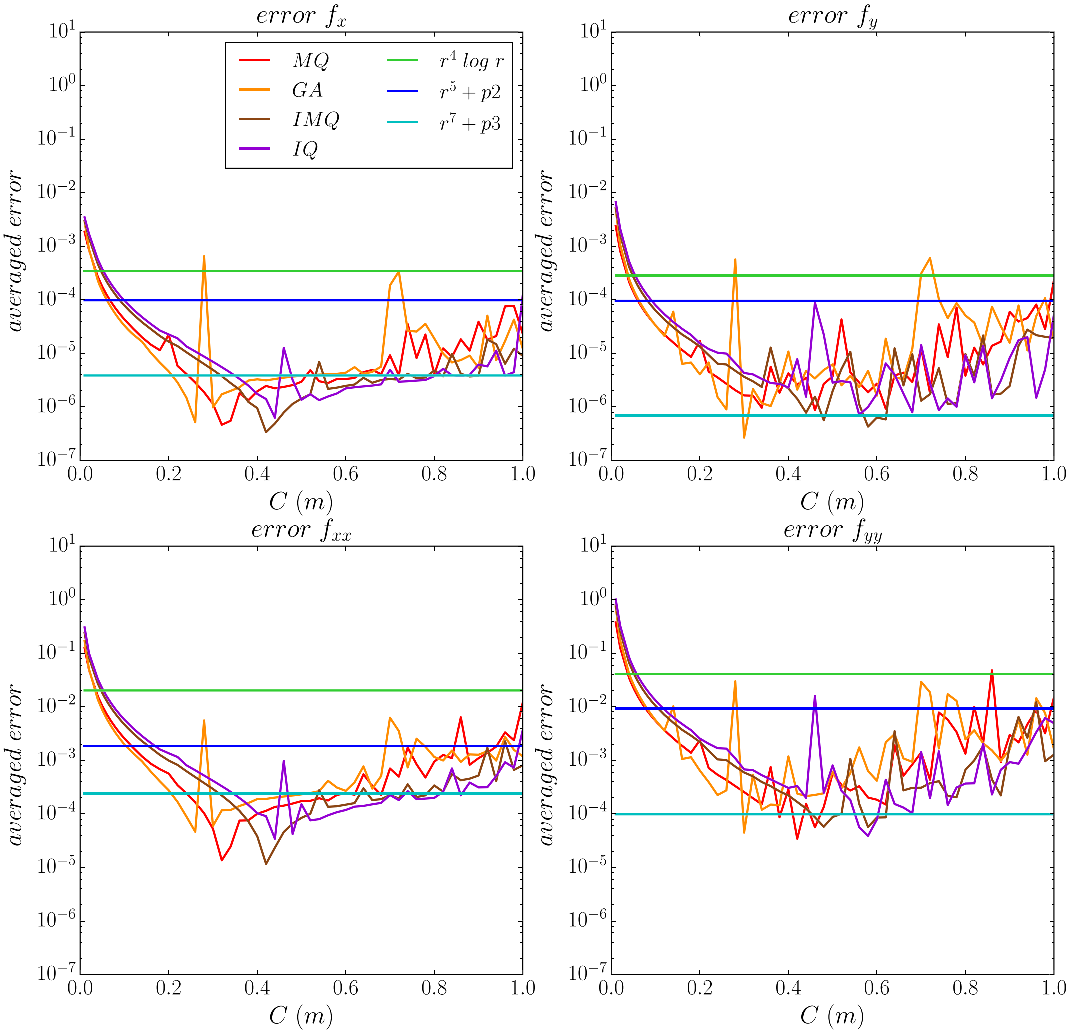

Fig. 2. Global errors of the four derivative estimates f_x, f_y, f_{xx}, and f_{yy} of the test function Eq. (18) for the four IS-RBFs and the three PS-RBFs as a function of the shape parameter C (with $N_{sten} = 21$ and an added polynomial of degree 0). (For interpretation of the colors in the figure(s), the reader is referred to the web version of this article.)

the four derivatives considered. Overall, PS-RBFs cause smaller errors than IS-RBFs for small values of C. The RBF $\psi(r) = r^7$ produces errors comparable to the minimum errors obtained with the IS-RBFs for f_y and f_{yy}, and slightly larger errors than what can be reached by the IS-RBFs near C_{opt}. Although the RBF $\psi(r) = r^7$ may not be the optimal choice for the presented derivatives, it offers the advantage of not relying on the choice of a shape parameter, whose selection is not a straightforward process, as previously mentioned. Finally, since the errors with PHS r^5 and r^7 are smaller than those with $r^4 log(r)$, only the PHS RBFs will be examined in the following tests.

4.2.2. Sensitivity to the stencil size and added polynomial degree

The dependence of the estimation accuracy on the stencil size (N_{sten}) and the degree of the added polynomial (l) demonstrates that the sensitivity is not the same for IS and PS-RBFs.

IS-RBFs. First, focusing on IS-RBFs, Fig. 3 shows the global error for the estimation of f_x as a function of C for three values of the stencil size, $N_{sten} = 5, 13$, and 21. The accuracy of the derivative estimates improves significantly by increasing the stencil size from 5 to 13 nodes, and even more by increasing to 21 nodes. However, C must be chosen carefully since the range of values of C producing a well-conditioned matrix is reduced. The matrix becomes ill-conditioned for smaller values of C when N_{sten} increases (e.g. $C \approx 0.8$ m for $N_{sten} = 13$, whereas $C \approx 0.5$ m for $N_{sten} = 21$). In addition, increasing N_{sten} increases the computational time (tests of regular wave propagation, not shown here, exhibited a computational time proportional to $N_{sten}^{1.36}$, using a fixed value of $NPXY$), so a compromise must be made between the desired accuracy, the difficulties in finding an optimal value of C, and the computational time.

The sensitivity of the error to the degree of the added polynomial is then studied by increasing l from 0 to 2 and comparing the results to those without an added polynomial. The boundary and interior nodes present different behavior as a function of l (Fig. 4). Despite the smaller number of boundary nodes (in comparison with interior nodes), the global error (calculated for all nodes, Fig. 4c) is dominated by the boundary errors, therefore presenting the same dependence on

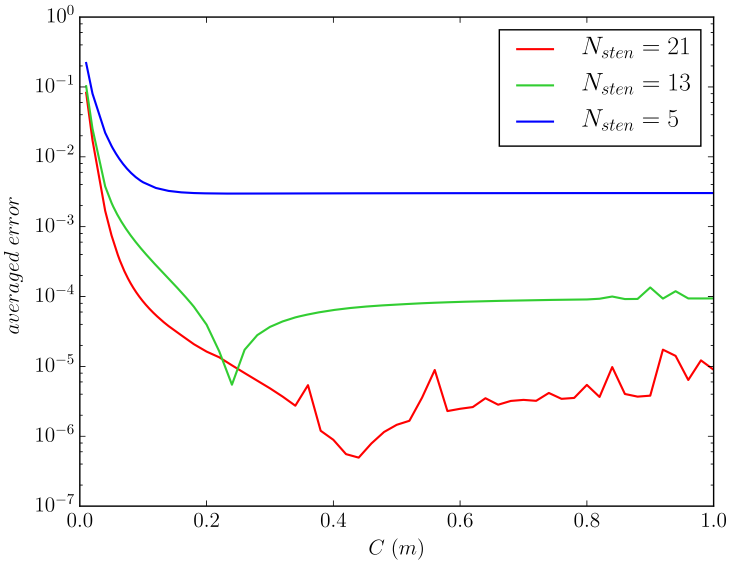

Fig. 3. Global error for the estimate of f_x for the IMQ RBF as a function of the shape parameter C (with an added polynomial of degree 0) for stencil sizes $N_{sten} = 5, 13$ and 21.

the shape parameter C. For interior nodes (Fig. 4a), adding higher degree polynomials decreases the error for $C < 0.18$ m, but this improvement is lost for higher values of C. For boundary nodes (Fig. 4b), the errors are reduced significantly with the addition of a polynomial and an increase in the degree of the polynomial for $C < 0.3$ m. Since RBFs are not exact approximations of polynomials, it is essential to add at least a constant to the RBF interpolant to be able to estimate accurately the derivative of a constant function.

For IS-RBFs, increasing the stencil size improves the accuracy but causes the matrix to become ill-conditioned for smaller values of C. The addition of high-order polynomials is only beneficial for small values of C, especially for the boundary nodes, in agreement with [36].

PS-RBFs. The addition of a high-order polynomial is essential to guarantee the inversibility of the collocation matrix for PHS RBFs. A minimum polynomial degree l is required, which depends on the degree of the PHS function. In addition, the maximum degree of the added polynomial is limited by the size of the stencil. To ensure that the problem is well-posed, N_{sten} must be larger than the number of independent monomials constituting the basis of polynomials of the same degree as the added polynomial (i.e. [3]). Given these constraints, a series of tests were conducted to study the sensitivity of the error estimation of the PHS r^5 and r^7 to the stencil size ($N_{sten} \in [9, 56]$) and to the degree of the added polynomial ($l \in [2, 5]$).

With regular node sets, the condition on the minimum stencil size for a given degree of added polynomial is not sufficient to ensure the non-singularity of the matrix. The regularity of the node set does not allow the matrix to be unisolvent for the polynomial basis [66]. The stencil size thus has to be increased to recover the inversibility of the matrix [3]. With an irregular node set, this may not occur.

The results obtained with both PHS (r^5 and r^7) are compared in Fig. 5 for the first derivative in x. Similar behavior is observed for the two PHS, but PHS r^7 produces smaller errors for a given degree of the added polynomial. The interior node and boundary node errors vary differently as a function of N_{sten} but in both cases, the errors decrease with an increase in the degree of the added polynomial. For an added polynomial with an even degree, the error for the interior nodes is weakly dependent on the stencil size N_{sten}, whereas for an added polynomial with an odd degree, a minimum is obtained for any stencil size with a symmetric distribution of nodes. This effect is caused by the regular distribution of the nodes and may not be observed with irregularly spaced nodes (for example, for boundary nodes with asymmetric stencils). The same trends are observed for the estimation of second-order derivatives, but for the inverse of odd and even added polynomials (not shown here). Contrary to the PHS r^7, the PHS r^5 has the advantage of being used with only a second degree added polynomial, thus requiring a smaller N_{sten} and allowing a reduction in the computational time.

4.2.3. Convergence study as a function of the grid spacing

For IS-RBFs (e.g. IMQ, Fig. 6) the optimal C is generally insensitive to the node spacing (here $C_{opt} \simeq 0.4$ m). As the node spacing decreases, the errors decrease until a certain limit below which the matrix becomes ill-conditioned. Thus C is generally decreased with the node spacing to keep the condition number of the collocation matrix roughly constant, at about 10^{15} according to Flyer et al. [29]. This causes error saturation and the loss of convergence, which can be restored by adding polynomials.

For PHS RBFs, there are no saturation errors, and the convergence rate depends on the degree of the added polynomial l ($\propto \Delta x^{l-k+1}$), where k is the order of the estimated derivative [29]. When the degree of the PHS RBF increases (from r^5 to r^7),

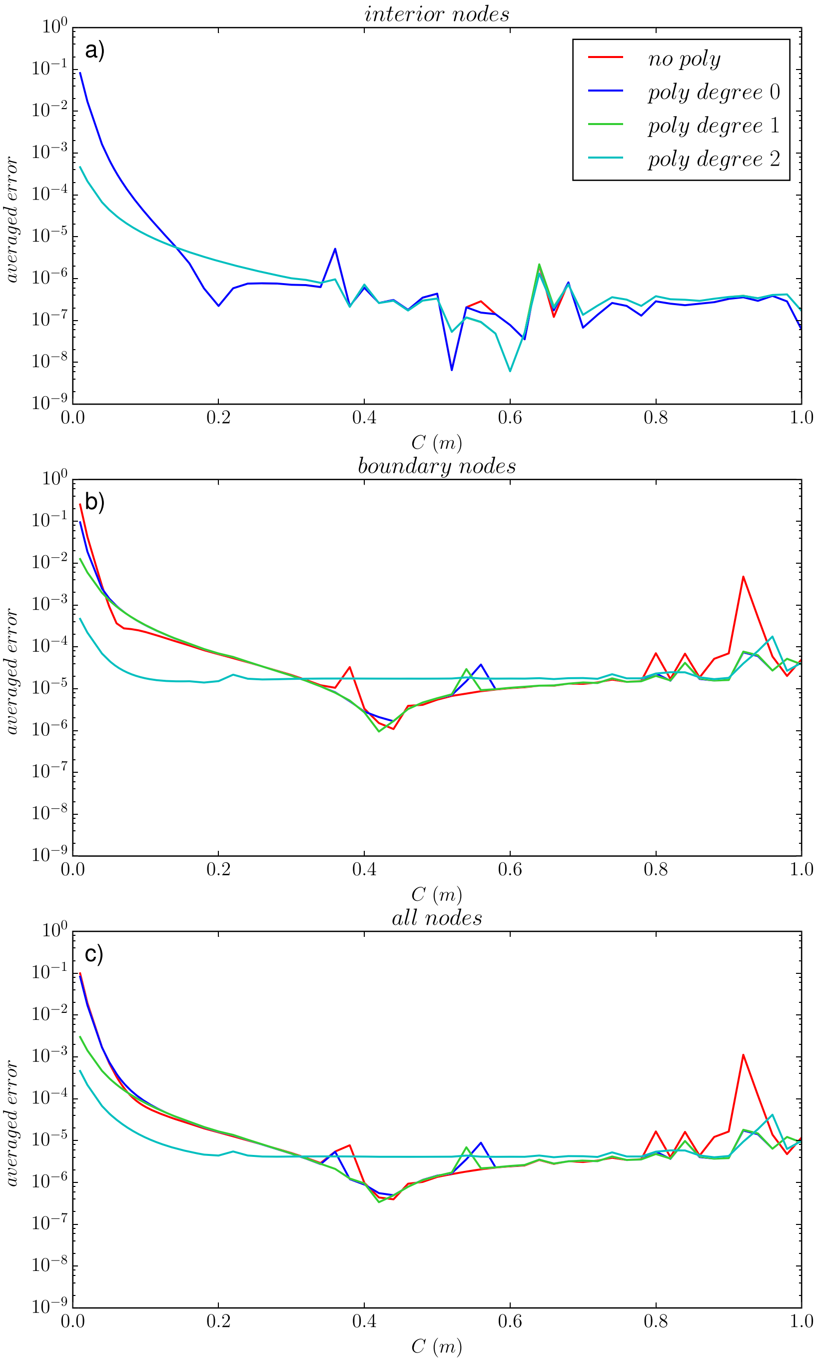

Fig. 4. Errors for the estimate of f_x, for the IMQ RBF as a function of the shape parameter C (with $N_{sten} = 21$) for added polynomials of degree 0 to 2: (a) interior nodes, (b): boundary nodes, and (c) all nodes.

the errors decrease slightly only for low order added polynomials (i.e. $l = 3$ and 4). The convergence rate is independent of the stencil size N_{sten} (Fig. 7).

These results, concerning error estimation as a function of node refinement for IS-RBFs and PS-RBFs (PHS), are in agreement with the studies of Bayona et al. [4] and Flyer et al. [29].

4.2.4. Summary of the derivative estimate tests

Finally, based on a literature review and a series of tests including, but not limited to those shown here, the use of the PHS r^7 with an added polynomial of degree 3 and $N_{sten} = 21$, appears to be a good compromise for applications similar to those presented here. For general applications, determining the optimal shape parameter may be challenging (where the derivatives of all variables are estimated with the same coefficients). It is more practical and efficient to use a RBF that does not depend on a shape parameter since C_{opt} depends strongly on the estimated derivative and the function itself. The PHS r^7 is preferred to the PHS r^5 because, for the same degree of added polynomial, the PHS r^7 tends to produce smaller errors. These choices are recommended to minimize the expected errors and stencil size (i.e. computational time)

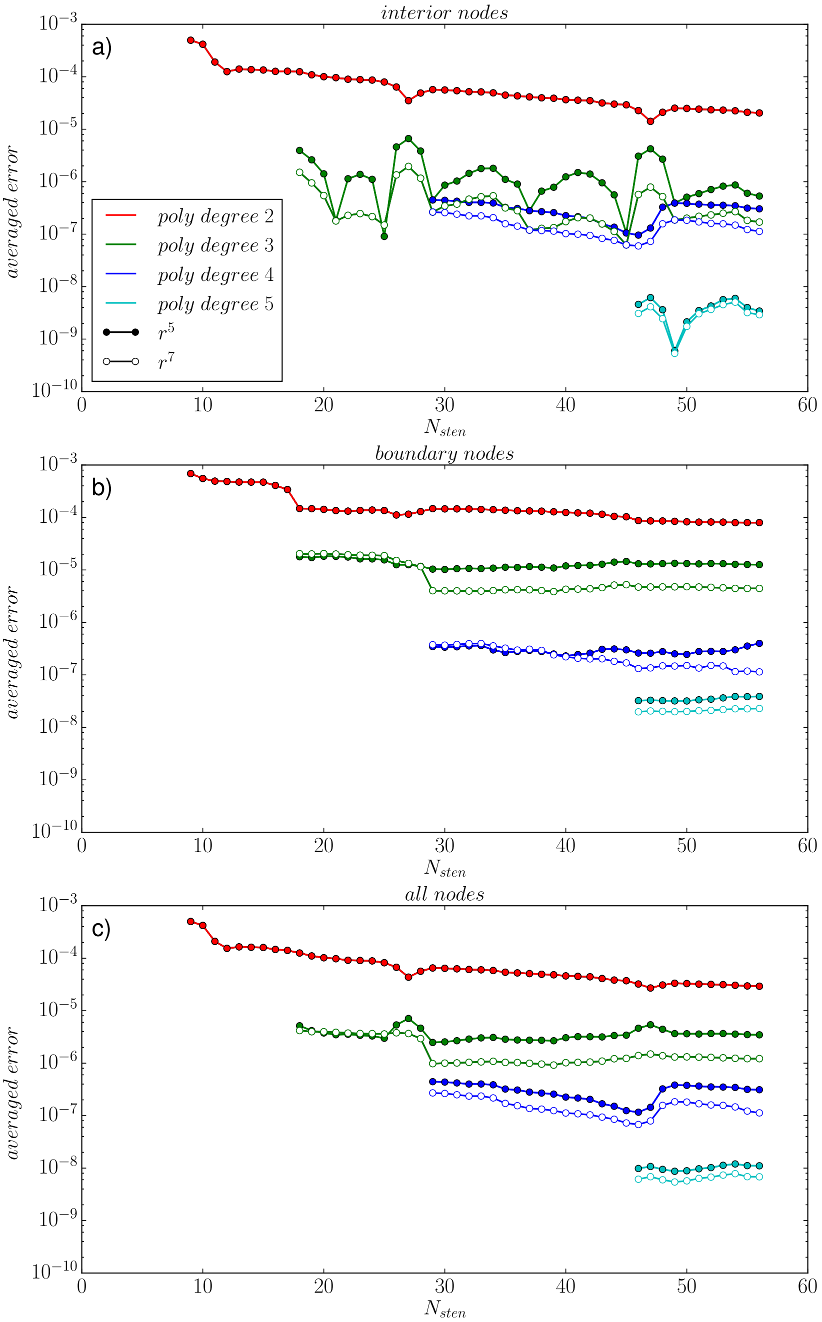

Fig. 5. Errors for the estimate of f_x for PHS r^5 and r^7 as a function of the stencil size N_{sten} and the degree of the added polynomial (shown in the legend) for: (a) interior nodes, (b) boundary nodes, and (c) all nodes.

for the estimation of first and second-order derivatives, and will be used in the subsequent test case simulations. This recommendation is derived from a sensitivity study testing a single function. Although there is no formal proof that these results can be extended to a wide range of functions, the chosen sinusoidal function is assumed representative of the type of functions encountered in real applications, suggesting the generalization of the conclusions concerning the efficiency and accuracy of this method for wave propagation simulation models.

5. Validation test cases

The 3D version of the model is validated by comparing simulation results to measurements from two laboratory experiments studying the convergence of regular and irregular waves propagating over two different bathymetric profiles: a semi-circular step based on the experiments of Whalin [64], and a submerged shoal based on the experiments of Vincent and Briggs [62].

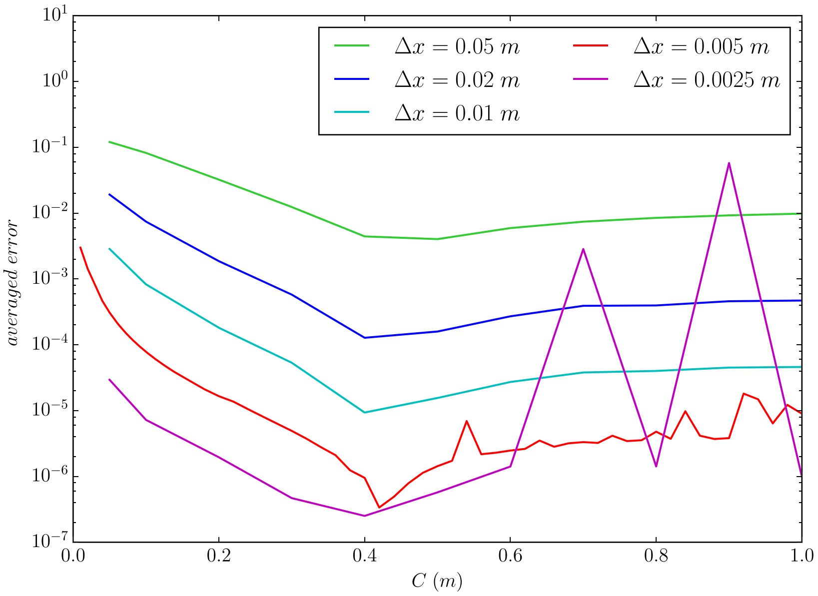

Fig. 6. Errors for the estimate of f_x for IMQ with $N_{sten} = 21$ and an added polynomial of degree one as a function of the shape parameter C for five different grid spacings (see legend).

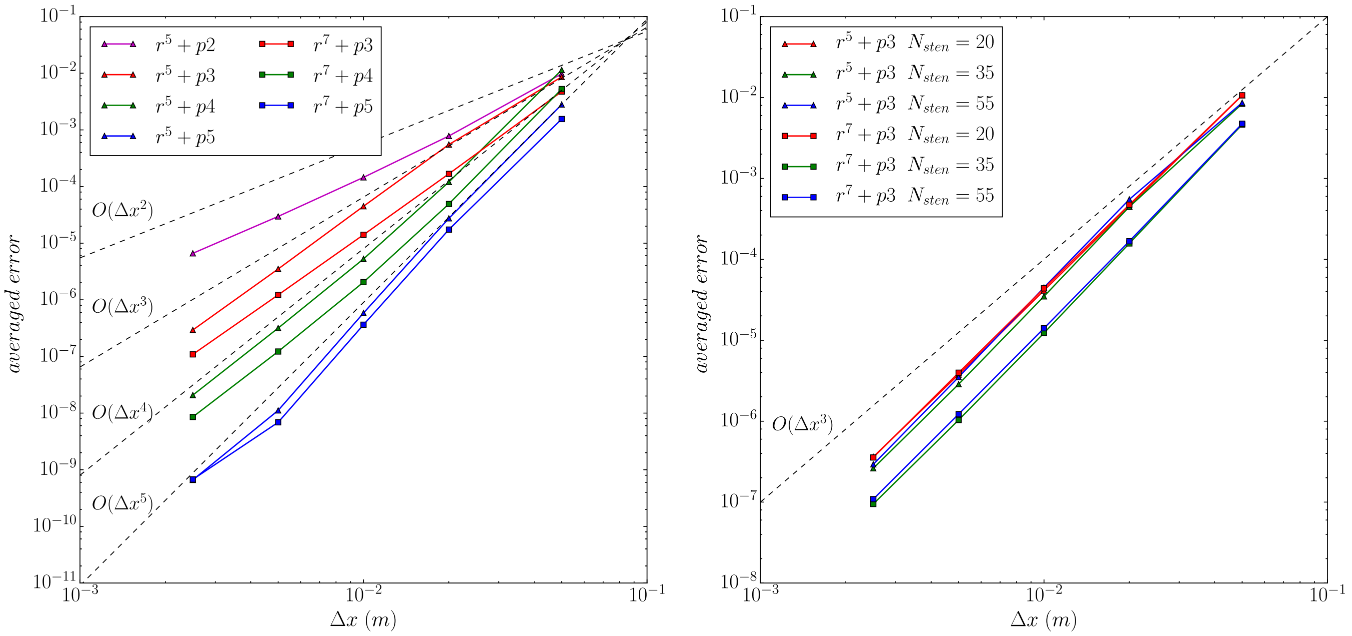

Fig. 7. Errors for the estimate of f_x for PHS r^5 and r^7 as a function of the grid spacing (same as in Fig. 6) for (left) different degrees of the added polynomial l, and (right) several stencil sizes N_{sten}.

5.1. Nonlinear wave propagation over a semi-circular step

Whalin [64] performed a series of experiments of regular waves propagating over a semi-circular bottom topography that acts as a focusing lens. These experiments were conducted to test the limit of linear and nondiffractive theory in a convergence zone, considering non-breaking waves with periods of 1, 2, and 3 s, for three wave heights. The bottom topography was designed to produce strong wave convergence along the centerline of the basin and to minimize sidewall effects and dissipation by bottom friction. The wave tank was 6.096 m wide and 25.603 m long. In the experiments, regular waves were generated with a piston wave maker and propagated from an initial water depth of $h_0 = 0.4572$ m to a shallower region of depth $h_1 = 0.1524$ m. The bathymetric profile (Fig. 8) is defined analytically by:

$$h(x, y) = \begin{cases} h_0, & -20.0 \le x \le 10.67 - G(y) \\ h_0 + \frac{1}{25}(10.67 - G(y) - x), & 10.67 - G(y) < x < 18.29 - G(y) \\ h_1, & 18.29 - G(y) \le x \le 35 \end{cases} \tag{20}$$

with $G(y) = \sqrt{y(6.096 - y)}$, ($h$, x and y in m).

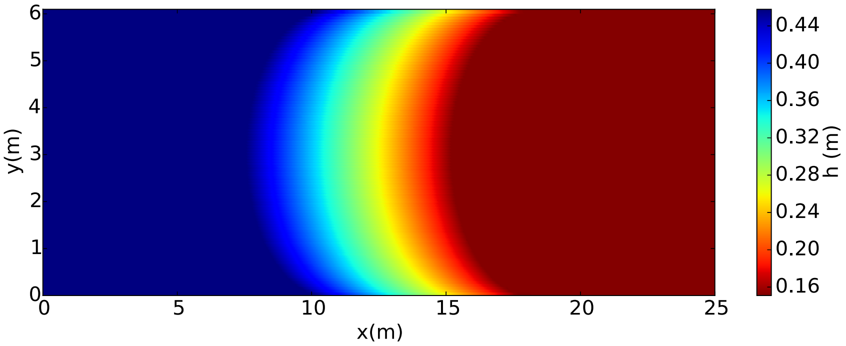

Fig. 8. Bathymetry of the experiments of Whalin [64].

Table 2
Wave characteristics for the four simulations of the experiments of Whalin [64], where the 0 subscript denotes deep water conditions.

Wave condition	T (s)	A (m)	L_0 (m)	k_0h_0	k_0A
A	2	0.0075	3.91	0.7347	0.01205
B	2	0.0108	3.91	0.7347	0.01736
C	3	0.0068	6.14	0.4663	0.006936
D	1	0.0195	1.50	1.9157	0.08171

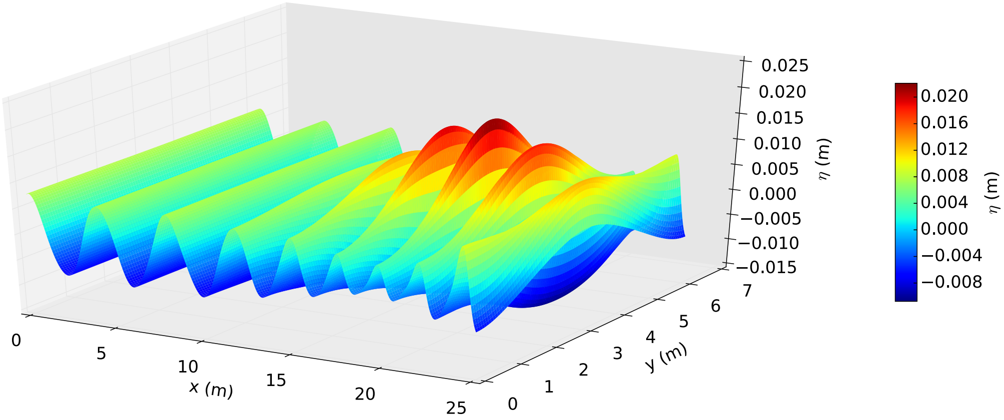

Fig. 9. 3D view of the free surface elevation at the end of the simulation ($t = 18T$), obtained with PHS $r^7 + p3$ and $N_{sten} = 21$ for wave condition A ($T = 2$ s, $A = 0.0075$ m and $L_0 = 3.91$ m) of the experiments of Whalin [64].

Four sets of wave conditions were simulated (see Table 2). For wave condition A, the computational domain extends from −3.91 m to 32.5 m in the x-direction and from 0 to 6.096 m in the y-direction. The computational domain is longer than the physical domain in the x-direction to include a one-wavelength long relaxation zone at the left boundary for wave generation and for the absorption of waves reflected from the underwater topography. A three-wavelength long relaxation zone is added at the right boundary for wave absorption. Impermeable conditions are applied at the lateral boundaries.

The domain is discretized with $NPXY = 137{,}712$ scattered nodes with regular node spacing ($\Delta x \approx \Delta y \approx 0.04$ m, or approximately $L/98$). Waves are propagated during 36 s (18 periods), with a constant time step $\Delta t = 0.0178$ s ($\approx T/112$) and $N_T = 7$.

The free surface profile at the end of the simulation (Fig. 9) shows a quasi-2D behavior with almost no variations in the y-direction in the deeper part of the domain ($x < 7.5$ m). The 3D wave patterns develop in the shallower zone where nonlinear effects are important. The convergence of wave energy is caused by a combination of shoaling, diffraction, and refraction over the convergent bathymetric profile.

The simulated crest and trough elevation envelopes along the centerline of the tank ($y = 3.048$ m) show that before the foot of the slope, the crest and trough are nearly symmetric with respect to the still water level (Fig. 10). In the shallower zone ($x > 15$ m), the waves are narrower and their amplitudes increase, with deeper troughs and higher crests, breaking the horizontal symmetry observed in the deeper part of the domain. The vertical asymmetry of the waves also increases around $x = 10$ m, displaying a steeper wave front. At the maximum of the crest envelope ($x \approx 20$ m), the wave has two small lobes on each side, a consequence of the increase of the second harmonic amplitude caused by nonlinear effects on the slope.

To examine more closely nonlinear effects and energy transfers between harmonics, a Fourier analysis of the simulated wave signal was completed along the centerline of the wave tank (Fig. 11). The model accurately reproduces the spatial evolution of the amplitudes of the first three harmonics (frequencies f, $2f$ and $3f$) in comparison to the measurements. The amplitude of the second harmonic is slightly underestimated in the deeper part of the domain (for $x \leq 12$ m), which

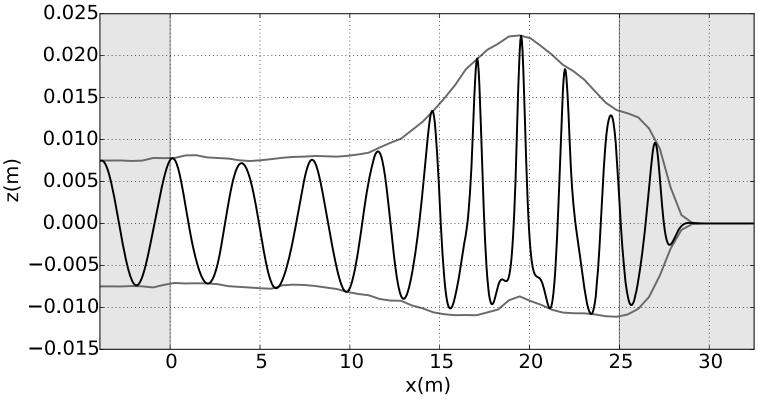

Fig. 10. Free surface elevation profile along the centerline of the tank at the end of the simulation $t = 18T$ (black line), for wave condition A ($T = 2$ s, $A = 0.0075$ m and $L_0 = 3.91$ m) of the experiements of Whalin [64]. The wave envelope indicates the maximum and minimum free surface elevation during the simulation (gray lines). The light gray shaded areas ($x < 0$ m and $x > 25$ m) indicate the relaxation zones for wave generation and absorption in the numerical model.

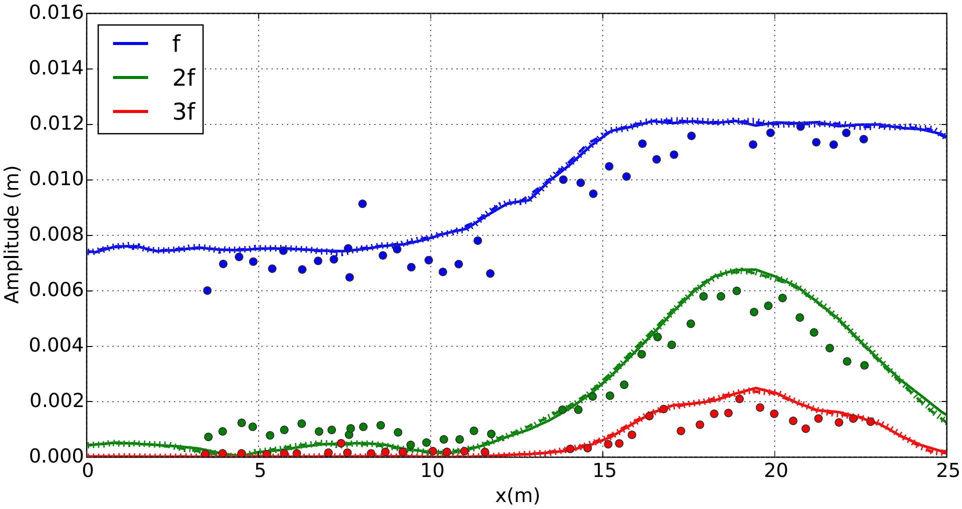

Fig. 11. Comparison of measured (circles) and simulated spatial evolution of the amplitude of first three harmonics with a regular (solid lines), and two irregular (dashed and dotted lines) node distributions (at frequencies f, $2f$, and $3f$) of the free surface elevation for wave condition A ($T = 2$ s, $A = 0.0075$ m and $L_0 = 3.91$ m) of the experiments of Whalin [64].

may be related to the linear method used to generate waves in the model. Conversely, in the shallower zone, the second harmonic amplitude is slightly overestimated. As mentioned previously, in the convergence region (around $x = 20$ m), the second and third harmonic amplitudes increase due to energy transfers from the first harmonic, and the second harmonic amplitude becomes nearly half of the first harmonic amplitude. Despite the energy transfers to higher order harmonics, the amplitude of the first harmonic does not decrease as one would expect in the case of an alongshore uniform bathymetric profile. According to Whalin [64], along the centerline of the tank, the rate of decrease in amplitude due to nonlinear transfers to higher harmonics is compensated by the rate of increase in amplitude due to refraction and shoaling.

To test the sensitivity and flexibility of the model to the computational domain node distribution, the simulation was also run using two irregular node sets, one with a homogeneous node spacing (≈ 0.06 m) and the second with node spacing varying with the water depth (between ≈ 0.06 m in the shallower part and ≈ 0.1 m in the deeper part). The first irregular node distribution was created with the 3D finite element generator Gmsh (gmsh.info) distributed under GNU GPL. A zoom of a small part of the domain is shown (Fig. 12) for the irregular (left) and regular (right) node sets. The irregular node set distribution is not quasi-uniform, however there were no instability problems. For the second irregular node distribution, another node generator [32] enabling easy refinement with the bathymetry and maintaining high regularity at local level was used. A repel algorithm, based on Bayona et al. [7], was also applied after the addition of nodes close to the boundary, in the deeper part, to ensure simulation stability. The resulting harmonic amplitudes are almost superimposed with those obtained with the regular node set for both irregular node sets (Fig. 11).

The sensitivity to the spatial resolution was studied by running seven simulations with regular node spacing ($\Delta x = 0.04$, 0.06, 0.075, 0.09, 0.16, 0.24, 0.32 m). The resulting harmonic amplitudes are nearly indistinguishable for $\Delta x \leq 0.16$ m (Fig. 13) with normalized root mean square errors less that 1.5%, 4% and 7% for the first three harmonics, respectively. For $\Delta x > 0.16$ m, larger differences appear for all three harmonics, in particular in the shallow water region over the step ($x > 15$ m). For simulations with $\Delta x \geq 0.09$ m, instabilities sometimes appeared at the boundaries. Therefore, in these

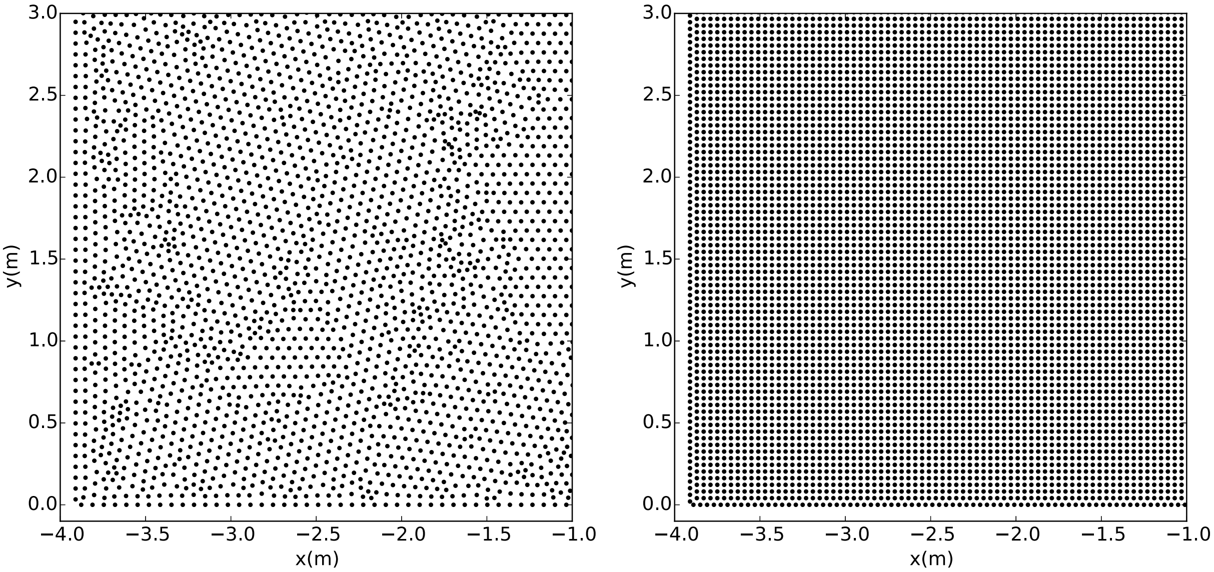

Fig. 12. Zooms of the bottom left corner of the domain for (left) irregular (≈ 0.06 m) and (right) regular (≈ 0.04 m) node distributions used to discretize the computational domain of the experiments of Whalin [64].

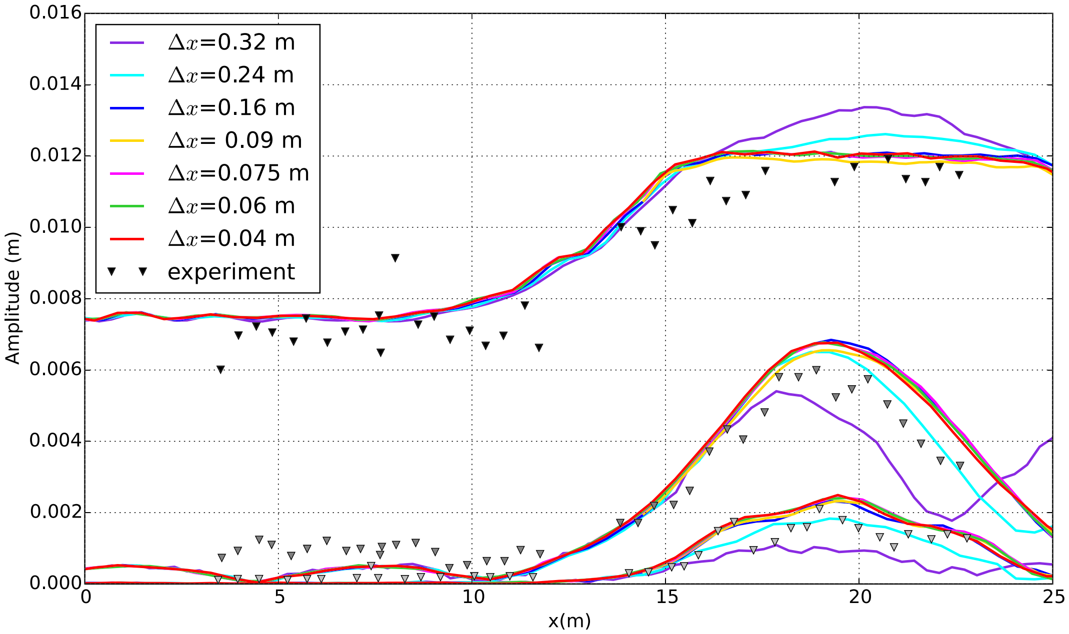

Fig. 13. Comparison of measured (triangles) and simulated (lines) spatial evolution of the amplitude of first three harmonics of the free surface elevation (at frequencies f, $2f$, and $3f$) for regular node distributions with different spatial resolution ($\Delta x = 0.04, 0.06, 0.075, 0.09, 0.16, 0.24, 0.32$ m) for wave condition A ($T = 2$ s, $A = 0.0075$ m and $L_0 = 3.91$ m) of the experiments of Whalin [64].

simulations, the internodal distance was decreased near the boundary to ensure stability. To evaluate the computational efficiency as a function of the number of nodes discretizing the computational domain ($NPXY$), the computation time of one iteration is shown for each simulation (Fig. 14). The CPU time is proportional to $NPXY^{1.76}$. This is lower than the cost of the traditional exact sparse factorization ($NPXY^2$), which may be due to the use of a multifrontal factorization method in the MUMPS solver. This demonstrates the advantages of minimizing $NPXY$ (Fig. 13) while maintaining satisfactory results.

The simulated spatial evolution of the first three harmonics along the centerline of the tank are compared to the experimental data for the other three wave conditions (Table 2, Fig. 15). For wave condition B (Fig. 15a), corresponding to the same wave period as case A but with a larger wave amplitude, nonlinear effects are more important, and the second harmonic amplitude is almost two-thirds of the maximum of the first harmonic amplitude. The amplitude of the first harmonic also decreases slightly around $x = 20$ m, suggesting that the nonlinear energy transfers to higher frequencies occur at a faster rate than the energy convergence from refraction [64]. The results of the simulation of wave condition D (Fig. 15c), which is less nonlinear but has more important dispersive effects, are in close agreement with the experiments. The last test, wave condition C (Fig. 15b), corresponds to nearly shallow water conditions. The simulation overestimates the first harmonic amplitude, but underestimates the second and third harmonic amplitudes. This behavior has been observed in

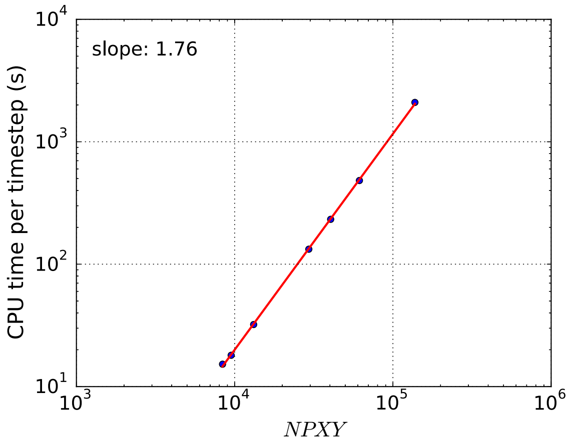

Fig. 14. CPU time per timestep as a function of the number of nodes discretizing the domain for wave condition A ($T = 2$ s, $A = 0.0075$ m and $L_0 = 3.91$ m) of the experiments of Whalin [64].

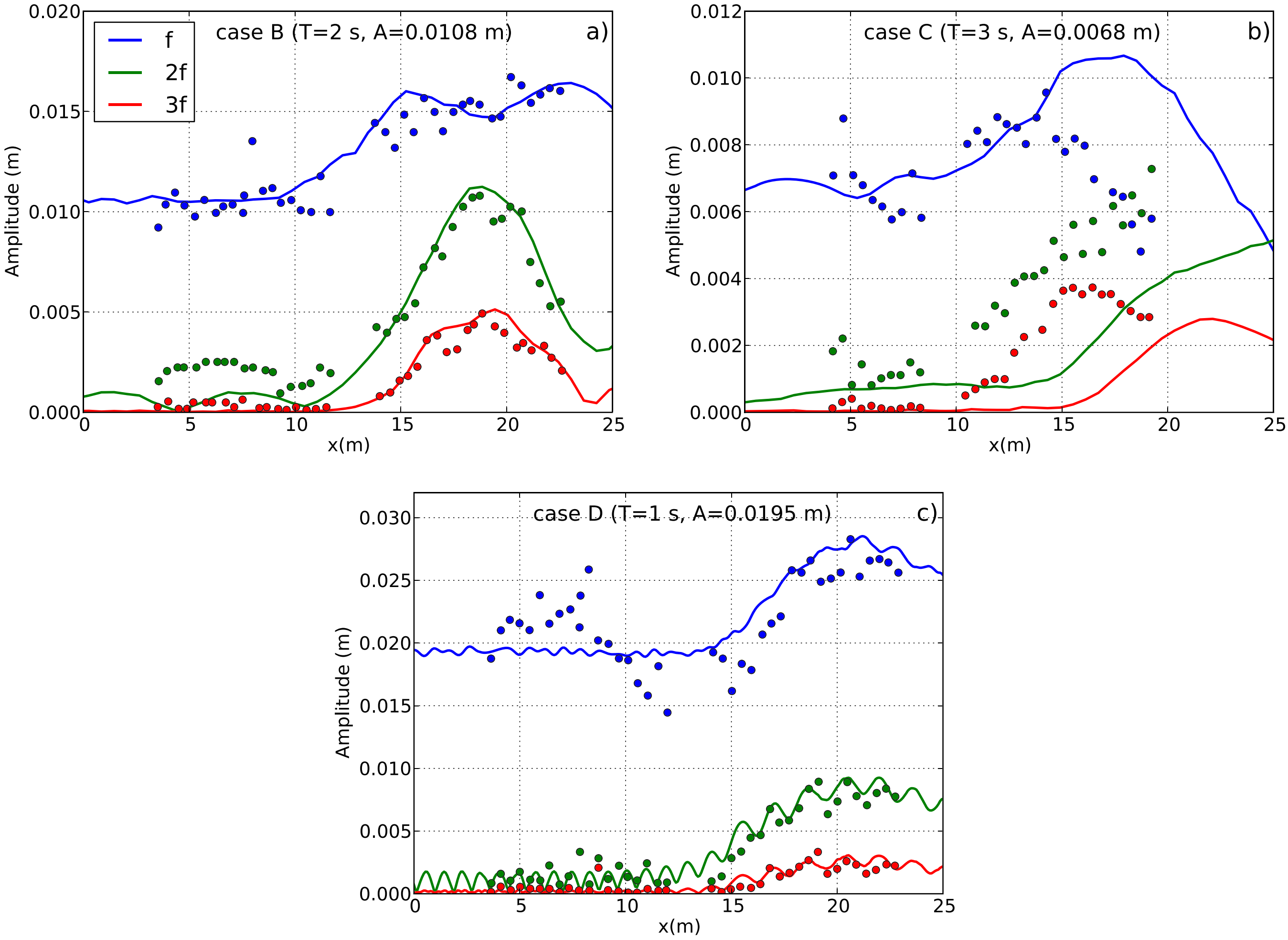

Fig. 15. Comparison of the observed (circles) and simulated (solid lines) spatial evolution of the amplitude of first three harmonics (at frequencies f, $2f$, and $3f$) of the free surface elevation for wave conditions B, C and D (see Table 2) of the experiments of Whalin [64].

previous studies using a variety of different numerical models (Madsen and Sørensen [51], Beji and Nadaoka [9], Engsig-Karup et al. [24], Wu et al. [69], Kazolea et al. [49], Filippini [28]). Kazolea et al. [49] suggested that the differences may be caused by the propagation of free reflected waves in the tank and the increased complexity of the case due to the shorter evolution distance and the combination of refraction-diffraction and nonlinearities. For case C, the model's sensitivity to the initial wave amplitude or the position and length of the absorption relaxation zone was not able to explain the differences between the experimental data and the numerical results.

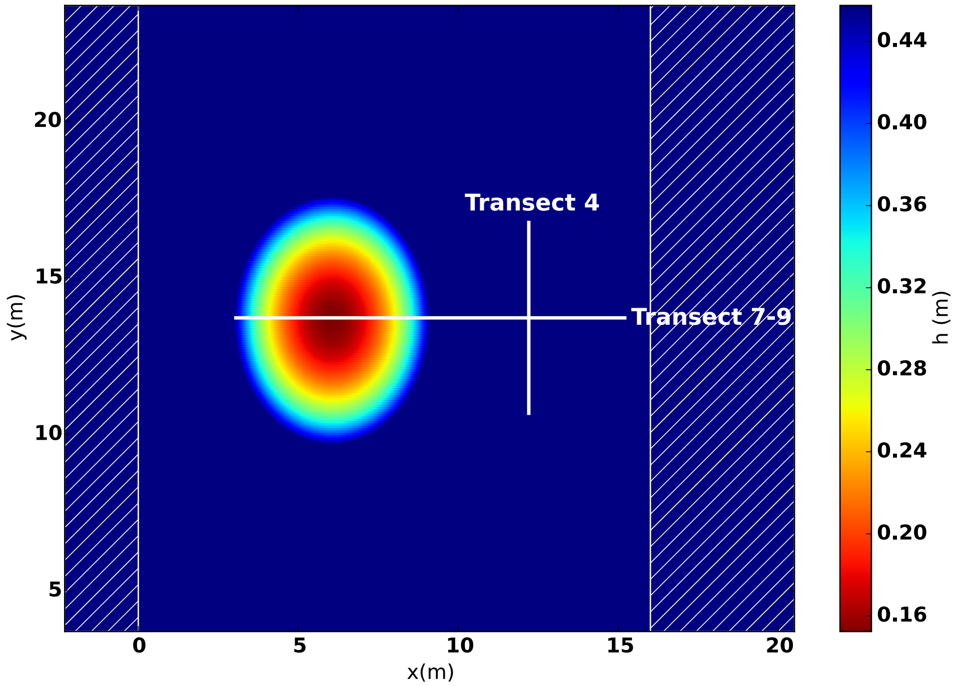

Fig. 16. The numerical domain and bathymetry of the experiments of Vincent and Briggs [62], with horizontal and vertical white lines indicating the transects along which the simulation results and experimental measurements are compared. Hatched zones indicate the wave generation (left) and absorption (right) zones used in the numerical model.

5.2. Wave refraction and diffraction over an elliptical shoal

The last test case simulates the propagation of regular and irregular waves over a submerged elliptical mound, reproducing the experiments of Vincent and Briggs [62]. The aim of the experiments was to investigate the limits of approximating irregular wave conditions with monochromatic waves, and they produced a large experimental data set of both monochromatic waves and irregular waves with narrow or broad frequency and directional spreading. Two cases are considered here: first the regular wave case $M1$, with $T = 1.3$ s, $L = 2.3$ m, and $A = 0.0275$ m, and then the irregular wave case $U3$, generated with a JONSWAP spectrum with $H_s = 0.0254$ m, $T_p = 1.3$ s, and a peak enhancement factor $\gamma = 2$.

The experiments were conducted in a directional wave basin that was 35 m wide and 29 m long. The measurement area was restricted to a 6.10 m wide by 15.24 m long zone around the elliptical shoal, which had a major axis of 3.96 m and a minor axis of 3.05 m, with the center at $(x_0, y_0) = (6.10 \text{ m}, 13.72 \text{ m})$. The shoal boundary (Fig. 16) is defined by:

$$S(x, y) = \left(\frac{x - x_0}{3.05}\right)^2 + \left(\frac{y - y_0}{3.96}\right)^2 = 1. \tag{21}$$

The water depth around the shoal is constant $h(x, y) = 0.4572$ m (i.e. for $S(x, y) > 1$), and the water depth over the shoal is:

$$h(x, y) = 0.9144 - 0.7620\sqrt{1 - \left(\frac{x - x_0}{3.81}\right)^2 - \left(\frac{y - y_0}{4.95}\right)^2}. \tag{22}$$

The minimum water depth above the center of the shoal is therefore $h_{min} = 0.1524$ m. In the experiments, waves were generated with a directional wave generator, located at $x = 0$ m. The free surface elevation was measured using an array of nine parallel resistive probes placed along nine different transects (five parallel and four perpendicular to the wave maker) during nine different experimental runs. In the following, two transects will be studied (Fig. 16): the transversal transect 4 ($x = 12.2$ m) and the longitudinal transect along the centerline of the tank, consisting of transects 7 and 9 ($y = 13.72$ m).

To limit the computational time, the simulated domain is smaller than the experimental wave basin. The numerical domain extends from $-2.3 \text{ m} \leq x \leq 20.5$ m and $3.7 \text{ m} \leq y \leq 23.7$ m. Two relaxation zones are added (hatched zones in Fig. 16): a one-wavelength long wave generation zone at the left side of the domain, and a two-wavelength long absorption zone at the right side of the domain. Impermeable conditions are applied at the lateral boundaries. The domain is discretized with regularly spaced nodes with $\Delta x = \Delta y = 0.075$ m, for a total of $NPXY = 81{,}435$ nodes.

For the regular wave case $M1$, waves were generated with an amplitude of $A = 0.02325$ m, using linear wave theory. This value is slightly smaller than the one prescribed to the wave maker in the experiments, but an adjustment of the incident wave amplitude was necessary to obtain a comparable average wave height ($H = 0.0445$ m) at a reference probe

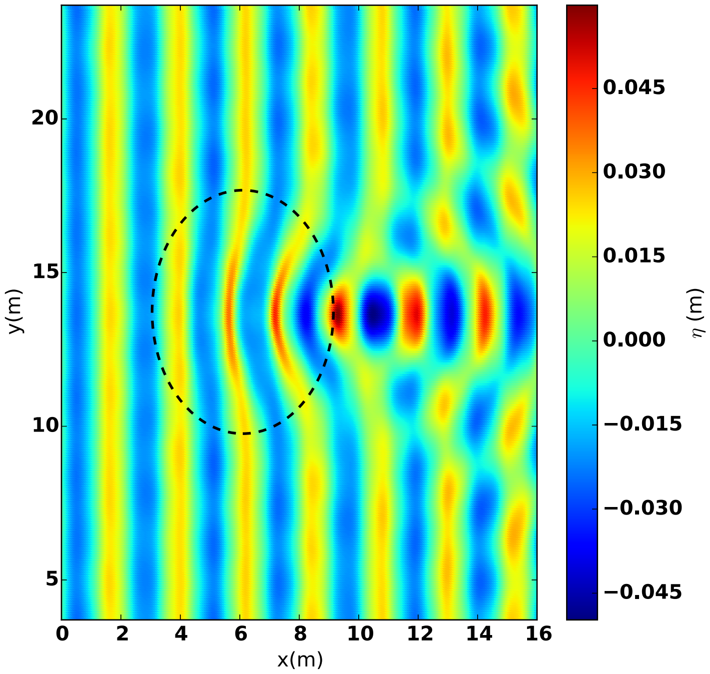

Fig. 17. Contour plot of the free surface elevation at the end of the simulation ($t \approx 78T$) for case $M1$ of Vincent and Briggs [62]. The dotted line indicates the limit of the elliptical shoal on the basin's floor.

located in an unperturbed zone of the domain upstream of the shoal ($x = 3.05$ m, $y = 21.34$ m). Waves are propagated during approximately 100 s ($\approx 78T$), with a constant time step $\Delta t = 0.036$ s ($\approx T/36$), using $N_T = 5$.

The contour plot of the free surface elevation at the end of the simulation, when the periodic steady state is reached, shows the wave pattern that developed around the shoal (Fig. 17). The wave height increases behind the shoal ($x > 6$ m), with complex 2D patterns with strong variations extending in both horizontal directions. The convergence zone along the centerline of the tank is surrounded by rectilinear zones of almost zero amplitude, looking like a wake. In addition, the crests and troughs in the y-direction are modulated with a characteristic length scale of approximately 3 m due to reflections from the lateral walls. The use of a computational domain smaller than the experimental one increases the importance of lateral reflections and possibly overestimates this effect.

To compare the simulation results to the experimental data, a zero up-crossing analysis of the free surface elevation time series is completed to compute the average wave height (H_m) along each transect. To conduct the analysis in the same way as for the experiments, a 28-period window of the free surface elevation time series is considered (once steady state is reached, from $t = 60$ to 96.4 s). Wave height profiles along the perpendicular transects show good agreement with the experimental data (transect 4, Fig. 18a). The wave height profile presents a maximum at the center, corresponding to the center of the shoal ($y = 13.72$ m), which is more than twice the incident wave height (ratio ≈ 2.03), but is slightly underestimated in the simulations. Moving symmetrically away from the center, two minima are reached, with wave heights less than half the incident wave height (ratios ≈ 0.21 and 0.43, respectively). Farther from the shoal, the wave height is nearly equal to the incident wave height. The simulated wave height profile in the wave propagation direction also agrees well with the experimental measurements (transect 7–9, Fig. 18b), with differences slightly larger than those observed along transect 4. In particular, the increase in the wave height between $x = 4$–6 m, and the small local peak around $x = 7.5$ m are not reproduced by the numerical model. After the shoal ($x = 9$ m), the simulated wave height profile shows small oscillations that may be caused by reflections from the relaxation zone that is not perfectly absorbing.

The experimental measurements vary between different runs. At a data measurement point ($x = 12.2$ m, $y = 13.72$ m) in two transects, the observed wave height is 0.0975 m and 0.104 m during 2 different runs (along transect 4 and transect 7–9, respectively), which is a difference of approximately 6.25%. Although the variability in the measurements at this location cannot be extended directly to the other measurement points, it can be used to estimate the order of magnitude of the experimental errors and variability.

A harmonic analysis was also performed on the simulated free surface time series along transect 7–9 to show the evolution of the first three harmonic amplitudes (Fig. 19). Before the shoal ($x < 4$ m), the waves are only weakly nonlinear, and the second and third harmonic amplitudes increase over the shoal. Over the shoal ($x = 6.10$ m), the second harmonic amplitude is more than half first harmonic amplitude. This effect is likely caused by wave convergence and the narrowing of the crest over the shoal (Fig. 17). After the shoal, the amplitude of the first harmonic more than doubles due to wave energy convergence induced by refraction. Nonlinearities are not significant after the shoal, although a modulation of the amplitude of the second harmonic is clearly observed. Comparison of the simulated and experimental harmonic amplitude evolution was not possible because of the lack of availability of the experimental time series.

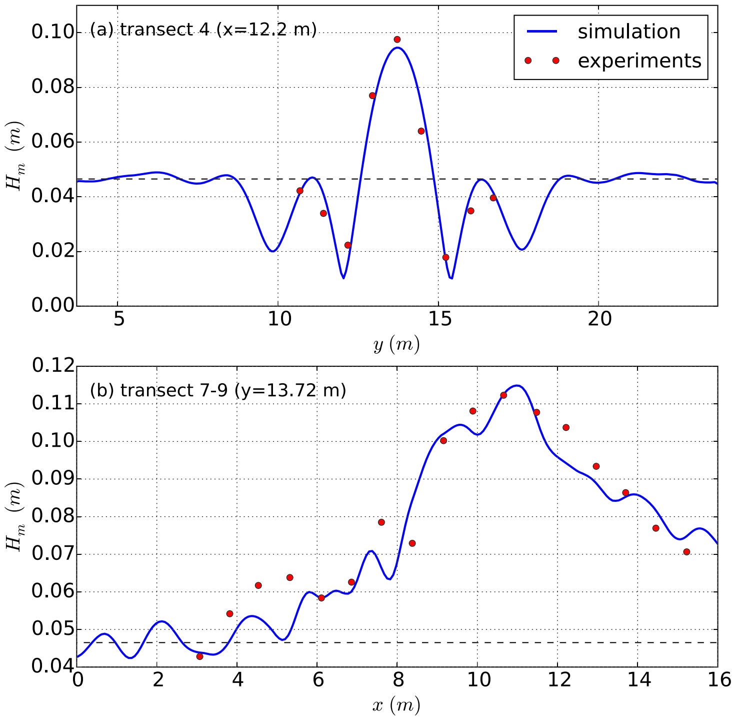

Fig. 18. Average wave height along (a) transect 4 and (b) transect 7–9, for case $M1$ of Vincent and Briggs [62]. The horizontal dashed line indicates the incident wave height.

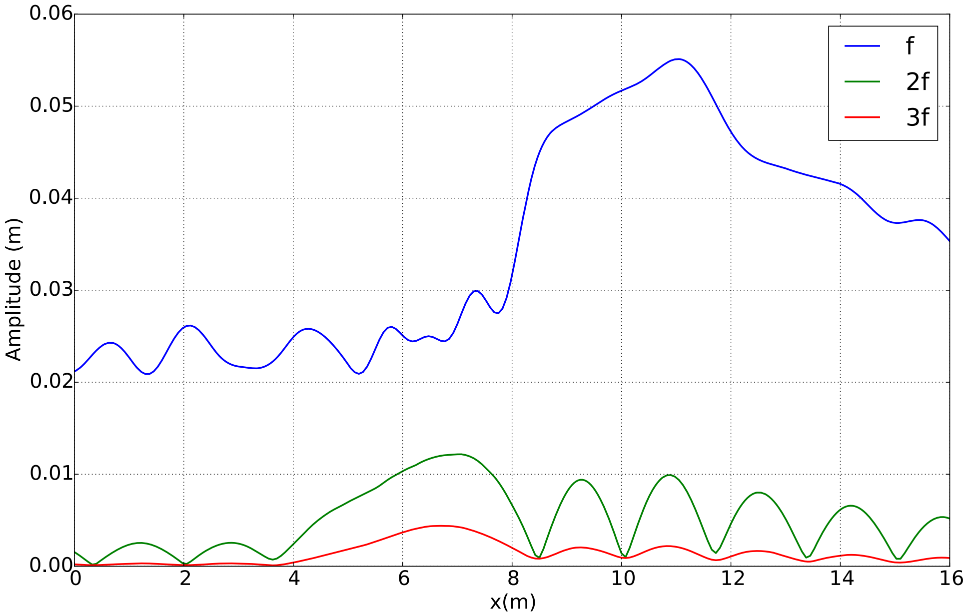

Fig. 19. Simulated spatial evolution of the first three harmonic amplitudes for case $M1$ of the Vincent and Briggs [62] experiments along transect 7–9 ($y = 13.72$ m).

For the irregular wave condition case $U3$, the computational domain and numerical parameters remained unchanged, except that the maximum order of the Chebyshev polynomial was increased to $N_T = 7$. N_T was increased to account for the presence of higher frequencies in the wave spectrum and the need to resolve accurately the dispersion relation for these frequencies. Waves were propagated during approximately 200 s (≈ 153 T_p). The high frequencies propagate at a lower celerity than the peak frequency, hence the transient period is longer than for case $M1$.

The contour plot of the free surface elevation at the end of the simulation ($t \approx 153$ T_p) for case $U3$ shows more complex and irregular 2D patterns than the regular wave case (Fig. 20), and the convergence zone is less well-defined. The effects of reflections from the lateral walls are still visible.

To compare to the experimental data (only available for transect 4), the significant wave height is computed from the free surface elevation time series by calculating $H_s = 4\sigma_\eta$, where σ_η is the standard deviation of the free surface elevation. Time

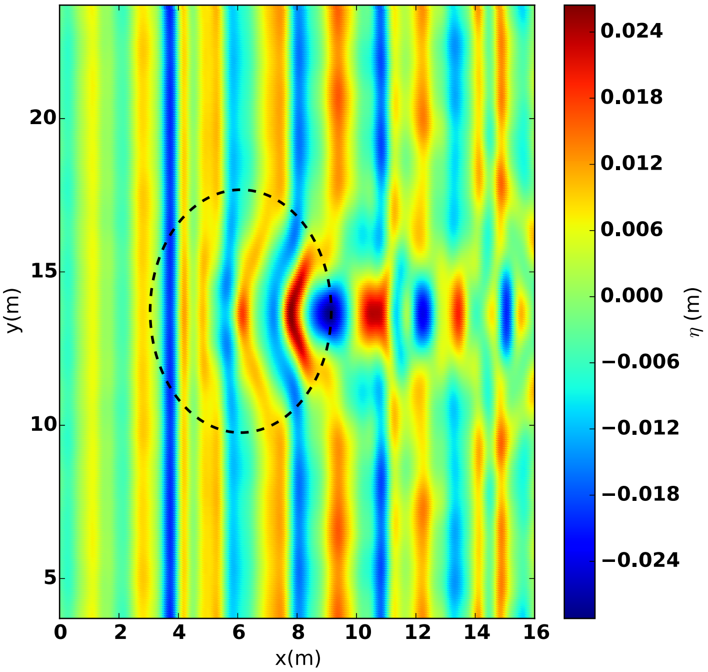

Fig. 20. Contour plot of the free surface elevation at the end of the simulation ($t \approx 153T_p$) for case $U3$ of Vincent and Briggs [62]. The dotted line indicates the limit of the elliptical shoal on the basin's floor.

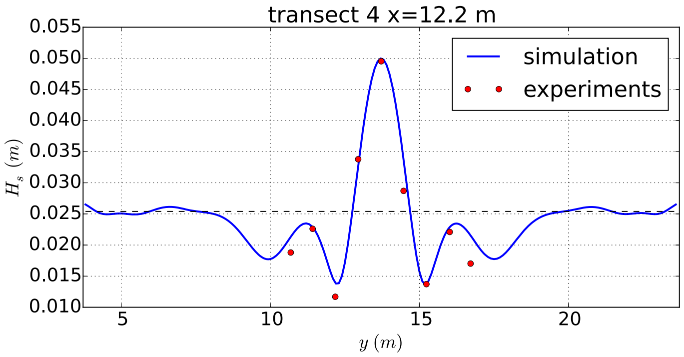

Fig. 21. Significant wave height along transect 4, for the irregular wave case $U3$ of the Vincent and Briggs [62] experiments. The horizontal dashed line indicates the incident significant wave height.

series of around one hundred wave periods are used for this analysis. The simulated H_s agrees well with the experimental observations (Fig. 21). The pattern of the significant wave height profile is similar to the one obtained for the regular wave case, with a maximum at the center due to wave convergence induced by the bathymetry (ratio ≈ 1.97).

6. Discussion and conclusions

A meshless approach, based on the RBF-FD method, was chosen for the extension of the 2DV version of a highly nonlinear and dispersive potential wave model to 3D domains. This method has the advantage of being both similar to finite difference methods and simple to implement, not requiring major adaptations to the structure of the 2DV code.

A series of sensitivity tests of the RBF-FD parameters were conducted to examine the robustness of this approach for estimating derivatives of a sinusoidal function. This study demonstrates that accurate results can be obtained with an IS-RBF without significant differences between the tested RBFs: MQ, GA, IMQ and IQ (Table 1). However, IS-RBFs depend on a shape parameter controlling the accuracy of the approximation, and the optimal value of this shape parameter depends on the estimated derivative and the form of the function. To avoid these limitations, it is recommended to use PS-RBFs, which do not depend on a shape parameter. The choice of the degree of the PS-RBF, the size of the stencil and the degree of the added polynomial is a compromise between the accuracy and computational time. For a targeted stencil size between 20 and 30 nodes, a PHS function of the form $r^7 + p3$ is recommended.

The application of the 3D version of the model to simulate two different wave basin experiments showed that complex free surface wave patterns induced by variable bathymetric profiles and the associated nonlinear effects are well reproduced by the model. The nonlinear and dispersive capabilities of the 3D model validate the use of the RBF-FD method for wave propagation in two horizontal directions.

Using the RBF-FD approach allows significant flexibility enabling the use of non-rectangular grids and local node refinement, which is of particular interest for applications to real coastal domains. Simulations of wave condition A of Whalin [64] experiments for two irregular node distributions show that a refinement following the water depth allows increasing node spacing in the deeper part of the domain, thus reducing the number of nodes (from 60,716 to 41,983) and the computational time by approximately 30% while maintaining the difference between harmonic amplitudes below about 2.5%.

With the long term objective of applying the model to real and complex nearshore domains, including wave propagation near coastal and harbor structures, work remains to be done to improve the robustness of the method and the computational efficiency of the numerical model. In some cases, instabilities may occur at or near the boundaries because of derivative estimate errors induced by asymmetric stencils at these locations. In the test cases presented here, refining the mesh close to the boundary was sufficient to avoid the appearance of instabilities. Another option is to add ghost nodes outside of the domain to reduce the one-sidedness of boundary node stencils [3], but the implementation of such a method is not trivial. More recently, Bayona et al. [7] showed that the development of instabilities at the boundaries could also be reduced by increasing the stencil beyond the threshold: $N_{sten} \geq 2M$. One last method used to stabilize the resolution of PDEs without a physical dissipative term (as is the case of the Zakharov equations) is to add a hyper-viscosity operator to the right hand-side of the evolution equation to introduce artificially a small amount of dissipation that will dampen spurious high frequency oscillations [33].

The extension of the 2DV code to 3D was accompanied by a significant increase in the computational time. The numerical efficiency of the 3D version of the model needs to be improved in order to perform simulations with large spatial domains. The resolution of the Laplace BVP linear system is the most computationally expensive part of the model, so a parallel version of the linear solver is currently used. Further work could include parallelizing the code with a domain decomposition approach. Other possibilities to reduce the computational cost are currently being explored, including using time integration schemes requiring fewer resolutions of the Laplace BVP (i.e. multi-step predictor-corrector schemes) and/or iterative solvers with suitable preconditioners.

Finally, ongoing work also includes the representation of physical processes, including depth-induced wave breaking and run-up processes to enable simulating nearshore wave environments. Further validation of the 3D version of the model is required, including cases with complex coastlines and variable bathymetries, islands, and coastal structures.

Acknowledgements

Cécile Raoult's PhD thesis was funded partially by the French ANRT (Association Nationale de la Recherche et de la Technologie) with CIFRE grant number 2013-1024.

Appendix A. m_{ijkl} terms in Eq. (10), (11) and (12)

The m_{ijkl} terms appearing in Eq. (10), (11) and (12) are terms that only depend on $h^+ = h + \eta$ and $h^- = h - \eta$ and their spatial derivatives:

$$
\begin{aligned}
m_{0220} &= h^{+2} \\
m_{0101} &= 2h^+ h_x^- \\
m_{1101} &= -2h^+ h_x^+ \\
m_{0011} &= 2h^+ h_y^- \\
m_{1011} &= -2h^+ h_y^+ \\
m_{0002} &= 4 + (h_x^-)^2 + (h_y^-)^2 \\
m_{1002} &= 2\,(h_x^- h_x^+ + h_y^- h_y^+) \\
m_{2002} &= (h_x^+)^2 + (h_y^+)^2 \\
m_{0001} &= -2h_x^- h_x^+ - 2h_y^- h_y^+ + h^+ h_{xx}^- + h^+ h_{yy}^- \\
m_{1001} &= 2(h_x^+)^2 + 2(h_y^+)^2 - h^+ h_{xx}^+ - h^+ h_{yy}^+ .
\end{aligned}
$$

Appendix B. B_{pikn} terms in Eq. (10), (11) and (12)

In Eq. (10), (11) and (12) the notation B_{pikn} is introduced:

$$
B_{pikn} \equiv \langle s^i \frac{d^k T_n}{ds^k} \rangle_p \tag{23}
$$

where $\langle f(s)\rangle_p$ is the inner product of any function f defined on the interval $[-1,1]$ with a Chebyshev polynomial T_p of order p such that:

$$\langle f\rangle_p \equiv \frac{2}{\pi c_p}\int_{-1}^{1} f(s)T_p(s)\,\frac{ds}{\sqrt{1-s^2}} \quad \text{with} \begin{cases} c_0=2\\ c_p=1 \text{ if } p\geq 1\end{cases} \tag{24}$$

The following terms have to be estimated: $\langle T_n\rangle_p$, $\langle T_{n,s}\rangle_p$, $\langle T_{n,ss}\rangle_p$, $\langle s\ T_{n,s}\rangle_p$, $\langle s\ T_{n,ss}\rangle_p$ and $\langle s^2\ T_{n,ss}\rangle_p$. They can be determined analytically as a function of n and p using the recurrence relation of the Chebyshev polynomials or from linear combinations of previously defined B_{pikn}. Only the final formulas are given below:

$$\begin{aligned}
\langle T_n\rangle_p &= B_{p00n} = \delta_{pn}\\
\langle T_{n,s}\rangle_p &= B_{p01n} = \tfrac{2}{c_p}\begin{cases} n \text{ if } p=n-1, n-3, n-5, \ldots\\ 0 \text{ otherwise}\end{cases}\\
\langle T_{n,ss}\rangle_p &= B_{p02n} = \tfrac{1}{c_p}\begin{cases} n\,(n^2-p^2) \text{ if } p=n-2, n-4, n-6, \ldots\\ 0 \ \text{ otherwise}\end{cases}\\
\langle s\ T_{n,s}\rangle_p &= B_{p11n} = \textstyle\sum_{r=0}^{n-1} B_{r01n}\begin{cases} \tfrac{1}{2}(B_{p00(r-1)}+B_{p00(r+1)}) \text{ if } r\geq 1\\ B_{p001} \text{ if } r=0\end{cases}\\
\langle s\ T_{n,ss}\rangle_p &= B_{p12n} = \textstyle\sum_{r=0}^{n-2} B_{r02n}\begin{cases} \tfrac{1}{2}(B_{p00(r-1)}+B_{p00(r+1)}) \text{ if } r\geq 1\\ B_{p001} \text{ if } r=0\end{cases}\\
\langle s^2\ T_{n,ss}\rangle_p &= B_{p22n} = \textstyle\sum_{r=0}^{n-2} B_{r02n}\begin{cases} \tfrac{1}{4}(B_{p00(r-2)}+2B_{p00r}+B_{p00(r+2)}) \text{ if } r\geq 2\\ \tfrac{1}{4}(3B_{p001}+B_{p003}) \text{ if } r=1\\ \tfrac{1}{2}(B_{p000}+B_{p002}) \text{ if } r=0\end{cases}
\end{aligned}$$

References

[1] P.R. Amestoy, I.S. Duff, J. Koster, J.-Y. L'Excellent, A fully synchronous multifrontal solver using distributed dynamic scheduling, SIAM J. Matrix Anal. Appl. 23 (1) (2001) 15–41.

[2] P.R. Amestoy, A. Guermouche, J.-Y. L'Excellent, S. Pralet, Hybrid scheduling for the parallel solution of linear systems, Parallel Comput. 32 (2006) 136–156.

[3] G.A. Barnett, A Robust RBF-FD Formulation Based on Polyharmonic Splines and Polynomials, PhD thesis, University of Colorado, 2015.

[4] V. Bayona, M. Moscoso, M. Carretero, M. Kindelan, RBF-FD formulas and convergence properties, J. Comput. Phys. 229 (2010) 8281–8295.

[5] V. Bayona, M. Moscoso, M. Kindelan, Optimal constant shape parameter for multiquadric based RBF-FD method, J. Comput. Phys. 230 (2011) 7384–7399.

[6] V. Bayona, M. Moscoso, M. Kindelan, Optimal variable shape parameter for multiquadric based RBF-FD method, J. Comput. Phys. 231 (2012) 2466–2481.

[7] V. Bayona, N. Flyer, B. Fornberg, G.A. Barnett, On the role of polynomials in RBF-FD approximations: II. Numerical solution of elliptic PDEs, J. Comput. Phys. 332 (2017) 257–273.

[8] R.K. Beatson, W.A. Light, S. Billings, Fast solution of the radial basis function interpolation equations: domain decomposition methods, J. Sci. Comput. 22 (2001) 1717–1740.

[9] S. Beji, K. Nadaoka, A formal derivation and numerical modelling of the improved Boussinesq equations for varying depth, Ocean Eng. 23 (1996) 691–704.

[10] K.A. Belibassakis, G.A. Athanassoulis, A coupled-mode system with application to nonlinear water waves propagating in finite water depth and in variable bathymetry regions, Coast. Eng. 58 (2011) 337–350.

[11] K.A. Belibassakis, G.A. Athanassoulis, Th.P. Gerostathis, Directional wave spectrum transformation in the presence of strong depth and current inhomogeneities by means of coupled-mode model, Ocean Eng. 87 (2014) 84–96.

[12] M. Benoit, M.L. Yates, F. Chazel, A comparison of simulation approaches based on the Zakharov equations for nonlinear waves in the coastal zone, in: Proceedings of the 28th International Workshop on Water Waves and Floating Bodies, L'Isle-sur-la-Sorgue, France, 2013.

[13] H.B. Bingham, H. Zhang, On the accuracy of finite-difference solutions for nonlinear water waves, J. Eng. Math. 58 (2007) 211–228.

[14] J.P. Boyd, Chebyshev and Fourier Spectral Methods: Second Edition, Revised, Dover Publications, Mineaola, NY, USA, 2001.

[15] R.E. Carlson, T.A. Foley, The parameter r^2 in multiquadratic interpolation, Comput. Math. Appl. 21 (1991) 29–42.

[16] W. Chen, L. Ye, H. Sun, Fractional diffusion equations by the Kansa method, Comput. Math. Appl. 59 (2010) 1614–1620.

[17] T.B. Christiansen, H.B. Bingham, A.P. Engsig-Karup, G. Ducrozet, P. Ferrant, Efficient hybrid-spectral model for fully nonlinear numerical wave tank, in: Proceedings of the 32nd International Conference on Ocean, Offshore Ad Arctic Engineering, Nantes, France, 2013.

[18] D. Clamond, J. Grue, A fast method for fully nonlinear water-wave computations, J. Fluid Mech. 447 (2001) 337–355.

[19] W. Craig, C. Sulem, Numerical simulation of gravity waves, J. Comput. Phys. 108 (1993) 73–83.

[20] D.G. Dommermuth, D.K.P. Yue, A high-order spectral method for the study of nonlinear gravity waves, J. Fluid Mech. 184 (1987) 267–288.

[21] G. Ducrozet, F. Bonnefoy, D. Le Touzé, P. Ferrant, 3-D HOS simulations of extreme waves in open seas, Nat. Hazards Earth Syst. Sci. 7 (1) (2007) 109–122.

[22] G. Ducrozet, F. Bonnefoy, D. Le Touzé, P. Ferrant, A modified high-order spectral method for wavemaker modeling in a numerical wave tank, Eur. J. Mech. B, Fluids 34 (2012) 19–34.

[23] A.P. Engsig-Karup, Analysis of efficient preconditioned defect correction methods for nonlinear water waves, Int. J. Numer. Methods Fluids 74 (2014) 749–773.

[24] A.P. Engsig-Karup, H.B. Bingham, O. Lindberg, An efficient flexible-order model for 3D nonlinear water waves, J. Comput. Phys. 228 (2009) 2100–2118.

[25] G.E. Fasshauer, Solving partial differential equations by collocation with radial basis functions, in: L.L. Schumaker, A.L. Mehaute, C. Rabut (Eds.), Surface Fitting and Multiresolution Methods, Chamonix, France, 1997, pp. 131–138.

[26] G.E. Fasshauer, J.G. Zhang, On choosing “optimal” shape parameter for RBF approximation, Numer. Algorithms 45 (2007) 345–368.
[27] A.I. Fedoseyev, M.J. Friedman, E.J. Kansa, Improved multiquadric methods for elliptic partial differential equations via PDE collocation on the boundary, Comput. Math. Appl. 43 (2002) 439–455.
[28] A.G. Filippini, Free Surface Flow Simulation in Estuarine and Coastal Environments: Numerical Development and Application on Unstructured Meshes, PhD thesis, Université de Bordeaux, Bordeaux (France), 2016.
[29] N. Flyer, B. Fornberg, V. Bayona, G.A. Barnett, On the role of polynomials in RBF-FD approximations: I. Interpolation and accuracy, J. Comput. Phys. 321 (2016) 21–38.
[30] C. Fochesato, S.T. Grilli, F. Dias, Numerical modeling of extreme rogue waves generated by directional energy focusing, Wave Motion 44 (2007) 395–416.
[31] B. Fornberg, N. Flyer, A Primer on Radial Basis Functions with Applications to the Geosciences, SIAM, Philadelphia, ISBN 978-1-611974-02-7, 2015.
[32] B. Fornberg, N. Flyer, Fast generation of 2-D node distributions for mesh-free PDE discretizations, Comput. Math. Appl. 69 (2015) 531–544.
[33] B. Fornberg, E. Lehto, Stabilisation of RBF-generated finite difference method for convective PDEs, J. Comput. Phys. 230 (2011) 2270–2285.
[34] B. Fornberg, C. Piret, A stable algorithm for flat radial basis functions on a sphere, SIAM J. Sci. Comput. 30 (2007) 60–80.
[35] B. Fornberg, Wright, Stable computation of multiquadric interpolants for all values the shape parameter, Comput. Math. Appl. 48 (2004) 853–867.
[36] B. Fornberg, T.A. Driscoll, G. Wright, R. Charles, Observation on the behaviour of radial basis function approximation near boundaries, Comput. Math. Appl. 43 (2002) 473–490.
[37] B. Fornberg, G. Wright, E. Larsson, Some observation regarding interpolants in the limit of flat radial basis functions, Comput. Math. Appl. 47 (2004) 37–55.
[38] B. Fornberg, E. Lehto, C. Powell, Stable calculation of Gaussian-based RBF-FD stencils, Comput. Math. Appl. 65 (2013) 627–637.
[39] R. Franke, Scattered data interpolation: tests of some methods, Math. Comput. 38 (1982) 181–200.
[40] D. Fructus, D. Clamond, J. Grue, Ø. Kristiansen, An efficient model for three-dimensional surface wave simulations: Part I: free space problems, J. Comput. Phys. 205 (2005) 665–685.
[41] M. Gouin, G. Ducrozet, P. Ferrant, Development and validation of a non-linear spectral model for water waves over variable depth, Eur. J. Mech. B, Fluids 57 (2016) 115–128.
[42] S.T. Grilli, P. Guyenne, F. Dias, A fully non-linear model for three-dimensional overturning waves over an arbitrary bottom, Int. J. Numer. Methods Fluids 35 (2001) 829–867.
[43] R.L. Hardy, Multiquadric equation of topography and other irregular surfaces, J. Geophys. Res. 76 (1971) 1905–1915.
[44] Y.C. Hon, K.F. Cheung, X.Z. Mao, E.J. Kansa, Multiquadric solution for shallow water equations, J. Hydraul. Eng. 125 (2014) 524–533.
[45] E.J. Kansa, Multiquadrics – a scattered data approximation scheme with application to computational fluid-dynamics – II solution to parabolic, hyperbolic and elliptic partial differential equations, Comput. Math. Appl. 19 (1990) 147–161.
[46] E.J. Kansa, R.E. Carlson, Improved accuracy of multiquadric interpolation using variable shape parameters, Comput. Math. Appl. 24 (1992) 99–120.
[47] E.J. Kansa, H.C. Hon, Circumventing the ill-conditioning problem with multiquadric radial basis functions: applications to elliptic partial differential equations, Comput. Math. Appl. 39 (2000) 123–137.
[48] E.J. Kansa, R.C. Aldredge, L. Ling, Numerical simulation of two-dimensional combustion using mesh-free methods, Eng. Anal. Bound. Elem. 33 (2009) 940–950.
[49] M. Kazolea, A.I. Delis, I.K. Nikolos, C.E. Synolakis, An unstructured finite volume numerical scheme for extended 2D Boussinesq-type equations, Coast. Eng. 69 (2012) 42–66.
[50] M. Kindelan, F. Bernal, P. González-Rodríguez, M. Moscoso, Application of the RBF meshless method to the solution of the radiative transport equation, J. Comput. Phys. 229 (2010) 1897–1908.
[51] P.A. Madsen, O.R. Sørensen, A new form of the Boussinesq equations with improved linear dispersion characteristics. Part 2. A slowly-varying bathymetry, Coast. Eng. 18 (1992) 183–204.
[52] S.B. Nimmala, S.C. Yim, S.T. Grilli, An efficient three-dimensional FNPF numerical wave tank for large-scale wave basin experiment simulation, J. Offshore Mech. Arct. Eng. 135 (2) (2013) 021104.
[53] N. Nishimura, Fast multipole accelerated boundary integral equation methods, Appl. Mech. Rev. 55 (4) (2002) 299–324.
[54] C. Raoult, M. Benoit, M.L. Yates, Validation of a fully nonlinear and dispersive wave model with laboratory non-breaking experiments, Coast. Eng. 114 (2016) 194–207.
[55] S. Rippa, An algorithm for selecting a good value for the parameter c in radial basis function interpolation, Adv. Comput. Math. 11 (1999) 193–210.
[56] J.E. Romate, P.J. Zandbergen, Boundary integral equation formulations for free-surface flow problems in two and three dimensions, Comput. Mech. 4 (4) (1989) 276–282.
[57] C. Shu, H. Ding, K.S. Yeo, Local radial basis function-based differential quadrature method and its application to solve two-dimensional incompressible Navier–Stokes equations, Comput. Methods Appl. Mech. Eng. 192 (2003) 941–954.
[58] S.E. Stead, Estimation of gradient from scattered data, Rocky Mt. J. Math. 14 (1984) 265–280.
[59] Y. Tian, S. Sato, A numerical model on the interaction between nearshore nonlinear waves and strong currents, Coast. Eng. J. 50 (4) (2008) 369–395.
[60] A.I. Tolstykh, D.A. Shirobokov, On using radial basis functions in a ‘finite difference mode’ with applications to elasticity problems, Comput. Mech. 33 (2003) 68–79.
[61] B. Šarler, R. Vertnik, Meshfree explicit local radial basis function collocation method for diffusion problems, Comput. Math. Appl. 51 (2006) 1269–1282.
[62] C.L. Vincent, M.J. Briggs, Refraction-diffraction of irregular wave over a mound, J. Waterw. Port Coast. Ocean Eng. 115 (1989) 269–284.
[63] B.J. West, K.A. Brueckner, R.S. Janda, M. Milder, R.L. Milton, A new numerical method for surface hydrodynamics, J. Geophys. Res. 92 (1987) 11803–11824.
[64] R.W. Whalin, The Limit of Applicability of Linear Wave Refraction Theory in a Convergence Zone, Technical report, DTIC Document, 1971.
[65] A.S.M. Wong, Y.C. Hon, T.S. Li, S.L. Chung, E.J. Kansa, Multizone decomposition for simulation of time-dependent problems using the multiquadric scheme, Comput. Math. Appl. 37 (1999) 23–43.
[66] G.B. Wright, Radial Basis Function Interpolation: Numerical and Analytical Developments, PhD thesis, University of Colorado, 2003.
[67] G.B. Wright, B. Fornberg, Scattered node compact finite difference-type formulas generated from radial basis functions, J. Comput. Phys. 212 (2006) 99–123.
[68] G.B. Wright, B. Fornberg, Stable computations with flat radial basis functions using vector-valued rational approximations, J. Comput. Phys. 331 (2017) 137–156.
[69] C.H. Wu, C.C. Young, Q. Chen, P.J. Lynett, Efficient nonhydrostatic modeling of surface waves from deep to shallow water, J. Waterw. Port Coast. Ocean Eng. 136 (2010) 104–118.
[70] G.X. Wu, R. Eatock Taylor, Finite element analysis of two-dimensional non-linear transient water waves, Appl. Ocean Res. 16 (1994) 363–372.
[71] G.X. Wu, Q.W. Ma, R. Eatock Taylor, Numerical simulation of sloshing waves in a 3D tank based on a finite element method, Appl. Ocean Res. 20 (1998) 337–355.
[72] H. Yan, Y. Liu, An efficient high-order boundary element method for nonlinear wave–wave and wave–body interactions, J. Comput. Phys. 230 (2) (2011) 402–424.
[73] M.L. Yates, M. Benoit, Accuracy and efficiency of two numerical methods of solving the potential flow problem for highly nonlinear and dispersive water waves, Int. J. Numer. Methods Fluids 77 (2015) 616–640.

[74] M.L. Yates, M. Benoit, Modélisation non-linéaire et dispersive des vagues en zone côtière: étude comparative de deux méthodes de simulation précises, in: Actes des 13èmes Journées de l'Hydrodynamique, Chatou, France, 2012.
[75] V.E. Zakharov, Stability of periodic waves of finite amplitude on the surface of a deep fluid, J. Appl. Mech. Tech. Phys. 9 (2) (1968) 190–194.
[76] X. Zhou, Y.C. Hon, J. Li, Overlapping domain decomposition method by radial basis functions, Appl. Numer. Math. 44 (2003) 241–255.
[77] X. Zhou, Y.C. Hon, K.F. Cheung, A grid-free, nonlinear shallow-water model with moving boundary, Eng. Anal. Bound. Elem. 28 (2004) 967–973.